Fundamental modelling of the expansion injection moulding with its simulation and the material degradation analyses on the moulded parts

An der Montanuniversität Leoben zur Erlangung des akademischen Grades

Doktor der montanistischen Wissenschaften

eingereichte

Dissertation

von

Dipl.-Ing. Jegadeesan Rajganesh

geb. in Sivakasi / India

AFFIDAVIT

I declare on lieu of oath, that I wrote this thesis and performed the associated research myself, using only literature cited in this volume.

10.01.2011
Datum

Unterschrift

Acknowledgements

The research work of this dissertation was performed at the Institute of Polymer Processing, Montanuniversitaet Leoben, Austria in cooperation with Engel Austria GmbH, Schwertberg, Austria within a so-called BRIDGE project titled “Fundamentals of Expansion Injection moulding and its Simulation (Project no. 812967)”. The Austrian Research Promotion Agency (FFG) funded the BRIDGE-project.

I wish to thank my adviser, Em.Univ.Prof.Dr.-Ing.Günter R. Langecker for his valuable guidance and instructions that made this dissertation possible. In addition, I wish to thank him for his active commitment and encouragement that were invaluable to me.

Foremost, my grateful acknowledgement is to Univ.Prof.Dr.mont.W. Friesenbichler for provided me this opportunity to perform this research work at the Institute. I must convey my sincere thanks to him for his active guidance and practical support on my work.

I would like to express my gratitude to Univ.Prof.Dr.G. Steinbichler, for his strong cooperation during the research period. I also wish to thank both Dipl.-Ing.J. Giessauf and Dr.G. Pillwein for their constructive guidance and assistance during the development of the simulation software. I am very thankful to Prof.Dr. A. Lampl for his help and support during the modelling of the expansion injection moulding process.

I convey my heartfelt thanks to Ao.Univ.-Prof. Dipl.-Chem. Dr. N. Aust for performing molar mass analyses and his supports for the research work about the molar mass degradation analyses on the moulded parts.

I would like to convey my special thanks to both Dipl.-Ing. I. Duretek and Dr.mont. T. Lucyshyn. They supported and guided me during the practical works and helped me a lot to solve problems. I would like to thank Ms. A. Germuth, for helping me to carry out the measurements on the injection moulding machine. I am grateful to all the staffs and colleagues at the Institute of Polymer Processing, for all the assistance and advice I received over the years.

I am very thankful to my ex-student colleagues Dipl.-Ing. M.Kipperer, Dipl.-Ing. M. Battisti, Dipl.-Ing. M. Narnhofer, B.Sc. M. Mach, B.Sc. G. Brend , H. Juster and M. Fasching for their help in the research work during their master thesis and bachelor thesis.

This is an opportunity to express my heartfelt thanks to Prof.Dr.Dr.mont.C.T. Vijayakumar, for his encouragement.

I convey my sincere gratitude to my wife Mrs. R. Jaya Sudha for all her aid and support I received during the VBA programming. Without her helps, it would not be possible for me to complete the software program successfully.

Finally, I wish to thank my parents Mr. D. Jegadeesan and Mrs. J. Kalavasugi, my kids both R. Hrithik Sreekumar and R. Naveen Srikumar, and my family members for their emotional support, encouragement, and love.

Leoben, January 2011

Jegadeesan Rajganesh

Abstract

For the injection moulding of thin wall parts with wall thicknesses of less than 1 mm and flow length/wall thickness ratios up to 400:1, an innovative injection moulding technique called expansion-injection moulding (ENGEL X-Melt) was developed by ENGEL Austria GmbH, Austria. The main feature of this process is the separation of the melt compression and injection phases. First, the melt is compressed to a maximum compression pressure in the space in front of the injection screw. When the pressure is relieved, the melt will expand explosively inside the cavity, thus filling the cavity at a high volume flow rate. To reduce development times in the field of expansion injection moulding it is intended to use simulation programs. For this reason, it is necessary to develop suitable calculation software based on a physical model for this technique. Within this research work, a physical model for the simulation of the expansion phase was developed. Based on the physical model, a calculation program called Xmeltsoft V.1.0 was developed for the simulation of the expansion injection mould process for simple thin-wall parts.

The calculated compression pressure can be set on the machine. However, in contrast to the compression pressure, the geometry and thickness of the mould cavity and the viscosity of the chosen thermoplastic material influence the end pressure. During the expansion phase of injection moulding, the pressure in the injection unit drops from a pre-set compression pressure to an end pressure. The methodical approach for the calculation of the minimum required filling pressure involves segmentation of the longest flow path into several serially connected small segments. To improve the calculation results, the effect of the frozen skin layer thickness is taken into account. For the purpose of verification, a check card part with a wall thickness of 0.5mm was chosen for the simulation. The check card parts were produced by the expansion injection moulding process using a hybrid Engel injection moulding machine (Type VC 940/130 Electric). The experimental results in comparison with the simulation results of the check card part are presented for a PP, PS and ABS/PC materials.

Additionally within this research work, molar mass degradation analyses were done on the moulded parts in order to assess the influence of the processing parameters on material degradation. For the degradation analyses, the samples were collected from different sections of the moulded part. The molar mass analyses were carried out using Size Exclusion Chromatography (SEC) at the Institute of Chemistry of Polymeric Material, Montanuniversitaet Leoben. The material degradation analysis were done on the moulded parts with materials of PP and PS.

.

Kurzfassung

Für das Spritzgießen extrem dünner Wandstärken (kleiner 1 mm und Fließweg/Wanddicken-Verhältnissen bis 400:1) entwickelte ENGEL Austria GmbH (Österreich) das Expansionsspritzgießen, eine innovative Neuheit in der Spritzgießtechnik. Hauptcharakteristikum dieses Verfahrens ist die Trennung von Schmelzekompression und Einspritzphase. Als erstes wird die Schmelze im Schneckenvorraum bei geschlossener Nadelverschlussdüse bis zu einem maximalen Vorkompressionsdruck komprimiert. Nach dem Öffnen des Nadelverschlusses wird die Schmelze plötzlich entlastet, expandiert und füllt in Sekundenbruchteilen mit einem hohen Volumenstrom die Werkzeugkavität. Um Entwicklungszeiten auf diesem Gebiet zu verkürzen strebt man den Einsatz von Simulationsprogrammen an. Aus diesem Grund ist es nötig, eine eigenständige, dem physikalischen Modell des Expansionsspritzgießens gerecht werdende Berechnungssoftware zu entwickeln. Im Zuge dieser Forschungsarbeit ein physikalisches Modell zur Simulation der Expansionsphase entwickelt. In weiterer Folge wurde auf diesem Modell basierend ein Berechnungsprogramm Xmeltsoft V.1.0 zur Simulation des Expansionsspritzgießprozesses für dünnwandige Teile erstellt.

Der berechnete Kompressionsdruck kann auf der Maschine eingestellt werden. Im Gegensatz zum Kompressionsdruck ist der Enddruck durch die Geometrie der Werkzeugkavität und der Viskosität des Materials bestimmt. Während der Expansionsphase fällt der eingestellte Kompressionsdruck auf den Enddruck ab. Der methodische Zugang zur Berechnung des Minimalfülldruckes beinhaltet die Segmentierung des längsten Fließweges in mehrere seriell gelegene Einzelsegmente. Die Einflüsse der eingefrorenen Randschicht werden mitberücksichtigt, um die Genauigkeit der Berechnungsergebnisse zu verbessern. Als Referenzobjekt zur Überprüfung der Simulationsgenauigkeit wurde ein Modellbauteil (Scheckkarte) mit einer Wandstärke von 0,5 mm gewählt. Diese Bauteile wurden daraufhin mit einer Hybridspritzgussmaschine der Firma ENGEL Austria GmbH (Type VC 940/130 Electric) hergestellt. Der Vergleich von experimentellen Daten und berechneten Daten wurde für die Scheckkarte anhand PP, PS und eines ABS/PC durchgeführt.

Zusätzlich wurde der Molmassenabbau im fertigen Spritzgießteil gemessen, um die Auswirkung der Verarbeitungsparameter auf den Materialabbau zu untersuchen. Hierzu wurden an verschiedenen Stellen des Formteiles Proben entnommen. Die Untersuchung der Molmassen wurde anschließend am Institut für Chemie der Kunststoffe an der Montanuniversität Leoben mithilfe der Size Exclusion Chromatography (SEC) durchgeführt. Die zur Probenentnahme verwendeten Spritzgießteile bestanden aus Polystyrol und Polypropylen.

Table of contents

1 INTRODUCTION AND OBJECTIVES 9

2 EXPANSION INJECTION MOULDING (EIM) 11

2.1 High speed thin-wall injection moulding - Theory and practice 11
2.2 Expansion injection moulding process (EIM) 14
2.3 Technical concept for EIM 15
2.4 Multi-shot expansion injection moulding 16

3 PHYSICAL MODEL TO DESCRIBE THE PROCESS 18

3.1 Relationships between the compressed melt cushion and shot weight 19
3.2 Calculation of the total compression work 21
3.3 Calculation of the needed melt cushion or the required compression pressure 22
3.4 Calculation of the mass flow rate during the melt expansion 25

4 THEORETICAL BACKGROUND OF THE MOULD FILLING PHASE 28

4.1 Governing equations for the filling phase 28
4.1.1 Continuity equation 28
4.1.2 Momentum equation 28
4.1.3 Energy equation 29
4.2 Viscosity model for the filling calculation 30
4.2.1 Viscosity model requirements 31
4.2.2 Power law model 31
4.2.3 Moldflow second order Model 32
4.2.4 The Ellis viscosity model 32
4.2.5 The Carreau Model 32
4.2.6 The Cross Model 33
4.3 Concept of representative viscosity 33
4.4 No-flow temperature 36
4.5 Formation of the frozen skin layer 37
4.5.1 Dietz and White model 38
4.5.2 Influence of frozen skin layer 40
4.6 Change in melt temperature due to effect of cooling 43
4.7 Viscous dissipation 44
4.7.1 Change in melt temperature due to viscous dissipation 45

5 CALCULATION PROCEDURE FOR THE SIMULATION 48

5.1 Introduction to the calculation method 48
5.2 Approximate calculation of the filling time 50
5.3 Methodical approach used for the calculation of minimum required end pressure 52
5.4 Steps involved in the calculation of minimum required injection pressure 53
5.5 Calculation of maximum compression pressure 59
5.6 Calculation of mass flow rate as a function time 59
5.7 Optimization of calculated minimum required end pressure and calculated compression pressure 60

6 THE DEVELOPED SIMULATION SOFTWARE - *XMELTSOFT* 62

7 IMPROVED MATERIAL DATA 75

7.1 Material data requirements for the expansion injection moulding 75
7.2 Approach of acquiring reliable material data 75
7.3 Investigated thermoplastic materials 77
7.3.1 Polypropylene (PP HG313MO) 77
7.3.2 Polystyrene (PS 495F) 77
7.3.3 ABS/PC blend (Bayblend T65) 78
7.4 Pressure-volume-temperature (pvT)-diagram 78
7.4.1 Theoretical fundamentals 78
7.4.2 Experimental Procedure 81
7.4.3 Results of the pvT- data measurement 83
7.4.3.1 PP HG313MO 83
7.4.3.2 PS 495F 85
7.4.3.3 Bayblend T65 86
7.5 Viscosity data 88
7.5.1 Theoretical background 88
7.5.2 Temperature dependency of viscosity 89
7.5.3 Pressure dependency of viscosity 91
7.5.4 Temperature- and Pressure invariant master curve 93
7.5.5 Different methods to calculate the pressure coefficient of viscosity 95
7.5.5.1 Analysis of non-linear pressure profile 95
7.5.5.2 Calculation of pressure coefficient of viscosity from pvT-data 97
7.5.5.3 Determination of β value by enhanced exit pressure method 98
7.5.6 Influence of the viscous dissipation 100
7.5.7 Rheological measurement techniques 102
7.5.7.1 High pressure capillary rheometer with round capillary die 102
7.5.7.2 High pressure capillary rheometer with back pressure chamber 105
7.5.7.2.1 Evaluation methods of the pressure coefficient of viscosity (β) 108
7.5.7.3 Injection moulding machine rheometer with the rheological injection mould 110
7.5.8 Experimental results 114
7.5.8.1 PP HG313MO 114
7.5.8.2 PS 495F 122
7.5.8.3 Bayblend T65 127
7.6 Thermal conductivity 130
7.6.1 Theoretical background 130
7.6.2 Measurement techniques 132
7.6.3 Experimental results 134
7.7 Specific heat capacity 137
7.7.1 Theoretical background 137
7.7.2 Measurement method 137
7.7.3 Experimental results 138

8 SIMULATION FOR A MODEL THIN-WALL PART 140

8.1 Simulation of the check-card part for PP HG313MO 140
8.2 Simulation of the check-card part for PS 495F 146
8.3 Simulation of the check-card part for Bayblend T65 150

9 SYSTEMATIC EXPANSION INJECTION MOULDING EXPERIMENTS 153

9.1 Experimental setup 153
9.1.1 Injection moulding machine 153
9.1.2 Check card mould 154
9.1.3 Experimental procedure 155
9.2 Experimental results for PP HG313MO 156
9.2.1 Mould filling analysis 156
9.2.2 Influence of the needle-valve opening duration on the part quality 166
9.3 Experimental results for PS 495F 168
9.3.1 Mould filling analysis 168

9.4 Experimental results for ABS/PC Bayblend T65 171
9.4.1 Mould filling analysis 171

10 MOLAR MASS DEGRADATION ANALYSES OF THE MOULDED PART 173

10.1 Theoretical background about molar mass of polymers 174
10.2 Over view of the size exclusion chromatography 175
10.3 Experimental setup and evaluation technique for MMD 176
10.4 Sample preparation technique for SEC analyses 177
10.5 Results of the molar mass analyses for check-card parts 178
10.5.1 For check-card produced with PP HG313MO 178
10.5.2 For check-card produced with PS 495 F 183
10.6 Molar mass degradation analyses for a practical thin-wall part 187
10.6.1 Results of the molar mass analyses for battery cover parts 188

11 FUTURE PERCEPTIVE 193

11.1 Influence of elastic deformation in expansion injection moulding 193
11.2 Further development potentials for EIM process simulation 195

12 SUMMARY AND CONCLUSION 197

13 LIST OF LITERATURES 200

14 LIST OF SYMBOLS AND UNITS 206

1 Introduction and Objectives

Today's injection moulding faces many new challenges including cost-efficient moulding production and further pushing the limits of what is currently possible in modern injection moulding. In modern injection moulding, the key words used are faster cycles, thinner wall thicknesses with the part weight from 0.1 g to 50 g and more precise higher quality parts. Thin-wall injection moulding has become increasingly important due to the explosive growth of wireless telecommunication and portable electronic devices that required thinner and lighter plastic housings some of which exhibit micro-scale features. The most important user industries of thin-walled as well as micro technology are the automotive industry, the consumer goods industry, medical technology, telecommunications and industrial process technology. The findings of a Nexus market study [1] estimated that the market for micro- and thin-walled technical products increased from a base figure of 11.5 billion USD in 2004 to a worth of 24 billion USD in 2009. A further growth of the market for micro system is predicted [1,2].

In current high-speed injection moulding of thin-walled precision parts the main benchmarks considered by part manufactures are reduced cycle time, reduced wall thickness, and high part quality with tight tolerances. Since the wall thickness is entered in the calculation for the cooling time in squared form, reducing the wall thickness makes the process cycle faster, which leads to more profit for the part manufactures. Reducing the wall thickness of the part not only reduces the cooling time as well as the cycle time but also material costs. In modern electronic and communication devices, a wall thickness of less than 0.3 mm and a flow length/wall thickness ratio up to 450:1 is common. The prerequisites for such electronic products are tight tolerances and precision of the moulded part, which is achieved by using a highly accurate injection moulding machine and a perfectly build mould. Apart from a very high level of reproducibility, the machine must be designed for high speed, since the injection mouldings of the thin wall parts demands high injection speeds (injection velocity up to 1000 mm/s). Materials with extremely high Melt-Volume Flow rate (MVR) are used in combination with injection speeds of approximately 300 mm/s [3]. To achieve this high speed, the injection moulding machine is equipped with a separate hydraulic accumulator for the injection unit. In the testing stage these machines, a mould with several pressure transducers in the flow path were used. Surprising results were seen; although the screw reached a speed of 1000 mm/s, the melt flow front of the material did not match the screw speed [4,5]. A large part of the energy introduced during the screw moving is used to compress the melt in the barrel in front of the screw. Further, the melt continued to flow into the cavity even after the screw stopped. There are several reasons for this deviation such as the compressibility of the hydraulic fluids, the elastic deformation of machine parts, and more importantly, the compressibility of the polymer melt. The highly compressed melt in front of the screw expands into the mould until pressure equilibrium is attained. Because of this investigation, ENGEL Austria GmbH developed an alternative process for thin wall injection moulding namely the

ENGEL “X-melt” process, which can be described as an expansion injection moulding process. The expansion injection moulding is a completely new process for the injection moulding of small, thin-walled parts. The basic idea behind this new process is that the pressure of the melt itself can be used for the injection process, waiving the need for a separate hydraulic accumulator for the injection unit. The main feature of the expansion injection moulding process is dividing the injection process into two completely separate processes of compression and expansion. For that, the injection unit or the mould should be equipped with a shut-off nozzle. The compression phase is completed once there is enough energy stored in the melt for the injection process. Injection is effected simply by opening the shut-off nozzle and allowing the melt to expand into the mould.

To reduce development times in the field of expansion injection moulding it is intended to use simulation programs. For this reason, it is necessary to develop suitable simulation software based on a physical model for this technique. The objectives of this research work were at first to develop a physical model for the expansion injection moulding based on the scientific knowledge and to develop a user-friendly simulation program to simulate the expansion injection moulding process for a chosen thin walled part. For the accurate simulation of the expansion injection moulding, the necessary material data for the simulation has to be measured under real practical conditions, which are applicable for the thin walled injection moulding. For instance, the melt viscosity data has to be measured not only as a function of shear rate and temperature, but also the viscosity as a function of pressure is significant. Further, the pvT-data measured up to 2500 bar and thermal data like the thermal conductivity as a function of temperature and pressure and the specific heat capacity as a function of temperature are important material data. With the improved material data of a chosen material, the expansion injection moulding simulation was carried out for a model thin-walled part. In order to verify the simulation results, the model thin walled parts were produced on a hybrid injection moulding machine, which was supplied by ENGEL Austria GmbH. Additionally within this research work, the molar mass degradation analyses were done on the expansion injection moulded parts in order to find the influence of the processing parameters on the material degradation. For the degradation analyses, the samples were collected from different sections of the moulded part. The molar mass analyses were carried out with the help of the Size Exclusion Chromatography (SEC) at the Institute of Chemistry of Polymeric Material, University of Leoben. The material chosen for the degradation analyses were PP and PS.

Thus, the scientific tasks of the work were categorized within four sections, which were titled as follows:

a) Improved material data
b) Modelling the expansion injection moulding
c) Systematic expansion injection moulding experiments
d) Molar mass degradation analysis

2 Expansion injection moulding (EIM)

2.1 High speed thin-wall injection moulding - Theory and practice

To mould thin-walled and micro scaled parts, high melt flow rates and injection speeds are necessary. Otherwise, an incomplete filling can occur due to rapid cooling of the polymer. For the injection moulding of very thin parts with wall thicknesses significantly below 1 mm and flow length/wall thickness ratios of up to 450:1, are primarily being produced by injection moulding machine equipped with a hydraulic accumulator system. Hydraulic accumulators allow fluids to be stored under pressure. Use is made of the high compressibility of gases, mainly nitrogen, to pressurise the hydraulic oil at high pressure in a bladder or a ram accumulator. With the aid of highly dynamic servo-valves, this energy can be used, for example, to attain high injection speed. With the help of high flow bladder accumulators, the hydraulic fluid speeds of up to 140 l/s can be attained [5,6]. Figure 1 shows an injection moulding unit equipped with a hydraulic accumulator and mounted with a rectangular test strip mould.

Tests carried out by ENGEL Austria GmbH during the production of thin-walled parts on injection moulding machines with hydraulic accumulators showed a major discrepancy between theory and practice. The test was carried out on a thin-walled part having a wall thickness of 0.4 mm, a width of 10 mm and a flow distance of 150 mm. The test was carried out on an Engel Victory 200/120 injection moulding machine with the clamping force of 1200 kN. The material used for the investigation was a conventional polystyrene injection moulding grade. The total part weight including sprue runner system is 3.94 g. To record the flow front development during the process, the mould was equipped with three pressure sensors (DS 2 to DS 4). The pressure sensor (DS1) measures the melt pressure in the screw antechamber. The hydraulic accumulator was set to a pressure of 160 bar. With a transmission ratio between the effective injection piston surface area and the screw cross section of 15.9:1, this is equivalent to a specific injection pressure of 2545 bar. After opening of the machine shut-off nozzle, the sprue is first filled at a mean injection pressure of approximately 530 mm/s. When the melt front reaches the mould cavity, the flow resistance and melt pressure at DS1 increases rapidly to a maximum pressure of 2300 bar (see figure 2).

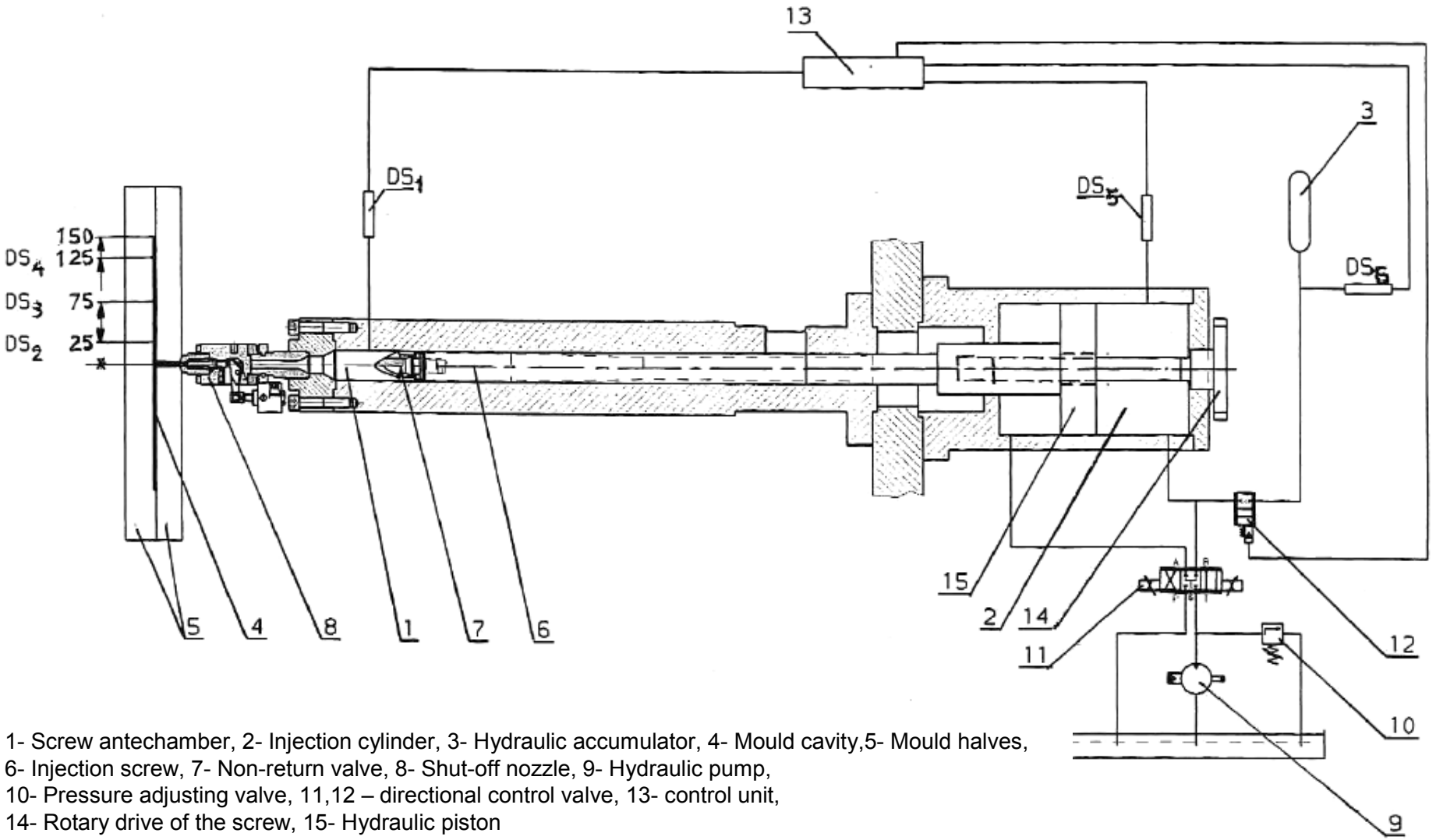

1- Screw antechamber, 2- Injection cylinder, 3- Hydraulic accumulator, 4- Mould cavity,5- Mould halves,
6- Injection screw, 7- Non-return valve, 8- Shut-off nozzle, 9- Hydraulic pump,
10- Pressure adjusting valve, 11,12 – directional control valve, 13- control unit,
14- Rotary drive of the screw, 15- Hydraulic piston

Figure 1: Injection unit equipped with a hydraulic accumulator [7].

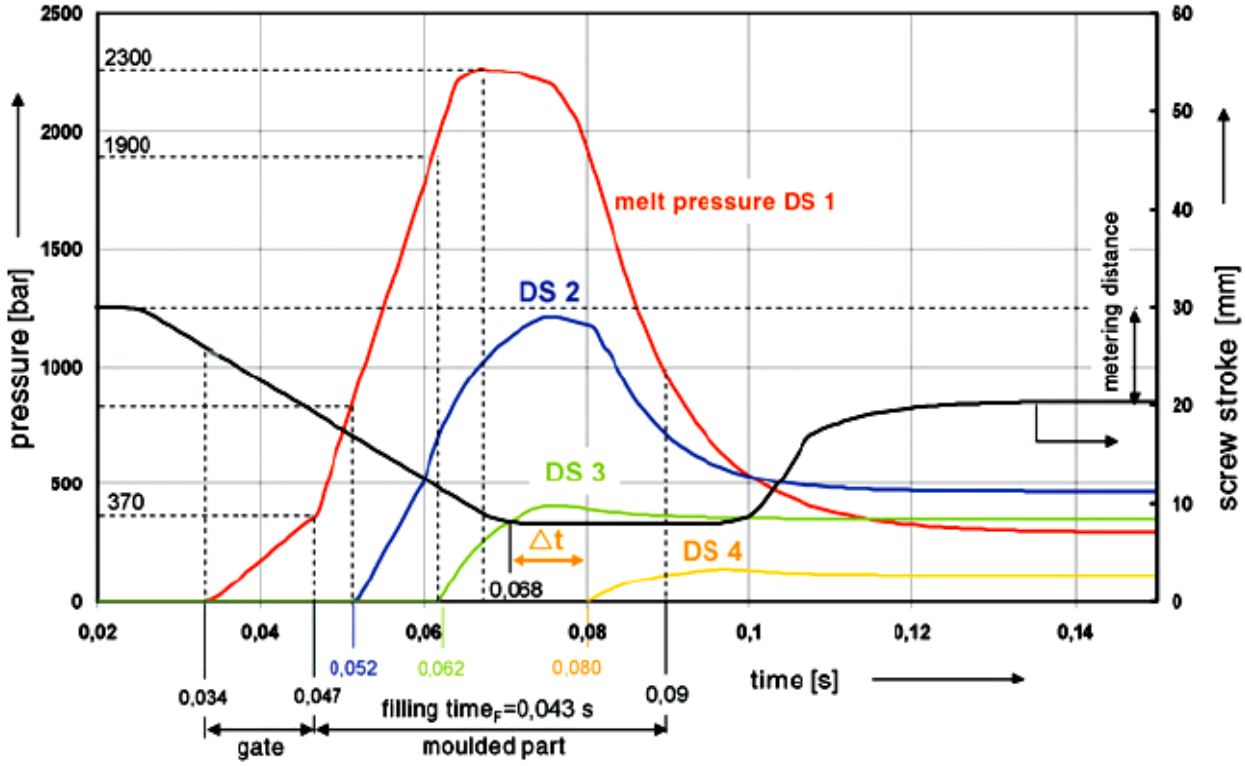

Figure 2: Process profile for thin-wall injection moulding (test strip part) with hydraulic accumulator, shown by the measured melt pressure in the screw antechamber and along the flow path in the cavity [5].

The cavity is not yet completely filled until the screw reached its maximum forward motion. The pressure transducer DS 2 shows at this point a pressure value of about 850 bar and the melt front reached the pressure transducer DS 3 a hundredth of a second later at 1900 bar in the screw antechamber. The melt front reached the cavity position DS 4 only after the screw has remained at its final position after 0.012 s (see Δt in figure 2). After 0.068 s, the screw has displaced the entire melt volume. More than 75% of the filling time 0.047 s is needed solely to fill the sprue. However, the remaining 0.021 s until the end position of the screw is reached account only 50% of the time needed to volumetrically fill the cavity. The experimental results showed that it is impermissible to deduce the position of the melt front in the cavity from the injection speed. There are several reasons for this deviation such as the compressibility of the hydraulic fluids, the elastic deformation of machine parts, and more importantly, the compressibility of the polymer melt. The highly compressed melt in front of the screw expands into the mould until pressure equilibrium is attained. The compressibility of the melt is acting more or less as an intermediate energy and melt accumulator. Through the rapid pressure build-up with the hydraulic accumulator, the plastic melt is compressed in the screw antechamber and the nozzle area. At the same time, the hydraulic fluid in the injection cylinder also becomes compressed and the parts of the injection unit under pressure become deformed. These test results show clearly that the filling of the cavity when injection moulding very thin parts with a hydraulic accumulator occurs for the most part

without any screw advance, solely through expansion of the pressurised melt. Because of this investigation, ENGEL Austria GmbH developed an alternative process for thin wall injection moulding namely the ENGEL “X-melt” process, which can be described as an expansion injection moulding.

2.2 Expansion injection moulding process (EIM)

The expansion injection moulding (EIM) process can be divided into the two process steps of compression and expansion. For that, the injection unit is equipped with a controllable shut-off nozzle or the mould with hot runner shut-off nozzles. From the process-engineering point of view, the variant with the shut-off nozzle in the hot runner nozzle is preferable because the pressurised melt accumulator can move as close as possible to the mould cavity with the result that only low pressure losses occur in the dynamic filling phase. This makes it possible to achieve the short filling time necessary for extremely thin walled injection moulded parts. After the mould has be closed and the injection unit pressed against it, the melt is compressed with the shut-off nozzle closed (figure 3). The melt is compressed to the maximum compression pressure of approximately 1800 to 2500 bar in the space in front of the injection screw. Since the compression phase brings about an increase in the melt temperature, the processing temperature in the plasticizing unit can be reduced on average by around 15% compared with injection moulding with a hydraulic accumulator. The short delay time after the compression allows pressure equilibrium to be established in the melt. After a uniform pressure level has been attained, the shut-off nozzle opens, enabling the melt to expand into the cavity. The cavity starts to fill up without any forward movement of the screw. The servo-electric drive unit of the injection device guarantees the consistency of the pre-loaded melt volume. With the servo-electric drive unit, the screw can be axially positioned as desired and kept exactly in this position even under high pressure and during the sudden pressure change. During the expansion phase, the melt pressure in the screw antechamber drops from the maximum compression pressure to

an end pressure value. Due to the pressure drop, the volumetric flow required to fill the cavity changes during the filling time. The pre-compressed pressure, the compressed melt volume and the flow resistance influence the generated volumetric flow rate. The end pressure will act as a holding pressure just like in the conventional injection moulding machine. The holding pressure time is very short in practice. With very thin or injection moulded using this process, the end pressure should ensure a secure part filling.

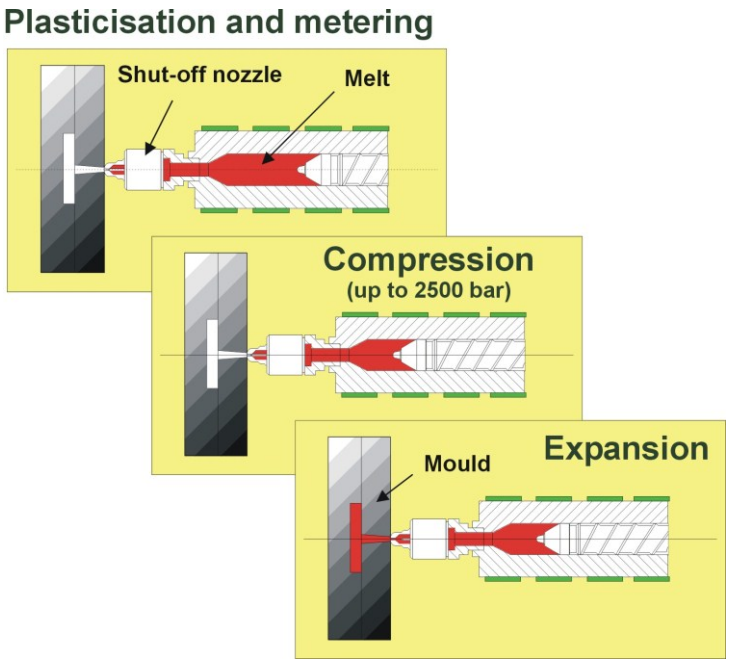

Figure 3: Processing steps for the expansion injection moulding [4].

The expansion injection moulding improves the reproducibility of the process parameters during injection moulding, as a result of which the precision is increased, especially with small parts. The variations in part weight are reduced by half percent, from +/- 0.07% to +/-0.03% [4]. Typical shot weights are between 0.1 and 20 g, and wall thicknesses of 0.8mm down to approx. 0.1 mm. The ultra-thin 0.17 mm battery housing made of a PC/ABS blend was produced by using this innovative process by Engel [5].

2.3 Technical concept for EIM

The machine particularly suitable for use with the expansion injection moulding is all electric injection moulding machine or hybrid machines with the electrical injection units [3]. With the electric injection unit machine, the screw can be placed in any desired axial position and be kept at precisely this position even with high pressures. In addition to the ability to lock the screw in the axial position, an appropriate locking system is also required for closing of the injection nozzle. A hydraulically or pneumatically driven shut-off nozzle achieves this. The injection pressure usually opens the needle on shut-off nozzle in the standard injection moulding. However, in the expansion injection moulding, the needle must remain closed during the entire compression phase and only open when the expansion phase starts. As an another option with the expansion moulding, this shut-off nozzle with needle valve can also be integrated in the hot runner nozzle. In multi-cavity expansion moulding, the basic requirement for high and uniform part consistency in all cavities is an absolute synchronous filling of the cavities. So the hot-runner system should be optimised in such a way that the needle valve nozzles open at exactly same time. The needle valves in the hot runner nozzle are controlled via a common frame synchronising all nozzle movements. Individually controlled needle

valves are unable to satisfy the requirements of multi-cavity expansion injection moulding.

2.4 Multi-shot expansion injection moulding

In the multi-shot expansion injection moulding, about 10 to 15 times part volume of the melt is metered in front of the screw. The large stored melt volume makes use of the metered melt volume to fill the small cavity volume repeatedly without any separate metering stock. Lampl, A. in his publication [7] showed the possibility of the multi-shot expansion injection moulding. The check card part with 0.5 mm wall thickness was used for the multi-shot expansion injection moulding. The dimension of the used check-card part is 85mm X 54 mm X 0.5 mm and the part volume is 2.295 cm^3. The material used for the investigation was a polystyrene (PS 143E from BASF). The parts were produced on the Engel injection moulding machine (type E-300/100). The mould is equipped with a hot runner shut-off nozzle with pinpoint gate for the injection. After the melt in the screw antechamber and hot runner nozzle (volume of 54 cm^3) was compressed to the maximum compression pressure (p_c) of 1400 bar, the needle valve of hot runner nozzle was opened. During the part filling, the pressure in the screw antechamber drops from 1400 bar to the end pressure (p_E) of 891 bar. With the same manner, seven expansion-moulded parts were produced with the seven shots. The maximum compression pressure was kept constant at all shots. Lampl, A. noticed that with the constant compression pressure during the multi-shot, the end pressure value at each shot decreases linearly with the increasing shot numbers. Ultimately Decreasing end pressure at each shot causes a decrease in part weight. Figure 4 show the values of the measured end pressure, the cavity pressure and part weight during seven shots with the constant compression pressure of 1400 bar.

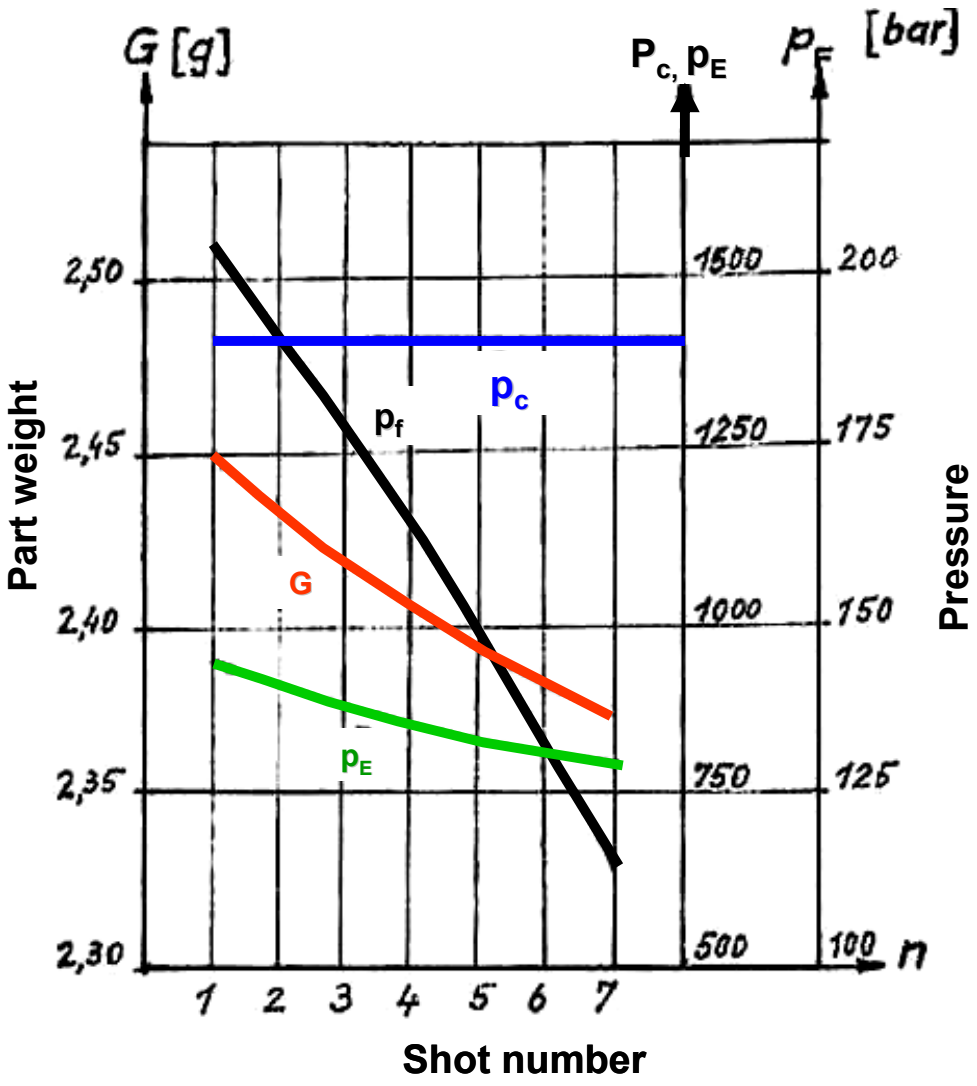

Figure 4: Measured values of pressures and part weight in multi-shot expansion injection moulding [7], where p_c is the compression pressure, p_E is the end pressure, p_f is the pressure in the cavity near to injection point and G is the part weight.

As shown in figure 4, the part weight value drops from 2.450 g to 2.381 g, this is about the weight difference of about 0.069 g. The part weight is the important quality parameter. Therefore, a constant part weight must be ensured at every injection shot. For that, we need a physical model to adapt the compression pressure in order to reach a constant end pressure for each shot.

3 Physical model to describe the process

The process cycle of the expansion injection moulding can be described in the pvT-diagram as in figure 5. After the mould halves are closed, the melt is compressed to the maximum compression pressure (p_C) in the injection unit with the shut-off nozzle closed. Due to the compression heat at high pressure, the melt temperature increases to a higher melt temperature. Rogelj et. al. showed that for the investigated polystyrene material, the melt temperature increases due to compression was approx. 18.5°C when compressing the melt up to 2000 bar [8]. Due to the increase in the melt temperature, the specific volume of the melt shifts to the higher temperature value. By opening the shut-off nozzle, the compressed melt is allowed to expand, which leads to a decrease in pressure at the screw antechamber from maximum compression pressure (p_C) to an end pressure (p_E) as a function of expansion time (t). These pressure differences generate volumetric flow rates to fill the cavity.

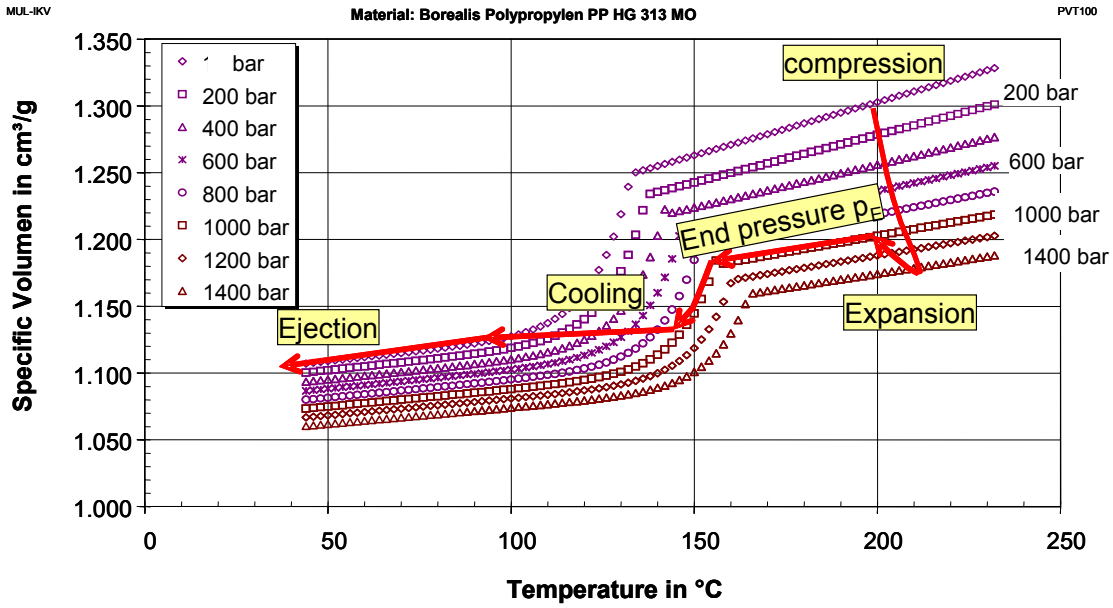

Figure 5: Process cycle of the expansion injection moulding in the pvT-diagram of a semi crystalline material.

In current practise, the maximum compression pressure is chosen manually until achieving a proper filling of the cavity during the expansion phase. Therefore, there is a demand for the mathematical process model, in order to calculate the maximum compression pressure for the selected thermoplastic material at the chosen processing conditions and for the chosen thin wall part geometrical dimension.

3.1 Relationships between the compressed melt cushion and shot weight

The expansion process can be described by the pvT- relationship of the thermoplastic materials and the processing conditions such as backpressure (p_{st}), end pressure (p_E), compression pressure (p_c) and melt cushion (m_0). The relationships between the shot weight (m), compressed melt cushion (m_0) and pressure can be found from the knowledge of specific volume v(p,T) of the material as a function of pressure and temperature as shown in equation 1 [9, 10, 11, 12, 13, 14,15].

$$m = \frac{m_0}{v(p_E, T_m)} \int_{p_c}^{p_E} - \kappa(p,T)\, v\,(p,T)\, dp \qquad (1)$$

Where

m	shot weight (g)
m_0	melt cushion (g)
v (p, T)	specific volume as a function of pressure and temperature (cm^3/g)
κ	compressibility as a function of pressure and temperature (bar^{-1})
p_c	compression pressure (bar)
p_E	end pressure (bar)
T_m	melt temperature (°C)

The isothermal compressibility of a thermoplastic melt is defined as in the equation 2.

$$\kappa = - \frac{1}{v_i} \left(\frac{\partial v}{\partial p} \right) \Bigg|_{T_i} \qquad (2)$$

Where v_i is the specific volume and p is the pressure. In isothermal measurements the specific volume as well as the compressibility shows a dramatic change at the glass transition (T_g) [16]. The bulk modulus is the reciprocal value of the compressibility. The values of compressibility and the bulk modulus differ widely above and below the glass transition. Above T_g the compression of the melt leads to a reduction of the free volume as well as the segmental mobility. Below T_g only the segmental mobility can be reduced [17, 18]. Figure 6 shows the specific volume change of polycarbonate (PC) at isothermal compression at the melt temperature of 200°C with several pressures and subsequent cooling (3 K/min) measured in a pvT device.

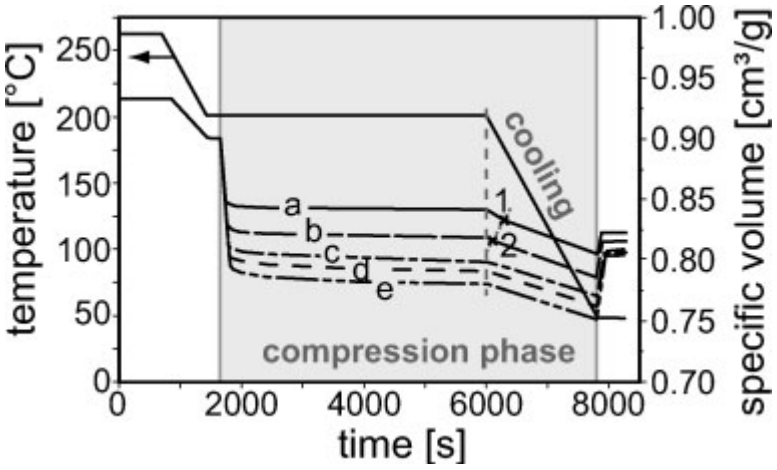

Figure 6: Specific volume change of PC at isothermal compression at 200°C with several pressures (a = 1000 bar, b=1400 bar, c=1700 bar, d=2000 bar, e=2300 bar) and subsequent cooling [19].

As shown in figure 6, during the compression stage, the volume decreased linearly with increasing pressure while the pressure increases from 1000 bar to 1700 bar. The amount of compressibility between these three curves is same as can be seen in figure 6. At the compression with 2000 bar, the relative volume change is significantly smaller. This effect is related to a temperature drop that associated with the reduced mobility. The molecular mobility is also decreases with an increase in pressure. At the melt glass transition, the compressibility shows the largest change [19]. During cooling from 200°C to 50°C at constantly applied pressure, the volume showed a bend in its cure at 177°C for 1000 bar and at 192°C for 1400 bar. However, this bend is not found at higher pressures (see figure 6; curve c, d and e). Since the compression pressure moves the glass transition temperature to higher temperature range, the melt solidification starts at higher temperature. This effect is called as the pressure solidification. The effect of pressure on the material properties, such as glass transition is more depends on the molecular structure of the material. Polymer with higher chain flexibility exhibits stronger dependence on pressure [19].

Another effect of the compression of the melt is the expected increase in temperature because of the input of the work into the system. When high pressure is applied, one has to expect a volume change that is directly linked to a rise in melt temperature. Because the pressure acts homogeneously over the entire material, the resultant temperature rise is also uniform. For an adiabatic system, the temperature rise due to the compression pressure is calculated by equation 3.

$$\Delta T = \frac{\alpha}{\rho\,(p,T)\,C_v} \cdot \overline{T} \cdot \Delta p \qquad (3)$$

Where α is the coefficient of volume expansion, $\rho(p,T)$ is the density, C_v is the specific heat capacity at constant volume, T is average melt temperature and Δp is the pressure rise. At very high compression rates there are almost adiabatic conditions prevail. The

value calculated with equation 3 presents the maximum temperature increase by pressure load. In the case of non-adiabatic pressure build-up, the increase in melt temperature can be transmitted through the wall into the surroundings. In that case, temperature increase of substance is balanced and the measured value does not match to the calculated temperature increase. The volumetric coefficient of thermal expansion is calculated by equation 4. In average, the volumetric coefficient of thermal expansion in melt state is about twice as high as in the solid state [19].

$$\alpha = \left| \frac{1}{v} \left(\frac{\partial v}{\partial T} \right) \right|_P \tag{4}$$

3.2 Calculation of the total compression work

As stated earlier, during the compression phase in the expansion injection moulding the melt in the screw antechamber is compressed from its back pressure value (p_{st}) to the maximum compression pressure (p_c). The compressibility of the melt is used to store the energy, which is later used to fill the cavity at high velocity during the expansion phase. The metered melt in the screw antechamber is used as melt accumulator. Figure 7 shows the changes in specific volume values during the compression at 200°C for a polystyrene (PS) material.

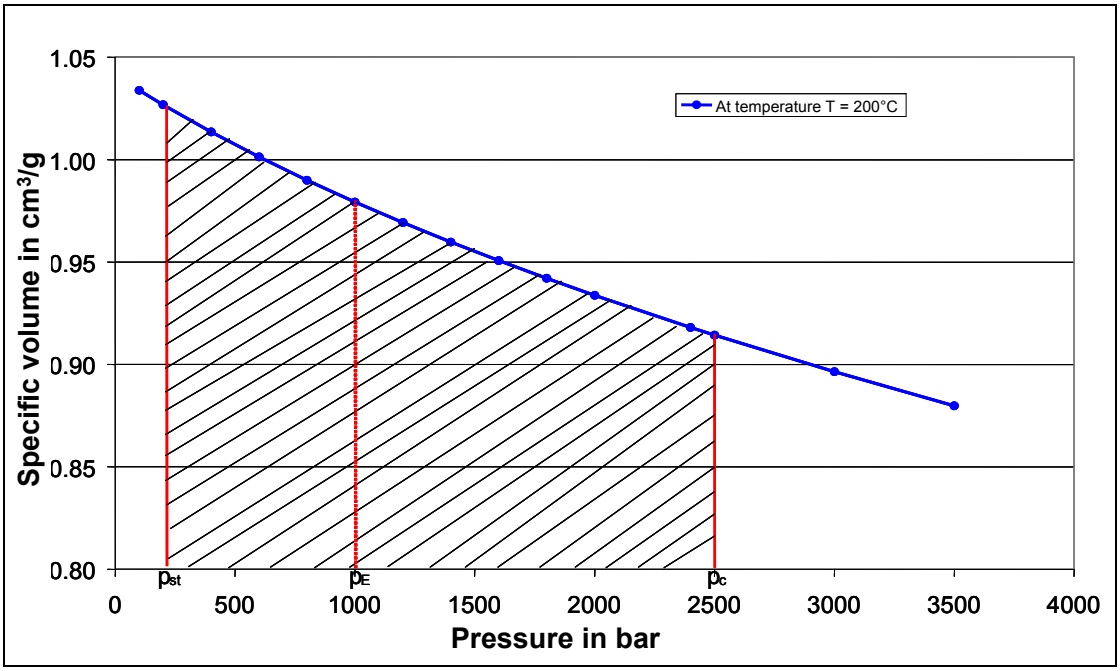

Figure 7: Specific volume change of PS at isothermal compression at 200°C; the area under the curve is the total compression work.

At first melt is compressed from the back pressure of about 100 bar to the maximum compression pressure of about 2500 bar. The specific volume of the melt decreases linearly with the increasing compression pressure. The area under the curve represents

about the amount of energy stored in the melt. The information about the stored energy in the melt during the compression of melt from back pressure to the maximum compression pressure is represented by equation 5 [9]. Where A_c is the compression work, V is the total volume of the melt in front of screw, m_0 is mass of the melt cushion, v(p,T) is the specific volume, p_c is the maximum compression pressure and p_E is the end pressure.

$$A_k = \int_{p_{st}}^{p_c} V \, dp = m_0 \int_{p_{st}}^{p_c} v\,(p, T)\, dp \qquad (5)$$

During the expansion phase, the melt pressure in the screw antechamber drops from the maximum compression pressure to an end pressure. The expansion volume is calculated with the equation 6, is strongly depending on the volume of the compressed melt, the chosen compression pressure and the end pressure reached at end of the expansion phase [9]. In contrast to the compression pressure, the end pressure is depending on the volume of the compressed melt and flow resistance in the cavity during the filling phase.

$$\Delta V = \int_{p_c}^{p_E} - \kappa \, V \, dp \qquad (6)$$

Where ΔV is the expansion volume, V is the volume of the compressed melt and κ is the compressibility of the melt.

3.3 Calculation of the needed melt cushion or the required compression pressure

In order to find out the shot weight coming out of the injection cylinder during the expansion phase, the equation 1 has to be solved. The equation 1 shows the relationships between the shot weight (m), the amount of compressed melt cushion (m_0) and the changes in the thermo-dynamic properties of the melt during the expansion. The changes in the thermo-dynamic properties of the melt is defined by the integration of the material compressibility (κ) and the specific volume (v) between the integration intervals of the compression pressure (p_c) and the end pressure (p_E) [9]. The solution according to the equation 1 is as shown in the equation 7.

$$m = \frac{m_0}{v(p_E, T_m)} \int_{p_c(t=0)}^{p_E(t=t_{end})} dv \qquad (7)$$

By solving equation 7, one can calculate the total shot weight (m) coming out of the injection unit at the end of the expansion phase (equation 8).

$$m = \frac{m_0}{v(p_E, T_m)} \cdot [(v(p_E) - v(p_c)] \quad (8)$$

Where m is the total mass of the melt comes out at the end of expansion (g), m_0 is mass of the compressed melt (g), $v(p_E)$ is the specific volume of melt at the end pressure (cm^3/g) and $v(p_c)$ is the specific volume of the melt at the maximum compression pressure (cm^3/g). The equation 9 signifies that the amount of shot weight comes after the expansion is directly propositional to the mass of the melt cushion and the melt specific volume difference between the end pressure and the compression pressure. Usually in the expansion injection moulding, 10 to 15 times of part volume of the melt is plasticized in front of screw. When the larger amount of material is metered in front screw, the residence time of melt in the plasticizing unit is increasing. For thermally sensitive materials, the long residence time in the injection unit may cause material damage. In addition to that, the repetitive compression and expansion cycle can bring a high amount of thermo-mechanical stress in the melt, which leads to the material damage.

The required shot weight is the sum of the total mass of the part and the mass of the gate/runner system. From the viewpoint of process engineering, the required shot weight is a known value. Therefore, for the chosen melt cushion, the maximum compression pressure has to be calculated in order to get the required shot weight or else for the chosen compression pressure, one has to calculate the needed melt cushion. The value of the needed melt cushion (m_0) is calculated by equation 9.

$$m_0 = \frac{m \cdot v(p_E, T_M)}{v(p_E) - v(p_c)} \quad (9)$$

As discussed previously, the large stored melt volume in the injection unit makes it possible to fill the small cavity volume repeatedly without any separate metering stock in between. One major problem in the multi-shot expansion injection moulding is that with the constant compression pressure at each shot can lead to reduction in the part weight due to dropping end pressure values. In multi shot expansion injection moulding a correction for the maximum compression pressure is necessary at every shot. Injecting without the pressure correction leads to decreasing end pressure at every shot, which causes a decrease in part weight. The end pressure should be kept constant at every shot. By increasing the shot number (i) in equation 10, we can calculate the specific volume of the melt at the max. compression pressure at every shot.

$$v(p_c)_i = v(p_E)\left(1 - \frac{m}{m_0 - (i-1) \cdot m}\right) \quad (10)$$

Where $v(p_c)$ is the specific volume of the melt at the maximum compression pressure, $v(p_E)$ is the specific volume of the melt at the end pressure, m is the required shot weight, m_0 is the mass of the melt cushion ,i is the shot number (i = 1,2,…,Z), and Z is the total

shot number. The corresponding compression pressure (p_c) for the calculated specific volume v (p_c) is calculated from the p-v-T diagram of the chosen thermoplastic melt at the particular melt temperature.

The calculated compression pressure can be set on the machine. However, in contrast to the compression pressure, the geometry and thickness of the mould cavity and the viscosity of the chosen thermoplastic material influence the end pressure. In the expansion injection moulding, during the expansion phase the pressure in the injection unit drops from pre-set compression pressure to an end pressure. This end pressure acts as a packing pressure like as in standard injection moulding. Thus, the end pressure should ensure a complete part filling in the cavity. The developed calculation method for the simulation of the injection moulding creates the possibility of calculating the minimum required filling pressure for the secure filling of the cavity. The minimum require injection pressure is calculate with taking into account of the geometry of the thin wall part, the formation of the frozen layer along the flow length and the changes in melt temperature due to the effect of cooling and dissipation. For the clear understanding of the calculation method for the minimum required injection pressure, one has to understand the theoretical background of the mould-filling phase, which is discussed later in this work.

3.4 Calculation of the mass flow rate during the melt expansion

The process analysis of expansion injection moulding shows a characteristic pressure curve in the injection unit is different from the one for the conventional injection moulding [15]. The figure 8 shows the comparison of measured pressure curves while filling the rectangular bar (4 x 140x 0.5 mm) by the expansion injection moulding and by the conventional injection moulding process.

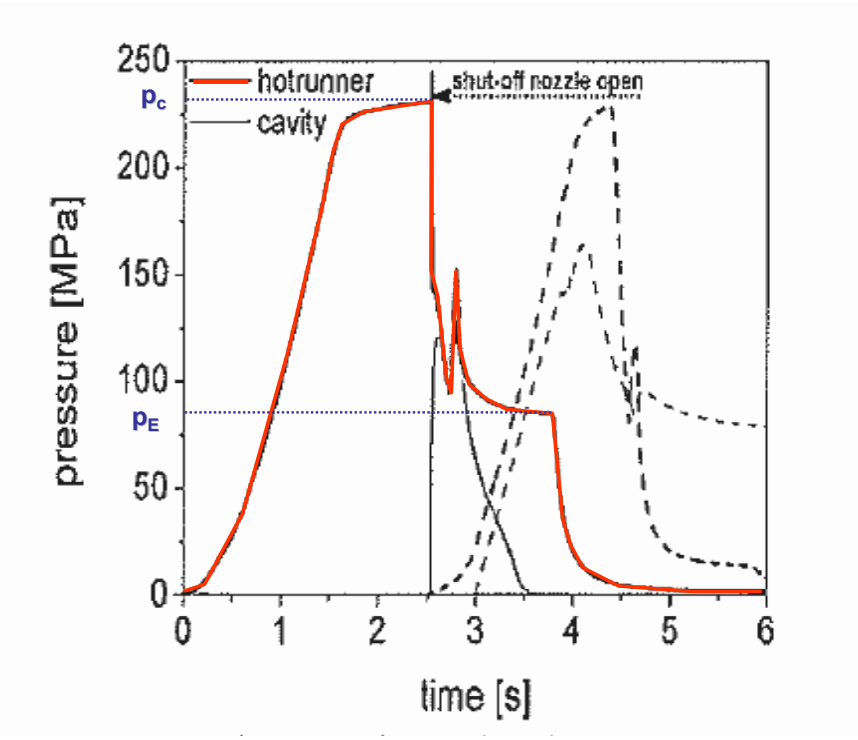

Figure 8: Compression and cavity pressure characteristics for the expansion injection moulding (Solid line in red colour; with pc =2400 bar) and the conventional injection moulding (dashed line; with injection velocity of 20 mm/s) using the rectangular bar [15].

The material used for the investigation was a polyoxymethylene copolymer (POM) at the melt temperature of 210°C. For the expansion injection moulding, the pre-set compression pressure was 2400 bar. As figure 8 shows, after the hot runner shut-off nozzle is opened, the melt pressure in the hot runner nozzle drops from 2400 bar compression pressure to the end pressure value of 950 bar as function time. The pressure drop shows an exponential pressure decreases as a function of time.

In expansion injection moulding during the melt expansion phase, the pressure in the screw antechamber starts decreasing from the pre-set compression pressure (p_c) to an end pressure (p_E) as a function of expansion time (t_{ex}). Further, during melt expansion phase the injection screw is kept at constant position. Therefore, for the given time interval, the generated mass flow rate during the melt expansion phase is purely

depends upon the pressure drop in the screw antechamber and its corresponding changes in the melt specific volume. Since the pressure drop in front of screw decreases exponentially during the expansion, the generated mass flow rate also decreases exponentially as function of time. To find out the mass flow rate as function time, we have to differentiate the equation 1 as a function of time as in equation 11 [9].

$$\dot{m}_s = \frac{m_0}{v(p_E, T_M)} \frac{d}{dt} \int_{p_c}^{p_c(t)} -\kappa\,(p,T)\, v\,(p,T)\, dp \qquad (11)$$

The solution of equation 11 is as follows:

$$\dot{m}_s = \frac{m_0}{v(p_E, T_M)} \cdot \frac{d}{dt} \int_{p_C}^{p_C(t)} dv \quad = \frac{m_0}{v(p_E, T_M)} \cdot \frac{d}{dt} \left(v\left(p_C(t), T\right) - v\left(p_E, T\right) \right) \qquad (12)$$

$$\dot{m}_s = \frac{m_0}{v(p_E, T_M)} \cdot \frac{d}{dt} \left(v\left(p_c(t), T\right) - v(p_E, T) \right) = \frac{m_0}{v(p_E, T_M)} \cdot \frac{\partial v\left(p_c(t), T\right)}{\partial p_c} \cdot \frac{\partial p_c}{\partial t} \qquad (13)$$

$$\dot{m}_s = \frac{m_0}{v(p_E, T_M)} \cdot \frac{\partial\, v\left(p_c(t), T\right)}{\partial p_c} \cdot \dot{p}_c \qquad (14)$$

In equation 14, the mass flow rate is a function of two interlinked complex functions such as the change in specific volume with respect to the change in melt pressure and the change in melt pressure with respect to expansion time. To solve this equation, we have to define the pressure as a function of expansion time. For that, we have to model the pressure drop as function the expansion time. As stated earlier, during the expansion phase, the pressure in the screw antechamber decreases exponentially with increasing expansion time (t) as shown in figure 9.

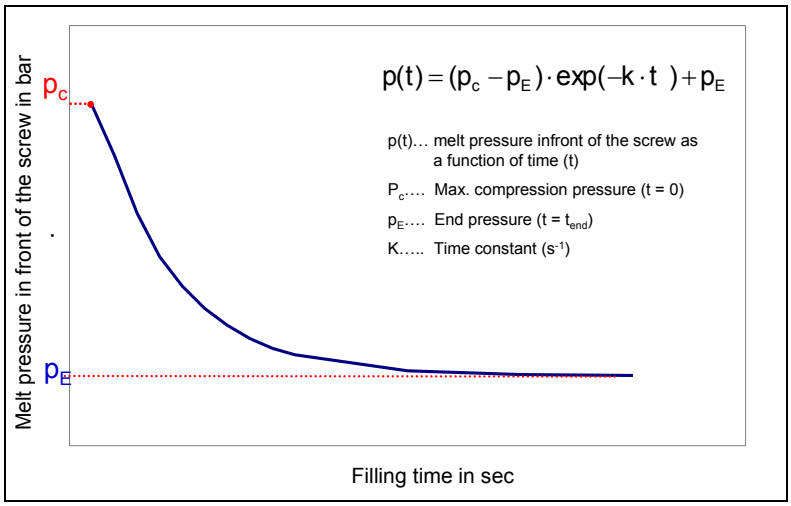

Figure 9: The exponential decrease of the pressure in the screw antechamber during the melt expansion phase

The mathematical formulation of the pressure decrease in front of the screw antechamber is defined by the equation 15.

$$p(t) = (p_c - p_E) \cdot \exp(-k' \cdot t) + p_E \qquad (15)$$

where as:

p(t) melt pressure in front of the screw as a function of time (bar)

p_c max. compression pressure (bar)

p_E end pressure (bar)

k' time constant (s^{-1})

By differentiating the equation 15 with the respect of time, we can define the change in pressure with increasing expansion time as in equations 16:

$$\frac{\partial p}{\partial t} = -(p_k - p_E) \cdot k' \cdot \exp(-k' \cdot t) \qquad (16)$$

The specific volume of the melt as a function of pressure and temperature can be expressed by equation 17 :

$$v(p,T) = \frac{K_{1M}}{p + K_{4M}} + \frac{K_{2M} \cdot T}{p + K_{3M}} \qquad (17)$$

In equation 17, K_{1m}, K_{2m}, K_{3m} and K_{4m} are approximation coefficients of the pvT-diagram in the melt range.

By differentiating the equation 17 with the respect of pressure, we can define the change in specific volume of the melt as a function of decreasing pressure as in equation 18.

$$\frac{\partial v}{\partial p} = - \frac{K_{1m}}{(p + K_{4m})^2} - \frac{K_{2m}}{(p + K_{3m})^2} \cdot T \qquad (18)$$

The Solution for the equation 14 to calculate the mass flow rate from the injection unit during the expansion phase is given in equation 19.

$$\dot{m}_s = \frac{m_0}{v(p_E, T_M)} \cdot \left(- \frac{K_{1m}}{(p_k + K_{4m})^2} - \overset{(I)}{\frac{K_{2m}}{(p_k + K_{3m})^2} \cdot T_M} \right) \cdot \left(\overset{(II)}{-(p_k - p_E) \cdot k' \cdot \exp^{-k' \cdot t_i}} \right) \qquad (19)$$

In equation 19, the term (I) describes the change in melt specific volume with the change in pressure and the term (II) defines the change in pressure with the change in the expansion time. With the help of the equation 19, we can calculate the change in mass flow rate during the expansion phase.

4 Theoretical background of the mould filling phase

4.1 Governing equations for the filling phase

In this chapter, the equations governing the flow of a compressible, viscous fluid are derived. These equations are applicable to the flow of a polymer melt and are obtained using the principles of conversion of mass, momentum, and energy. In deriving the governing equations for the flow of a polymer melt, we assume that the fluid is a continuum. These mean that we ignore the molecular structure of the material and assume that it is possible to define physical variables such as velocity and density at a point in the fluid.

4.1.1 Continuity equation

The general equation for describing the mass conservation for compressible fluids is in vector notation:

$$\frac{\partial \rho}{\partial t} + \rho(\nabla \bar{v}) + (\bar{v} \nabla \rho) = 0 \tag{20}$$

The continuity equation (20) for an incompressible, generalized non-Newtonian fluid may be written in Cartesian coordinates as follows:

$$\frac{\partial v_x}{\partial x} + \frac{\partial v_y}{\partial y} + \frac{\partial v_z}{\partial z} = 0 \tag{21}$$

4.1.2 Momentum equation

The general momentum equation is the rate of change of momentum of the liquid with the external forces acting on the fluid equal. In vector notation it is:

$$\frac{\partial}{\partial t}(\rho \bar{v}) = \rho \bar{g} + [\nabla . \underline{\sigma}] - [\nabla (\rho \bar{v} \bar{v})] \tag{22}$$

Where $\bar{g}$ is the total body force per unit mass and $\underline{\sigma}$ is the stress tensor. When the equation 22 is expressed in Cartesian coordinates, it yields the following equation for x-component of momentum (equation 23):

$$\underset{(1)}{\rho \frac{\partial v_x}{\partial t}} = \underset{(2)}{\rho f_x} \underset{(3)}{- \frac{\partial p}{\partial x}} + \underset{(4)}{\frac{\partial}{\partial x}\left(2\eta \frac{\partial v_x}{\partial x}\right)} + \underset{(5)}{\frac{\partial}{\partial y}\left[\eta\left(\frac{\partial v_y}{\partial x} + \frac{\partial v_x}{\partial y}\right)\right] + \frac{\partial}{\partial z}\left[\eta\left(\frac{\partial v_x}{\partial z} + \frac{\partial v_z}{\partial x}\right)\right]} - \underset{(6)}{\rho\left(v_x \frac{\partial v_x}{\partial x} + v_y \frac{\partial v_x}{\partial y} + v_z \frac{\partial v_x}{\partial z}\right)} \tag{23}$$

(7)

In the above equation, it is worth noting the physical significance of the terms. Term (1) is the rate of change of momentum, term (2) represents forces due to gravity, term (3) is the pressure gradient, terms (4) to (6) represent viscous forces and term (7) represents the inertial forces. Assuming a narrow wall thickness that prevails commonly in the thin-wall injection moulded parts, some terms are neglected. After the simplification, the momentum equations for the three coordinate directions (z-coordinate = thickness direction) respectively:

$$\frac{\partial p}{\partial x} = \frac{\partial}{\partial z}\left(\eta \frac{\partial v_x}{\partial z}\right)$$

$$\frac{\partial p}{\partial y} = \frac{\partial}{\partial z}\left(\eta \frac{\partial v_y}{\partial z}\right) \tag{24}$$

$$\frac{\partial p}{\partial z} = 0$$

From the last momentum equation (24), we see that the pressure is a function of x and y only. For this reason, it is convenient to integrate the momentum equations across the thickness with the aim of obtaining expression for the velocities v_x and v_y. In injection moulding, the material is in both solid and liquid phases. The melt is sandwiched between layers of frozen material that adheres to the cavity walls. The governing equations were derived for fluids only and it is inappropriate to apply these to the frozen layer. Therefore, we use the concept of no-flow temperature to distinguish between solid and liquid phases. During filling phase, there exists a region called the frozen skin layer, where the velocities v_x, v_y and v_z are zero. Moreover, the frozen layer is defined to be the material which lies below the no-flow temperature.

4.1.3 Energy equation

The general form of the energy equation during the filling process is represented as in equation 25.

$$\rho c_p\left(\frac{\partial T}{\partial t} + \vec{v}\nabla T\right) = \beta T\left(\frac{\partial p}{\partial t} + \vec{v}\nabla p\right) + p\nabla\vec{v} + \left(\underline{\sigma} : \{\nabla\vec{v}\}\right) + \nabla\left(k\nabla T\right) \tag{25}$$

Neglecting the viscoelastic effects and assuming that the thermal conductivity k is constant, the equation 25 is simplified as follows:

$$\rho c_p\left(\frac{\partial T}{\partial t} + \vec{v}\nabla T\right) = \beta T\left(\frac{\partial p}{\partial t} + \vec{v}\nabla p\right) + \eta\dot{\gamma}^2 + k\nabla^2 T \tag{26}$$

The energy equation 26 can be written in Cartesian coordinates as follows:

$$\underset{(1)}{\rho c_p\left(\frac{\partial T}{\partial t}+v_x\frac{\partial T}{\partial x}+v_y\frac{\partial T}{\partial y}+v_z\frac{\partial T}{\partial z}\right)}=\underset{(2)}{\beta T\left(\frac{\partial p}{\partial t}+v_x\frac{\partial p}{\partial x}+v_y\frac{\partial p}{\partial y}+v_z\frac{\partial p}{\partial z}\right)}+\underset{(3)}{\eta\dot{\gamma}^2}+\underset{(4)}{k\left(\frac{\partial^2 T}{\partial x^2}+\frac{\partial^2 T}{\partial y^2}+\frac{\partial^2 T}{\partial z^2}\right)} \tag{27}$$

The physical significance of the terms is as follows. Term (1) is the total rate of energy change plus the energy due to convection in the x, y and z directions. Term (2) is the total rate of energy change due to compression/expansion of the melt. Term (3) is the rate of energy generation due to viscous dissipation or shear heating and term (4) represents the rate of energy change due to conduction in the x, y and z directions. The terms involving the change of energy due to compression/expansion and conduction in the x and y direction are significantly lower magnitude. Therefore, we can drop these terms and obtained the following energy equation:

$$\rho c_p\left(\frac{\partial T}{\partial t}+v_x\frac{\partial T}{\partial x}+v_y\frac{\partial T}{\partial y}\right)=\eta\dot{\gamma}^2+k\frac{\partial^2 T}{\partial z^2} \tag{28}$$

Where shear rate is defined as

$$\dot{\gamma}^2=\left(\frac{\partial v_x}{\partial z}\right)^2+\left(\frac{\partial v_y}{\partial z}\right)^2 \tag{29}$$

4.2 Viscosity model for the filling calculation

To model the injection moulding process, a viscosity function is required. A number of well-known models are available. It is important to choose a model that is both accurate over the processing range and for which data can be readily be obtained. Some common viscosity model are:

- Power law models
- Moldflow second order model
- Ellis model
- Carreau model
- Cross model

4.2.1 Viscosity model requirements

The most important requirement of a viscosity model is that it should represent the observed behaviour of polymer melts. In particular, a viscosity model should meet the following requirements:

- the viscosity should decrease with increasing shear rate
- the curvature of the isotherms should be such that the viscosity decreases at a decreasing rate with increasing shear rate
- the isotherms should never cross over
- the viscosity should decrease with increasing temperature
- the iso shear rate curves should never cross over

The plot of viscosity versus shear rate at a constant temperature is shown in figure 10. The scope of the viscosity model is to match the observer behaviour of the material as closely as possible.

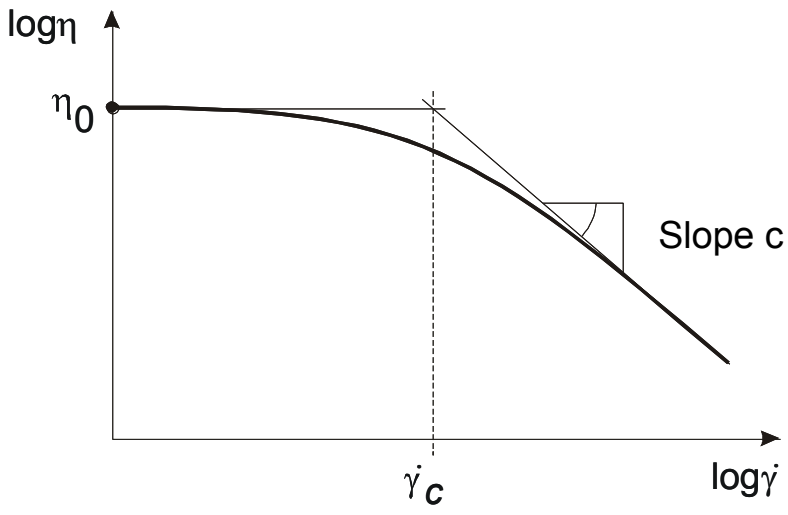

Figure 10: Typical graph of viscosity versus shear rate at a constant temperature.

4.2.2 Power law model

The power law model has the form with the temperature shifting as in equation 30.

$$\eta = K \cdot \dot{\gamma}^{n-1} \tag{30}$$

Where K and n are the material constants. For polymer melts, the constant n lies between 0 and 1. By taking natural logarithms of the both sides of the equation 30, we obtain the equation 31.

$$\ln \eta = (n-1)\cdot \ln \dot{\gamma} + \ln K \tag{31}$$

A plot of ln η against ln $\dot{\gamma}$ shows this relationship to be linear. The slope (n-1) is represented as c in figure 10. The power law model is representing the behaviour of polymer melts in the high shear region. It is also quite easy to fit experimental data to this model and so to determine the constant K and n.

The main disadvantage of this model is in the low shear rate range. Here it is incapable of predicting the Newtonian viscosity, η_0, which is defined as the viscosity at zero shear rate. Despite this disadvantage, the model has been widely used for modelling flow in injection moulding.

4.2.3 Moldflow second order Model

In order to improve the modelling of viscosity in the low shear rate region, the following model has been used for the viscosity approximation.

$$\ln \eta = A_0 + A_1 \cdot \ln \dot{\gamma} + A_2 \cdot T + A_3 \cdot (\ln \dot{\gamma})^2 + A_4 \cdot T \cdot \ln \dot{\gamma} + A_5 \cdot T^2 \tag{32}$$

where the Ai are constants. This model is able to characterize the observed viscosity behaviour of polymer melts. However, this model has some disadvantages. The most important is that the model can introduce behaviour that is not rheologically sensible. For example, it is possible that $\frac{\partial \eta}{\partial \dot{\gamma}} > 0$. This means that viscosity increases with increasing shear rate and is not realistic. Such behaviour requires that care be taken when fitting the experimental data to the model, to ensure that suitable cut offs are used at the low shear rate range, to prevent this happening [20].

4.2.4 The Ellis viscosity model

The Ellis model express the viscosity as a function of shear stress τ. It has the form as in equation 33.

$$\frac{\eta_0}{\eta} = 1 + \left(\frac{\tau}{\tau_{1/2}} \right)^{\alpha - 1} \tag{33}$$

Where $\tau_{1/2}$ is the value of shear stress for which $\eta = \frac{\eta_0}{2}$ and α-1 is the slope of the graph ln[(η_0/η) – 1] versus ln(τ/$\tau_{1/2}$).

4.2.5 The Carreau Model

The Carreau model is more realistic than power law model because it fits the data very well at both high and low shear rates. Due to the mathematical complexities, it is not possible to obtain analytical solutions with Carreau model, but it is excellent for numerical simulation of flow processes. The general form of the Carreau model is as follows:

$$\frac{\eta - \eta_\infty}{\eta_0 - \eta_\infty} = \left[1 + (\lambda \cdot \dot{\gamma})^2\right]^{\frac{n-1}{2}} \tag{34}$$

where η_∞ is the viscosity at infinite shear rate, η_0 is the viscosity at zero shear rate, n is a constant and λ is a time constant. The modified form of the Carreau approach is shown in equation 35, without taking into account the constant viscosity at high shear rates.

$$\eta = \frac{A}{(1 + B \cdot \dot{\gamma})^C} \tag{35}$$

where A = η_0, B = $\frac{1}{\dot{\gamma}_c}$ and C is the slope of the viscosity curve.

4.2.6 The Cross Model

The rheological model based on Cross model is one of the most commonly used models for the viscosity approximation. Most of the rheometer packages and simulation software use this model. The Cross model has the form:

$$\eta(\dot{\gamma}) = \frac{A}{1 + (B\dot{\gamma})^C} \tag{36}$$

Where A - Zero shear viscosity, B - Cross time constant (or consistency) and C - Slope of power law region.

The zero shear viscosity is the magnitude of the viscosity at the lower Newtonian plateau. The reciprocal of B gives us the critical shear rate that proves a useful indicator of the onset shear rate of shear thinning. The constant C is dimensionless and is a measure of the dependence of the viscosity on shear rate in the shear thinning region. A value of zero indicates Newtonian behaviour and with C tending to unity for increasing shear thinning behaviour.

4.3 Concept of representative viscosity

In practical flow calculation with in the flow channel, the calculation equations must be simplest possible form. The uses of various empirical constitutive law equations for the calculation of volume flow are more or less complex equations. A simplified method to compute the viscosity was developed by Schümmer and Worthoff [21]. This method takes advantage of the fact that the Newtonian and shear thinning materials have a common streamline at which the strain rate is same. The strain rate distribution and velocity distribution in Newtonian and non-Newtonian fluid flowing through a capillary are shown in figure 11.

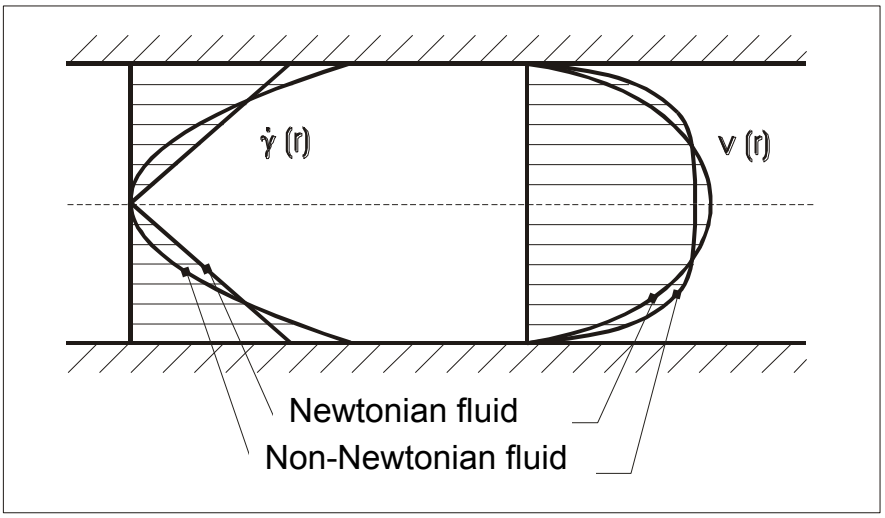

Figure 11: Strain rate and velocity distribution in Newtonian fluid and non-Newtonian fluid flowing through a capillary [39].

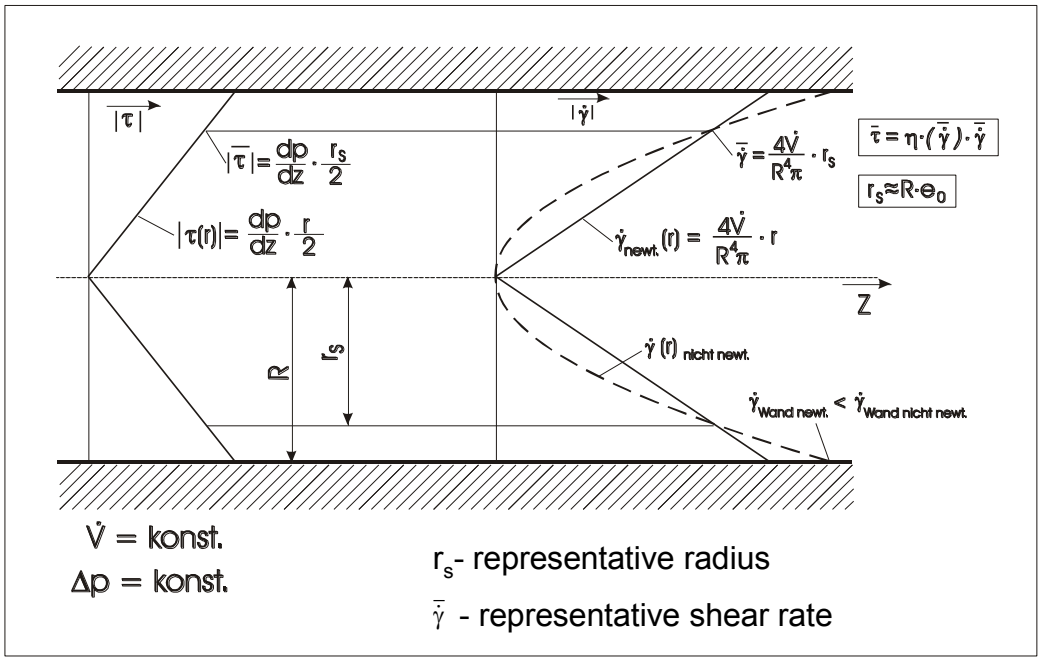

Figure 12: Determination of the viscosity from the "representative" shear rate - shear stress in the capillary rheometer [39].

Determination of the viscosity from the representative shear rate and representative shear stress in the capillary rheometer is shown in figure 12. The following tables (Table 1 and 2) summarize the representative shear rates, the representative shear stresses, and wall shear stresses given for different channel cross sectional geometries.

Table 1: Representative shear rates for different channel cross sections

Geometries	Non-Newtonian: representative shear rates	
Pipe flow	$\bar{\dot{\gamma}}_{rep} = \frac{4 \cdot \dot{V}}{\pi \cdot R^3} \cdot \bar{e}_0$ with $\bar{e}_0 \approx 0{,}815$	(37)
Flow in annular gap	$\bar{\dot{\gamma}}_{rep} = \frac{\dot{V}}{(R_a^2 - R_i^2) \cdot \bar{R}} = \pi \cdot \frac{\bar{v}_z}{\bar{R}}$ $\bar{R} = R_a \sqrt{1 + k^2 + \frac{1 - k^2}{\ln(k)}}$ with $k = \frac{R_i}{R_a}$	(38)
Rectangular slit die flow	$\bar{\dot{\gamma}}_{rep} = \frac{6 \cdot \dot{V}}{B \cdot H^2} \cdot \bar{e}$ with $\bar{e}_{\square} = 0{,}772$ Die $\bar{e}_{o,}$ $\bar{e}_{\square}$ values valid for the flow index between $2 \le m \le 4$	(39)

Table 2: Representative shear stresses and wall shear stresses for different channel cross sections

Geometries	Non-Newtonian: representative shear stress	
Pipe flow	$\tau = \frac{\Delta p}{2L} \cdot r$ $\tau_w = \frac{\Delta p}{2L} \cdot R \qquad \tau = \tau_w \left(\frac{r}{R} \right)$	(40)
Flow in annular gap	$\tau = \frac{\Delta p}{L} \cdot y$ $\tau_w = \frac{\Delta p}{2L} \cdot H \qquad \tau = \tau_w \left(\frac{2y}{H} \right)$ $\tau = \frac{R}{2} \cdot \frac{\Delta p}{L} \left[\frac{r}{R} - \frac{1 - k^2}{2 \cdot \ln \frac{1}{k}} \cdot \frac{R}{r} \right]$ with $k = \frac{R_i}{R_a}$	(41)
Rectangular slit die flow	$\tau = \frac{\Delta p}{L} \cdot y$	(42)

	$\tau_w = \frac{\Delta p}{2L} \cdot H \qquad \tau = \tau_w \left(\frac{2y}{H} \right)$

4.4 No-flow temperature

No-flow temperature is defined to be that temperature at which the plastic material effectively ceases to flow. Although No-flow temperature is not a fundamental physical property of a material, it is useful for modelling the effect of the frozen skin layer that is deposited on the wall of the mould during the filling phase. Figure 13 shows typical temperature and shear rate distribution across the cavity thickness. The corresponding viscosity distribution is shown in figure 14.

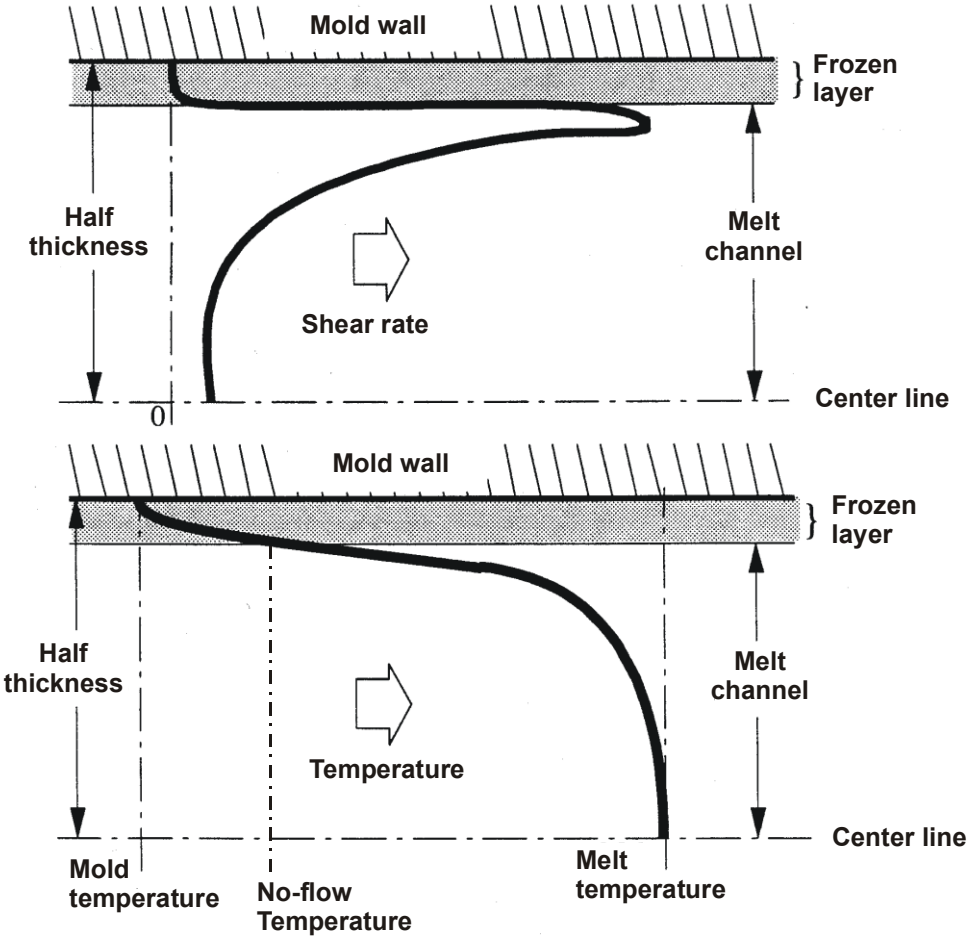

Figure 13: Shear rate and temperature distribution across the cavity [20].

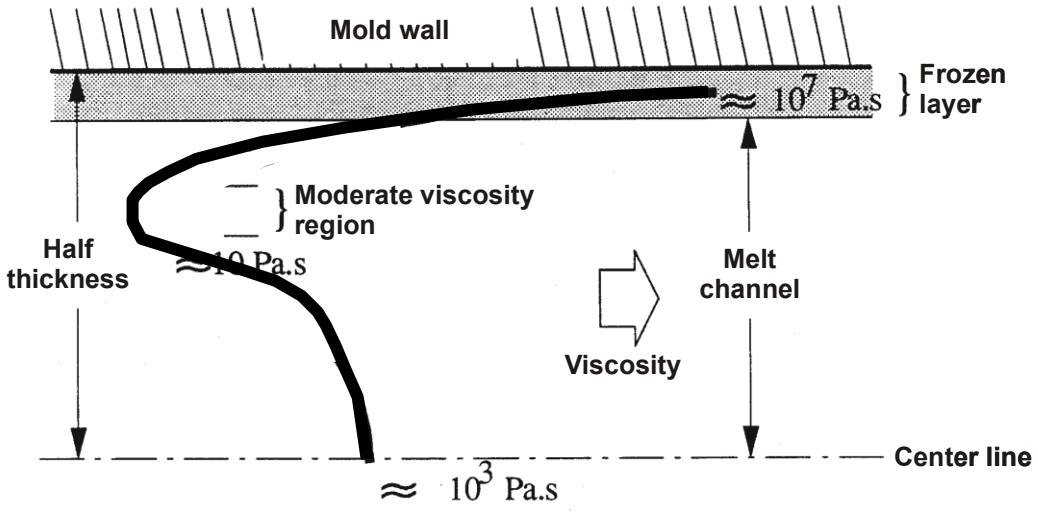

Figure 14: Viscosity distribution across the cavity [20].

The shape of the viscosity distribution is a consequence of its dependence on both shear rate and temperature. Polymer melts are in general shear thinning. In the absence of temperature effects, the viscosity will decrease with increasing shear rate. On the other hand, if we ignore shear rate, the viscosity tends to decrease with increasing temperature. Both these factors contribute to the shape of the viscosity distribution in figure 14.

During the cooling process, the melt will cool down so far that the material will no longer be able to flow. The temperature at which this occurs is called no-flow temperature. In reality, the melt will not stop flowing immediately at one temperature but this will happen in a temperature range. For simulation, it must be sufficient to give this one value due to lack of knowledge what really goes on [22].

For a semi-crystalline material, the no-flow temperature is in the range of the sharp bend in the pvT-diagram at the transition from the melt state into the solid state. For an amorphous plastic, it is approximately 20°C above the transition point. A further indication is that this temperature should coincide with the sharp drop in the shear modulus curve, as at the transition from solid to softening the mechanical stiffness drops.

4.5 Formation of the frozen skin layer

During the injection phase of the conventional injection moulding cycle, the forward motion of the screw, at a given velocity, injects the polymer melt into a mould with the desired part shape. When the hot polymer melt contact the cold mould walls, it freezes off and creating a solid frozen layer. This effect imparts important consequences:

- The reduction of the flow cross-sectional area increasing the pressure drop to fill the cavity.

- The creation of an insulation barrier due to the low thermal conductivity of the polymer in the frozen layer is leading to a slower cooling rate of the inner material.

For a given material, the frozen layer thickness depends on the local thermal conditions, which may vary during the filling phase. The formation of the solidified material evolutes dynamically because of the temperature changes due to viscous dissipation. The thickness of the skin layer is controlled by the combined effect of the thermal and the stress field imposed during the processing [23].

For thin-wall injection moulding, it is well know that the formation of the frozen layer due to fast cooling has a much greater influence on pressure prediction compared to standard injection moulding with thick-wall parts. The frozen skin layer reduces the wall thickness of the flow channel and thus increases the flow resistance. Dietz et al. showed a method to calculate the distribution of the frozen skin layer in a rectangular flow channel [24].

4.5.1 Dietz and White model

Dietz and White made a quantitative analyse of the filling phase of a cavity with a rectangular flow channel [24]. For the quantitative analysis, it was considered as a non-isothermal mould filling process of an amorphous polymer. The cavity to be analysed was a rectangular slit (L x W x H) and is the width B>>10 H. Thus, one can consider the flow process as a two dimensional flow. The coordinates used are x as the direction of the flow, y as the shear direction and z as the neutral direction. The mould wall temperature (T_w) is less than the no-flow temperature (T_{No}) of the polymer, so that a frozen skin layer (δ) is formed between the boundary of the flowing melt and the cooled mould wall.

For the simplicity of the calculation of the filling phase, the flow behind the flow front is assumed as an isothermal steady shear flow. Since the mould filling process in the injection moulding happened within a short time interval, the frozen skin layer due to its very low thermal conductivity of the polymer has a thermal isolation effect. Therefore, the assumption of isothermal steady flow in injection moulding is permissible [24, 25]. In addition that, the shear heating effect provides for a partial or even a complete compensation of thermal conduction loss through the cool mould wall.

For the calculation of frozen skin layer thickness distribution (δ), Dietz and White proposed two equations. The first equation describes the unsteady growth of the frozen skin layer thickness. Therefore, the thickness of the frozen skin layer is a function of

time (t) and the distance in the flow direction (x). Figure 15 is showing the flowing melt front in a rectangular flow channel.

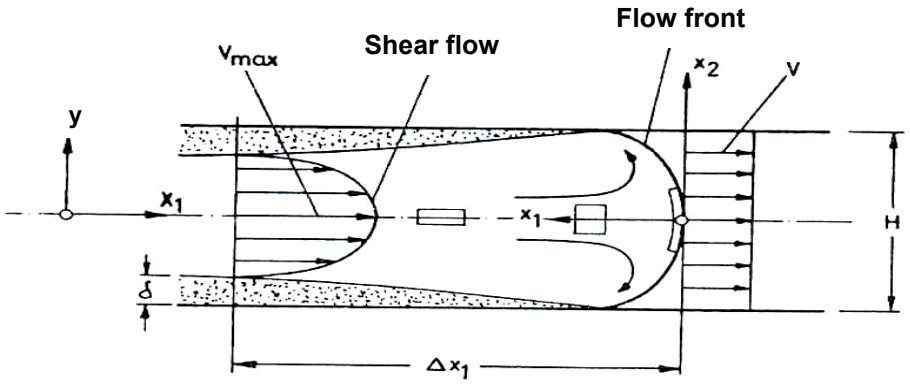

Figure 15: Flowing melt front in a rectangular flow channel [24].

The equation 43 calculates the thickness of the frozen skin layer (δ (x,t)) at unsteady state, which is function of time (t) and the distance from the injection point (x).

$$\delta(x,t) = 1.9 \cdot \frac{T_{No} - T_w}{T_M - T_w} \cdot \sqrt{a_{eff} \cdot t_c} \qquad (43)$$

Where:

t_f filling time (s)

t_c contact time at each segment (s)

a_{eff} effective temperature conductivity (m^2/s)

δ thickness of the frozen layer (mm)

T_{NO} no flow temperature (°C)

T_M melt temperature (°C)

T_W mould wall temperature (°C)

The local contact time (t_c) of melt with the mould wall can be calculated easy from the flow front velocity (v_F) as in equation 44.

$$t_c = t_f - \frac{x}{v_F} \quad 0 \le x \le v_F \cdot t \qquad (44)$$

With t_f as time since the beginning of the mould filling and $v_F.t$ as the location of the flow front in the mould, we can calculate the contact time. The growth of frozen skin layer thickness as a function of time, calculated with equation 43, can be slowed down due to dissipative shear heating of flowing melt.

Therefore, Dietz and White proposed the second equation (equation 45) to calculate the frozen layer thickness at the equilibrium condition, which is taking into account of

reduction in thickness of the frozen layer due to shear heating on the melt. The second equation is the stationary final value of the frozen layer thickness as a function of the flow path (x) at the equilibrium state.

$$\delta(x) = 1.86\frac{T_{No} - T_W}{T_M - T_{No}}\left(\frac{a_{eff}}{2}\cdot\frac{s}{\bar{v}_F}\cdot\frac{n}{2n+1}\right)^{\frac{1}{3}}\cdot x^{\frac{1}{3}} \qquad (45)$$

Where:

s	wall thickness (m)
v_F	flow velocity (m/s)
a_{eff}	effective temperature conductivity (m^2/s)
n	exponent of Power law (/)
δ	thickness of the frozen layer (m)
T_{No}	no flow temperature (°C)
T_M	melt temperature (°C)
T_W	mould wall temperature (°C)

The calculation of the thickness of the frozen skin layer at certain location of the cavity starts with the equation 43. When the value is reached by equation 43, the calculations proceed with the equation 45. The equation 45 describes the thickness of the frozen skin layer especially good close to the injection point of the cavity [24].

4.5.2 Influence of frozen skin layer

In order to analysis the influence of frozen skin layer on the injection pressure calculation results, the calculations were done for the rectangular strip mould with the wall thickness of 0.3 mm with flow length of 100 mm. The material chosen for the calculation was PP HG313MO with the melt temperature 230°C. The mould temperature was chosen as 40°C. The no-flow temperature was 120°C. The calculation results are shown below. The frozen skin layer thickness distribution calculated with the equation 43 is shown in figure 16.

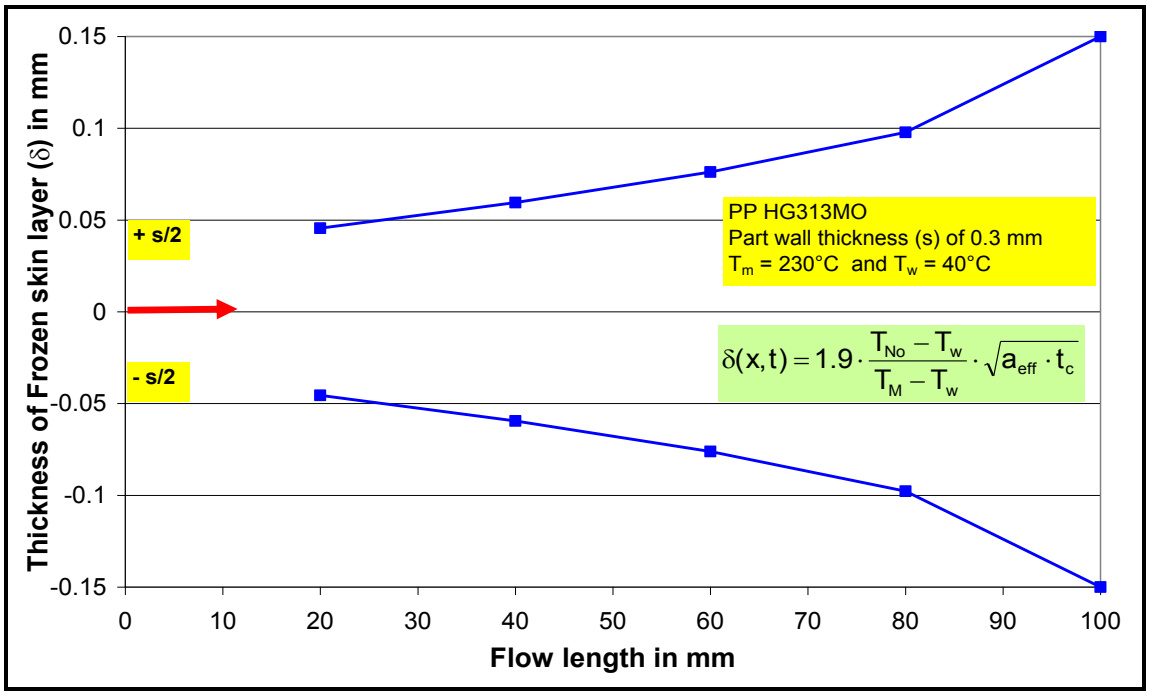

Figure 16: Calculated initial frozen skin layer thickness distribution along the flow front direction for PP HG313MO at 230°C

Once the initial value of the thickness is attainted, the calculation proceeds with the equation 45, which accounts reduction of frozen skin layer thickness due to the shear heating. The frozen skin layer distribution calculated with equation 45 is shown in figure 17. The equation 45 describes the thickness of the frozen skin layer especially good close to the injection point of the cavity. When comparing the frozen skin layer thickness distribution curves of figures 16 and 17, the both curves intersect at the flow length of 80 mm. For the final thickness distribution prediction, the thickness values calculated with the equation 45 are taken up to the flow length of 80 mm and for the remaining flow length the thickness values calculated with the equation 43 are used. The figure 18 shows the final distribution of the frozen skin layer thickness for the calculation of the injection pressure.

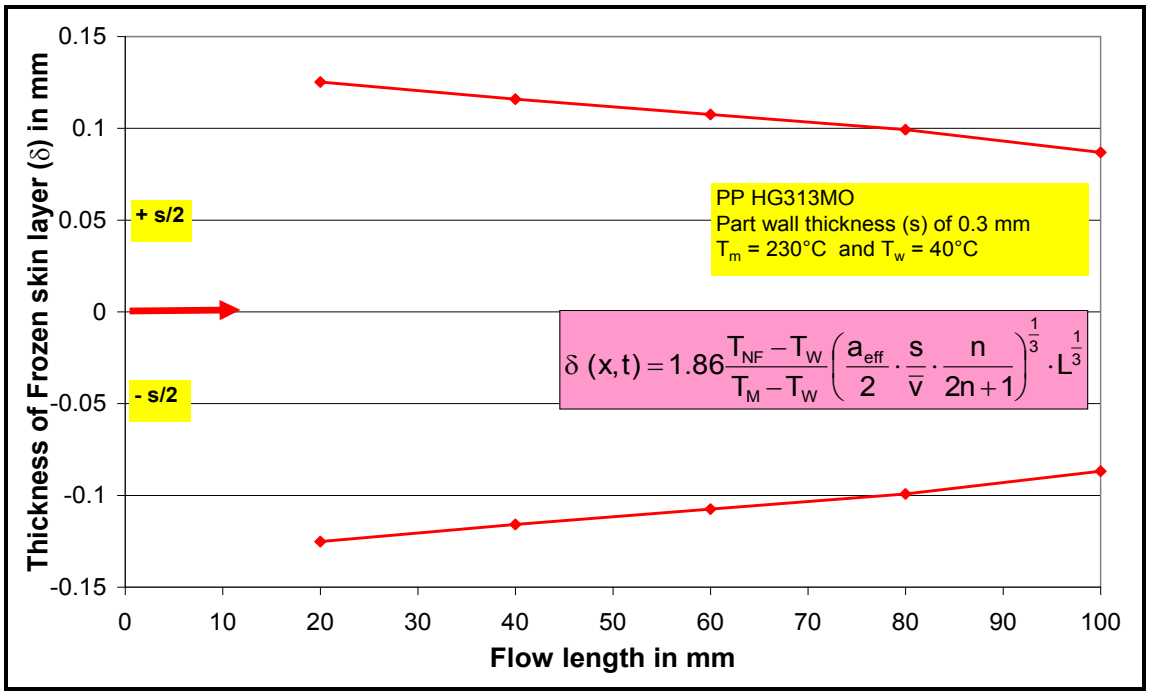

Figure 17: Calculated frozen skin layer thickness distribution with account of shear heating effect along the flow front direction for PP HG313MO at 230°C

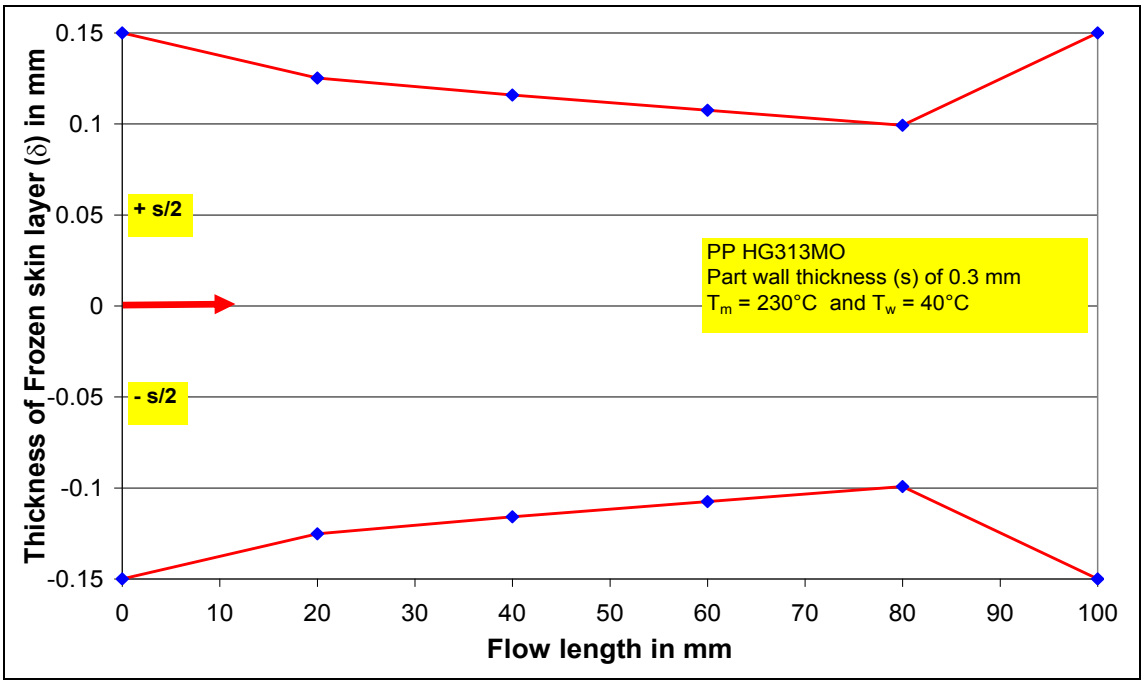

Figure 18: Calculated final frozen skin layer thickness distribution along the flow front direction for PP HG313MO at 230°C

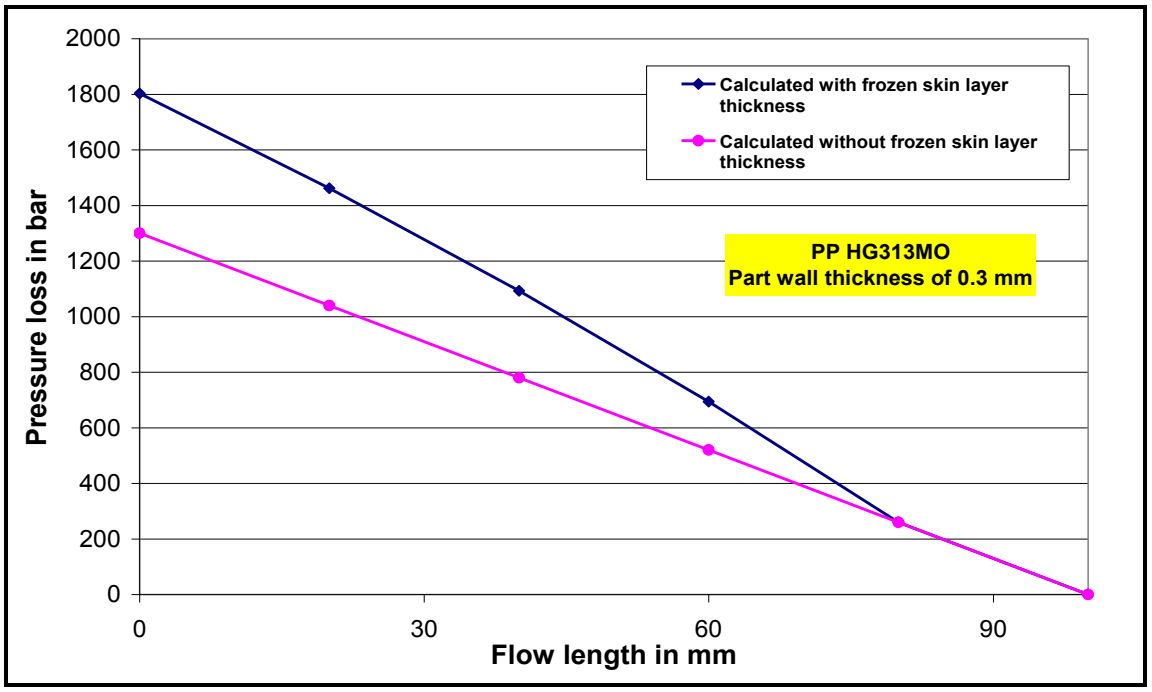

Figure 19: Calculated injection pressure with and without taken into frozen skin layer thickness for PP HG313MO at 230°C

The figure 19 shows the calculated injection pressure with and without the influence of frozen skin layer thickness. The calculated pressure with taken into account of the frozen skin layer thickness distribution is significantly higher than the calculated pressure without taken into account the frozen skin layer distribution. For thin wall parts with wall thickness less than 0.5 mm, effect of frozen skin layer thickness should be taking into account for the calculation of injection pressure.

4.6 Change in melt temperature due to effect of cooling

Cooling of the melt commences right at the cavity filling stage. During the cooling phase, however, it is essential that the melt be prevented from freezing through the shear heat. The major quantity of heat is exchanged after the filling phase. The exchange of heat between the mould and the cooling medium takes place by heat conduction through the cavity walls. Such a heat conduction effect can be described by Fourier differential equation as in equation 46.

$$\frac{\partial T}{\partial t} = a_{eff} \cdot \frac{\partial^2 T}{\partial x^2} \qquad (46)$$

In the above equation, a_{eff} is the effective temperature conductivity, which is calculated by using equation 47.

$$a_{eff} = \frac{\lambda}{\rho \cdot c_p} \tag{47}$$

a_{eff} effective temperature conductivity (m²/s)

λ thermal conductivity (W/(m K)

ρ density (kg/m³)

c_p specific heat capacity (J/kg.K)

The melt temperature distribution in the cavity is shown in figure 20.

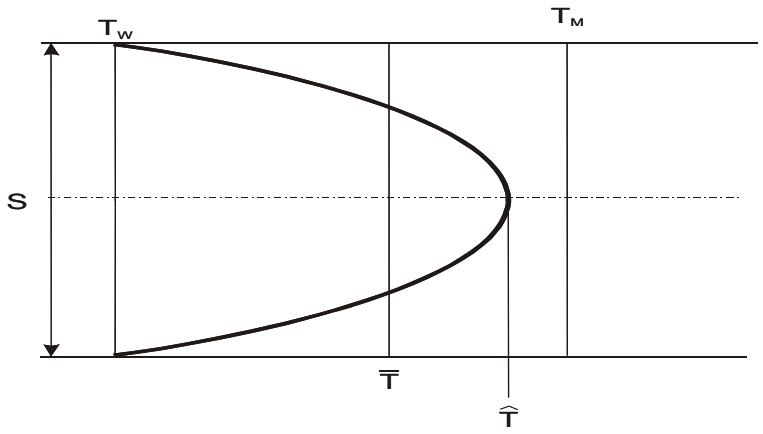

Figure 20: Melt temperature distribution in the thickness direction, T_m is the injection melt temperature, T_w is the mould wall temperature and $\overline{T}$ is the average bulk temperature.

The average bulk melt temperature is calculated by the equation 48 using the analytic solution:

$$\overline{T}(t_m) = T_W + \frac{8}{\pi^2} \cdot (T_M - T_W) \cdot e^{-\frac{a \cdot \pi^2}{H^2} \cdot t_m} \tag{48}$$

4.7 Viscous dissipation

The molten polymers are highly viscous but have a low thermal conductivity. It is therefore inefficient to transfer heat by conduction to molten polymer across a large thickness. On the other hand, the heat generated by viscous forces may be of importance and can represent an efficient mode of heating, as the heat losses to the surrounding are not rapid.

The relative importance of the principal physical phenomena occurring in the injection moulding process and their degree of interaction can be quantified by the calculation of dimensionless numbers.

The Cameron number (Ca) as in equation 49, relates the heat conduction in the thickness direction to the heat convection in the longitudinal one. If Ca>>1 then the heat convection dominates, when Ca<<10^{-2} it becomes negligible and flow can be assumed as occurring in quasi-adiabatic conditions and the heat conduction in the longitudinal direction dominates. In the interval 10^{-2} < Ca < 1 the temperature profile is in development and the flow is in a transition regime.

$$Ca = \frac{\lambda X_{cond}}{\rho c_p v_f X_{conv}} \tag{49}$$

where

λ	thermal conductivity (W/m.K)
ρ	density (kg/m^3)
c_p	specific heat capacity (J/mol.K)
$X_{cond/conv}$	characteristic dimension to conduction/convection
v_f	velocity (m/s)

The Brinkman number (Br) as in equation 50 is the ratio between the heat generated by viscous dissipation and heat exchanged by conduction through the moulding boundaries. If Br>>1, which indicates a strong effect of the heat generated by viscous dissipation. In case of Br << 1, the viscous dissipation can be neglected.

$$Br = \frac{\eta v_f^{\,2}}{\lambda(\overline{T}_m - T_w)} \tag{50}$$

where

η	viscosity (Pa.s)
λ	thermal conductivity (W/m.K)
v_f	velocity (m/s)
$\overline{T}_m$	melt average bulk temperature (°C)
Tw	mould temperature (°C)

The dimensionless numbers analysis has been used to interpret the main physical phenomena occurring in the injection moulding of different part geometries and processing conditions.

4.7.1 Change in melt temperature due to viscous dissipation

The temperature increase due the dissipation in the melt following through a die during the filling phase can be calculated by the equation which is derived from the energy equation. The following assumption are taken into consideration:

- Adiabatic condition
- no inner heat source

- one dimensional laminar flow

The simplified energy equation for the above mentioned assumption is shown in equation 51.

$$\rho \cdot c \cdot \frac{DT}{Dt} = \underbrace{-T \cdot \left(\frac{\partial p}{\partial T}\right)\Big|_v \cdot \frac{\partial v_z}{\partial z}}_{\Delta T \text{ due to compression / expansion}} + \underbrace{\sigma_{zz} \cdot \frac{\partial v_z}{\partial z}}_{\Delta T \text{ due to elongation}} + \underbrace{\sigma_{rz} \cdot \frac{\partial v_z}{\partial r}}_{\Delta T \text{ due to Dissipation}} \tag{51}$$

The shear rate can be represented as in equation 52.

$$\dot{\gamma}_{zr} = \frac{\partial v_z}{\partial r} \tag{52}$$

with following relationships are taken into the consideration, the above mentioned energy equation is formulated as in equation 57:

$$\frac{\partial p}{\partial T} \cdot \frac{\partial \rho}{\partial t} = \frac{\partial p}{\partial t} \cdot \frac{\partial \rho}{\partial T} \tag{53}$$

$$\rho = \frac{1}{\nu} \tag{54}$$

$$\partial \rho = -\frac{1}{\nu^2} \cdot \partial \nu \tag{55}$$

$$\tau = \eta \cdot \dot{\gamma} \tag{56}$$

$$\rho \cdot c \cdot \frac{DT}{Dt} = -T \cdot \frac{\partial p}{\partial t} \cdot \frac{\partial \nu}{\partial T} \cdot \frac{1}{\nu} + \sigma_{zz} \cdot \frac{\partial \nu}{\partial t} \cdot \frac{\nu}{\nu^2} + \eta \cdot \dot{\gamma}^2 \tag{57}$$

For the steady state condition $\left(\rho \cdot c \cdot \frac{\partial T}{\partial t} = 0\right)$, we simplify the energy equation as in equation 58 by neglecting the effect of elongation and the effect of compression.

$$\rho \cdot c_v \cdot v_z \cdot \frac{\partial T}{\partial z} = \eta \cdot \dot{\gamma}^2 \tag{58}$$

From the above equation, we can calculate approximately the temperature increase due to the dissipative effect as in equation 59.

$$\Delta T = \frac{\eta \cdot \dot{\gamma}^2 \cdot L}{\rho \cdot c_v \cdot v_z} \tag{59}$$

5 CALCULATION PROCEDURE FOR THE SIMULATION

5.1 Introduction to the calculation method

The developed physical model to describe the expansion injection moulding process was discussed in the capital 3. For the given shot weight (m), the developed process model enables us to calculate the needed maximum compression pressure (p_c) for the chosen melt cushion (m_0) or else for the chosen compression pressure (p_c), to calculate the needed melt cushion (m_0). The required shot weight is the sum of the total mass of the part and the mass of the gate/runner system.

The calculated compression pressure (p_c) can be set on the machine. However, in contrast to the compression pressure, the geometry and thickness of the mould cavity and the viscosity of the chosen thermoplastic material influence the end pressure (p_E). The end pressure acts as a packing pressure like as in the convectional injection moulding. Thus, the end pressure should ensure a complete part filling in the cavity. The developed calculation method creates the possibility of calculating the minimum required filling pressure for the secure filling of the cavity, taking into account of the geometry of the thin wall part, the formation of the frozen layer along the flow length and the changes in melt temperature due to the effect of cooling and dissipation.

The developed calculation program allows the prediction of:

- the approximated filling time
- the minimum required filling pressure, taking into account the distribution of the frozen layer and changes in viscosity values due to cooling effect
- the needed compression pressure for the chosen melt cushion and calculated end pressure
- or alternatively the calculation of the needed melt cushion for the chosen compression pressure and the end pressure

Figure 21 shows the flow chart of the calculation program. For the chosen part, the calculation for the expansion injection moulding starts with the calculations of the approximated filling time. The methodical approach for the calculation of the minimum required filling pressure is segmentation of the longest flow path into several serially connected small segments. In a serial connection, the volume flow rate at every segment is the same but the pressure drop of each segment is different. The total required filling pressure is the sum of the pressure drops at all segments. To improve

the calculation results, the effect of the frozen skin layer thickness is also taken into account. For that, the model proposed by Dietz and White (see capital 4.5) is used to calculate the thickness of the frozen skin layer.

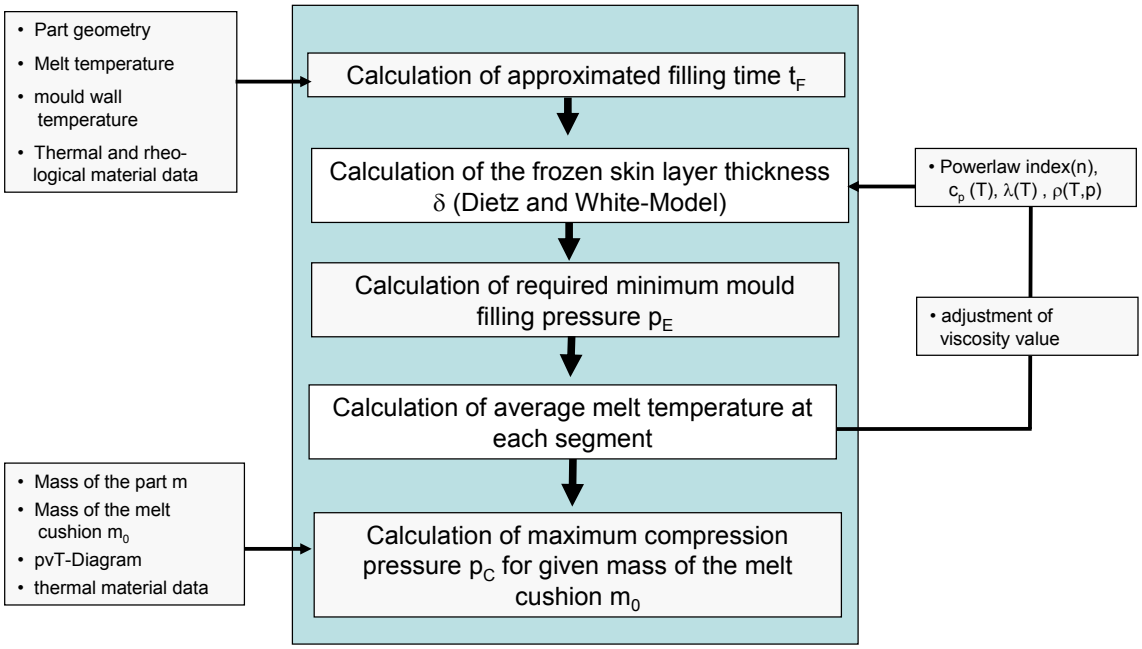

Figure 21: Flow chart of the calculation program

For thin-wall injection moulding, it is well know that the formation of the frozen layer due to fast cooling has a much greater influence on the pressure prediction. The frozen skin layer reduces the wall thickness of the flow channel and thus increases the flow resistance. So higher injection pressure is needed in order to counteract the fast cooling and thus the formation of the frozen layer. The formation of the frozen skin layer takes place along the flow path from the injection point to the end of the flow path. The maximum thickness of the frozen layer is at one third of the total flow path length and at the end of the flow path, the value is zero (Figure 22).

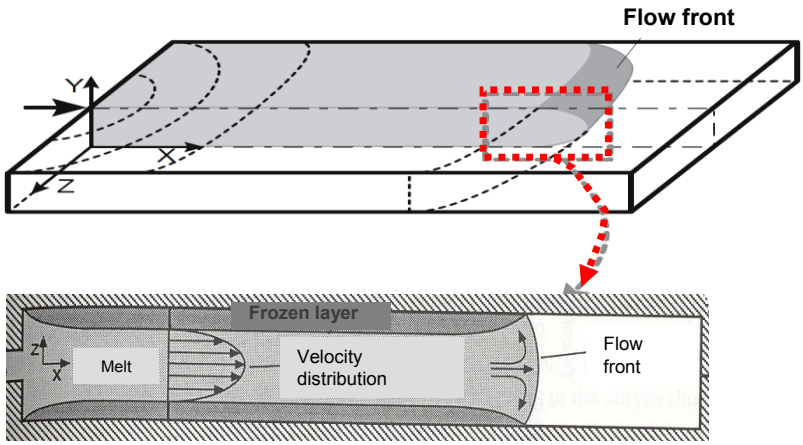

Figure 22: Distribution of the frozen layer in a rectangular flow channel

From the calculated frozen skin layer distribution at each segment the reduced wall thickness is obtained. These values are used for the calculation of the pressure drops at every segment. Further, the change in melt temperature at each segment due to the effect of dissipative heating and cooling is also taken into account for the calculation of melt viscosity.

The calculated minimum pressure required to fill the cavity is chosen as an end pressure (p_E). From the input values of the end pressure, part mass, mass of the compressed melt, melt temperature, melt compressibility and specific volume from p-v-T data, we can calculate the maximum compression pressure in order to fill the cavity during the expansion phase. As the shot number increases, we have to correct the maximum compression pressure accordingly for the multi shot expansion injection moulding.

Based on the above mentioned calculation approach a simulation program named as *Xmeltsoft V.1.0* was developed with the help VBA as an Excel add-in.

5.2 Approximate calculation of the filling time

In thin wall injection moulding, the important aspect is what filling time will be necessary from the process-engineering point of view to fill the planned thin-wall part in the first place. This approximated filling time (t_f) can be derived with a simple model for thin-walled injection moulded parts at a constant flow front velocity with taken into account the frozen skin layer [5]. Lampl, A. had proposed the simplest way to calculate the approximated filling time [26].

The approximated fill time (t_f) at minimum pressure requirement is calculated by following approach for a rectangular flow channel. The pressure needed (p) for filling the rectangular part is calculated by equation 60.

$$p = 12 \cdot \eta_{rep} \cdot L \cdot \frac{\bar{v}_f}{s^2} \qquad (60)$$

where

p pressure needed to fill (bar)

η_{rep} viscosity (Pa.s)

L flow length (m)

$\bar{v}_f$ average flow front velocity (m/s)

s wall thickness (m)

The representative shear rate in the rectangular flow geometry is given in equation 61 and the fill time can be calculated as in equation 62.

$$\dot{\gamma}_{rep} = 0.772 \cdot \frac{6 \cdot \overline{v_f}}{s} \tag{61}$$

$$t = \frac{\overline{v_f}}{L} \tag{62}$$

The formation of the frozen skin layer under the unsteady state can be calculated by using equation 63, which was proposed by Dietz and White.

$$\delta(x,t) = 1.9 \cdot \frac{T_{No} - T_w}{T_M - T_w} \cdot \sqrt{a_{eff} \cdot t_c} \tag{63}$$

The frozen skin layer thickness (δ) value calculated with the equation 63 is one-half of the total part wall thickness. So the total reduction in wall thickness can be calculated as in equation 64.

$$\Delta S = 2 \cdot \delta \tag{64}$$

The effective wall thickness (S_{red}) can be calculated as in the equation 65.

$$S_{red} = (S - \Delta S) = \quad 3.8 \frac{T_{No} - T_w}{T_M - T_w} \cdot \sqrt{a_{eff} \cdot t} \tag{65}$$

Thus inserting the effective wall thickness (S_{red}) in the equation 60 and the equation 61 will result the formation equation 66 and equation 67.

$$\Delta p_i = 12 \cdot \eta_{rep} \cdot L_i^2 \cdot \frac{1}{(S - \Delta S)^2 \cdot t} \tag{66}$$

$$\dot{\gamma}_{rep} = 4.632 \cdot \frac{L}{(S - \Delta S) \cdot t} \tag{67}$$

The Power law model defines the viscosity.

$$\eta = K \cdot \dot{\gamma}^{n-1} \tag{68}$$

By $\frac{d(\Delta p)}{dt} = 0$ follows an extreme value for the fill time. Thus, approximated filling time t_f at minimum pressure requirement is calculated with the equation 69 [5, 26].

$$t_f = \left(\frac{S}{3.8 \cdot \frac{T_{No} - T_w}{T_M - T_w} \cdot \sqrt{a_{eff}}} \right)^2 \cdot \left(\frac{2n}{1+3n} \right)^2 \qquad (69)$$

where:

t_f Optimum filling time (s)

a_{eff} effective temperature conductivity (m^2/s)

n Power law index

s Wall thickness of thin wall part (mm)

δ thickness of the frozen layer (mm)

T_{No} No flow temperature (°C)

T_M Melt temperature (°C)

T_W Mould wall temperature (°C)

In the simulation of the expansion injection moulding, the first step involved is calculation of the approximated filling time for the chosen part. In case of thin-wall part with varying wall thicknesses, an average value of the wall thicknesses is taken for the calculation of the approximated filling time as shown in figure 23.

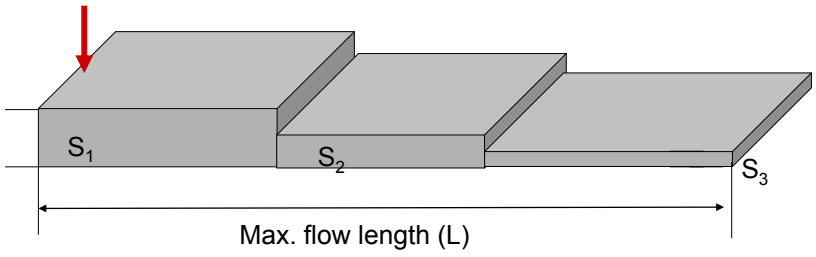

Average wall thickness $S_{average} = (S_1 + S_2 + S_3) / 3$

Figure 23: Average wall thickness value for the calculation of approximated fill time.

5.3 Methodical approach used for the calculation of minimum required end pressure

The methodical approach for the calculation of the minimum required filling pressure is segmentation of the longest flow path into several serially connected small segments as shown in figure 24.

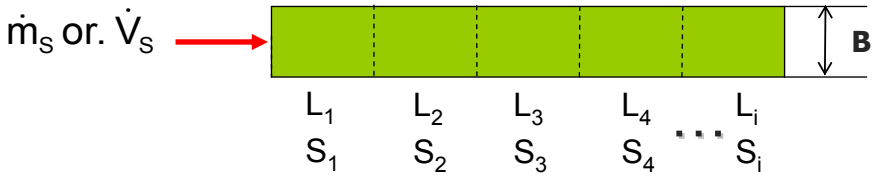

Figure 24: Methodical approach of the serial segmentation technique, where S_1, S_2...S_i are the segmental wall thicknesses and L_1, L_2,....L_i are the segmental lengths.

In a serial connection, the volume flow rate at every segment is the same but the pressure drop of each segment is different. The total required filling pressure is the sum of the pressure drops at all segments (figure 25).

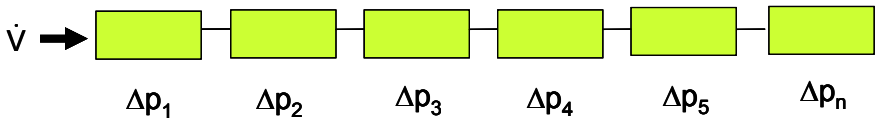

$$\Delta p_{total} = \Delta p_1 + \Delta p_2 + ... + \Delta p_n = \sum_{i=1}^{n} \Delta p_i$$

$$\dot{V} = \dot{V}_1 = \dot{V}_2 = Constant$$

Figure 25: Methodical approach of the serial segmentation technique for the calculation of minimum required filling pressure.

For the calculation of the pressure drop at each segment, the reduction in wall thickness (S_{red}) due to the formation of the frozen skin layer is taken into account. For the accurate calculation of melt viscosity at each segment, the change in melt temperature due to the effect of cooling as well as increase in melt temperature due to the effect of shear dissipation are taken into consideration. Finally, the sum of the pressure drops at all segments is taken as the minimum required filling pressure. The calculated minimum required filling pressure is consider as the end pressure (p_E) for the calculation of the maximum compression pressure (p_c).

5.4 Steps involved in the calculation of minimum required injection pressure

The step by step procedure to calculate the minimum injection pressure (p_E) is explained below.

Step 1: Dividing the cavity flow channel into small segments

At first, the longest flow length of the cavity is divided into several numbers of segments (n) for the accurate calculation of pressure loss in each segment. The total volume and total mass of the part are calculated as in equation 70 and equation 71.

$$V_{total} = \sum_{i=1}^{n} V_i \tag{70}$$

$$m_{total} = \rho_{20°C} \cdot V_{total} \tag{71}$$

Where:

V_{total} total volume of the part (m^3)

V_i volume of the segments (m^3)

m_{total} total mass of the part (kg)

n number of segments (/)

$\rho_{20°C}$ density at room temperature (kg/m^3)

Step 2: Calculating the filling time of each segment

From the calculated approximated filling time, the filling time of each segment is called as in equation 72.

$$t_i = \frac{V_i}{V_{total}} \cdot t_f \tag{72}$$

Where:

V_i volume of the segments (m^3)

t_i filling time of the segments (s)

t_f approximated filling time (s)

Step 3: To calculate the average flow velocity at each segment

The average melt flow velocity at each segment can be calculated as in equation 73.

$$\bar{v} = \frac{L_i}{t_i} \tag{73}$$

Where:

$\bar{v}_f$ average flow velocity (m/s)

L_i length of the segments (m)

t_i filling time of the segments (s)

Step 4: Determination of the frozen skin layer thickness (δ)

To calculate the frozen skin layer thickness (δ) we use two equations (equation 74 and equation 76) proposed by Dietz and White, which are shown below.

$$\delta(x,t) = 1.9 \cdot \frac{T_{No} - T_w}{T_M - T_w} \cdot \sqrt{a_{eff} \cdot t_c} \qquad (74)$$

$$t_{c,i} = t_f - \frac{1}{\bar{v}} \sum_{1}^{i} L_i \qquad i \geq 2 \qquad (75)$$

Where:

t_f filling time (s)

$t_{c,i}$ contact time at each segment (s)

a_{eff} effective temperature conductivity (m^2/s)

δ thickness of the frozen layer (mm)

T_{No} no flow temperature (°C)

T_M melt temperature (°C)

T_W mould wall temperature (°C)

The growth of frozen skin layer thickness as a function of time, calculated with equation 74, can be slowed down due to dissipative shear heating of the flowing melt. Therefore, we have to use the second equation 76 of Dietz and White model to calculate the frozen layer thickness at the equilibrium condition, which takes into account the reduction in thickness of the frozen layer due to shear heating on the melt.

$$\delta\,(x,t) = 1.86 \frac{T_{No} - T_W}{T_M - T_{No}} \left(\frac{a_{eff}}{2} \cdot \frac{s}{\bar{v}_f} \cdot \frac{n}{2n+1} \right)^{\frac{1}{3}} \cdot L^{\frac{1}{3}} \qquad (76)$$

Where:

s wall thickness (m)

v_f flow velocity (m/s)

a_{eff} effective temperature conductivity(m^2/s)

n exponent of Power law (/)

δ thickness of the frozen layer (m)

T_{No} no flow temperature (°C)

T_M melt temperature (°C)

T_W mould wall temperature (°C)

The calculation of the thickness of the frozen skin layer at a certain segment of the cavity starts with equation 74. When a value of initial thickness is calculated by equation 74, the calculations proceed with the equation 76. Equation 76 describes the thickness of the frozen skin layer especially good close to the injection point of the cavity.

The equations 74 and 76 calculate the thickness of the frozen skin layer for the half of the wall thickness. Thus, the total change in wall thickness (Δs) due to the frozen skin layer at each segment is calculated by using equation 77.

$$\Delta s_i = 2 \cdot \delta(x,t) \tag{77}$$

The reduced wall thickness can be calculated with equation 78.

$$s_{i,red} = s_i - \Delta s_i \tag{78}$$

The increase in average flow velocity at each segment due to reduced wall thickness can be calculated by using equation 79.

$$\overline{v}_{i,cor} = \overline{v}_i \cdot \frac{s_i}{s_{i,red}} \tag{79}$$

The corrected fill time for each segment has to be calculated with equation 80.

$$t_{i,cor} = \frac{L_i}{\overline{v}_{i,cor}} \tag{80}$$

Step 5: Representative shear rates and representative viscosity

The representative shear rates for a rectangular flow channel can be calculated at each segment with the help of equation 81.

$$\dot{\gamma}_{rep,i} = 0.772 \cdot \frac{6 \cdot \overline{v}_{i,cor}}{s_{i,red}} \tag{81}$$

The equations for calculating the representative shear rate of different flow channel geometries are listed in table 1.

The change in melt temperature due to the effect of cooling at each segment is calculated with the help of equation 82, which is based on the unsteady state heat conduction theory.

$$\overline{T}(t_i) = T_w + 2\cdot(T_m - T_w)\sum_{n=1}^{\infty}\frac{1}{k^2}\cdot e^{-\left(\frac{2k}{H_i}\right)^2\cdot a_{eff}\cdot t_{i,cor}} \qquad (82)$$

$$\text{with } k = \frac{2n-1}{2}\cdot\pi$$

The rise in melt temperature at each segment due to dissipative heating on the melt can be calculated with equation 83 assuming the adiabatic condition.

$$\Delta\overline{T}_{Diss} = \frac{a_{eff}}{\lambda}\cdot\eta_{rep}\cdot\dot{\gamma}_{rep}^2\cdot\frac{\Delta L}{\overline{v}_{i,corr}} \qquad (83)$$

The actual melt temperature for the calculation of viscosity at each segment is calculated as in equation 84.

$$\overline{T}_i = \overline{T}(t_i) + \Delta\overline{T}_{i,Diss} \qquad (84)$$

During the calculation of the melt temperature at each segment, the outlet temperature $(T)_i$ from the segment (i) is taken as the entry temperature in the segment (i+1).

The representative viscosity has to be calculated with the help of Carreau equation 85 for the calculated melt temperature at each segment (T_i).

$$\eta_{rep} = \frac{a_T\cdot A}{(1+a_T\cdot B\cdot\dot{\gamma}_{rep})^c} \qquad (85)$$

where A, B and C are the material constant of the Carreau viscosity model. a_T is the temperature shift factor in order to calculate the temperature dependency of the viscosity. The temperature shift factor (a_T) can be calculated with the help of Arrehnius equation or else with the help of the William-Landel and Ferry (WLF) equation as shown in equation 86 and in equation 87. The Arrhenius equation (equation 86) is used to find the temperature dependency of semi-crystalline polymeric materials. By using William-Landel and Ferry equation (equation 87) the temperature dependency of the amorphous polymer is determined.

$$a_T = \exp\left[\frac{E_0}{R}\left(\frac{1}{T}-\frac{1}{T_0}\right)\right] \qquad (86)$$

Where E_0 (kJ/mol) is the activation energy, R is the universal gas constant ($8.314*10^{-3}$ kJ/mol K) and T is the temperature in (K).

$$a_T = \exp\left[\frac{-c_1(T - T_0)}{c_2 + (T - T_0)}\right] \quad (87)$$

Where C_1 and C_2 are the material constant and T_0 is the reference temperature.

Step 6: Calculation of the pressure requirement to fill the cavity

The pressure loss (Δp) at each segment can be calculated by using equation 88.

$$\Delta p_i = \frac{12 \cdot \eta_{rep} \cdot \bar{v}_{i,corr}}{s_{i,red}^2} \cdot \Delta L_i \quad (88)$$

The equations for calculating the pressure loss for different flow channel geometries are listed in table 3.

Table 3: Pressure loss equations for different geometries

Geometries	Pressure loss equations	
Pipe flow	$\Delta p = \frac{8 \cdot \bar{v} \cdot \eta_{rep}}{R^2} \cdot \Delta L$	(89)
Flow in the disc	$\Delta p = \frac{12 \cdot \bar{v}_r \cdot \eta_{rep}}{s^2} \cdot \Delta r$	(90)
Rectangular slit die flow	$\Delta p = \frac{12 \cdot \bar{v} \cdot \eta_{rep}}{s^2} \cdot \Delta L$	(91)
Flow in annular gap	$\Delta p = \frac{12 \cdot \bar{v} \cdot (R_a^2 - R_i^2) \cdot \eta_{rep}}{(R_a + R_i) \cdot (R_a - R_i)^3} \cdot \Delta L$	(92)

The total specific injection pressure required to fill the cavity can be calculated by using equation 93.

$$p_E = \sum_{i=1}^{n} \Delta p_i \quad (93)$$

The calculated specific injection pressure is assumed as the end pressure during the calculation of the maximum compression pressure.

5.5 Calculation of maximum compression pressure

As stated earlier, the minimum filling pressure calculated for the approximated fill time for a chosen thin-wall part is consider as the end pressure for the further calculation steps. After the end pressure calculation, the calculation program has two options. Either one can calculate the needed compression pressure (p_c) for a chosen melt cushion (m_0) or else for the chosen compression pressure (p_c) one could calculate the needed melt cushion (m_0).

The melt specific volume $v(p_c, T_m)$ at maximum compression pressure is calculated by using equation 94. The mass of melt cushion (m_0), the needed shot weight (m) and the melt specific volume $v(p_E, T_m)$ at the calculated end pressure are the require calculation parameters.

$$v(p_c)_i = v(p_E)\left(1 - \frac{m}{m_0 - (i-1)\cdot m}\right) \qquad (94)$$

where

$v(p_c)_i$ melt specific volume at maximum compression pressure (m^3/kg) at i^{th} shot

$v(p_E)$ melt specific volume at minimum required end pressure (m^3/kg)

m needed shot weight (g)

m_0 mass of the melt cushion (g)

Z total shot number (/)

i 1,2,….,Z

For the chosen thermoplastic material, the change in specific volume as a function of pressure is plotted for the melt temperature from the measured pvT-data. From that plot, we can calculate corresponding pressure value for the calculated specific volume with equation 94.

5.6 Calculation of mass flow rate as a function time

As discussed in previously, the generated mass flow rate during the expansion phase decreases with the function of time. The generated mass flow rate at particular time interval is depending on the change in melt pressure in front screw and also change in the melt specific volume due to the change in pressure. For the calculation of mass flow rate, at first we need to calculate the pressure change in the screw antechamber as a function of time. The pressure change in the screw antechamber as a function time is calculated by using equation 95.

$$p(t) = (p_c - p_E)\cdot \exp(-k'\cdot t) + p_E \qquad (95)$$

By using equation 95, we can calculate the pressure value at every time interval during the expansion time. The mass flow rate at the particular time interval is calculated by using equation 96.

$$\dot{m}_s = \frac{m_0}{v(p_E, T_M)} \cdot \left(- \frac{K_{1m}}{(p_k + K_{4m})^2} - \frac{K_{2m}}{(p_k + K_{3m})^2} \cdot T_M \right) \cdot \left(-(p_k - p_E) \cdot k' \cdot \exp^{-k' \cdot t_i} \right) \quad (96)$$

The typical mass flow rate curve as a function time is shown in figure 26. By integrating the area under the mass flow rate curve at definite time interval, we can calculate the mass of melt comes out due to the expansion at that particular time interval.

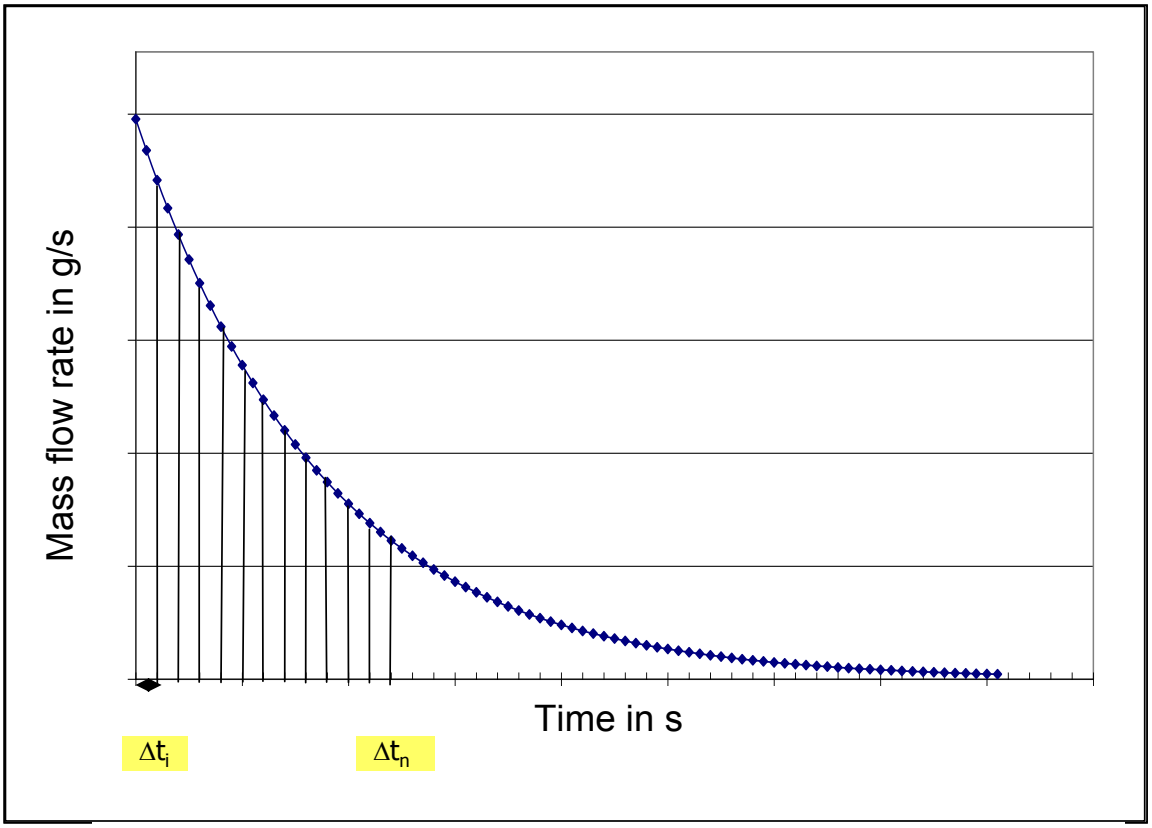

Figure 26: Mass flow rate as a function time during the expansion

5.7 Optimization of calculated minimum required end pressure and calculated compression pressure

As explained in the chapter 5.4, for the calculation of the minimum required fill pressure at first we assumed a constant filling time for each segment. However, in reality due to the change in mass flow rate as a function time, every segment in the part is filled with a different filling time.

The filling time of the each segment can be calculated from the plot of mass flow rate. By integrating the area under the mass flow rate curve, one can easy calculate the mass of melt comes out of injection unit. Whereas every part segments have a mass which can be calculated with respect of the segmental volume and melt density. From the integration area under the mass flow rate curve, we can calculate at what time interval (Δt) every segment is filled. In this manner, we can calculate the new filling times of the every segment. The total sum of each segment filling time is taken as the part filling time, which should be lower than the approximated filling time calculated at first.

After the calculation of new filling time, we once again go for the calculation of the minimum required fill pressure with taken into account of the formation of the frozen skin layer and change in melt temperature. Then we calculate the maximum compression pressure. These calculation steps are carried out iteratively until we reach no changes in the filling time and changes in the calculated end pressure as well as in the calculated compression pressure.

6 The developed simulation software - *Xmeltsoft*

Based on the above mentioned calculation approach a simulation program named as *Xmeltsoft V.1.0* was developed with the help of the visual basics application (VBA) as an Excel add-in. The Visual Basic 6.0 editor was used for coding the program and it works in Microsoft Excel 2002. The program performs the simulation of the expansion injection moulding process for simple thin-wall geometries. For the chosen thin-wall part, the simulation software permits us to carryout the calculations of the approximated filling time, the minimum required filling pressure, the needed compression pressure and the mass flow rate. Figure 27 shows two screenshots of the developed simulation software.

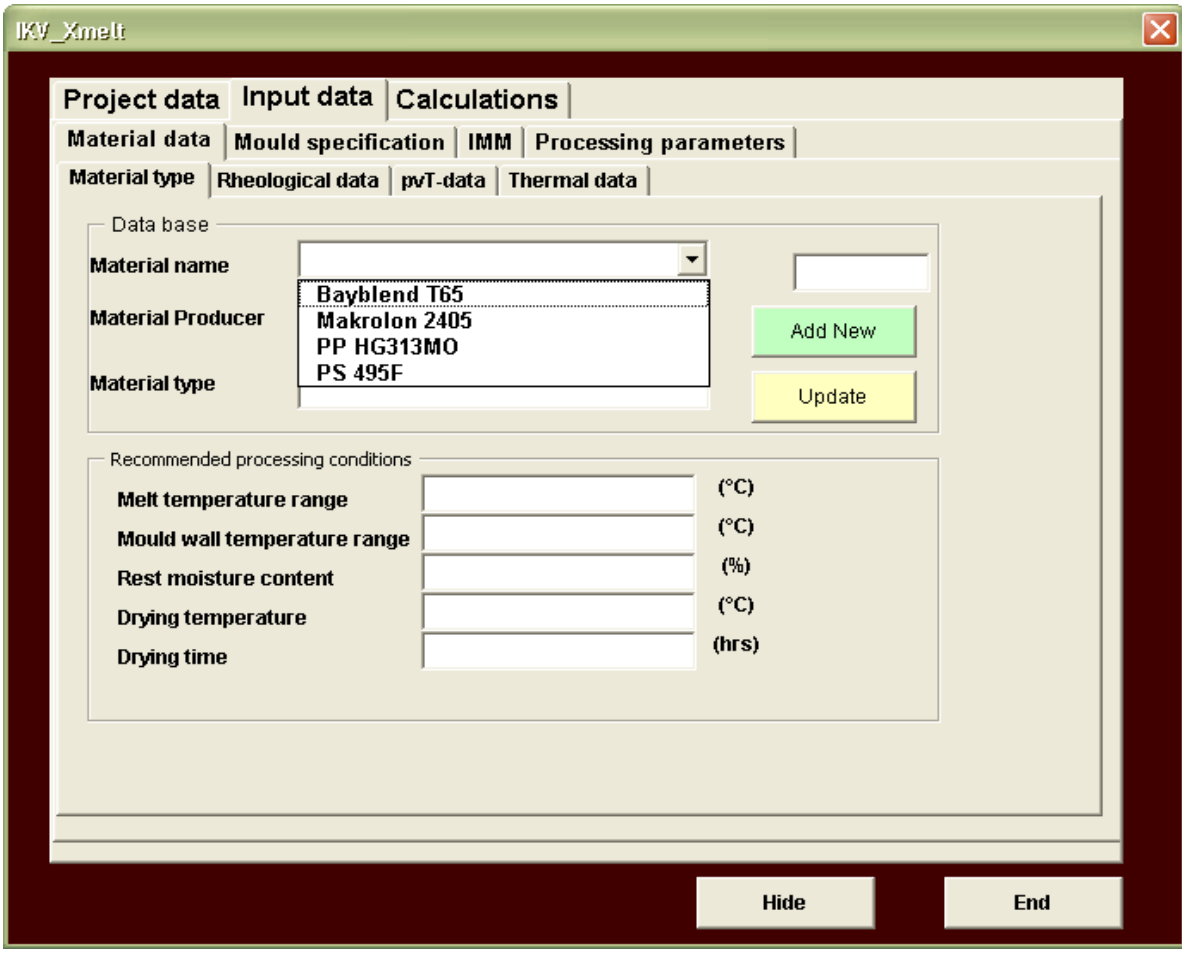

Figure 27: Screenshot of the developed calculation program Xmeltsoft V.1.0.

The developed software is user-friendly software and it works with the MS Excel environment. The software is supplied as an Excel Add-In file. An Excel add-In is a file (usually with an .xla or .xll extension) that Excel can load when it starts up [27-31]. The file contains code (VBA in the case of an .xla Add-In) that adds additional functionality to Excel, usually in the form of new functions. Add-Ins provides an excellent way of

increasing the power of Excel and they are the ideal vehicle for distributing your custom functions. The user can create their own customised macro program in Excel with the help of the Visual basic editors. In the Visual Basic Editor, we can use object-oriented programming to create our own programs. A program is, in principle, nothing more than a set of instructions that the computer runs in a specified order. The Xmeltsoft V.1.0 was developed in that manner to compute series of data. The user can call the program in the excel environment to carry out the simulation. Figure 28 shows the screenshot of Excel 2003 program loaded with *Xmeltsoft* -software user form.

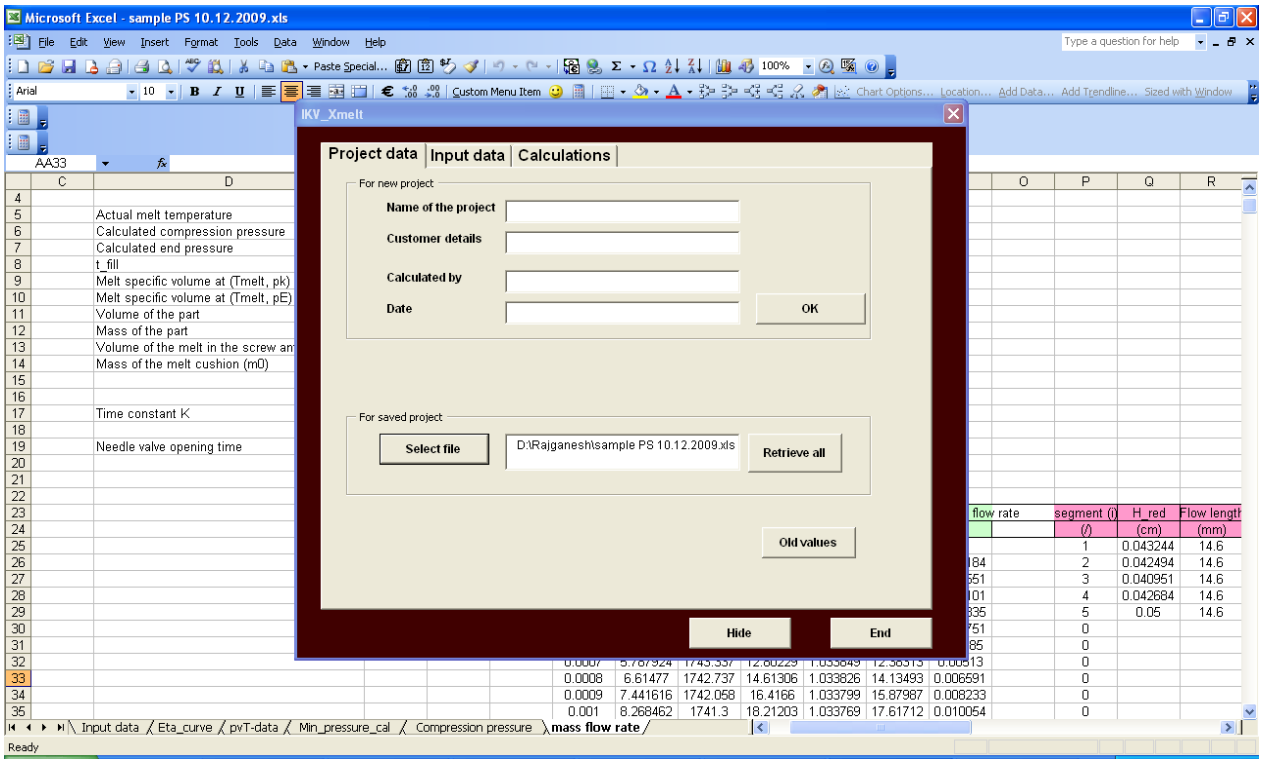

Figure 28: Screenshots of an Excel 2003 file loaded with the Xmeltsoft V.1.0.

Upon loading the program in Excel, the user form has three main pages as follows:

1. Project data
2. Input data
3. Calculations

In project data, the user can save project relevant information for e.g. about the customers details and name of the project etc. Further, the user can open the already saved project for any modification. The Input data consists of four main pages such as material data, mould specification, injection moulding specification and process parameters. The material data consists of material type, rheological data, pvT-data and

thermal data (Figure 29). The user has to input the necessary material data in these four category for the simulation.

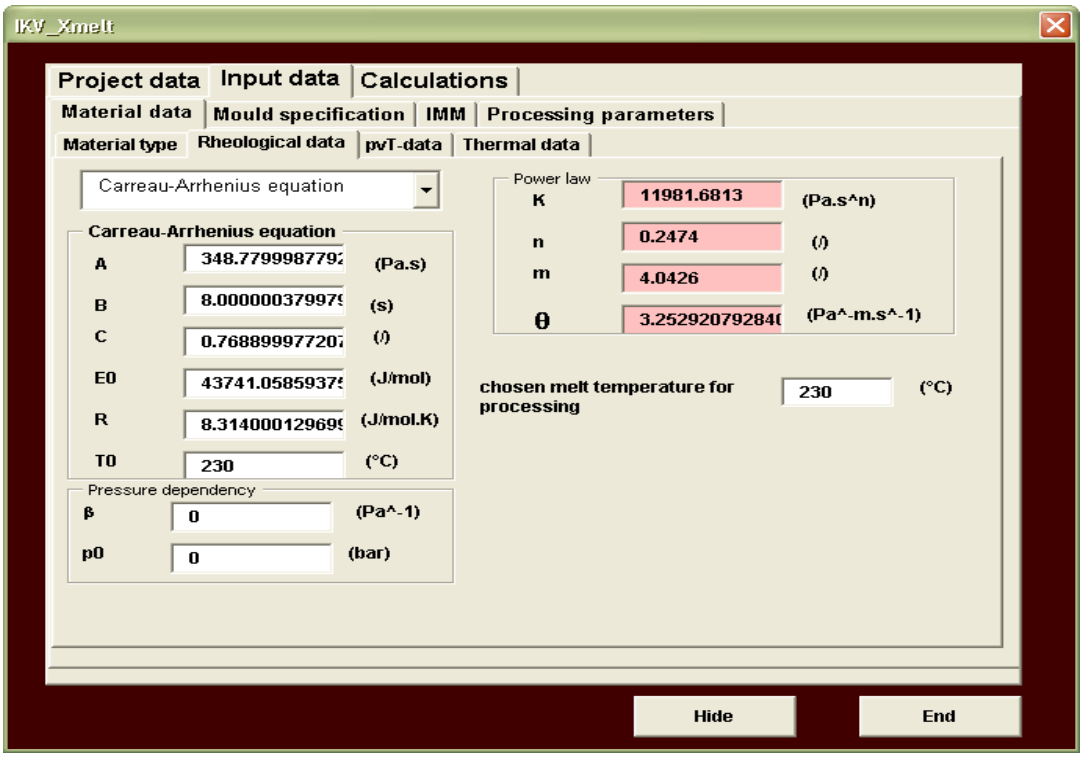

(A) Rheological data

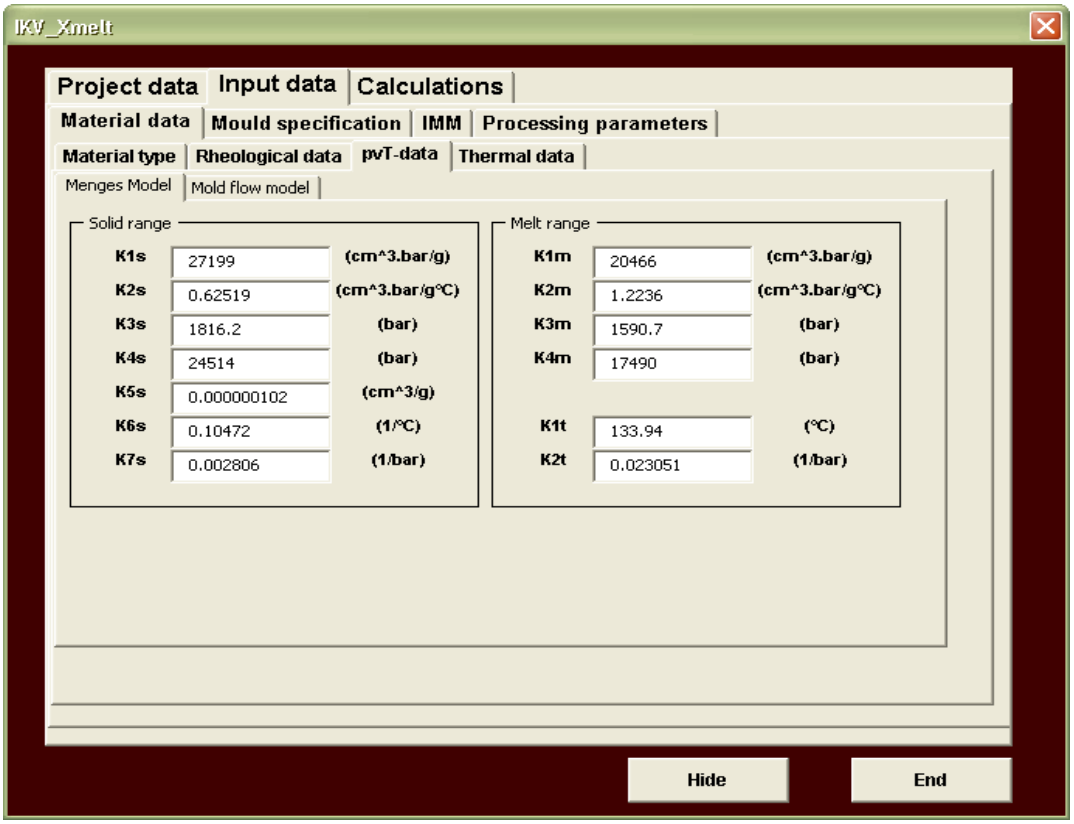

(B) pvT- data

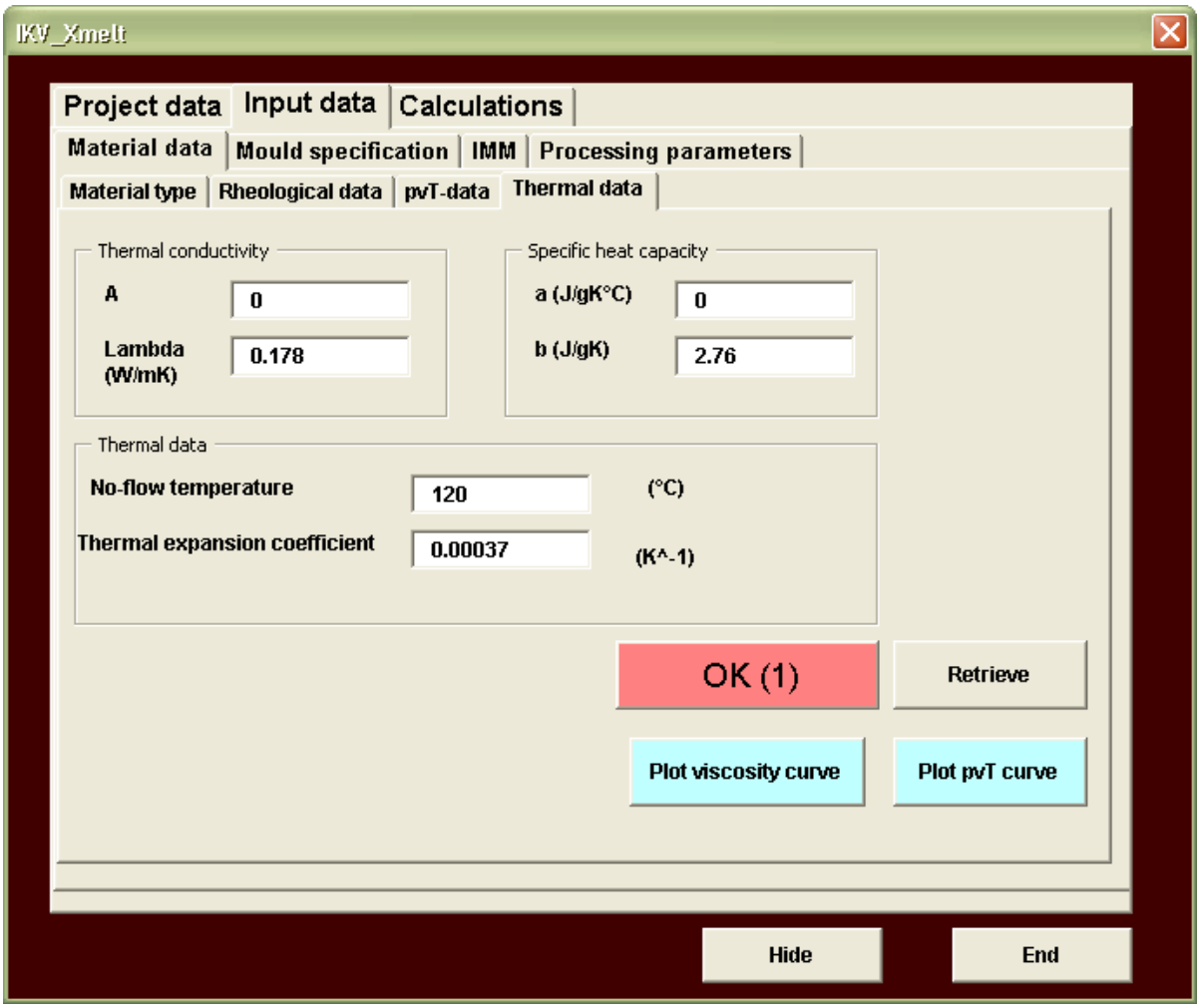

(C) Thermal data

Figure 29: Screenshots of the Xmeltsoft V.1.0 about material data

After entered the needed material data for the simulation, the user has to specify the mould details, about injection moulding machine related parameters and about the chosen the process parameters for the simulation. Once all the input data are entered, one can shift to the calculation section. The calculation part consists of three levels:

- Calculation of the approximated filling time and the end pressure.
- Calculation of the needed compression pressure or else calculation of needed melt cushion.
- Mass flow rate calculation and iterative calculation of the actual filling time.

The calculation procedure of the Xmeltsoft V.1.0 is shown in following figures (figure 30 to figure 37).

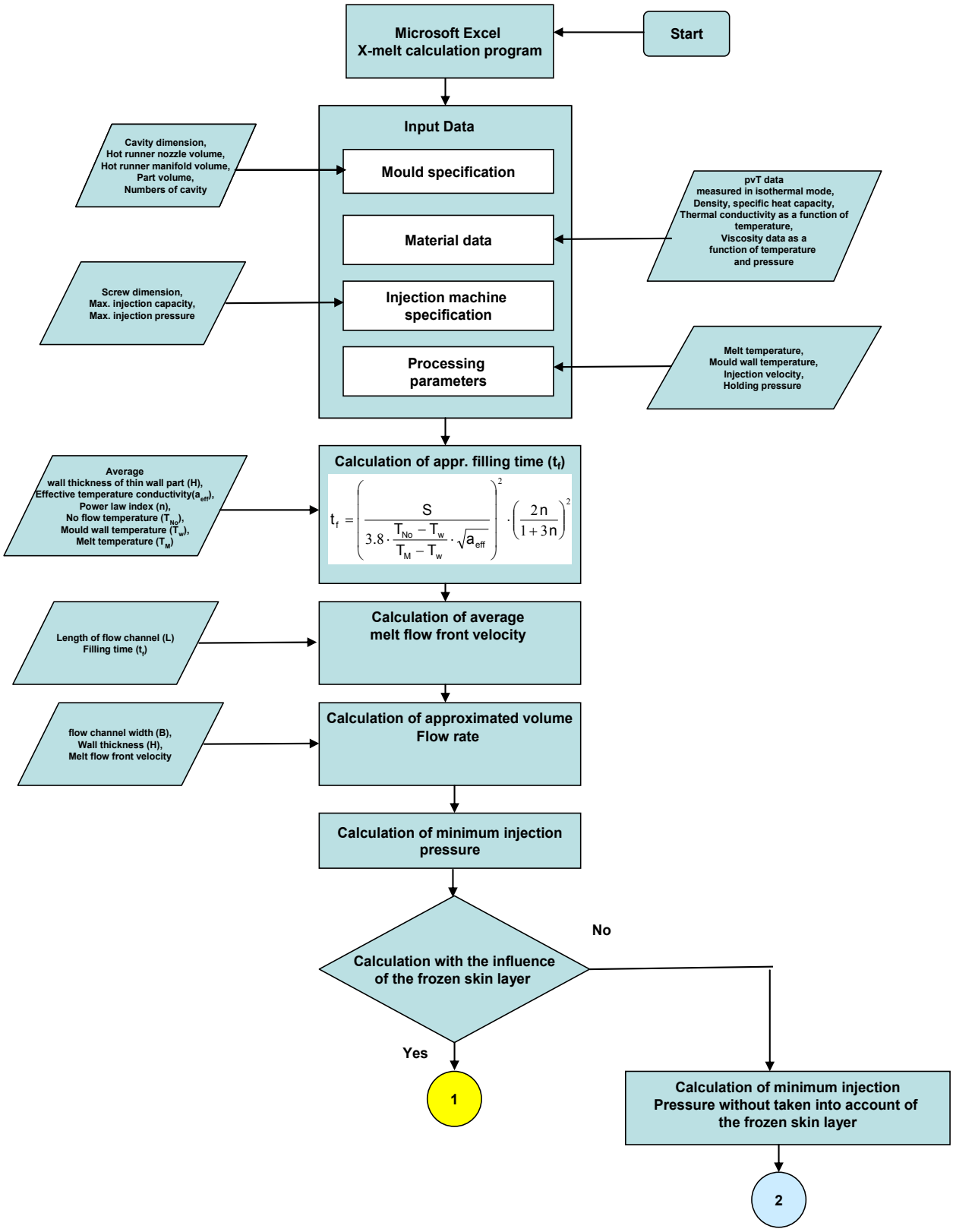

Figure 30: Calculation procedure followed for approximated filling time.

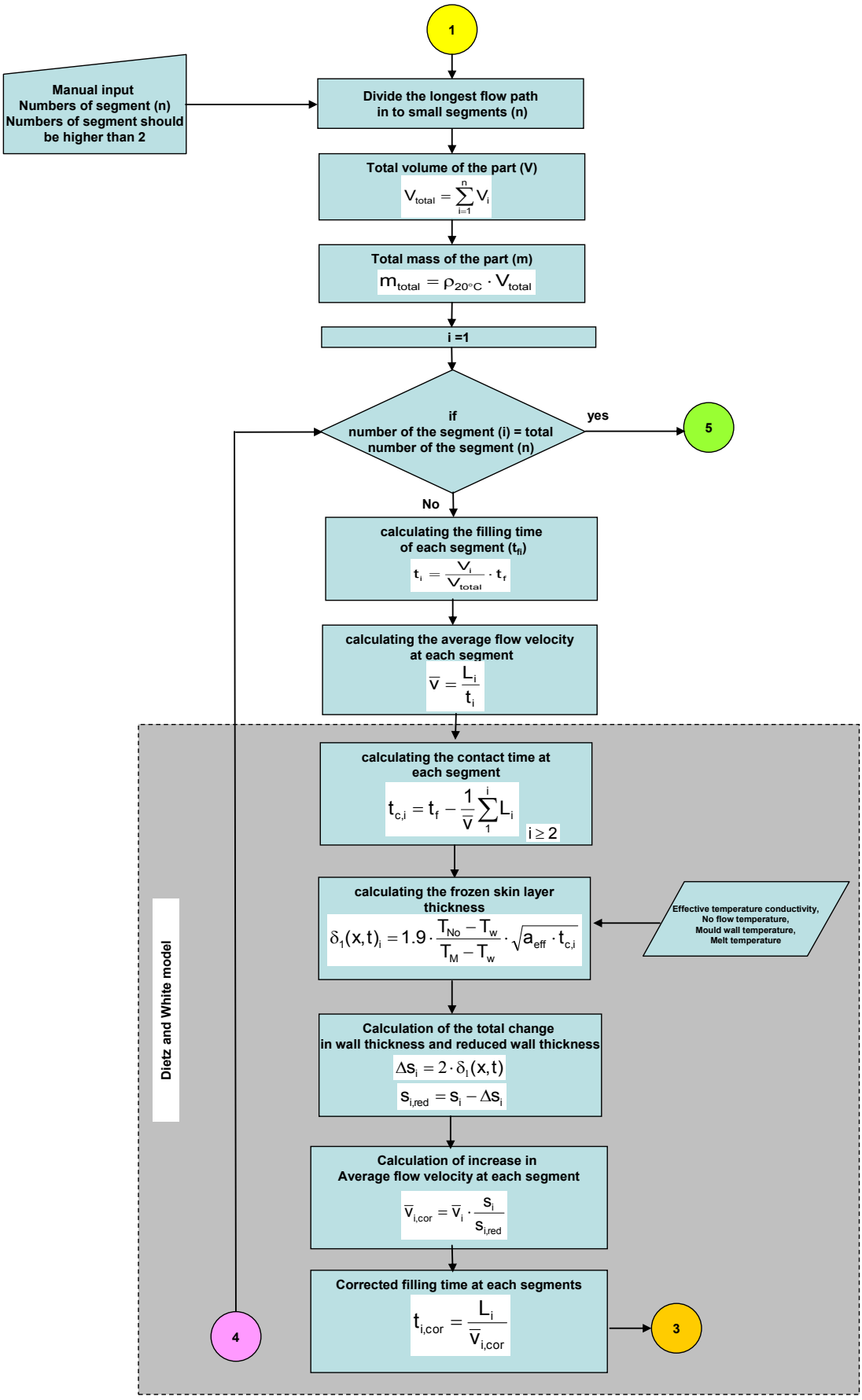

Figure 31: Calculation procedure followed for the frozen skin layer thickness.

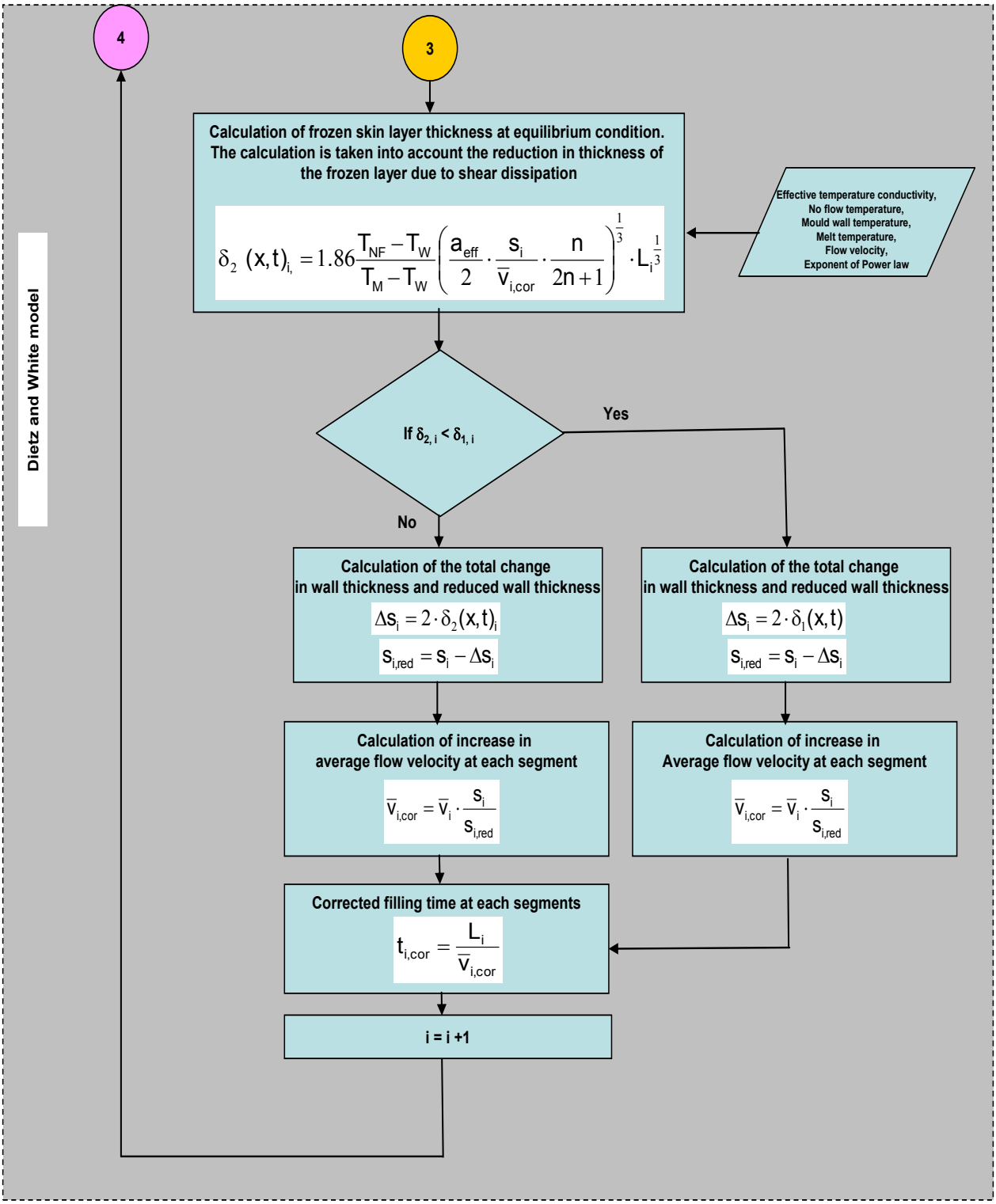

Figure 32: Calculation procedure followed for wall thickness reduction

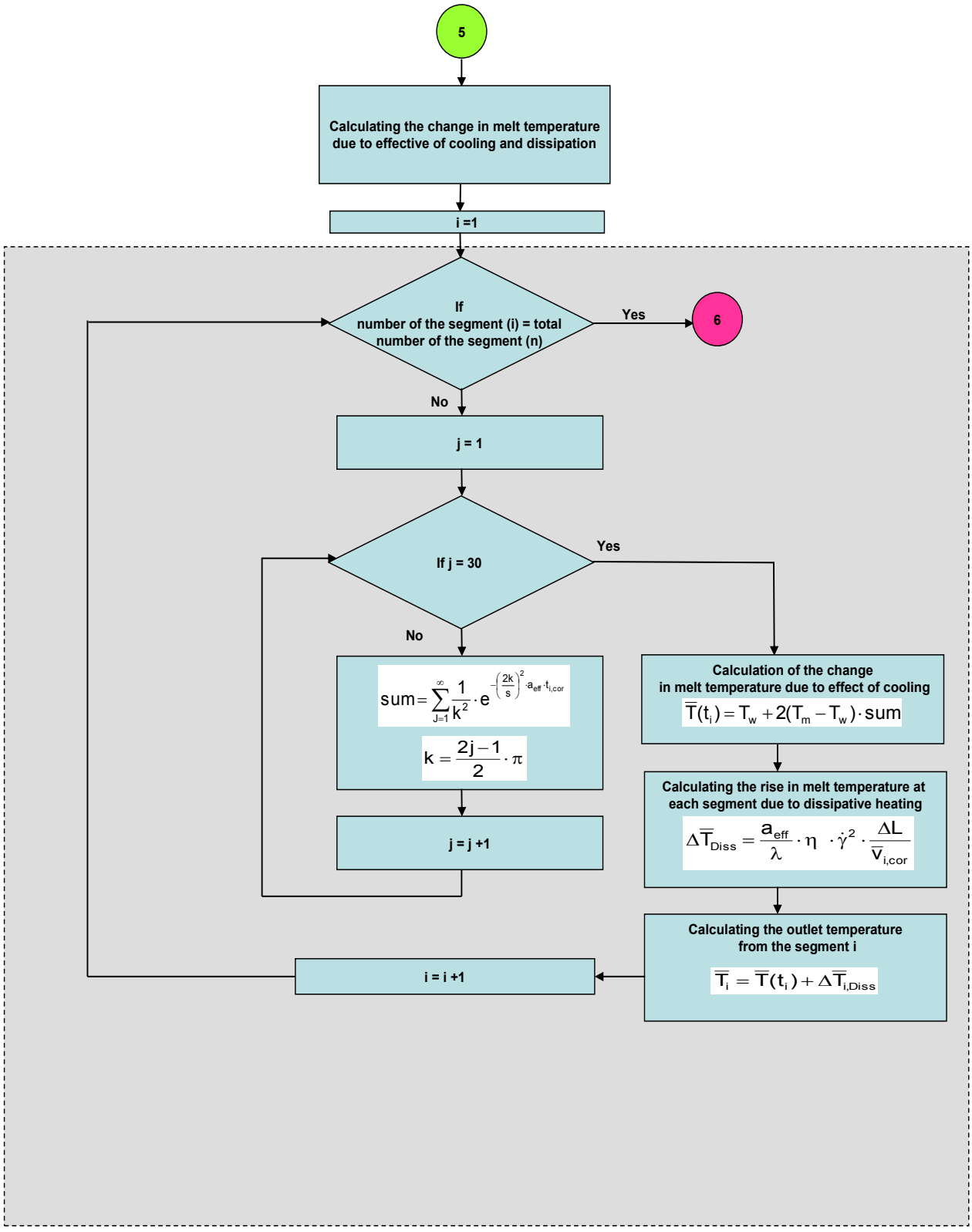

Figure 33: Calculation procedure followed for the melt temperature change due to dissipation and effect of cooling.

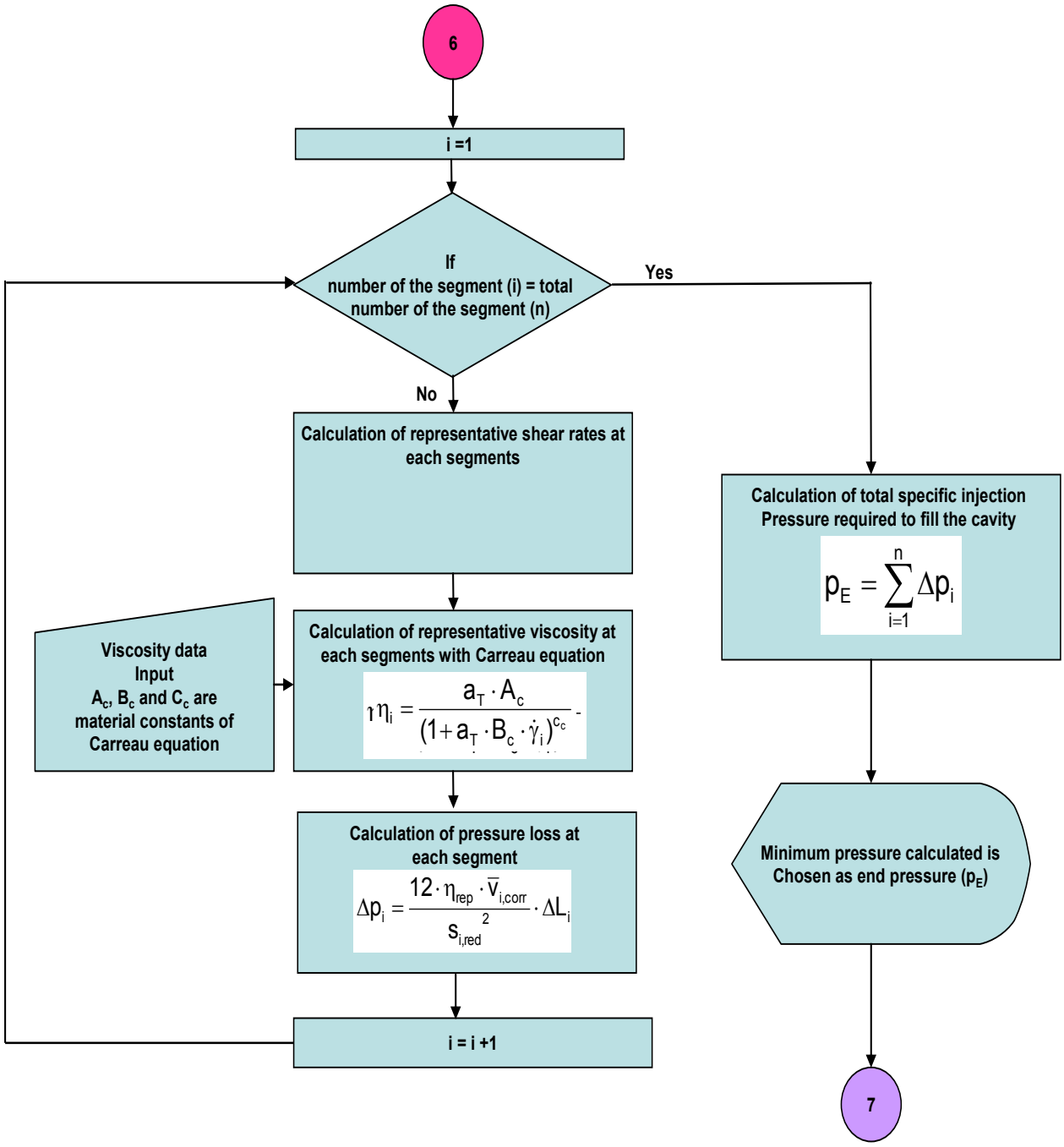

Figure 34: Calculation procedure followed for the viscosity calculation and press drop

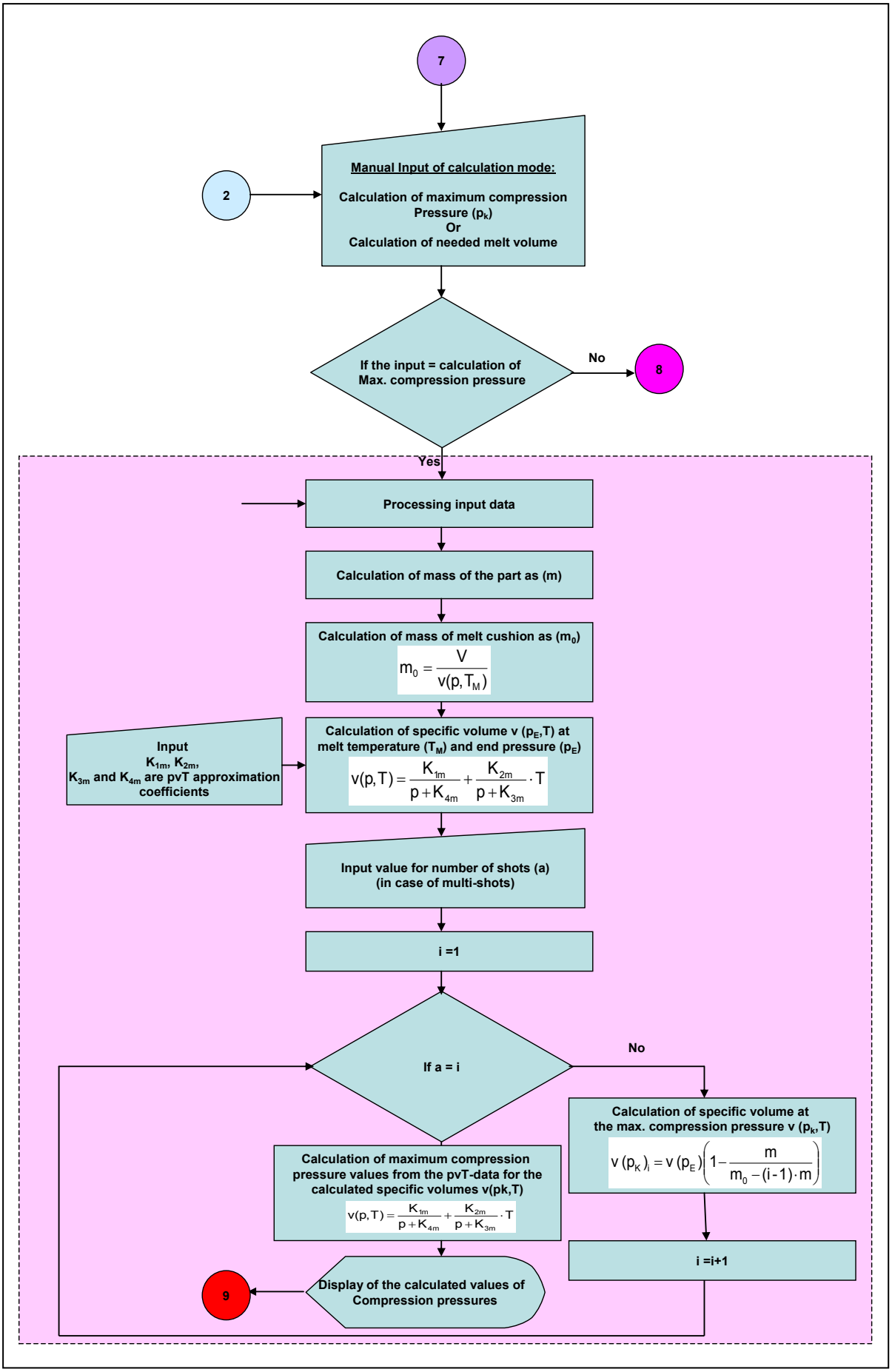

Figure 35: Calculation procedure followed for the maximum compression pressure

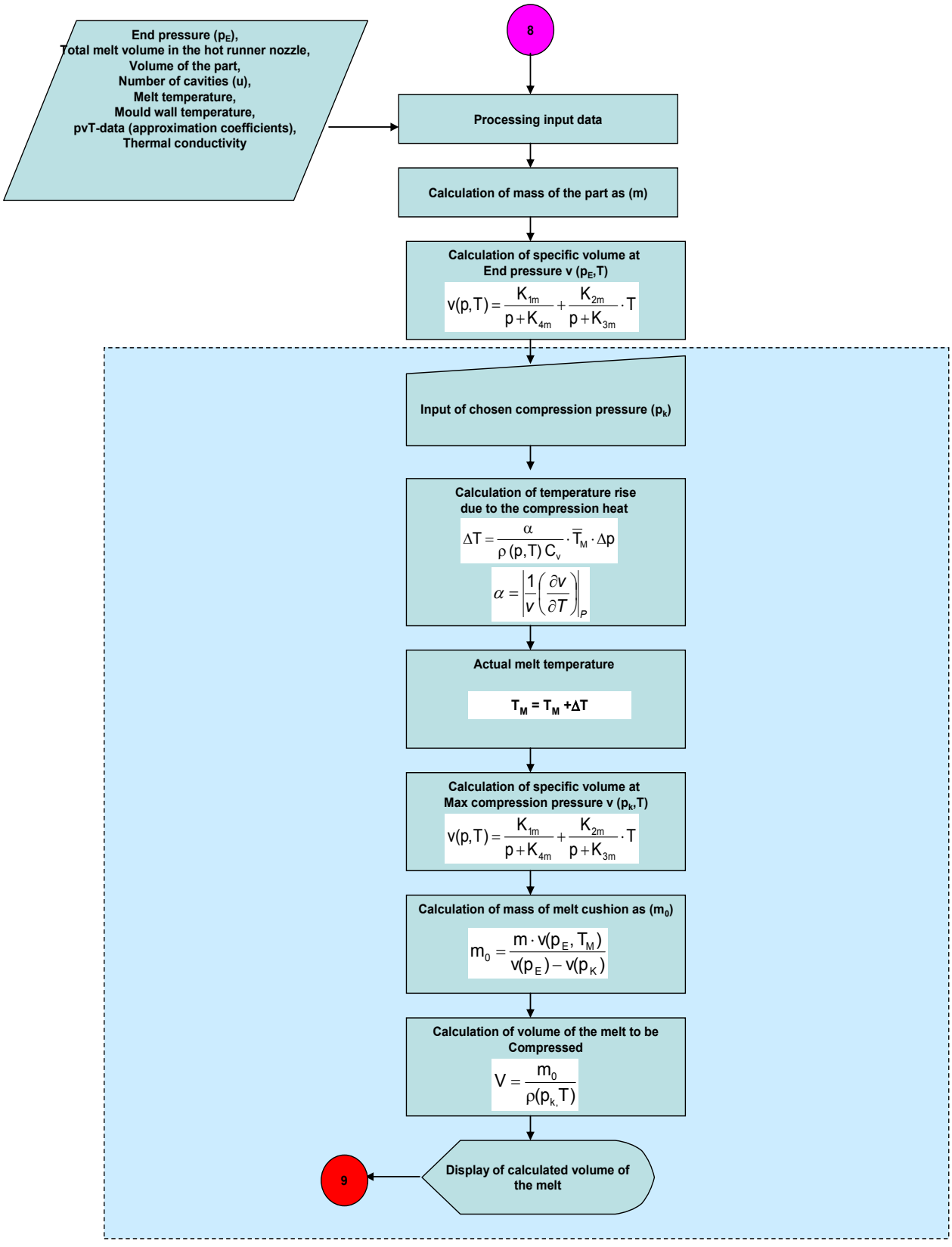

Figure 36: Calculation procedure followed for the needed melt cushion

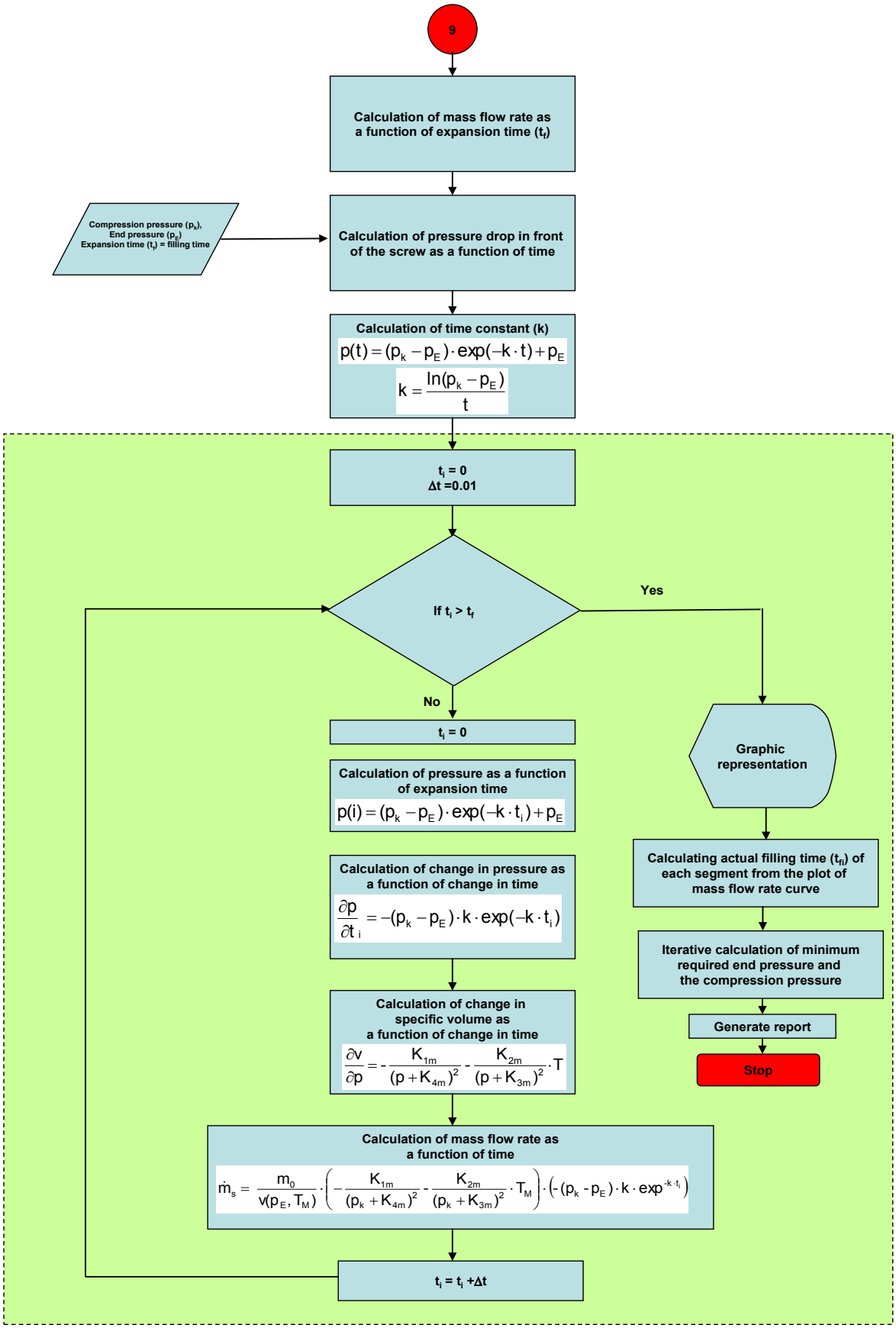

Figure 37: Calculation procedure followed in mass flow rate and iterative correction of the filling time

The simulation program has a build-in material database, which consists of complete material data for four materials. The material database was created in MS Access and connected to VBA user-form by ActiveXData Object (ADO). Figure 38 shows screenshots of the material database listed with four materials.

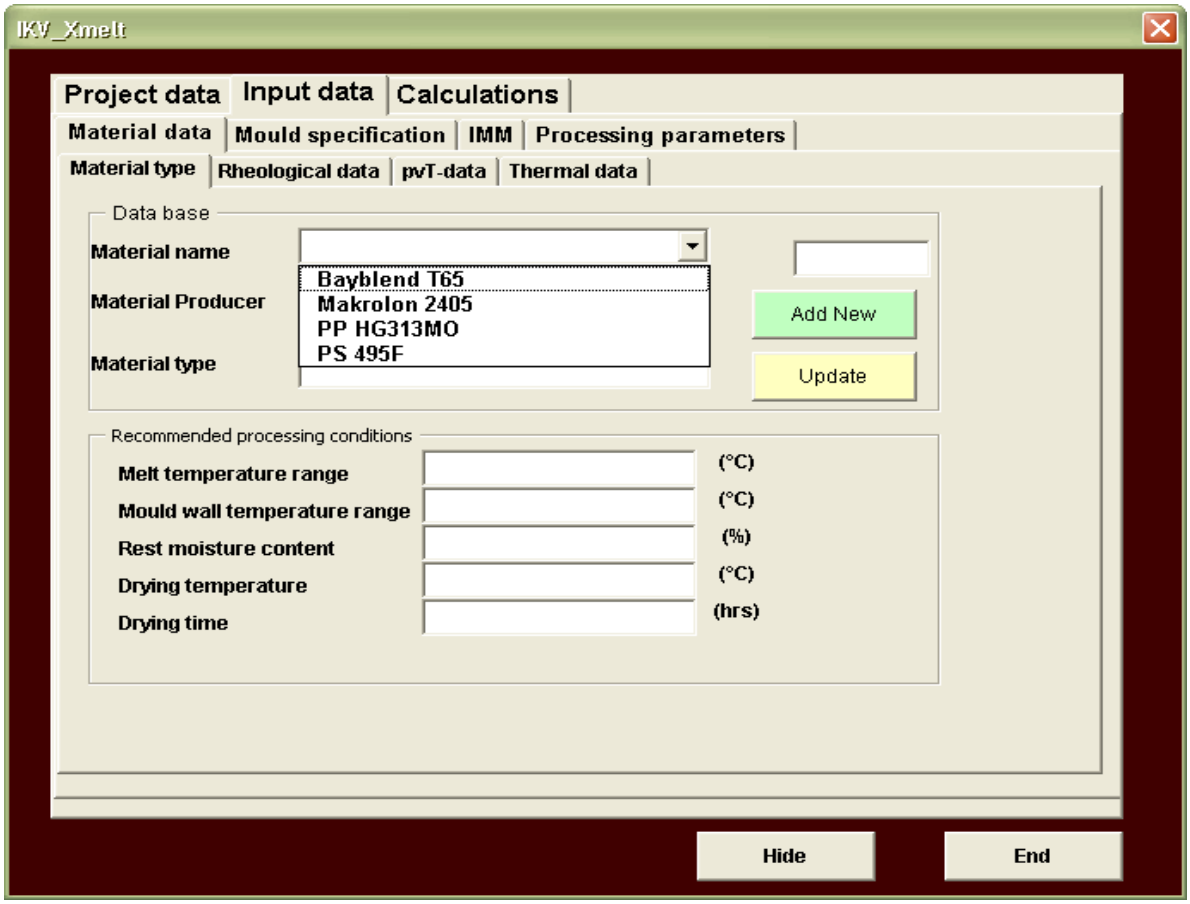

Figure 38: Screenshot of the build-in material database listed with four materials.

The reliability of the simulation results depends mainly on the following factors: quality of the input material data, process parameters, and the calculation model. More importantly, the practically relevant material data are necessary to improve the quality of the simulation results. Therefore, within this project work, a significant focus was given for the improved material data. The necessary material data such as the viscosity data, pvT-data and thermal data were measured in practically relevant conditions which prevail in thin-wall injection moulding for four thermoplastic materials. The improved material data of the four materials were included in the material database of the *Xmeltsoft V.1.0*. In the next chapter, the different aspect of measurement techniques and testing methods for acquiring the improved material data are explained.

7 Improved material data

7.1 Material data requirements for the expansion injection moulding

The temperature dependent material properties such as melt viscosity, thermal conductivity, and specific heat capacity are commonly available for the injection moulding simulations. However, these material properties have a significant dependency on the pressure and such pressure and temperature dependent material data are not available in any commercially available material database. In thin-wall expansion injection moulding, the thermoplastic melt undergoes a high pressure (up to 2500 bar) and temperature during the compression phase and it undergoes a high shear rate (up to 10^6 s^{-1}) during the filling phase. In those processing conditions, the pressure dependent material properties cannot be neglected. Because of the strong compression and shearing, there is a significant temperature rise, which directly affects the viscosity of the melt.

The expansion injection processability of thermoplastic melt is characterized in terms of their thermodynamic properties, which is depends on the accuracy of measured PVT data. The very high pressures cause a strong compression of the melt. Knowledge of the compressibility is a very important aspect and is used to determine the expansion volume. The high accurate pvT-data measured up to 2500 bar and temperature and pressure dependent thermal conductivity data are necessary. Furthermore, in thin-wall injection moulding the melt undergoes rapid cooling in the cavity which resulting the demand for pvT-data measured with relatively higher cooling rate.

7.2 Approach of acquiring reliable material data

Figure 39 shows the approach of acquiring the improved material data for the expansion injection moulding simulation. The needed material data for the simulation are as follows:

1. Viscosity data as a function of shear rate, temperature and pressure
2. Pressure-specific volume-temperature relationship (pvT-data)
3. Specific heat capacity as a function of temperature
4. Thermal conductivity data as a function of temperature and pressure

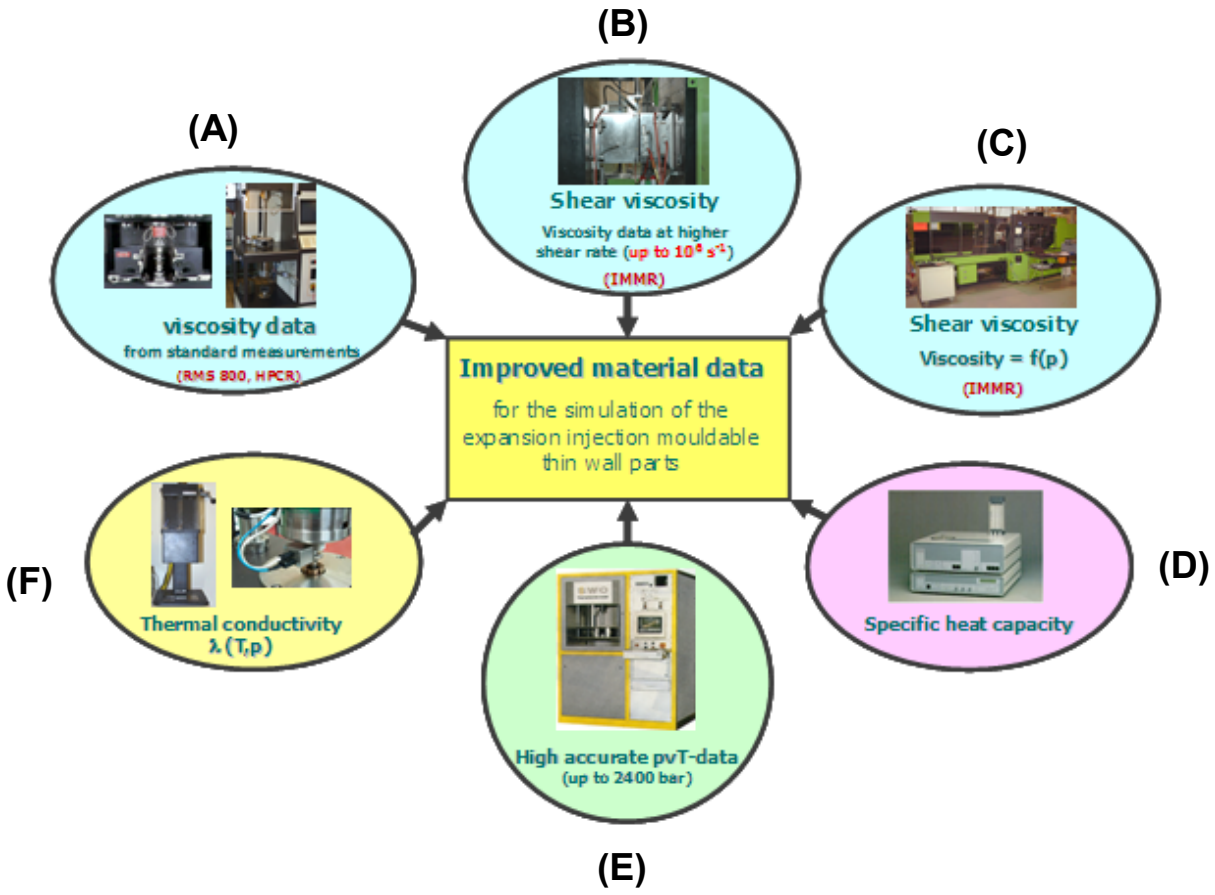

Figure 39: Approach of acquiring improved material data.

The standard rheological measurements at lower shear rates (from 0.001 s^{-1} to 100 s^{-1}) were carried out on the rotational rheometer RMS 800 from Rheometric Inc., Piscataway, N.J., USA. The viscosity measurements at higher shear rates from 100 s^{-1} to 100,000 s^{-1} were carried out on the high pressure capillary rheometer (HPCR) Rheograph 2002 from Göttfert Werkstoff-Prüfmaschinen GmbH, Krefeld, Germany (see Figure 39-A) [32]. The counter-pressure measurement technique is generally used for the pressure dependent viscosity measurements on the standard high pressure capillary rheometer with the round capillary die. For that, a backpressure chamber is attached in series with the round capillary die in HPCR. However, the commercial high-pressure capillary rheometer equipments have its own measurement limitations in terms of its maximum force and its maximum melt volume in the measurement cylinder. For rheological measurements at high shear rates and at high counter pressures, the measurements require a higher volume of the melt together with a higher injection speed in addition to higher injection pressure. These requirements are realized by doing the rheological measurements on the injection moulding machines. Further, the injection mouldings machine rheometer (IMMR) facilitates the possibility to measure the viscosity at process relevant measurement conditions. To fulfil the above mentioned requirements a new rheological injection mould (see in figure 39-B) was developed by

the Institute of Plastics Processing within an EU funded project. The rheological injection mould (see in figure 39-C) was mounted on the Engel injection moulding machine for high shear rates viscosity measurements and to measure viscosity with different counter pressure.

The specific heat capacity as a function of temperature was measured in a differential scanning calorimeter (DSC) based on ISO standard ISO 11357-4 (see in figure 39-D). The pvT-data were measured in a standard pvT measuring instrument, type PVT100 from SWO Polymertechnik (see in figure 39-E). The pvT data were measured using the isobaric cooling mode (6 K/min) in a pressure range from 200 bar to 2400 bar. The measured pvT-diagrams were approximated with the help of the 7-coefficients Menges model. The thermal conductivity as a function of temperature was measured with K-system II, which works on the principle of linear line heat source method (see in figure 39-F). The used measurement standard is ASTM D5930-97. The thermal conductivity as a function of temperature and pressure was measured on the high pressure capillary rheometer with the help of the thermal conductivity measurement sensor from Göttfert Werkstoff-Prüfmaschinen GmbH, Buchen, Germany.

7.3 Investigated thermoplastic materials

The material data were measured at the Institute of Polymer Processing for three chosen thermoplastic materials such as PP HG313MO from Borealis, PS 495F from BASF and ABS/PC Bayblend T65 from BASF.

7.3.1 Polypropylene (PP HG313MO)

PP HG313MO is a high melt flow polypropylene, which is a homopolymer specially designed for product with long flow length and manufactured by Borealis AG, Austria. PP HG313MO is formulated for high speed injection moulding and it has a narrow molecular weight distribution. Based on ISO 1133 test standard, the melt flow rate (MFR) is 30 g/10 min measured at 230°C. The recommended melt temperature for the processing is 210°C - 250°C [33].

7.3.2 Polystyrene (PS 495F)

Polystyrene PS 495F is a high flow and high impact polystyrene manufactured by BASF. PS 495F can be injection moulded under different conditions depending on the machinery available and article moulded. Based on ISO 1133 test standard, the melt volume flow rate (MVR) of PS 495F is 9.5 cm^3/10 min at melt temperature of 200°C

[34]. The recommended melt temperature range for injection moulding is 180°C - 260°C.

7.3.3 ABS/PC blend (Bayblend T65)

Bayblend T65 is the non-reinforced, amorphous thermoplastic polymer blends based on polycarbonate (PC) and acrylonitrile butadiene styrene (ABS). The material has ideal combination of toughness, rigidity and flowability. Bayblend T65 is manufactured by Bayer material science. Based on ISO 1133 test standard, the melt volume flow rate (MVR) of Bayblend T65 is 12 cm^3/10 min at 260°C [35]. It is essential for Bayblend T65 to be dried prior to processing. For injection moulding, there must be less than 0.02 % residual moisture in the granules. Moisture in the plastic melt can lead to surface defects in the form of streaks and to hydrolytic degradation (reduction in mechanical properties). The drying condition recommended for Bayblend T65 is 2-4 hours drying at 110°C. The optimum processing melt temperature range is 240°C - 280°C. Overheating, and excessively long residence times for the melt in the barrel must be avoided, since this can lead to material damage, i.e. to a reduction in toughness, or to surface defects in the form of streaks on the injection moulded part.

7.4 Pressure-volume-temperature (pvT)-diagram

7.4.1 Theoretical fundamentals

A pressure-volume-temperature (pvT) relationship for polymeric materials is a subject of importance to polymer scientists and engineers, particularly from a process design standpoint. Equally important is the need for equations of state that adequately described this behaviour over a wide range of temperature and pressure [36].

Solidification is the process in which a material undergoes a phase change. A thermoplastic polymer solidified as the temperature of the material is lowered below either the melting temperature for a semi-crystalline polymer or the glass transition temperature for an amorphous thermoplastic. The solidification of most materials is defined at a discrete temperature, whereas amorphous polymers do not exhibit a sharp transition between the liquid and solid states. Once the material has cooled below the glass transition temperature (T_g), the polymer becomes stiff and brittle. At glass transition temperature, the specific volume and enthalpy curves experience a significant change of slope. With semi-crystalline thermoplastics, at crystallization temperature near the melting temperature, the molecules start arranging themselves in small crystalline and amorphous regions. During the process of crystalline structure formation, the heat of crystallization or heat of fusion is released. At onset of the crystalline growth,

the material becomes rubbery but not brittle. Since the amorphous regions are still above the glass transition temperature. For common semi-crystalline polymers, the degree of crystallization can be between 30 -70 %.

Figure 40 shows the typical temperature dependency of the specific volume of the thermoplastic materials. In the melt state, polymer chains have empty spaces in which molecules can move freely. Hence, the undercooled polymer molecules can still move as long as space is available. The point at which this free movement ends for a molecule or segment of chains is called the glass transition temperature or solidification point.

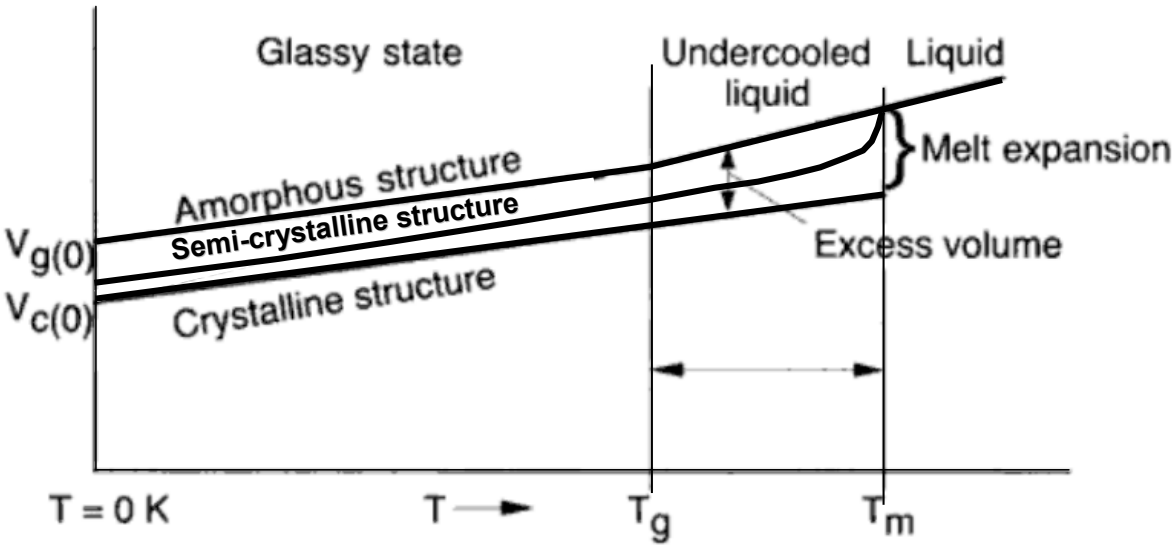

Figure 40: Thermal expansion model for thermoplastic polymers [37].

In the case of crystallization, the volume should jump to a lower specific volume. The specific volume is a commonly used property for polymeric materials. A pvT diagram is simply the presentation of the series of curves obtained when the measurement of specific volume versus temperature is repeated at different pressures. The schematic pvT-diagrams of an amorphous thermoplastic and of a semi-crystalline thermoplastic are shown in figure 41 and 42.

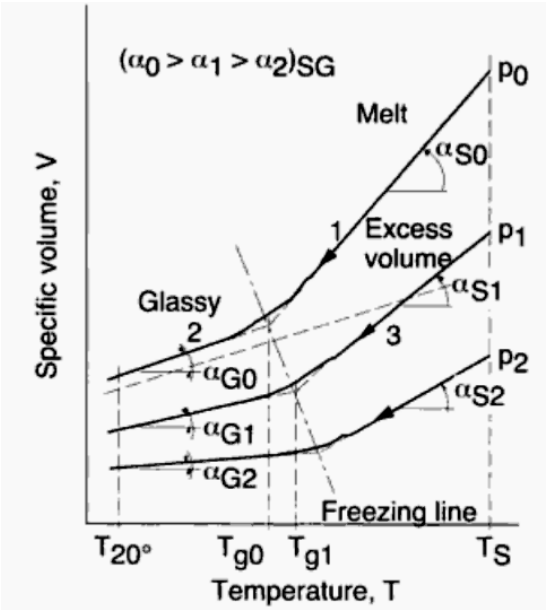

Figure 41: Schematic of a pvT-diagram for an amorphous polymer [37].

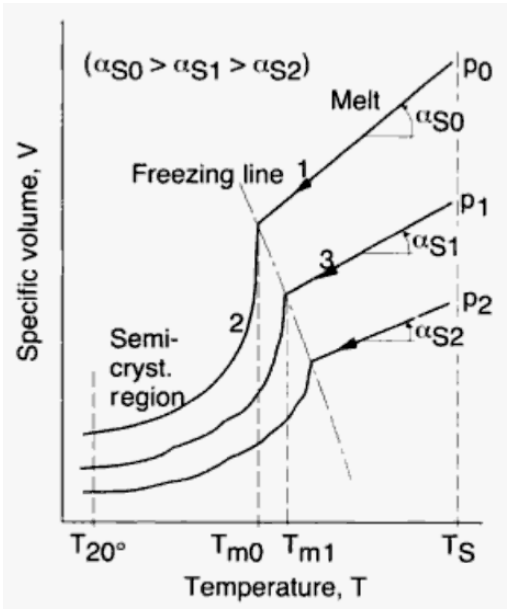

Figure 42: Schematic of a pvT-diagram for a semi-crystalline polymer [37].

For amorphous materials, the temperature at which the glass transition occurs on cooling depends on the one hand, the cooling rate and the other hand depends up on the applied pressure ($p_0 < p_1 < p_2$) (Figure 41). During the cooling process, the molecular chain mobility is hindered, especially in the area of the glass transition (T_{gi}) that the thermodynamic equilibrium and the relaxation of the macromolecules increases fast. This means that during rapid cooling of the melt, the molecules do not have enough time to regress. A faster cooling means a shorter measurement time and therefore a higher measurement frequency. The glass transition is a dynamic process, which

strongly depends on the cooling rate. The glass transition temperature shifts towards higher temperatures when measured at faster cooling rates and is a little further away from equilibrium, when cooled slowly [38]. The semi-crystalline polymers (Figure 42) show an abrupt transition in the pvT curve, which is associated with the crystallization temperature. The crystallization temperature is also a function of pressure. With the increasing pressure, the crystallization temperature shift to higher temperature range. The crystallization leads to a marked reduction in specific volume.

7.4.2 Experimental Procedure

The measurements were carried out on the measuring device type PVT 100 from the company SWO Polymertechnik Gmbh, Krefeld, Germany (figure 43). The p-v-T data were measured under isobaric cooling mode (6 K/min) in a pressure range from 200 bar to 2400 bar. The specimen is heated in an enclosed cell and change in its volume when subjected to pressure is measured. The pressure is applied directly to the specimen, using piston and cylinder set-up. The piston movement or deflections are used to measure volume change. Since the volume of the cell is known, the absolute specific volume can be measured by this technique. The specimens may be in the form of pellets. The quantity of specimen should not exceed 1-3 g. The measurable temperature range is in between 30°C to 400°C and pressure range from 200 to 2400 bar. Up to temperature range 290°C, we can use PTFE sealing. For above 290°C, we should use the Polyimid Vespel® as a sealing.

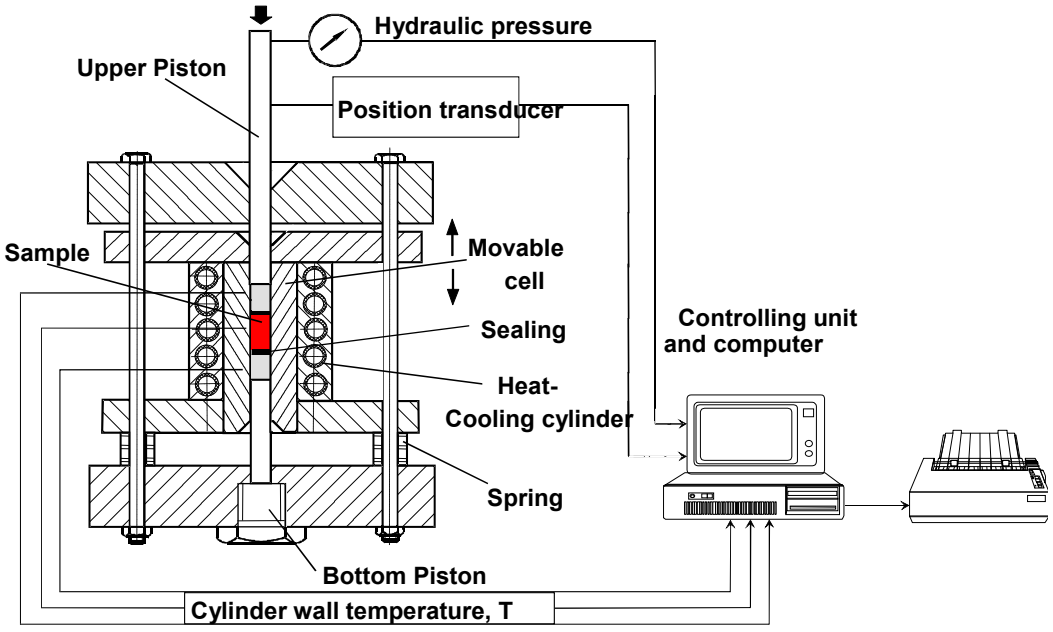

Figure 43: Measurement principle of PVT100 [39].

After the bottom piston is screwed tightly, the seals were placed inside the cell and calibration of the instrument was done. After the calibration, the cell was filled by polymeric material under high temperature (starting temperature). The test is started at the highest test temperature, which is typically the normal processing temperature. With the help of movable upper piston, we are able to change the pressure level in the cell. The position transducer monitors the movement of the upper piston with accuracy of less than 1µm. Electrical heaters and compressed air are used to heat or cool the cylinder to the required temperature during the measurement. With the help of the equation 97, the instrument calculates the change in specific volume during the measurement.

$$\Delta v(p,T) = \frac{\Delta l \pi r_c^{\,2}}{m_{sam}} \tag{97}$$

Where

Δv change in volume of the test sample

Δl change in length of the test sample

πr_c^2 cross sectional area of the cell

m_{sam} mass of the test sample

For the semi-crystalline polymer, the determined pvT curve can be approximated by using 7-parameter approximation model called as Menges model. The solid range of pvT curve is approximated with the equation 98:

$$v(p,T) = \frac{K_{1S}}{p + K_{4S}} + \frac{K_{2S} \cdot T}{p + K_{3S}} + K_{5S} \cdot \exp\left(K_{6S} \cdot T - K_{7S} \cdot p\right) \tag{98}$$

The above equation is valid only the temperature below the crystallization temperature. The pressure dependent crystallization temperature is calculated by the equation 99.

$$T(p) = K_8 + K_9 \cdot p \tag{99}$$

The temperature above the melt temperature the specific volume is determined by the equation 100.

$$v(p,T) = \frac{K_{1M}}{p + K_{4M}} + \frac{K_{2M} \cdot T}{p + K_{3M}} \tag{100}$$

The solid range of pvT diagram of the amorphous polymer is approximated with the equation 101.

$$v(p,T) = \frac{K_{1F}}{p + K_{4F}} + \frac{K_{2F} \cdot T}{p + K_{3F}} \tag{101}$$

where in above equations 98 -101 :

v	specific Volume (cm^3/g)
p	pressure (bar)
T □□□	Temperature (°C)
$K_{1M} – K_{4M}$	approximation coefficients for melt range
$K_{1S} – K_{7S}$	approximation coefficients for solid range of semi-crystalline materials
$K_{1F} – K_{4F}$	approximation coefficients for solid range of amorphous materials
$K_8 – K_9$	approximation coefficients of transition range

The isothermal compressibility (equation 102) is a very important parameter for describing the behaviour of the melt under pressure.

$$\kappa = -\frac{1}{v} \cdot \left(\frac{\partial v}{\partial p} \right)\Bigg|_T \qquad (102)$$

7.4.3 Results of the pvT- data measurement

7.4.3.1 PP HG313MO

The p-v-T data were measured in a standard pvT measuring instrument, Type PVT100 from SWO Polymertechnik GmbH. For polypropylene, the p-v-T data were measured using the isobaric cooling mode (6 K/min) in the pressure range from 200 bar to 2200 bar. The measured temperature range was 248°C - 42°C in the isobaric cooling mode [32]. Figure 44 shows the measured pvT-diagram of the PP HG313MO with the approximations. The measured pvT-diagram shows typical pvT behaviour of the semi-crystalline thermoplastics.

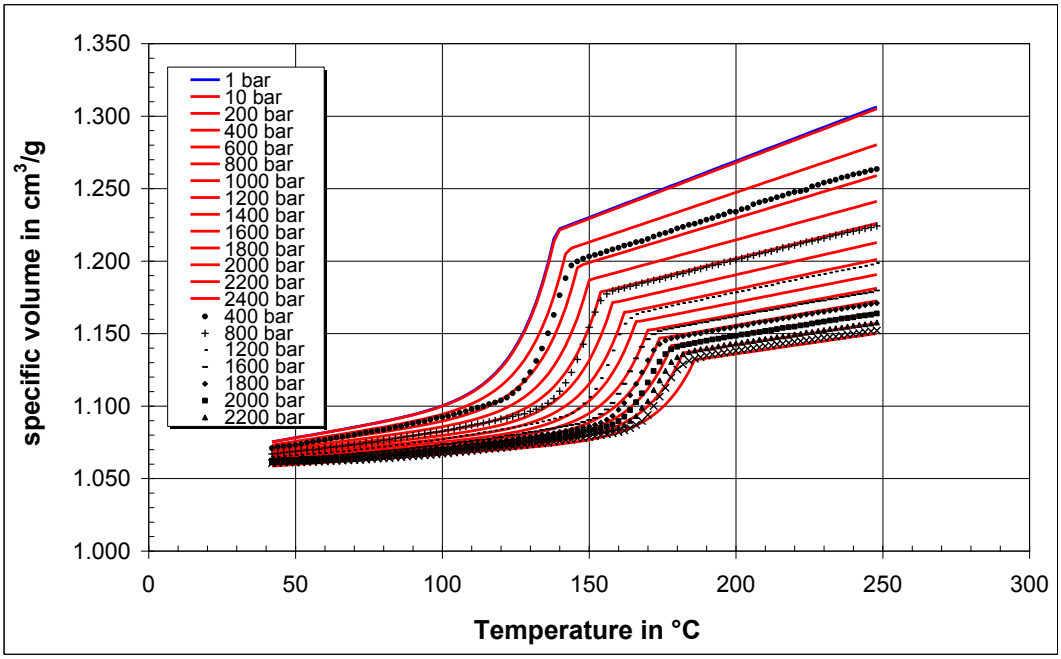

Figure 44: pvT-diagram of PP HG313MO, measured under isobaric cooling mode and constant cooling rate of 6 K/min.

The measured pvT curves were approximated with the help of the 7- coefficient Menges model. The material constants for the pvT data approximation of PP HG313MO are shown in table 4.

Table 4: Material constants for p-v-T data approximation based on Menges-model for PP HG313MO

PP HG 313 MO, Menges-model					
Solid range			Melt range		
K_{1S}	27199	(cm^3 bar/g)	K_{1M}	20466	(cm^3 bar/g)
K_{2S}	0.62519	(cm^3 bar/g °C)	K_{2M}	1.2236	(cm^3 bar/g °C)
K_{3S}	1816.2	(bar)	K_{3M}	1590.7	(bar)
K_{4S}	24514	(bar)	K_{4M}	17490	(bar)
K_{5S}	1.0227E-07	(cm^3/g)	Transition temperature		
K_{6S}	0.10472	(1/°C)	K_8	133.94	(°C)
K_{7S}	0.002806	(1/bar)	K_9	0.023051	(1/bar)

Figure 45 shows the calculated curves for the isothermal compressibility for PP HG 313 MO for 210°C, 230°C and 250 ° C. The calculated decrease of the isothermal compressibility from 200 bar to 2500 bar is about 45%.

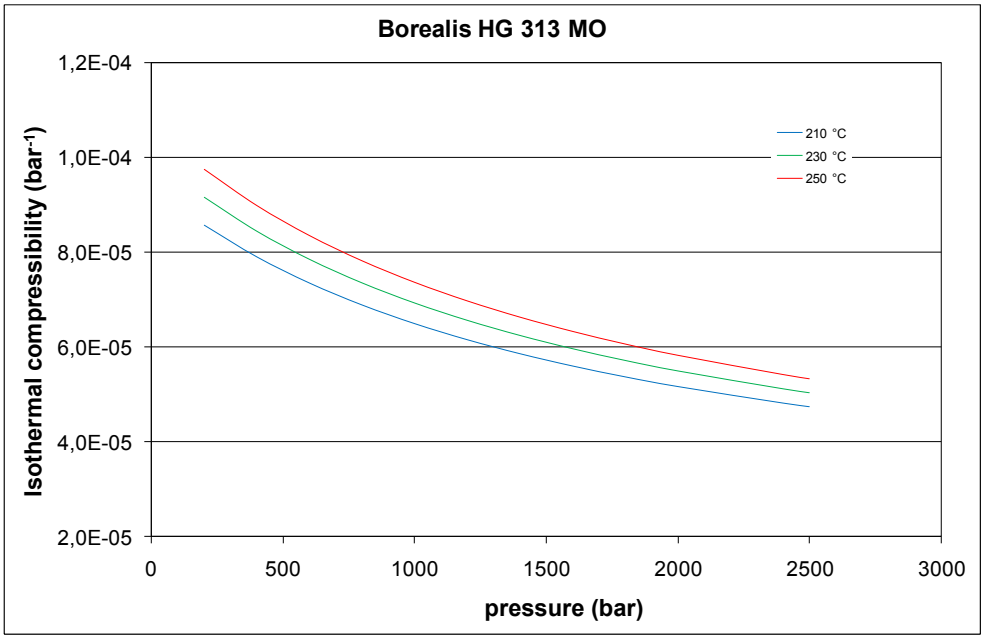

Figure 45: Calculated isothermal compressibility of PP HG313MO at 210°C, 230°C and 250°C.

7.4.3.2 PS 495F

For PS 495F material, the pvT diagram was measured in isobaric cooling mode in the pressure range from 200 bar - 2000 bar. The measured pvT-diagram of PS 495F is shown in figure 46 and the approximation coefficients of the measured pvT -diagram are listed in table 5.

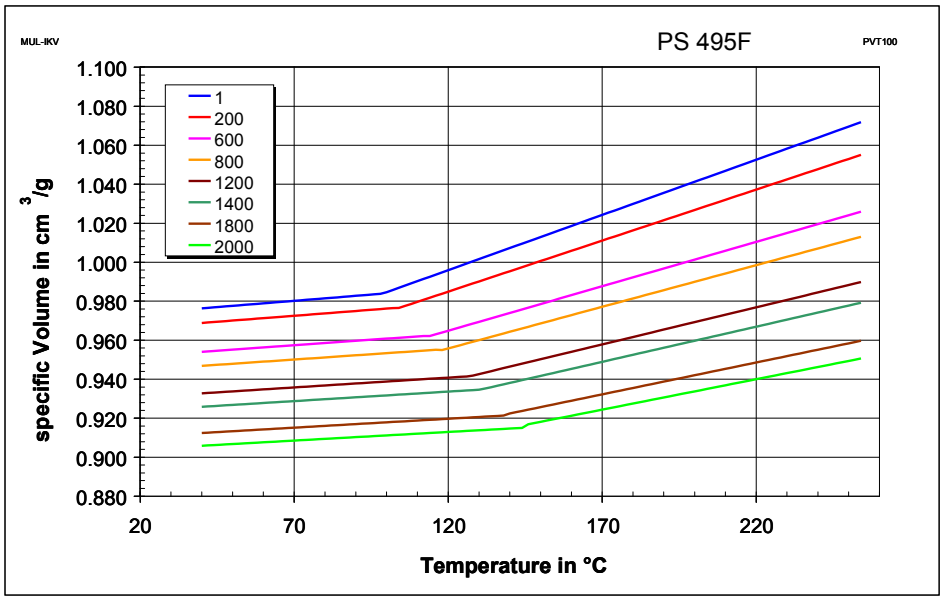

Figure 46: pvT-diagram of PS 495F, measured under isobaric cooling mode and constant cooling rate of 6 K/min.

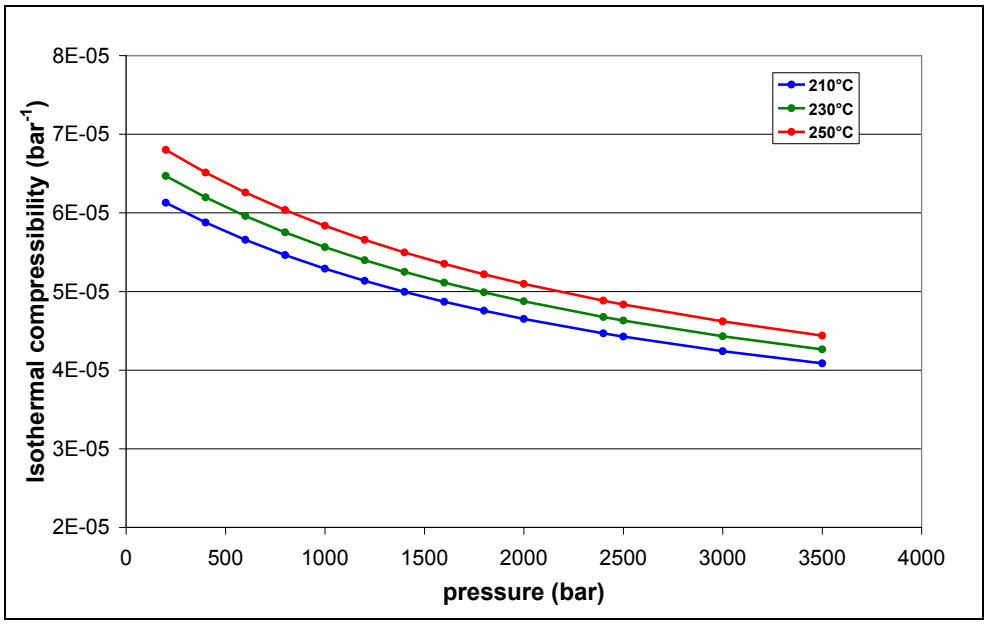

Figure 47: Calculated isothermal compressibility of PS 495F at 210°C, 230°C and 250°C.

Table 5: Material constants for p-v-T data approximation based on Menges-model for PS 495F

PS 495F					
Solid range			Melt range		
K_{1S}	29746	(cm³ bar/g)	K_{1M}	33978	(cm³ bar/g)
K_{2S}	0.58956	(cm³ bar/g °C)	K_{2M}	1.2167	(cm³ bar/g °C)
K_{3S}	3235.8	(bar)	K_{3M}	2218	(bar)
K_{4S}	30793	(bar)	K_{4M}	36543	(bar)
Transition range					
K_8	101.25	(°C)			
K_9	0.024318	(1/bar)			

7.4.3.3 Bayblend T65

For Bayblend T65, the pvT diagram was measured in isobaric cooling mode in the pressure range from 200 bar - 2400 bar. The measured pvT-diagram of Bayblend T65 is shown in figure 48 and the approximation coefficients of the measured pvT -diagram are listed in table 6.

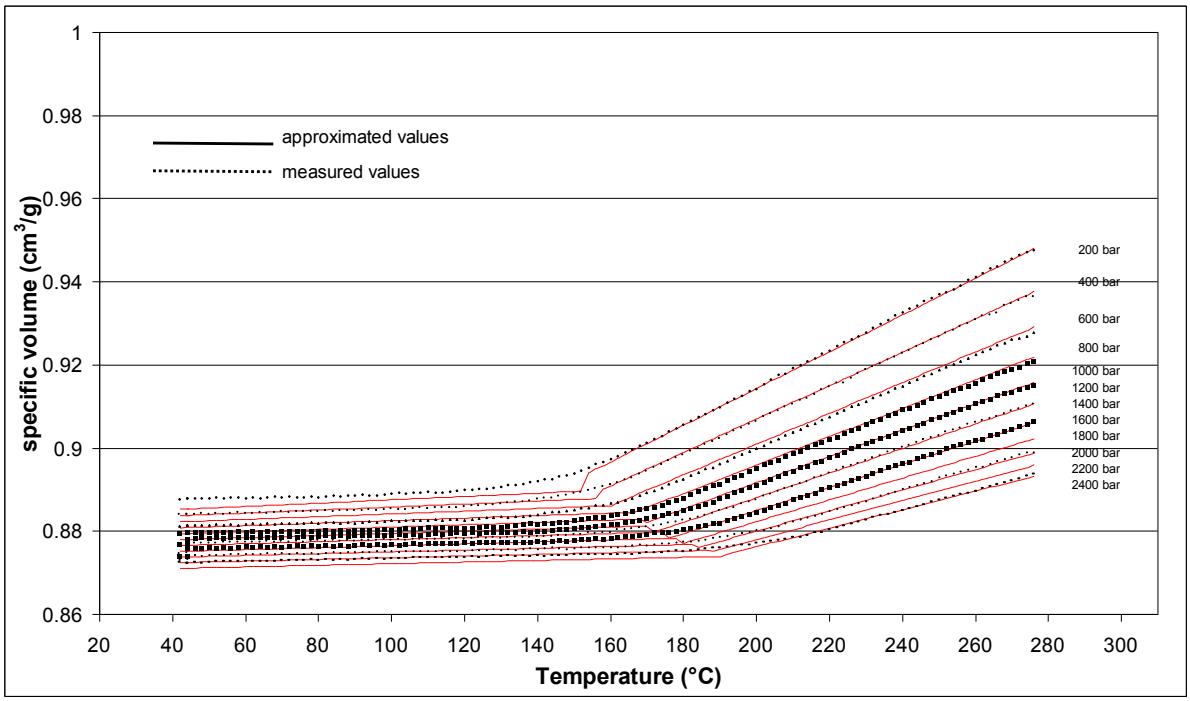

Figure 48: pvT-diagram of Bayblend T65, measured under isobaric cooling mode and constant cooling rate of 6 K/min.

Table 6: Material constants for p-v-T data approximation based on Menges-model for Bayblend T65

Bayblend T65					
Solid range			Melt range		
K_{1S}	115740.0	(cm³ bar/g)	K_{1M}	-241070.0	(cm³ bar/g)
K_{2S}	0.07444	(cm³ bar/g °C)	K_{2M}	0,89902	(cm³ bar/g °C)
K_{3S}	1462.40	(bar)	K_{3M}	1634.5	(bar)
K_{4S}	130590,0	(bar)	K_{4M}	-292240.0	(bar)
Transition range					
K_8	144,79	(°C)			
K_9	0,01941	(1/bar)			

7.5 Viscosity data

7.5.1 Theoretical background

Viscosity is an important parameter characterizing the flow properties of polymeric fluids. The factors affecting the fluid shear viscosity are complex, such as temperature, pressure, shear stress or shear rate, test time etc, in addition to molecular chain structure. Figure 49 shows factors, which are affecting shear viscosity of polymeric fluids, in which both the effect of temperature and shear rate are often investigated. But the effect of pressure is often neglected.

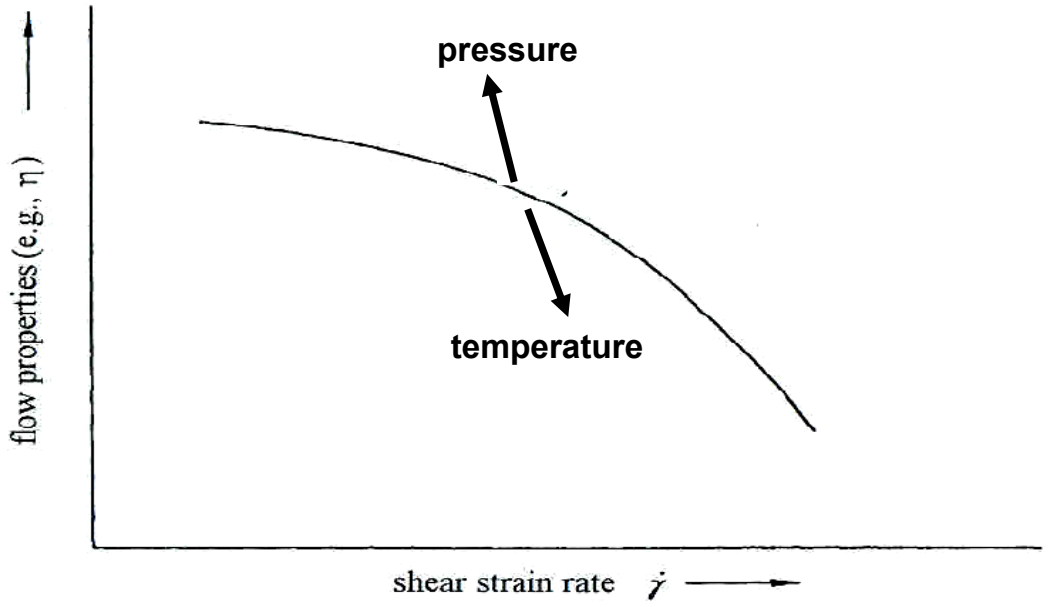

Figure 49: Factor affecting shear viscosity of polymeric fluid [42].

The mathematical model describing quantitatively the relationship between shear stress and shear rate during flow of the polymeric fluids is called the constitutive equation. For a general flow of polymer fluids, the following rheological equation is used:

$$\tau = \eta(\dot{\gamma}, T, p) \cdot \dot{\gamma} \qquad (103)$$

Where

τ	Shear stress
η	Viscosity
$\dot{\gamma}$	Shear rate
T	Temperature
p	Pressure

An outstanding characteristic of the polymer melt is their non-Newtonian behaviour whereby the viscosity decreases as the shear rate increases. This non-Newtonian behaviour is of tremendous practical importance in the processing and fabrication of plastics. The decreased viscosity makes the polymer easier to process and to inject the melt through small channel during the filling process. At the same time, the energy required by the injection moulding machine is reduced by the same phenomenon. For injection moulding processes, the shear rate is usually in the range of 10^3 s^{-1} to 10^6 s^{-1}. In the high shear rates range, the viscosity is usually extrapolated from the measured viscosity data at lower shear rates. However, the polymer viscosity at very high shear rate is not linear. A very little is known on the rheology of polymer melts at very high shear rate up to 10^6 s^{-1} or more [44-46].

The temperature and shear rate dependence of viscosity has been commonly taken into account for years; the effect of pressure on the flow properties of materials is usually ignored. However, the effect of pressure on viscosity is significant. In [47], it was found in experiments that the apparent shear viscosity of polystyrene (PS) increased by 135 times at a temperature of 190°C, when pressure was increased from 0 to 1240 bar. It is therefore necessary to understand the dependency of the materials to be processed on pressure for polymer processing, especially in the design of injection mouldings or in the choice of injection pressure.

7.5.2 Temperature dependency of viscosity

The viscosity of polymeric materials is a very strong function of temperature. A temperature difference of 10°C can make a 30-50% difference in the viscosity of many polyolefins, and as much as 200% for some engineering polymers [48]. Because of the great sensitivity of polymer viscosity to both temperature and shear rate, a large amount of data is required to characterize the flow behaviour of a polymer. Thus, there is a great need to predict the viscosity from small amount of experimental data. Time-temperature superposition determines the effect of temperature by shifting viscosity curves measured at different temperature onto a single, temperature independent master curve. The temperature shift factor (a_T) is descried as follows:

$$a_T = \frac{\eta_0(T)}{\eta_0(T_o)} \tag{104}$$

Where T is the actual melt temperature of the viscosity and T_0 is the reference temperature of the master curve. Once the shift factor is determined for each curve, plotting $\eta(\dot{\gamma})/a_T$ verses $a_T \cdot \dot{\gamma}$ produces the master curve. The master curve will cover a larger shear rate range than the individual curves because the curves are shifted along the shear rate axis.

Once the shift factors has been determined for large enough number of viscosity curves, the shift factors themselves may be fitted to a viscosity model. This allows the determination of shift factors and master curves at any temperature. The temperature dependency of the semi-crystalline polymeric material above its melting point purely depends up on the movement of the molecules. Viscosity values have an exponential dependence on temperature, which can be expressed by Arrhenius expression (equation 105).

$$a_{T\,(Arrh)} = \exp\left[\frac{E_0}{R}\left(\frac{1}{T} - \frac{1}{T_0}\right)\right] \tag{105}$$

where:

a_T temperature shift factor (/)

T melt temperature (K)

T_0 reference temperature (K)

E_0 activation energy (J/mol*K)

R universal gas constant (J/mol*K)

The value of the activation energy depends strongly on whether the viscosities at various temperatures are evaluated at constant shear stress or constant shear rate. If E_0 is evaluated at a constant shear stress, it is found that E_0 is essentially a constant independent of what value is chosen for shear stress. However, if E_0 is evaluated at a constant shear rate, the activation energy generally decreases with increasing rate of shear. The activation energy calculates the temperature shift factor for viscosity curves at two different temperatures. At temperature shifting under constant wall shear stress, the temperature shifting is based on the following two equations (equation 106 and 107).

$$\dot{\gamma}_{T_0} = a_T \dot{\gamma}_T \tag{106}$$

$$\eta_{T_0} = \frac{\eta_T}{a_T} \tag{107}$$

For amorphous thermoplastic materials, however, the glass transition regions are close to their fluid states. Free volume effects predominate and the dependence of viscosity on temperature is better described by the familiar WLF equation (Williams-Landel-Ferry) (equation 108), where c_1 and c_2 are the material constants.

$$a_{T\,(WLF)} = \exp\ \frac{-c_1(T - T_0)}{c_2 + T - T_0} \tag{108}$$

As stated before the rheological properties of the polymer melt are highly dependent on temperature and shear. In order to obtain the clear picture of this behaviour, experiments must be carried out over a range of temperatures and shear rates. These data can be brought onto a single master curve by means of the “Time-Temperature-superposition” principle, which greatly simplifies the description of the effect of temperature. The concept of superposition is that all the relaxation processes of a material have the same dependence on temperature. The temperature is assumed to be affected by the relaxation modulus by changing the relaxation time by a factor a_T. This factor can be empirically determined as a shift factor. For example, in case of shear viscosity function, temperature independent representations can be prepared by plotting $\eta(\dot{\gamma})/a_T$ versus $a_T \cdot \dot{\gamma}$ on a double logarithmic plot. The shift factor can be determined by examining the amount of shifting necessary to bring data measured at different temperatures and shear rates onto one curve. The factors are determined usually by an iterative procedure.

7.5.3 Pressure dependency of viscosity

The viscosity of most polymer melts is known to increase exponentially with pressure. As early as 1957, Maxwell and Jung (1957) observed that by increasing the pressure to 1680 bar, the apparent viscosity of a branched polyethylene melt increases 14-fold than the apparent viscosity curve measured at atmospheric pressure [47]. The pressure dependency has important consequences for polymer processing since, in process like injection moulding, polymers are subjected to rather elevated pressure. Especially in thin-wall injection moulding, pressures 1000 bar and more are common. Under such high pressures, the pressure dependence of melt viscosity is not negligible. Despite the significant effect of pressure on the melt viscosity, this effect is often ignored and the amount of experimental data on the pressure dependence of the viscosity is rather limited.

In general, the rheology of all flexible chain polymers is similar, because the chains are very long and flexible and the paths of the moving chains cannot cross those of the neighbours. In the absence of deforming force, the polymer chain takes random coil. When they are exposed to an external force, they undergo strain, but relax fully when the force is removed. In practice, the motion of coil structure is influenced by the presence of other atoms, either on the backbone chain of carbon atoms or on groups of atoms attached to the backbone. For example, the presence of strong interactions or of bulky pendant groups attached to the backbone will stiffen the polymer chain and makes it less flexible. The strength of the interactions with other atoms depends on the detailed molecular structure of the polymer. Thus, the rheological behaviour (e.g.

viscosity, elasticity, temperature and pressure dependency) of a given polymer will depend on a combination of its molecular structure and molecular weight distribution.

The zero shear viscosity η_0 is purely dependent on the average molecular weight M_w of the polymer. The variation of viscosity with shear rates, particularly the onset of viscoelasticity and power-law slope, is very dependent upon molecular weight distribution. Generally, polymers with broad molecular weight distributions exhibit the onset of shear thinning at low shear rates. In contrast, the temperature and pressure dependency of the viscosity of the polymer melts is determined by their molecular structure. An increase in pressure or a decrease in the temperature of a melt will result in a reduction of free volume between molecules. This causes a corresponding rise in intermolecular friction and a subsequent increase in the viscosity of the polymer. Polymers whose structures are more susceptible to increased levels of molecular interaction will generate larger intermolecular forces under these conditions, thereby shows greater temperature and pressure dependence.

According the Eyring hole theory of fluid, Hirai and Eyring proposed an expression for describing the relationship between viscosity and pressure as equation 109:

$$\eta_p = \eta_{p0} \exp[\beta \cdot (p - p_0)] \qquad (109)$$

where:

η_p viscosity at pressure (p) (Pa*s)

η_{p0} viscosity at atmospheric pressure (p_0) (Pa*s)

β pressure coefficient of viscosity (Pa^{-1})

Generally, the pressure dependency of viscosity is expressed by means of a pressure coefficient of viscosity (β) as expressed in equation 110.

$$\beta = \left(\frac{(d \ln \eta)}{(dp)} \right)_{T,i} \qquad (110)$$

In equation 110, i is either the shear rate or the shear stress. For molten polymers, this coefficient has typically a value of the order of 10^{-8} Pa^{-1} [49, 50]. The values of β in literature show large variation, even for the same polymer. This is probably due to the inherent difficulty in obtaining accurate data and the fact that different methods for determining the pressure effect lead to widely varying results [49]. Table 6 shows the pressure coefficient values reported in the literatures.

Table 7: Pressure coefficient of viscosity values reported in the literatures

Author	Material	β_S (10^{-9} Pa^{-1})	Quantity measured
Sedlacek et al. (2004) **[51]**	HDPE (ExxonMobil HMA 014)	10.4	Pressure drop in capillary
	LLDPE (ExxonMobil LD 600 BA)	11.7	
	LDPE (ExxonMobil LL6101 XR)	18.3	
	PP (ExxonMobil PP1374 F1)	21 ± 4.1	
	PC (Krasten 137, Kaucup-Unipetrol Group)	31.1	
	PS (DELPET 80N, Asahi Kasei Corp.)	43.5 ± 12.1	
	PMMA (Panlite AD-5503, Teijin Chemicals)	43.6	
Laun (2003) **[52]**	LDPE (BASF, Lupolen 1840H)	11.0	Pressure drop in capillary
Goubert et al. (2001) **[53]**	LLDPE (Atofina)	15.3 ± 1.5	Pressure drop in capillary
Couch and Binding (2000) **[50]**	HDPE (BASF, Lupolen 1840H5431P)	10 ± 0.5	Pressure drop in capillary
	LDPE (BASF, Lupolen 1840H)	16.5 ± 0.8	
	PP (ICI, GWM 213)	22 ± 1.1	
	PMMA (ICI, CLH374)	25 ± 1.25	
	PS (BASF, Polystyrol 143E)	29 ± 1.5	
Hay et al. (1999) **[54]**	LLDPE (ICI 501)	16.4	Axial pressure profile in slit die
	PS (Dow 555 PS)	45	
Koran and Dealy (1999) **[55]**	LLDPE (Dowlex 2049)	14	High pressure sliding plate rheometer
Kadijck and Van den Brule (1994) **[56]**	PS	31	Flow rate in fixed pressure drop slit rheometer
	ABS	24	
	PP	16	
Laun (1983) **[57]**	LDPE	7	Axial pressure profile in slit die
		20	Pressure drop in die
Penwell et al. (1971) **[58]**	PS	29 ± 1.4	Pressure drop in capillary
Choi (1968) **[59]**	PE (Phillips type)	12	Pressure profile in melt barrel of capillary rheometer
Semjonow (1962) **[60]**	PS (Polystyrol)	~10.4	Torque in pressurized Couette cell
	HDPE	~10.4	
Maxwell and Jung (1957) **[47]**	PE	16	Pressure drop in capillary
	PS	37	

7.5.4 Temperature- and Pressure invariant master curve

Figure 50 schematically depicts a double logarithmic plot of viscosity versus shear rate. A temperature decrease from T_0 (full line) to T or pressure increase to p, respectively (dotted line) shifts the whole curve parallel to lines of constant shear stress (slope -1), the vertical and horizontal shift both being equal to log a. Therefore, the shift factor for a constant shear rate will depend on the slop of the curve, i.e. the power law index, in contrast to the shift factor at constant shear stress as in equation 111.

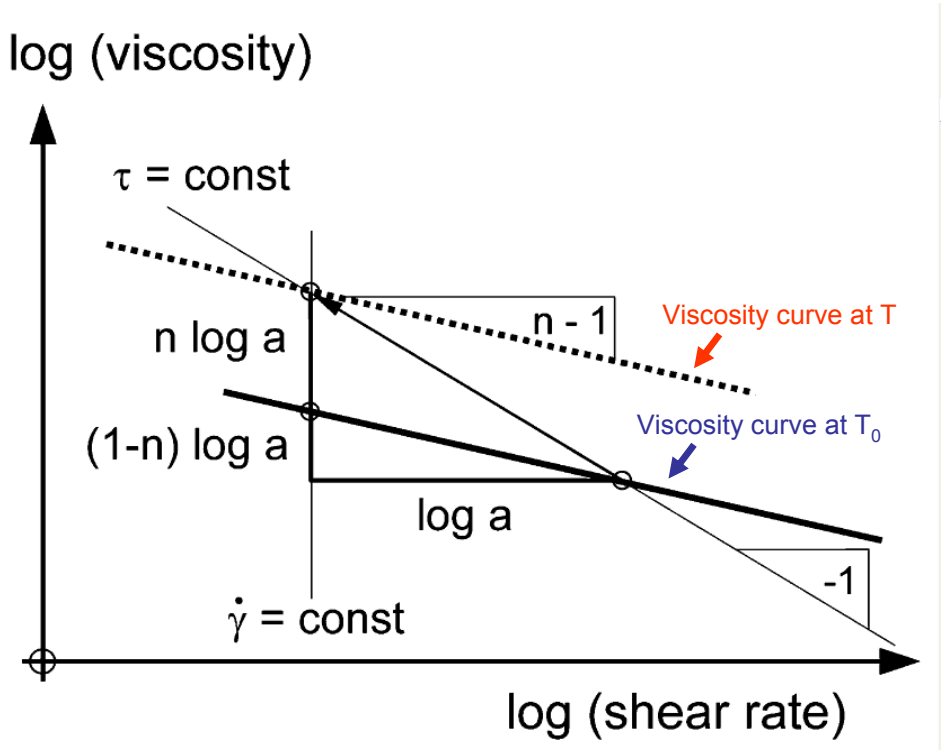

Figure 50: Comparison of temperature shifts factors of a power law fluid at constant shear stress and shear rate [52].

$$\log a_{\dot{\gamma}} = n \cdot \log a_{\tau} \qquad (111)$$

where:

n power law index (/)

$a_{\dot{\gamma}}$ shift factor at constant shear rate (/)

a_{τ} shift factor at constant shear stress (/)

The above relation holds for both pressure and temperature effects and is of relevance for relating the coefficients of temperature and pressure dependency for a given shear rate to their corresponding values of temperature coefficient of viscosity and pressure coefficient of viscosity as in equation 112 and in equation 114..

$$\alpha_{\eta} = n \cdot \alpha_{\eta}^{*} \qquad (112)$$

$$\beta_{\eta} = n \cdot \beta_{\eta}^{*} \qquad (113)$$

In equation 112, α_{η} is the temperature coefficient of viscosity at constant shear rate, n is power law index and α_{η} * is the temperature coefficient of viscosity at constant shear stress. Whereas in equation 113, β_{η} is the coefficient of pressure dependency of viscosity at constant shear rate, n is power law index and β_{η}^{*} is the pressure coefficient of viscosity at constant shear stress. For a given flow activation energy E, the

temperature coefficient of viscosity at constant shear rate simply follow as in equation 114

$$\alpha_\eta = n \cdot \frac{E}{RT_0^{\,2}} \tag{114}$$

7.5.5 Different methods to calculate the pressure coefficient of viscosity

The different methods used to measuring the effect of pressure on the viscosity of polymer melts are listed below [53]:

- Analysis of non-linear pressure profiles
- Estimation of pressure effect from pvT diagram
- Enhancing the exit pressure
- Drag flows under hydrostatic pressure

7.5.5.1 Analysis of non-linear pressure profile

The pressure dependency of the viscosity causes non-linearity in the pressure profiles observed during the flow in a capillary or slit die. Laun [57] used this method to find the pressure coefficient of viscosity from the nonlinear longitudinal pressure profile in the slit die. He takes into account an exponential dependence of the apparent viscosity at a constant apparent shear rate under hydrostatic pressure.

For capillary geometries, these pressure profiles cannot be measured directly. The high curvature of the capillary wall renders it virtually impossible to mount pressure transducers. The pressure profiles can be inferred from plots of the total pressure drop over a capillary as a function of the ration of length (L) over diameter (D), which is called as Bagley plot. Dudvani and Klein [61] proposed a method to use the curvature in the Bagley plots to estimate the pressure dependency of the viscosity. Assuming an exponential dependency of the viscosity on the pressure, the momentum balance in the axial (z) direction is given as in equation 115 can be integrated over the capillary between z=0 and z=L, considering atmospheric pressure at z=L.

$$\frac{\partial p}{\partial z} = \frac{1}{r} \cdot \frac{\partial(\tau_{rz} r)}{\partial r} \tag{115}$$

When the entrance pressure drop is neglected this yield the following expression for the total pressure drop (Δp_{tot}) as a function of the L/D ratio of the capillary (equation 116):

$$\Delta p_{tot} = -\frac{1}{\beta} \cdot \ln\left(1 - 4\beta\tau_0 \frac{L}{D}\right) \tag{116}$$

Where:

Δp_{tot} total pressure drop (Pa)

τ_0 wall shear stress (Pa)

L/D ratio between the length and diameter of the capillary die(/)

If the ln function is approximated by a series expansion of (L/D) up to the second order term, the pressure profile can be written as in equation 117.

$$\Delta p_{tot} = b \cdot \left(\frac{L}{D}\right) + c \cdot \left(\frac{L}{D}\right)^2 \qquad (117)$$

It follows for the pressure coefficients of the equation 118:

$$\beta = \frac{2c}{b^2} \qquad (118)$$

Hence the fit of either equation 116 or the qudaratic approximation of equation 117 to an experimentally measured Bagley plot seems the most simple method to determine the pressure coefficient of viscosity (β).

There are however some intrinsic problems with this technique:

- It should be kept in mind that pressure coefficient of viscosity are typically of the order of 10^{-9} – 10^{-8} pa^{-1}. For pressure drops typically encountered in standard capillary rheometer, the non-linearity will be small.
- Whenever the non-linearity becomes important, the exponential dependency can no longer be approximated by a second order equation and the use of a quadratic form will lead to an overestimation of the coefficient C.
- It should always be kept in mind that other effects can affect the non-linearity in the pressure profiles in a slit, or contribute to non-linearity in a Bagley plot. Hay et al [54] presented a detailed study of the combined effect of temperature and pressure. These authors demonstrate that the curvature of pressure profile is affected by both temperature and pressure. Viscous heating will typically produce a downward curvature of the pressure profile. On the other hand, wall slip with pressure dependent slip velocity leads to upwards concave pressure profile.

7.5.5.2 Calculation of pressure coefficient of viscosity from pvT-data

Utracki [62, 63] developed a semi-empirical method to relate the zero shear viscosity of polymeric melts to the free volume. This method is based on two assumptions:

- The equilibrium free volume fraction is computed from fitting the Simha-Somcynski equation of state to the pvT-data.
- A semi-empirical correlation between the zero shear viscosity and the inverse of the free volume fraction is used to deduce the pressure effects on the viscosity.

In order to calculate the free volume, the Simha-Somcynsky (SS) equation of state is fitted to the experimental pvT-data. The SS equation is formulated as in the following equations in terms of reduced variables.

$$\tilde{P} = \frac{P}{P^*} \tag{119}$$

$$\tilde{V} = \frac{V}{V^*} \tag{120}$$

$$\tilde{T} = \frac{T}{T^*} \tag{121}$$

p*,v* and T* are determined as indicated below. The SS equation of state for polymeric liquids simplifies to the following set of equations [63]:

$$\frac{\tilde{P}\cdot\tilde{V}}{\tilde{T}} = \frac{1}{1-2^{-1/6}\cdot y\cdot\Phi^{1/3}} + \left(\frac{2y}{\tilde{T}}\right)\Phi^2\left[1.011\cdot\Phi^2 - 1.2045\right] \tag{122}$$

$$\left[1+\frac{\ln(1-y))}{y}\right] = \frac{y}{6\tilde{T}}\Phi^2\left[2.409-3.033\Phi^2\right] + \left[\frac{2^{-1/6}\,y\cdot\Phi^{1/3}-1/3}{1-2^{1/6}\,y\cdot\Phi^{1/3}}\right] \tag{123}$$

where

$y = 1 - f$ and $\Phi = \frac{1}{y\cdot\tilde{V}}$

f free volume fraction (m^3)

The reducing parameters p*,v* and T*can be found by fitting the two coupled equations to the pvT-data using a multiparameter fit routine or using a simplified method by Utracki [63]. Once the reducing parameters are known, the free volume fraction can be determined for every combination of pressure and temperature.

Utracki suggested that the Doolittle equation (equation 124), to be used to relate the zero shear viscosity to the free volume fraction:

$$\ln\eta = A_D + \frac{B_D}{f + C_D} \tag{124}$$

C_D is usually small with respect to f and will be neglected, thereby reducing the number of parameters to two. Obtaining the zero-shear viscosity as a function of temperature at atmospheric pressure is straightforward. The reducing parameters enable one to calculate f. A linear regression of the experimental zero shear viscosity data plotted as a function of inverse free volume yields the parameters A_D and B_D. The linear relationship between 1/f and the reduced pressure at a given temperature is given in equation 125.

$$\frac{1}{f} = D(\tilde{T}) + E(\tilde{T}) \cdot \tilde{P} \tag{125}$$

The pressure coefficient of viscosity (β) can obtained by substituting equation 124 and 125 in equation 110 as follows:

$$\beta = \left(\frac{d\ln(\eta_0)}{dp} \right)_T = \frac{B \cdot E(\tilde{T})}{P^*} \tag{126}$$

The further detail information about this method is explained in [62,63,53].

7.5.5.3 Determination of β value by enhanced exit pressure method

The enhanced exit pressure method provides data of the apparent viscosity as a function of the pressure at a given shear rate. The major advantage of the exit pressure method is its increased accuracy moreover, it may be readily adapted with any standard rheological measurement methods. In literature [64] following three methods are discussed:

- High pressure sliding plate rheometer
- Counter-pressure nitrogen capillary rheometer
- piston capillary rheometer with throttle or with back pressure chamber

Koran and Delay [54] described the high pressure sliding plate rheometer (HPSPR). It was used to determine the effects of pressure and dissolved co_2 and N_2 on the viscosity of high density polyethylene and effect of pressure on the viscosity of PS. This instrument is capable of measuring viscoelastic properties at temperature up to 240°C and pressure up to 700 bar.

The counter-pressure nitrogen capillary rheometer (CPNCR) is a modification of the automated nitrogen capillary rheometer described by Laun in [65]. This counter-pressure measurement method has no mechanical throttle at die exit. The maximum counter pressure is 200 bar. The melt is exposed to nitrogen at both the inlet and outlet since the rim of the floating piston is not sealed to avoid friction, and the extrudate in the counter-pressure reservoir is exposed to gas.

The most important method to determine the pressure coefficient of viscosity is by use of a piston-driven capillary rheometer with throttle (PCRWT). In this apparatus, a throttle valve is placed at the exit of the die to increase the pressure in the capillary. The average hydrostatic pressure can be approximated by linear average between the pressure measured at the entrance of the die and the pressure at the exit. Binding et al [50] explored the use of the exit pressure technique, in combination with a variation of the L/D ratio, in order to evaluate the effect of pressure on both the shear and elongation viscosity.

7.5.6 Influence of the viscous dissipation

Temperature variations can be caused by temperatures external to the fluid or they can be caused by self-heating due to viscous dissipation, since the molten polymers are highly viscous, but have low thermal conductivity. Therefore, it is inefficient for the molten polymer to transfer the heat by conduction across the thickness of the flow channel. The performance of shearing itself would generate the heat within the melt and thus it might increase the temperature of the melt sufficient to reduce the viscosity. Therefore, it is often most important to consider the temperature variations in flow. The heat generated by viscous forces has a significant influence on the viscosity measurements [42, 65-70].

In order to describe the heat generation, let us consider the flow of a Newtonian polymer in a flow channel of length L with a constant wall temperature equal to T_0, the initial temperature of the polymer. The evolution of the temperature profile in the polymer along the flow length is shown in figure 51.

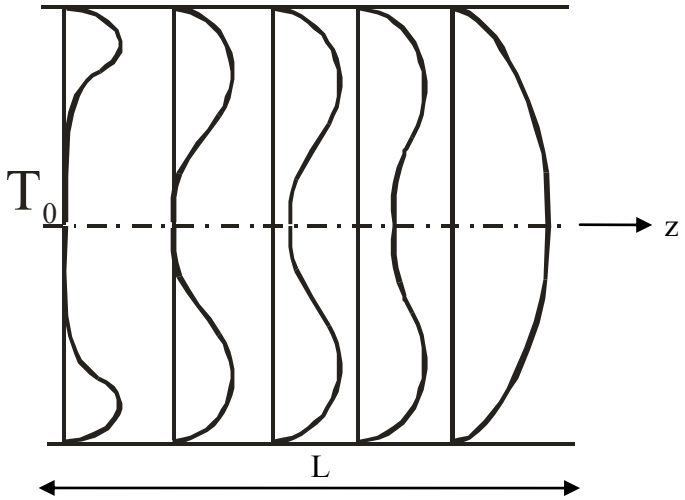

Figure 51: Temperature development along flow length [66]

Near the entrance, the maximum temperature is obtained close to the wall, since the shear forces are maximum at the wall. However, progressively, due to the heat conduction towards the centre, the temperature profile evolves towards an equilibrium profile with the temperature maximum at the centre. In general, three different zones can be described [66]:

- Near the entrance of the tube or gap, the heat transferred by conduction through the tube wall is negligible and power dissipated is used to heat the polymer melt in the die. The fluid behaves as if it was in thermal isolated wall. This is called “Adiabatic” regime.
- By proceeding, the heat conduction through the wall is not negligible. A part of the dissipative heat developed by viscous force is heating the polymer

and the other part is transferred by conduction to the surroundings. This is called “transition” regime.

• In the “equilibrium” regime all the dissipative power is transferred by conduction to the surroundings.

The temperature profile along the length of the capillary die or in the slit die is not constant. The Cameron Number Ca (equation 127) can be calculated to evaluate whether or not the temperature rise due to shearing must be taken into account during the rheological measurements [66]. Ca is the quotient of the heat conduction at 90° to the direction of flow and the convective heat transfer in the direction of flow.

$$Ca = \frac{\lambda \cdot L}{\rho \cdot C_p \cdot \bar{v} \cdot H^2} \qquad (127)$$

Where:

λ Thermal conductivity of the polymer at average melt temperature

L Axial characteristic dimension of the flow geometry

H Transverse characteristic dimension of the flow geometry

$\bar{v}$ Average velocity of the polymer flow inside the flow channel

ρ Density at average melts temperature

C_p Heat capacity at average melts temperature

Table 8: Thermal zones based on the Cameron number

$Ca < 10^{-2}$	Adiabatic regime
$Ca = 1$	Equilibrium regime
$10^{-2} < Ca < 1$	Transition regime

Rheological investigations at extremely high shear rates reported in the literature have not always taken into account the temperature rise due to shearing. The viscosity measurements with the help of a special slit-die system for micro-rheology, significantly showed that the effect of dissipative heating shear rates above 5000 s^{-1} can not be neglected [67-70]. Taking into account of the shear thinning behaviour by using the power law, the temperature rises along the round capillary die as well as along the slit die for three different thermal regime are derived in the works of [41, 69].

7.5.7 Rheological measurement techniques

7.5.7.1 High pressure capillary rheometer with round capillary die

The rheological measurements were carried out using a high pressure capillary rheometer, type RHEOGRAPH 2002, manufactured by Göttfert Werkstoff-Prüfmaschinen GmbH – Rheological testing devices, Buchen, Germany.

The RHEOGRAPH 2002 allows the routine analysis of the flow and viscosity of thermoplastics at shear rate from 100 s^{-1} to 10^5 s^{-1}. The maximum force is 20 kN, so this instrument can measure pressure up to 1200 bar. The transducer range must be selected depending on the measurement pressure range in order to avoid errors caused by the transducer at low pressure and to avoid the damage of the transducer membrane at high pressures. The maximum velocity of the piston is 20 mm/s.

The measurements are carried out using a 12 mm diameter cylinder and round capillary die. The measurements are performed using three dies of varying L/D ratios. The whole system is heated to the required temperature. The heating system is controlled by three separate Pt100-type thermocouples. Once the isothermal condition is obtained, the measurement cylinder is filled with the test material and compressed with a tamper, to avoid air entrapment. The measurement is started, once the material is filled the measurement can be started. The pre-heating time or the melting time runs when the measurement is started. When this pre-heating time is finished, the piston starts moving automatically at the specified velocity or flow rate. The melt pressure is measured using a pressure transducer placed near the entrance of the die. When the pressure is steady the program stores the pressure automatically and switch on to the next flow rate and continues until the cylinder is empty or all the flow rates are measured. With these pressure values, flow rates, and die geometry the viscosity can be determined. Capillary rheometers with circular dies (Figure 52) are widely used in polymer melt rheology. The round capillary dies consist of different lengths of dies with same diameter. The entrance angle of round capillary die is 180°. To measure the temperature development near to the die wall during the measurement, two 1mm diameter J-type thermo couples were attached to the die (position 2).

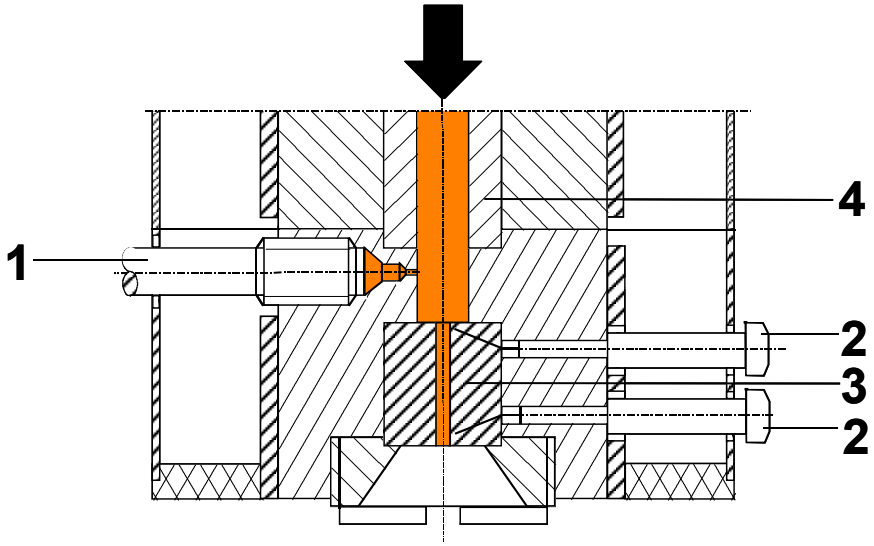

1 – Melt pressure transducer, 2 – J-type thermocouple
3 – Round capillary die, 4 – Test cylinder

Figure 52: High pressure capillary rheometer with round die

The volumetric flow rate can be calculated from the piston velocity as in equation 128.

$$\dot{V} = \frac{\pi \cdot D_p^{\,2}}{4} \cdot v_p \qquad (128)$$

where:

$\dot{V}$ volumetric flow rate (m^3/s)

D_p piston diameter (m)

v_p velocity of the piston (m/s)

The apparent shear rate is directly propositional to the volumetric flow rate, which is calculated by using equation 129.

$$\dot{\gamma}_{ap} = \frac{4 \cdot \dot{V}}{\pi \cdot R^3} \qquad (129)$$

where:

$\dot{\gamma}_{ap}$ apparent shear rate (1/s)

$\dot{V}$ volumetric flow rate (m^3/s)

R radius of the die (m)

From the measured pressure drop values, the apparent shear stress values were calculated using equation 129.

$$\tau_{ap} = \frac{p_{mea} D_d}{4 L_i} \qquad (130)$$

Where:

τ_{ap} apparent shear stress (Pa)

P_{mea} measured pressure (bar)

D_d diameter of the die (m)

L_i length of the die (m)

The apparent viscosity was calculated by using the below equation 131.

$$\eta_{ap} = \frac{\tau_{ap}}{\dot{\gamma}_{ap}} \tag{131}$$

Two corrections are commonly applied to the round capillary data in order to obtain correct viscosity of polymeric materials. They are Bagley correction and Weissenberg-Rabinowitsch correction.

The pressure is measured in the cylinder, at the entrance of the capillary, then Bagley correction must be done. The change in the cross section from large diameter cylinder to the small one of the capillary causes deviations from an ideal fully developed flow. Due to these changes in cross section additional pressure losses occur. To eliminate this pressure loss at the entrance, Bagley correction is done. These additional pressure losses can be eliminated by measuring the pressure drop at constant shear rate for several capillary lengths and extrapolating to zero length. Plotting pressures in front of the capillary measured versus L/D-ratio in a linear graph, in general gives straight lines for the individual shear rate. The extrapolation of these straight lines on the L/D-ratio = 0 provides the correction factor P_{en} mentioned in the equation 132.

$$\tau_w = \frac{(p_{mea} - p_{en})D_d}{4L} \tag{132}$$

Where

τ_w Wall shear stress (Pa)

p_{en} Entrance pressure loss (bar)

The Weissenberg-Rabinowitsch correction (equation 133) considers the fact that the relation mentioned in the equation 128 is only valid for Newtonian fluids and provides the true shear rate at the capillary wall for them.

$$\dot{\gamma}_W = \frac{\dot{\gamma}_{ap}}{4}\left(3 + \frac{d\log\dot{\gamma}_{ap}}{d\log\tau_{ap}}\right) \tag{133}$$

Finally the true viscosity is calculated from the equation 134.

$$\eta_w = \frac{\tau_w}{\dot{\gamma}_w} \qquad (134)$$

7.5.7.2 High pressure capillary rheometer with back pressure chamber

The viscosity curves were first determined with ambient exit pressure, using a standard high pressure capillary rheometer. For the measurement under elevated pressures, the enhanced exit pressure techniques was used by attaching a back pressure chamber, developed by Göttfert Werkstoff-Prüfmaschinen GmbH, underneath the capillary die [41]. A schematic of the experimental setup is shown in figure 53.

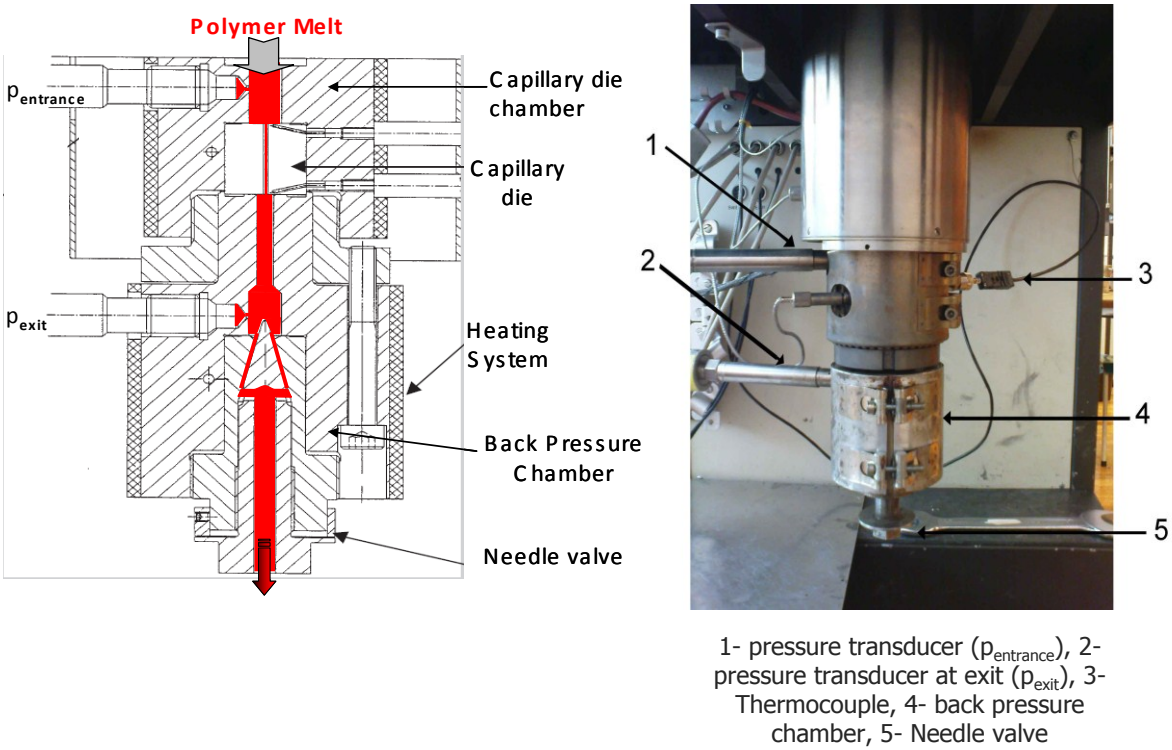

Figure 53: Schematic of the pressure chamber attached beneath the capillary die [71].

The needle valve of the back pressure chamber can be moved vertically to change the level of flow restriction, thus it changes the pressure in the back pressure chamber. Melt pressures were measured at the position before entrance of the die ($p_{entrance}$) and in the pressure chamber (p_{exit}) after the melt exits the capillary die. With the back pressure chamber a constant exit pressure (back pressure) can be set at different shear rates by varying the flow restriction manually with help of the needle value. Exit pressures ranging from 100 bar to 600 bar were achieved. The melting time before starting the measurement was kept at 4 min. During the measurement, the piston is moved constantly at pre-set piston velocity. The resulting pressure drops over the capillary were measured. The pressure transducers are Dynisco class 1 transducers with a nominal range of 1000 -2000 bar. An external temperature regulator controlled the

temperature of the pressurized chamber with a Pt100 sensor. To ensure good thermal stability the instrument was heated for at least 3 hours before starting the experiments. A capillary dies with length of 10 mm, 20 mm and 30 mm and with diameter of 1mm were used. This measurement technique has some limitation in terms the maximum measured apparent shear rate. The maximum permitted piston velocity and the allowed maximum pressure limit the maximum apparent shear rate. At higher piston velocity, the operator has to set quickly the desired back pressure by setting the needle valve opening since the measurement time is relatively short. The apparent shear rate 10,000 s^{-1} is the maximum apparent shear rate measured in this work using the high pressure capillary rheometer with the back pressure chamber. At each temperature, the experiments were carried out at four different back pressures such as 1 bar, 100 bar, 300 bar and 600 bar.

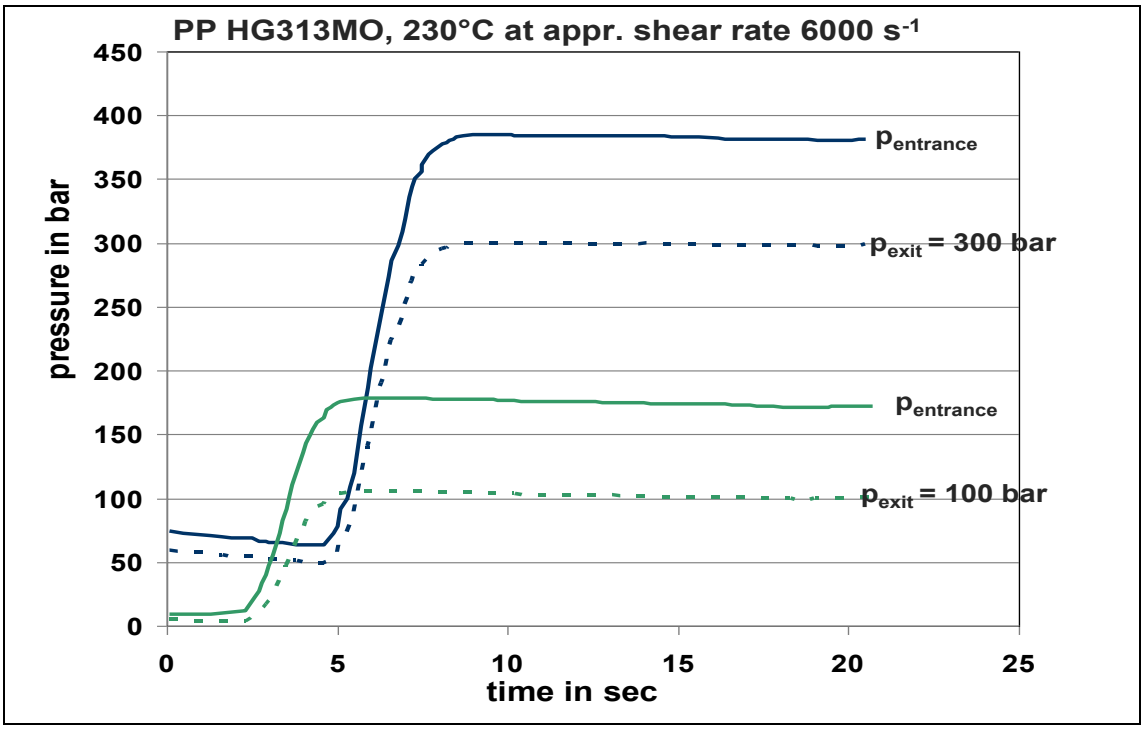

Figure 54: Measured pressures in the entrance of capillary die ($p_{entrance}$) and in the back pressure chamber (p_{exit}) at constant apparent shear rate of 6000 s^{-1} for PP HG313MO at 210°C.

Figure 54 shows the measured pressure of PP HG313MO material at the entrance of the capillary die at two different back pressures for the apparent shear rate of 6000 s^{-1}. The measured pressure at the entrance of the capillary die increases with the increasing back pressure. The pressure drop in the capillary at constant shear rate is calculated by using equation 135.

$$\Delta p_{corr} = (p_{entrance} - \Delta p_e) - p_{exit} \qquad (135)$$

Where:

Δp_{corr} pressure drop in the capillary (bar)

$p_{entrance}$ measured pressure at the entrance of the die (bar)

p_{exit} measured pressure at the exit of the die (bar)

Δp_e entrance pressure loss after Bagley correction (bar)

The mean pressure in the capillary can be calculated with the help of equation 136:

$$p_{mean} = p_{exit} + \frac{\Delta p_{corr}}{2} \quad (136)$$

In reality, the pressure profile in the capillary die is non-linear due to the pressure effect. The mean pressure calculated with the equation 135 is the arithmetic average of the entrance pressure and the exit pressure [48]. From the corrected pressure drop, the shear stress at the wall for each couple of mean pressure and wall shear rate can be calculated as in equation 137.

$$\tau_W = \frac{(\Delta p_{corr}) \cdot R}{2 \cdot L} \quad (137)$$

The Figure 55 shows the linear increase of the calculated pressure drop values with the increasing back pressure at five different apparent shear rates. The rise in the calculated pressure drop value ultimately increases the calculated shear stress value at constant volumetric flow rate measured at different back pressures.

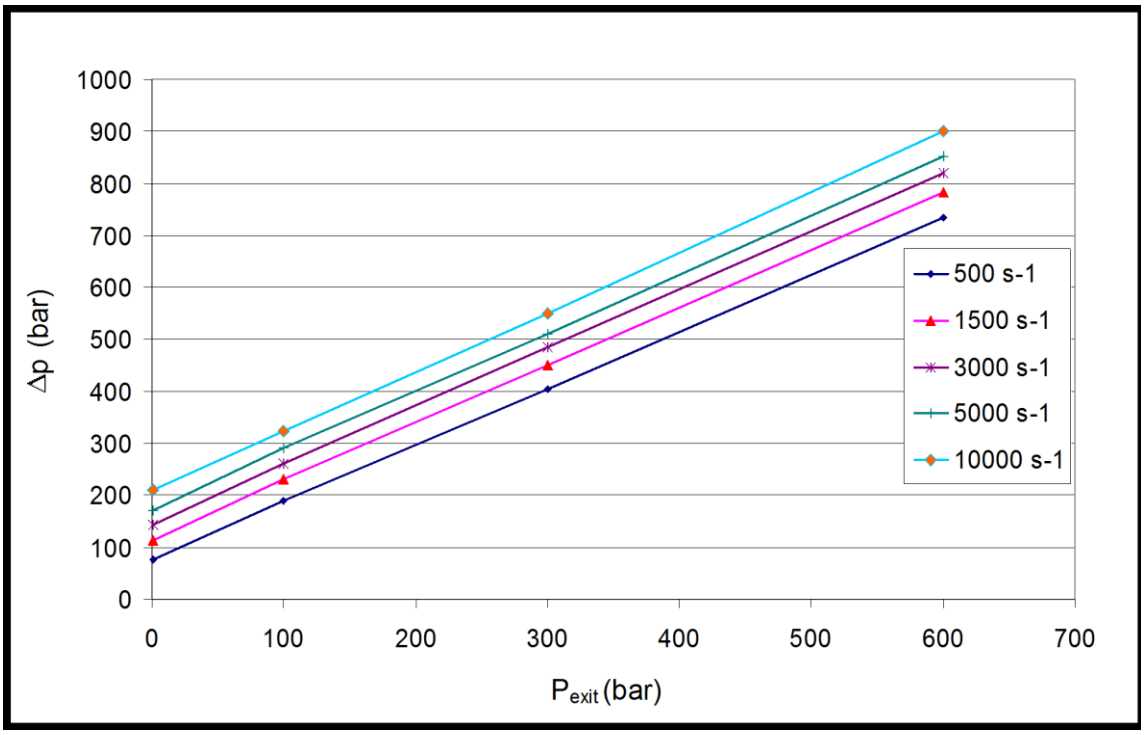

Figure 55: Calculated pressure drop values at different back pressures for PP HG313MO at 210°C at five apparent shear rates.

7.5.7.2.1 Evaluation methods of the pressure coefficient of viscosity (β)

Method 1: Direct calculation of the constant shear rate pressure coefficient

By using the definition of the pressure coefficient at constant shear rate as in equation 138, it is possible to calculate $\beta_{\dot{\gamma}}$ as the slope of the curves of the logarithm of the viscosity at a given shear rate plotted versus the mean pressure in the die.

$$\beta_{\dot{\gamma}} = \left(\frac{d\ln(\eta)}{dP} \right)_{T,\dot{\gamma}} \qquad (138)$$

Such an approach can lead to coefficients that depend not only on pressure and temperature but also on shear rate. Hence such a procedure will not lead to a real thermodynamic property of the polymer melt [49,53]. The viscosity values were obtained after Weissenberg-Rabinowitch correction and subsequent fitting with the appropriate viscosity model. From the known exit pressure and pressure drop for every shear rates, the corresponding arithmetic mean pressure was calculated. Cardinaels et al [49] showed that for measured three polymers (PMMA, LDPE and PαMSAN) the pressure coefficients decrease with increasing shear rate and tend to reach a constant value in the power law region of the viscosity curves. The region of constant value of the pressure coefficient is called as „*high shear rate limit* (β_{HS})".

Method 2: calculation of the pressure coefficient by superposition

The pressure coefficient of viscosity at constant shear stress can be extracted from the superposition method. According to Couch and Binding [50], the three processing parameters such as the shear rate, temperature and pressure that influence viscosity can be taken into account by defining a single shift factor a_{Tp} as in the equation 139.

$$\frac{\eta(\dot{\gamma}, p, T)}{a_{TP}} = \eta(a_{TP} \cdot \dot{\gamma},\, T_0, p_0) \tag{139}$$

The effect of pressure and temperature can be separated from effect of shear rate, resulting the shift factor (a_{Tp}) is independent of the shear rate. Viscosity curves at different pressures and temperature can be shifted onto a master curve by using the shift factor for each combination of pressure and temperature. This valid in the power law region of the flow curve for most of thermoplastics, implying that the power law index (n) is independent of pressure and temperature. Different expressions are used to model the pressure and temperature dependency of this shift factor. Most commonly used expression to describe a_{Tp} is by combining Barus and Arrhenius terms in a product, which led to the following expression:

$$a_{pT} = \exp\left[(\beta_\tau \cdot p) + \frac{E_0}{R} * \left(\frac{1}{T} - \frac{1}{T_0}\right)\right] \tag{140}$$

Where E_0 is the activation energy and R is the universal gas constant. β_τ defines the pressure coefficient of viscosity at constant shear stress.

Another important expression to describe a_{Tp} is WLF –Barus equation as shown in the equation 141.

$$\log(a_{Tp}) = \left(\frac{8.86(T_0 - T_s)}{101.6 + T_0 - T_s} - \frac{8.86(T_m - T_s)}{101.6 + T_m - T_s} + \frac{\beta_\tau \cdot p}{\ln(10)}\right) \tag{141}$$

7.5.7.3 Injection moulding machine rheometer with the rheological injection mould

During the small and thin-walled injection moulding process, shear rates often exceed 10^6 s^{-1} and the injection pressures often exceed 2000 bar. Hence, for the simulation of such injection moulded parts, accurate viscosity data measured at shear rates up to 800,000 s^{-1} and more including pressure dependence are important. Goubert et al. [53] showed the different measurement techniques available for measuring viscosity curves at elevated pressures. The counter-pressure measurement technique, which is discussed in the previous chapter, is generally used for the pressure dependent viscosity measurements on the standard high pressure capillary rheometer with the round capillary die or with the rectangular slit die. However, the commercial high pressure capillary rheometer equipment has its own measurement limitations in terms of its maximum force and its maximum melt volume in the measurement cylinder. For rheological measurements at high shear rates and at high counter pressures, the measurements require a higher volume of the melt as well as a higher injection speed in addition to higher injection pressure. These requirements are satisfied by doing the rheological measurements on the injection moulding machine. Further, the injection moulding machine rheometer facilitates the possibility of measuring the viscosity at process-relevant measurement conditions.

Relatively small numbers of literatures are available regarding the injection moulding machine rheometer. W. Knappe et al. [72] showed viscosity measurement techniques for four rigid PVC compound using a slit die rheometer in combination with an injection moulding machine. C. Bader et al. [73] showed the possibility to measure the viscosity of a LCP material on the injection moulding machine by using a round capillary die which was attached in the machine nozzle. O. Amano et al. [74] developed a new measurement adaptor with a capillary die to measure the flow properties of polymer melt on the injection moulding machine up to shear rate of 10^6 s^{-1}. He also investigated the effect of pressure on the viscosity for that a manually adjustable the needle valve was used to regulate the exit pressure to the required pressure level. In his study, he demonstrated that for four investigated thermoplastic materials the pressure dependent viscosity data measured in the extremely high shear rate region has a significant influence to improve the accuracy of simulation with a FEM simulation. A. L. Kelly et al. [73] measured the rheological behaviour of polymer melts using an instrumented nozzle adaptor with a capillary die at high strain rate up to 10^7 s^{-1}. Both H. Takahashi et al., [76] and A. L. Kelly et al. [75] observed a second Newtonian plateau at shear strain rates above 10^6 s^{-1}. In literature, the rheological measurements up to shear rates of 10^6 s^{-1} were carried out without taken into account the temperature rise due to viscous heating. Hence, for a number of thermoplastics the measured data are presented in the form of apparent viscosity curve only. Therefore, within the EC project “Pro4Plast” an easy to

handle and in-house to use rheological measurement system applicable by SEMs was developed by the Institute of Plastics Processing, University of Leoben, Austria [77-79]. A software package called *Rheosoft* was developed for the rheological evaluation of measured values and the approximation of true viscosity taken into account the temperature rise due to shear heating and compression heating by temperature correcting the measured pressure values with respect to actual temperatures [42,70].

In order to measure the flow behaviour within a wide shear rate range, a special injection mould (figure 56) with interchangeable conical slit-die inserts with varying slit heights was developed. This rheological mould is very similar to a standard injection mould, but is constructed without a sprue, runner system and cooling circuit. It can be easily mounted on the injection moulding machine and enables SMEs to measure viscosity on their own machines. In order to achieve a wide range of practically relevant shear rates three dies with different slit heights (1 mm, 0.5 mm and 0.35 mm, entrance angle of 60°) were used. The width of the flow channel was 10 mm and the total length was 105.5 mm in order to achieve a fully developed flow and to avoid entrance effects.

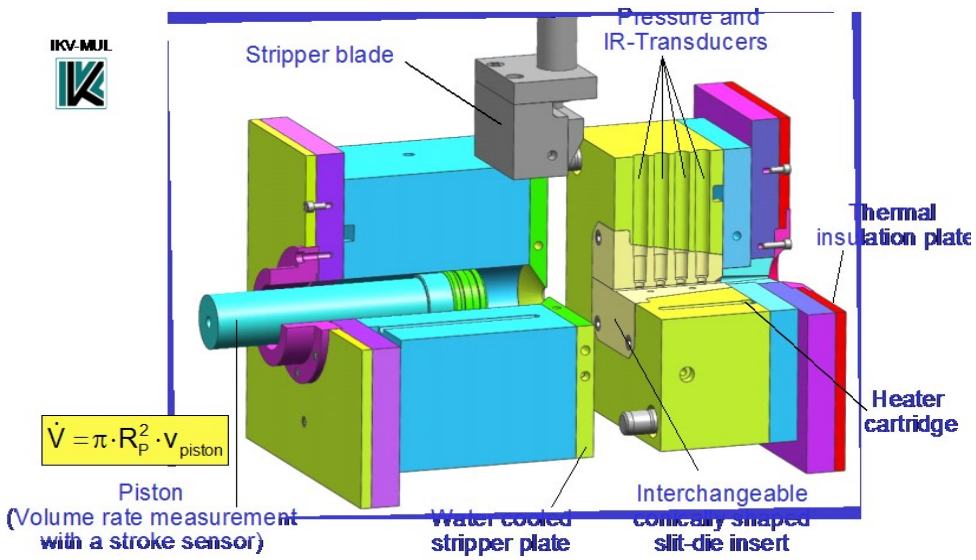

Figure 56: Rheological injection mould, using slit die inserts.

Along the flow path on the top and bottom side, pressure and temperature are measured by using four sensors which are 20 mm apart form each other in order to calculate shear stress and to find the wall temperature increases along the flow length due to shear heating. The pressure sensors are flush type sensors that have direct contact with the melt. Melt temperature is directly measured by infrared sensors. The wall temperature is measured using a special kind of heat flux sensors with three thermocouples positioned in such a way that each thermocouple measures the temperature 1 mm, 1.5 mm and 3 mm away from the flow channel wall. Extrapolating

these temperatures, the wall temperature is calculated both near the entrance and near the exit.

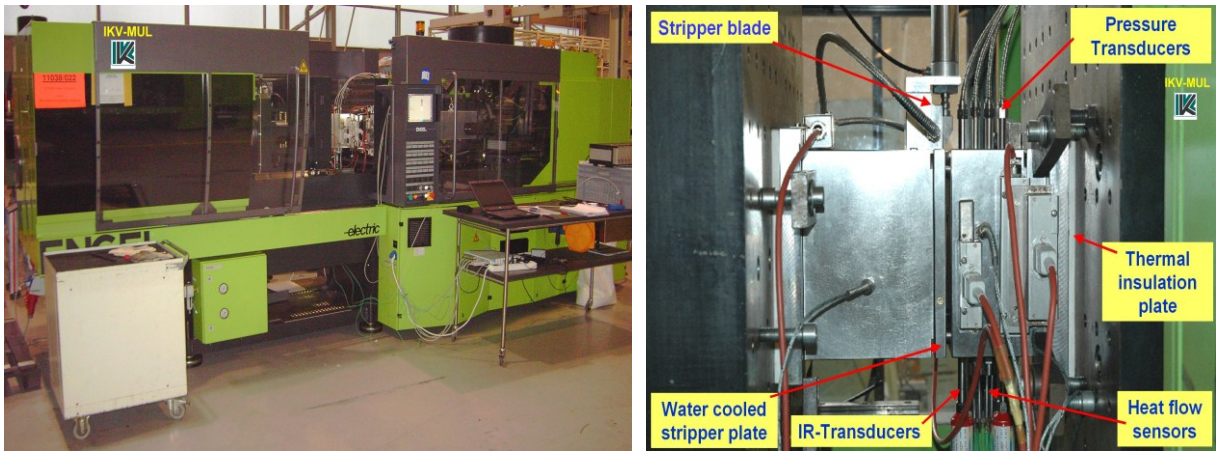

Figure 57: Injection moulding machine with rheological injection mould using slit die insert.

The movable mould half consists of a cylinder and a piston system to measure the volumetric flow rate and to calculate the corresponding apparent shear rate. Thus, measurement errors due to leakage flow in the back flow valve of the plasticizing unit can be avoided. The displacement rate of the piston is measured using an integrated stroke sensor within the piston. The forward and backward motion of the piston is attained by the movement of the machine ejection system. To measure the pressure dependency of viscosity, a closed-loop back pressure control system is used, which controls the pressure at the pressure transducer p_4 located nearest to the exit. With the help of the attached servo valve controlled hydraulic cylinder, the system controls the backward motion of the piston during injection in order to regulate the counter pressure to the pre-set pressure value. The volumetric flow measurement cylinder has a maximum storage capacity of 424.115 cm^3. A pneumatically operated stripper blade is attached on the top to wipe the melt flowing out of the cylinder during ejection of the melt from the water cooled stripper plate. Heating of the mould is done using four cartridge heaters as well as four heater plates covering the movable mould half, which are regulated directly by the injection moulding machine.

The experimental procedures are as follows: After closing the mould, the measurement starts with melt injection at the specified constant injection velocity. The main parameters to be measured for calculating the viscosity are pressure loss along the flow length, temperature of the polymer melt, wall temperature increase along the flow length and volumetric flow rate. The melt exits the flow channel and enters into the cylinder making the piston to move in the backward direction. Data acquisition is done by commercial software, while the rheological data evaluation is done by the software *"Rheosoft V.1.0"* developed by the Institute of Plastics processing, University of Leoben,

Austria. The measurements were performed using a special hybrid injection moulding machine, type ENGEL VC 940/130, supplied by ENGEL Austria GmbH, Schwertberg, which is equipped with an electrical plasticizing unit. To test and optimize the new measurement system, the viscosity values were measured for several polymers and counter pressure up to 500 bars. The injection moulding machine with the complete measurement system is shown in figure 57.

7.5.8 Experimental results

7.5.8.1 PP HG313MO

The higher shear rate range was measured by Kipperer [32] using the high pressure capillary rheometer with round capillary die with diameter of 0.5 mm at three different temperatures. The shear rate range was covered between 100 s^{-1} and 100000 s^{-1}. The viscosity curves without temperature correction are shown in figure 58.

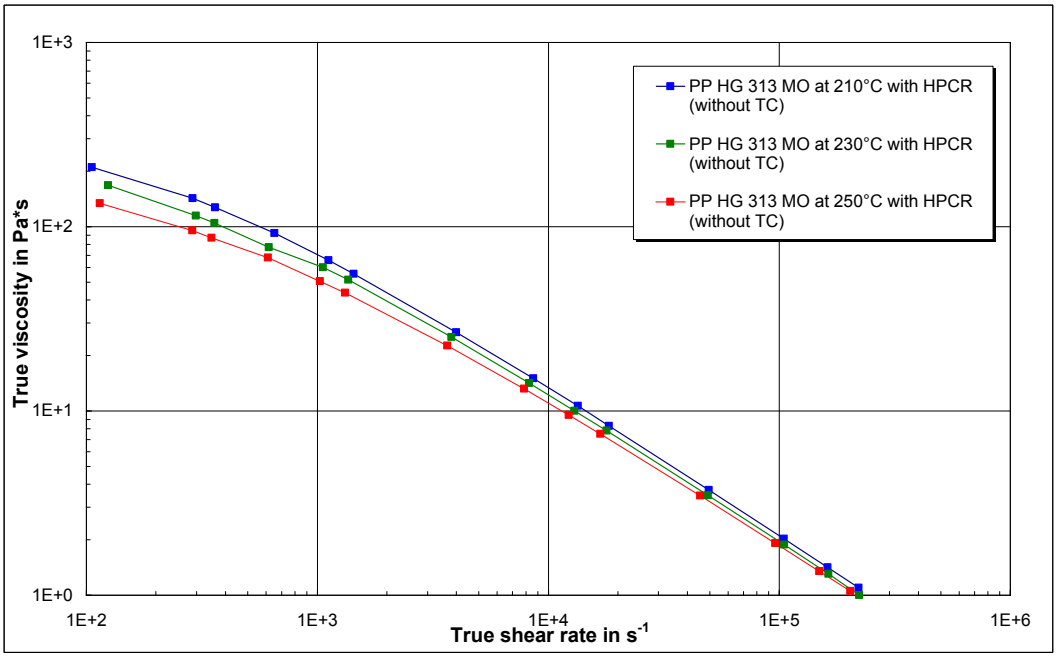

Figure 58: Viscosity curves measured with capillary die without temperature correction (without TC).

At shear rates above 1000 s^{-1} there was an increase in the calculated melt temperature up to 8°C due to shear heating. This shear heating can influence the viscosity and should not be neglected. Due to this reason, the temperature correction was carried out for the viscosity values. The viscosity values above this shear rate has been temperature corrected. It can be clearly seen in the graph (figure 59) that above shear rate 2000 s^{-1} the viscosity values have been temperature shifted and the temperature corrected values has higher viscosity compared to the measured values. From the plot shown in figure 59, it is clear that shear heating has high influence on the true viscosity values above 10^4 s^{-1}. Hence, these uncorrected viscosities show lower values.

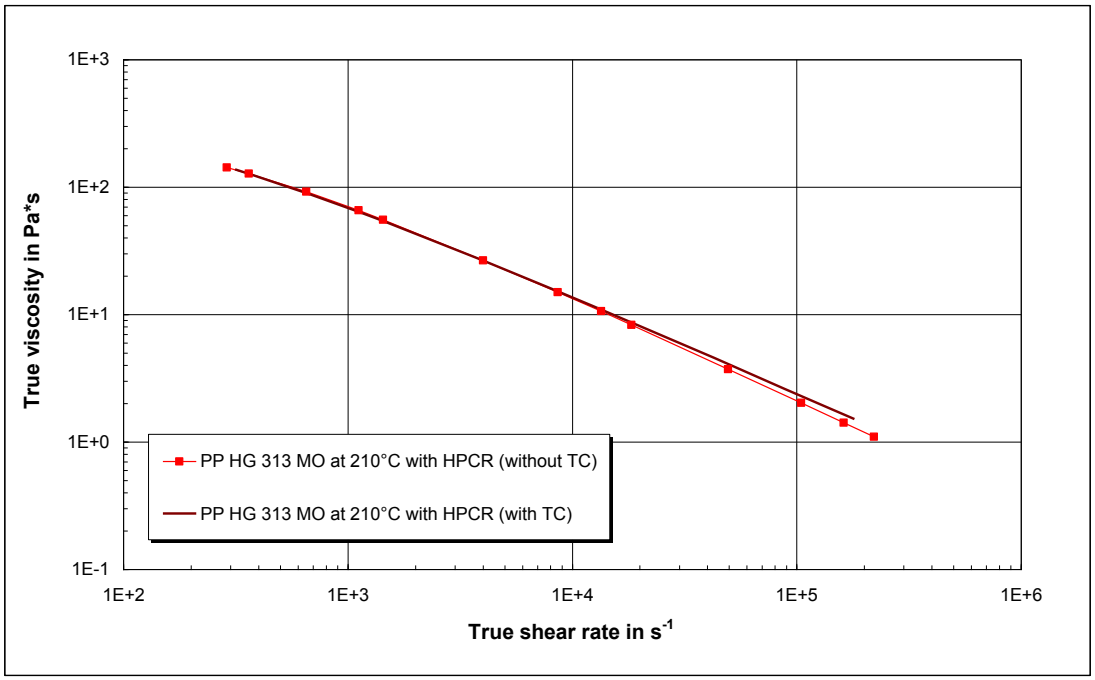

Figure 59: True viscosity curves measured on high pressure capillary rheometer (HPCR) with and without temperature correction.

The viscosity measurement at high volume rates were performed using an Engel injection moulding machine with a clamping force of 1300 kN, equipped with a 50 mm diameter screw, together with the newly developed rheological mould. The machine operates via a microprocessor system that allows the machine to operate automatically and adjust the different injection moulding parameters (injection rate, injection pressure, shot volume etc.). The rheological mould with a die insert having a slit height of 1 mm was used for the entire measurements. The heating of the mould was done using four cartridge heaters and four heating plates fixed on the mould surface, which are regulated directly by the injection moulding machine. For the measurement of pressure along the flow channel, four Dynsico MDA 462-1/2 UNF flush type pressure transducers were used. All the pressure sensors were placed 20 mm apart. The experimental investigations were done with the material PP HG313MO from Borealis at melt temperatures of 210°C, 230°C and 250°C. The results from the measurements are discussed below. The viscosity values measured on the injection moulding machine rheometer (IMMR) at three melt temperatures without considering the heat dissipation are shown in figure 60.

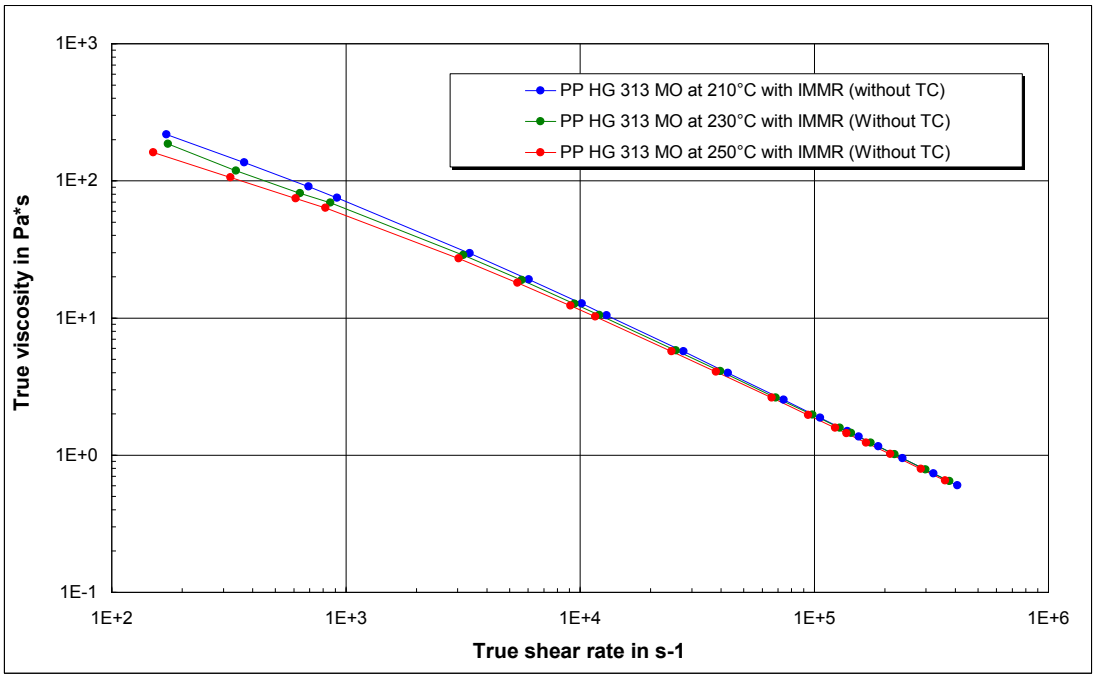

Figure 60: Viscosity curves measured with IMMR without temperature correction (without TC) for PP HG313MO at three different temperatures.

The increase in the calculated wall temperature and the calculated mean melt temperature using the improved Agassant method [66,69] is shown below.

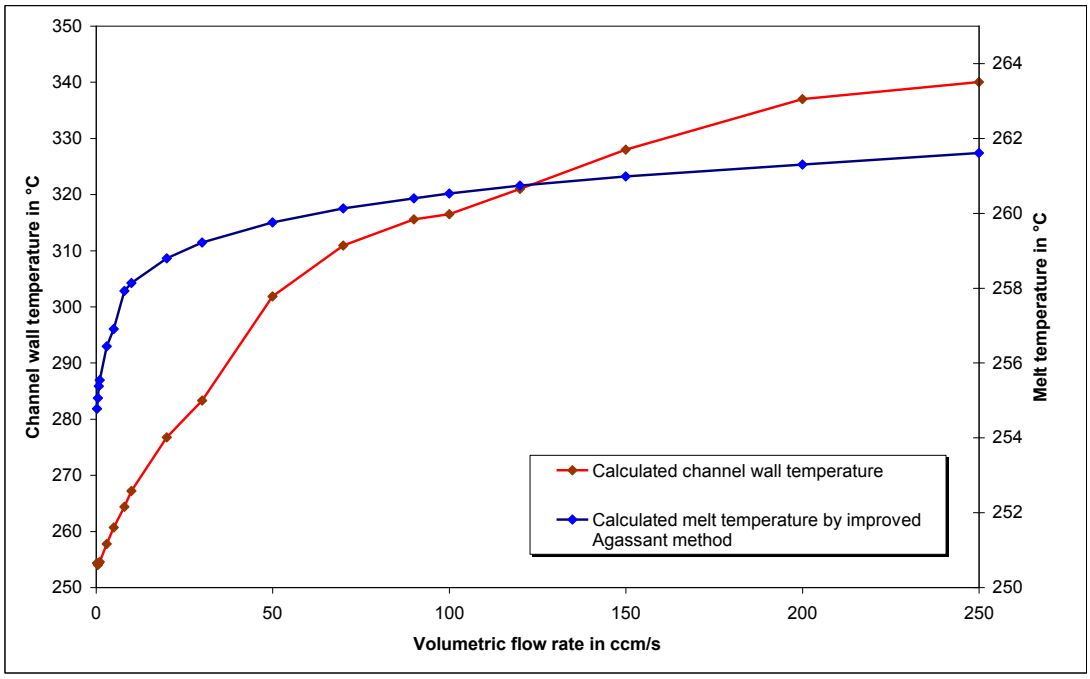

Figure 61: Increase in calculated wall temperature and calculated mean melt temperature at different flow rates for PP HG313 MO at 250°C, measured with injection moulding machine rheometer (IMMR).

Figure 62 shows the comparison of the viscosity curves with and without temperature correction, in which the temperature corrected viscosity values at lower shear rates have no significant changes but at higher shear rate range the viscosity values are shifted to higher viscosities. There are significant changes in the viscosity values at high shear rate region.

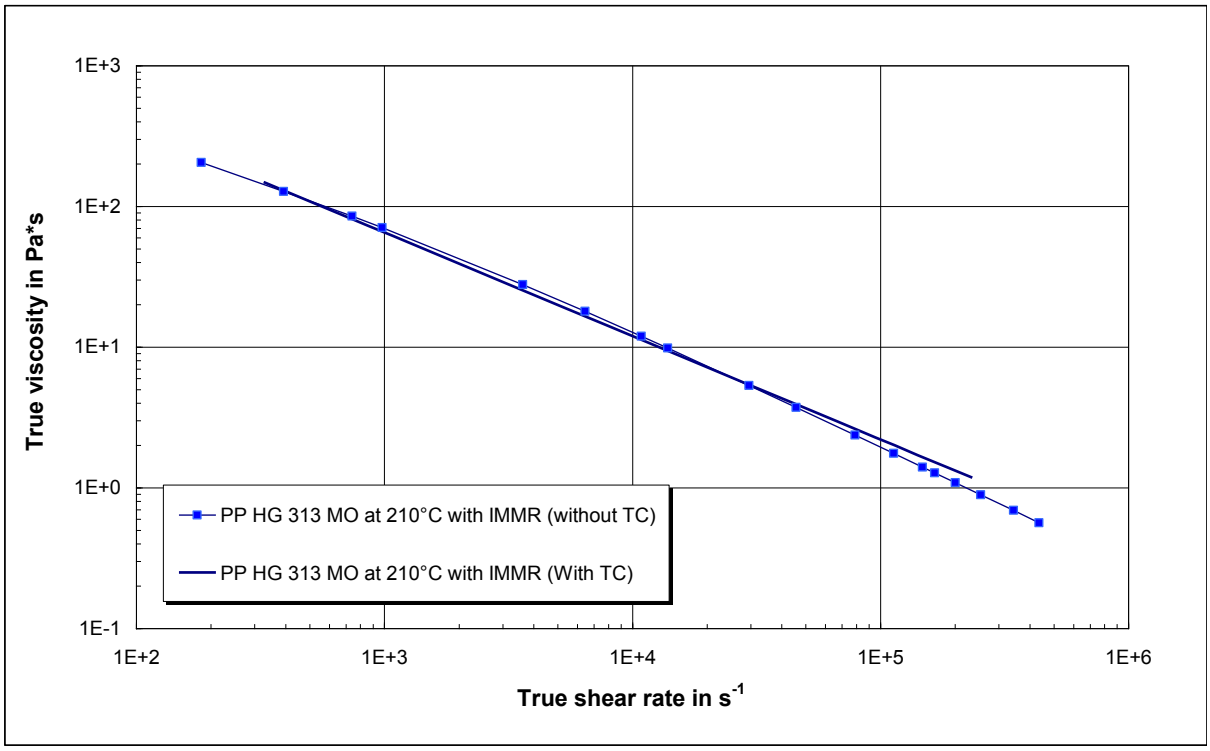

Figure 62: True viscosity values measured with injection moulding machine rheometer with and without temperature correction for PP HG313MO at 210°C.

The complete viscosity curve for PP HG313MO measured at 210°C and approximated with Cross model is shown in figure 63. The shear viscosities obtained from different rheometers at three different melt temperatures were brought into a single master curve by time-temperature superposition principle. The temperature master curve for PP HG313MO, approximated with Cross model with the reference temperature of 230 °C is shown in figure 64. Table 9 shows the material constants for PP HG313MO using Cross- und Arrhenius- model after the temperature correction (TC).

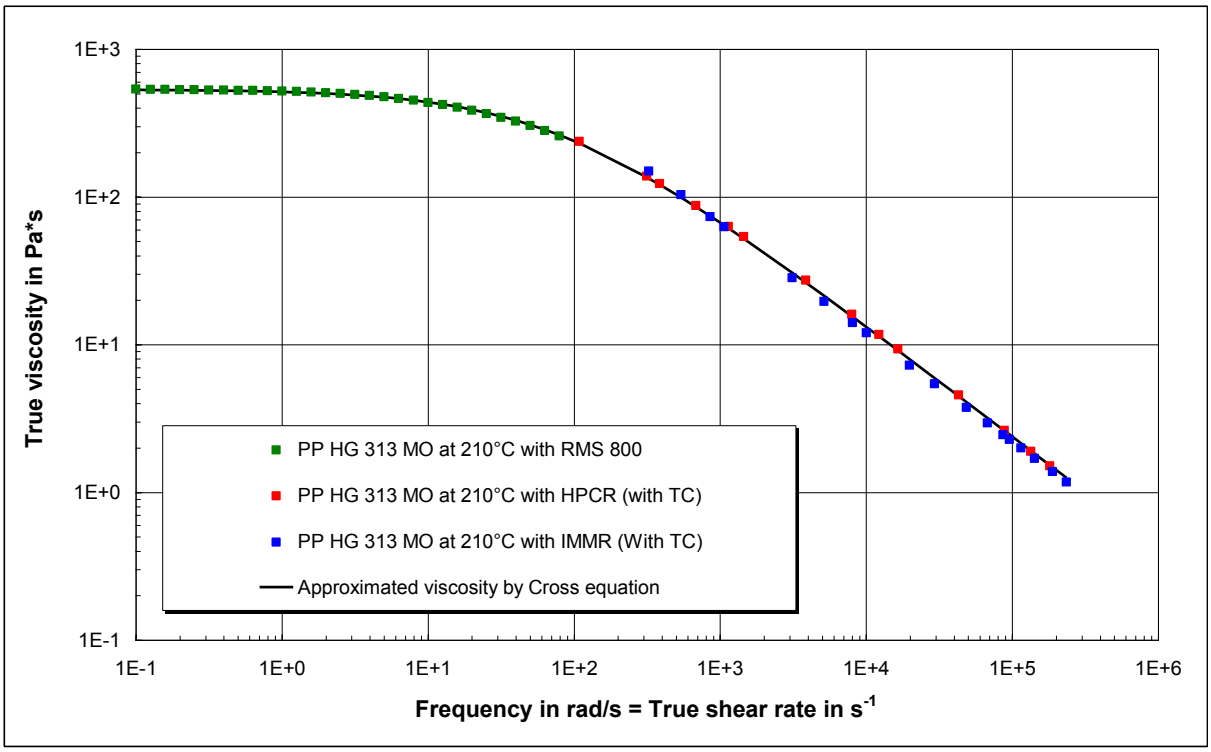

Figure 63: The temperature corrected viscosities values of PP HG313MO measured on RMS800; measured with the HPCR and measured with IMMR at 210°C with Cross approximation.

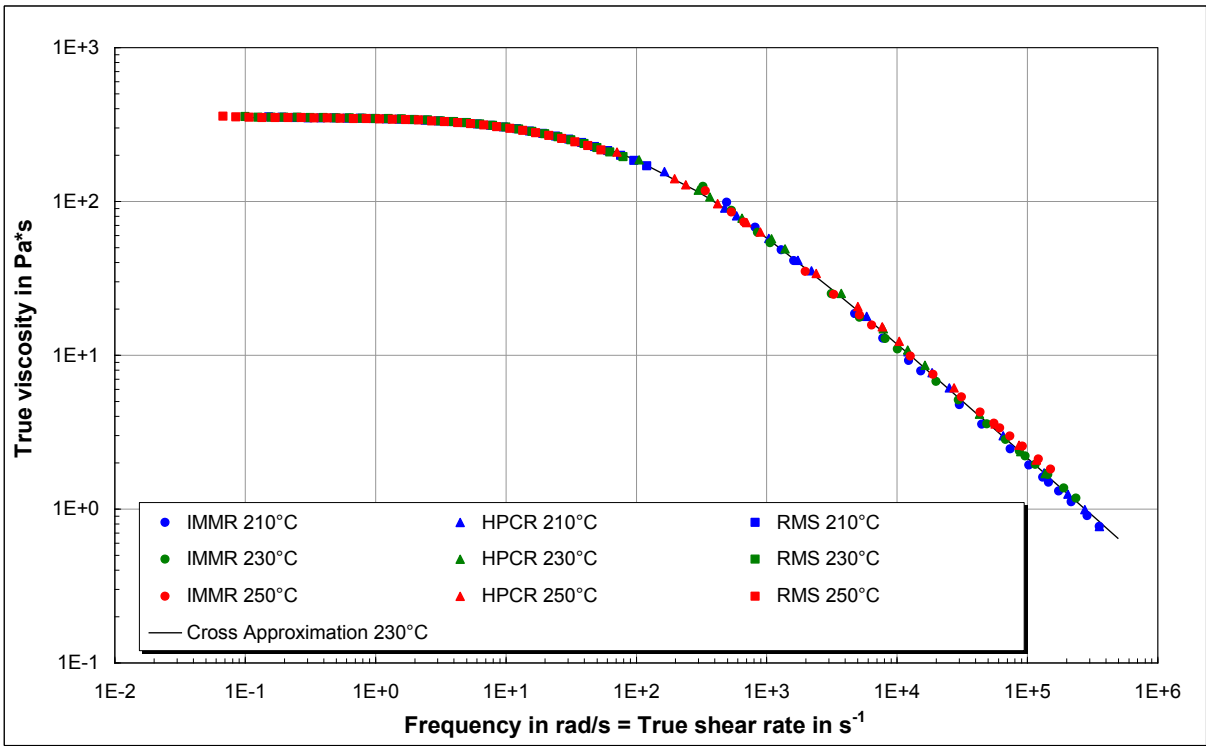

Figure 64: Temperature independent master curve of PP HG313MO at reference temperature of 230°C after temperature correction (TC).

Table 9: Material constants for PP HG313MO using Cross- and Arrhenius - model

A	351.7975	Pas
B	0.0086	s
C	0.7536	/
E_0	41.6591	kJ/mol
$T_{reference}$	230	°C

In order to investigate the pressure dependency of viscosity of PP HG 313MO, the viscosity measurements were carried out in the high pressure capillary rheometer with the back pressure chamber. The viscosity curves were measured at three different melt temperatures of 210°C, 230°C and 250°C and at the back pressures of 100, 300 and 600 bar. Figure 65 shows the true viscosity curves measured at different back pressures.

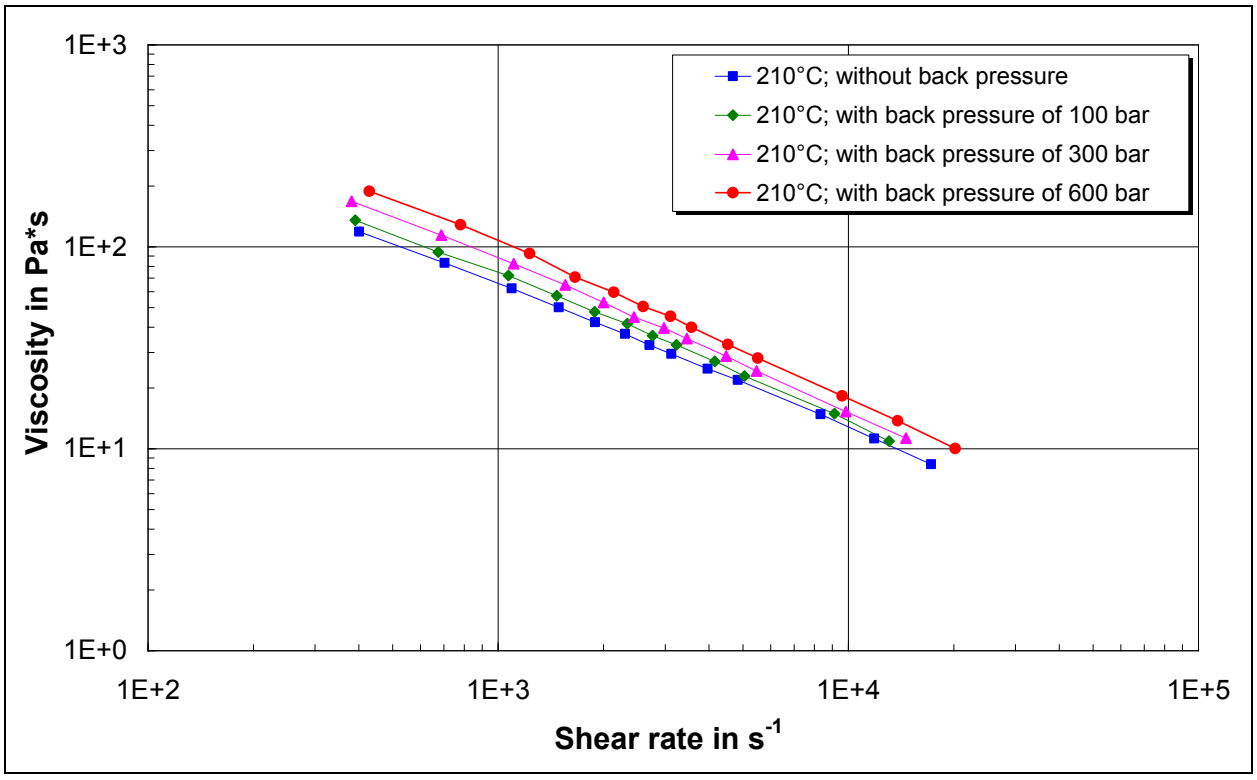

Figure 65: True viscosity curve of PP HG313MO at 210°C measured with and without back pressure in the high pressure capillary rheometer.

The viscosity increases at a shear rate of 1000 s^{-1} (1 bar) of 65.6 Pas to 88.7 Pas (300 bar). This corresponds to a pressure-induced increase in the viscosity by about 35%. The viscosity measurements carried out at melt temperatures of 230°C and 250°C shows a same pressure dependency as measured at 210°C [41].

The viscosity was measured in the injection moulding machine rheometer (IMMR) with back pressure of up to 400 bar with a slit die (slit height H of 1 mm). Figure 66 shows the true viscosity curves measured at different back pressures for PP HG313MO at test temperature of 210°C. For the measured PP HG313MO, the injection moulding rheometer enables us to measure the effect of pressure on viscosity up to a wall shear rate of 136,325 s^{-1}.

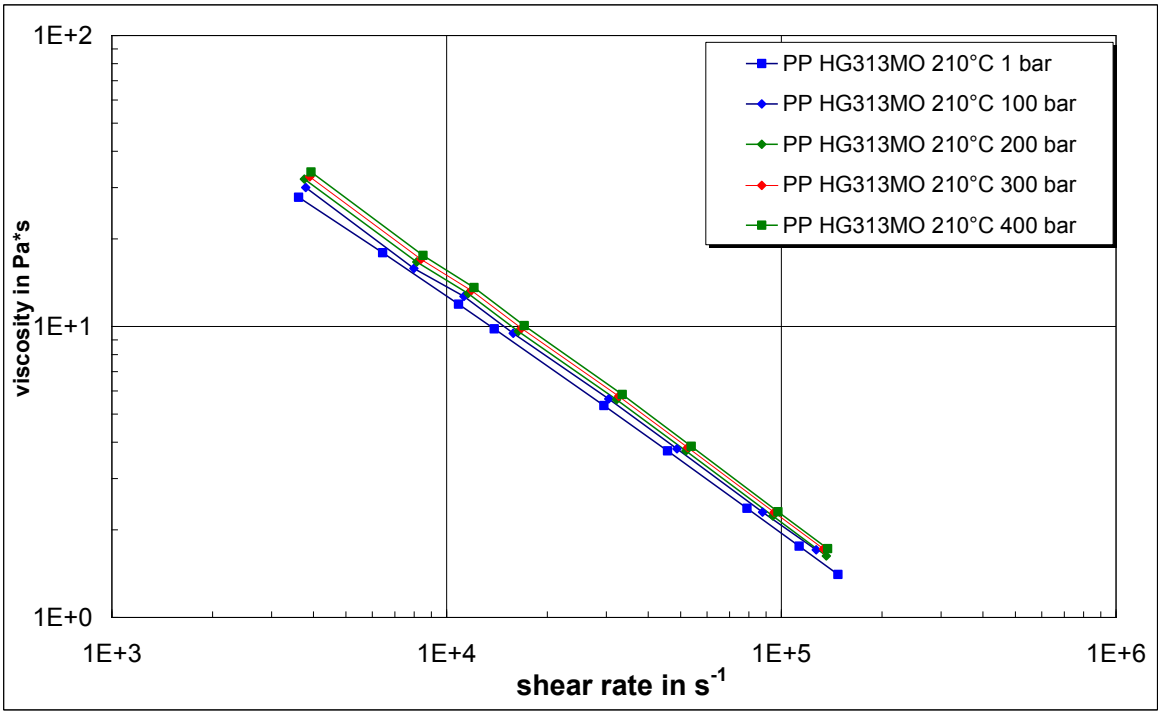

Figure 66: Viscosity curves measured with injection moulding machine rheometer at different back pressures for PP HG313MO at 210°C.

A temperature- and pressure- independent viscosity curve is obtained by shifting the measured viscosity curves by 45° into a reference curve. The Carreau viscosity model as in equation 142 was used for the approximation of the shear dependency of the measured viscosity curves. A, B and C are the approximation coefficients and a_{Tp} is the shift factor.

$$\eta = \frac{a_{Tp} \cdot A}{\left(1 + a_{Tp} \cdot B \cdot \dot{\gamma}\right)^{C}} \qquad (142)$$

The dependency of viscosity on temperature and pressure is introduced via the shift factor according to the pressure dependent Williams-Landel-Ferry (WLF) type equation (equation 143).

$$\log(a_{Tp}) = \left(\frac{8.86(T_0 - T_s)}{101.6 + T_0 - T_s} - \frac{8.86(T_m - T_s)}{101.6 + T_m - T_s} + \frac{\beta \cdot p}{\ln(10)} \right) \qquad (143)$$

Figure 67 shows the pressure and temperature invariant master curve of PP HG313MO at a reference temperature of 230°C. For the temperature- and pressure shifting, the viscosity curve measured with the rotational rheometer, the viscosity curves measured with and without back pressures in the high pressure capillary rheometer as well as the viscosity curves measured with and without back pressure in IMMR were taken into account for the shifting. The least-squares method was used to find the best fit for the approximation coefficients. The calculated pressure coefficient of viscosity for the chosen PP HG313MO is 24 x10^{-9} Pa^{-1}. The calculated pressure coefficient of viscosity at constant shear stress is fitting closely with the value calculated by Sedlacek et al. [51]. The approximation coefficients of Carreau-WLF viscosity model are listed in table 10.

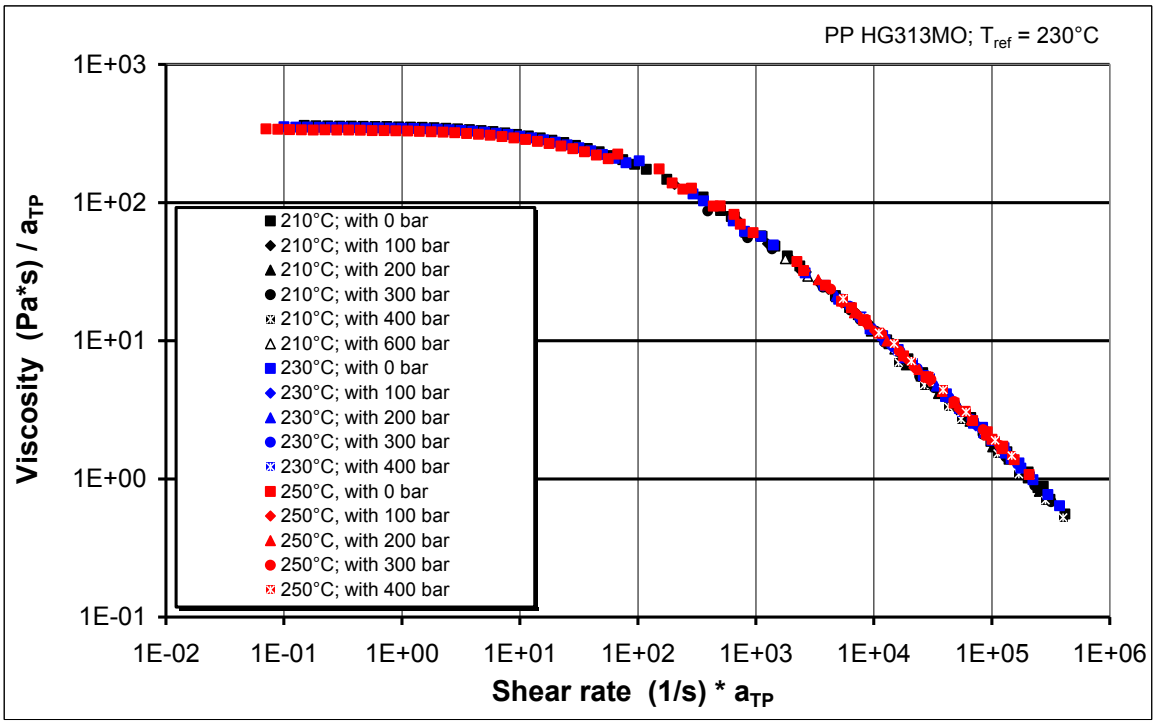

Figure 67: Temperature and pressure invariant master curve of PP HG313MO at a reference temperature 230°C.

Table 10: Material constants for PP HG313MO using Carreau- and WLF- model

A	328.42	Pas
B	0.0075	s
C	0.772	/
T_0	230	°C
T_s	-2.47	°C
β_τ	24.6x10^{-9}	Pa^{-1}

The above material constants are used for the simulation of expansion injection moulding of PP HG313MO as the viscosity data.

7.5.8.2 PS 495F

The standard rheological measurements at lower shear rates from 0.001 s^{-1} to 100 s^{-1} were carried out on the rotational rheometer RMS 800 from Rheometrics Inc., Piscataway, N.J., USA. The temperature and shear rate dependent viscosity curves were measured using cone-plate geometry under isothermal condition in either steady state or dynamic mode. The viscosity curves were measured at test temperatures of 210°C, 230°C and 250°C. The viscosity at high shear rates from 100 s^{-1} to 100,000 s^{-1} was measured on the high pressure capillary rheometer by using round capillary dies. Figure 68 shows the temperature corrected true viscosity cures measured in the high pressure capillary rheometer together with the viscosity curves measured with RMS 800.

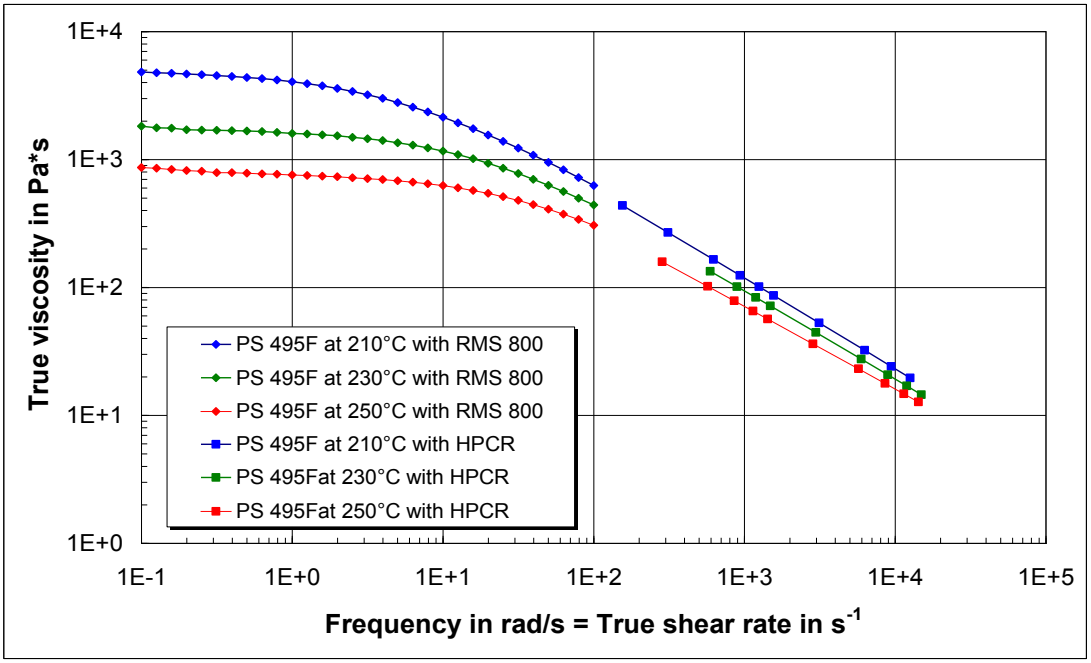

Figure 68: Comparison of viscosity curves of PS 495F measured on different rheometers at three different melt temperatures.

Figure 69 shows the comparison of the viscosity curves with and without temperature correction, in which the temperature corrected viscosity values at lower shear rates have no significant changes but at higher shear rate range the viscosity values are shifted to higher viscosities.

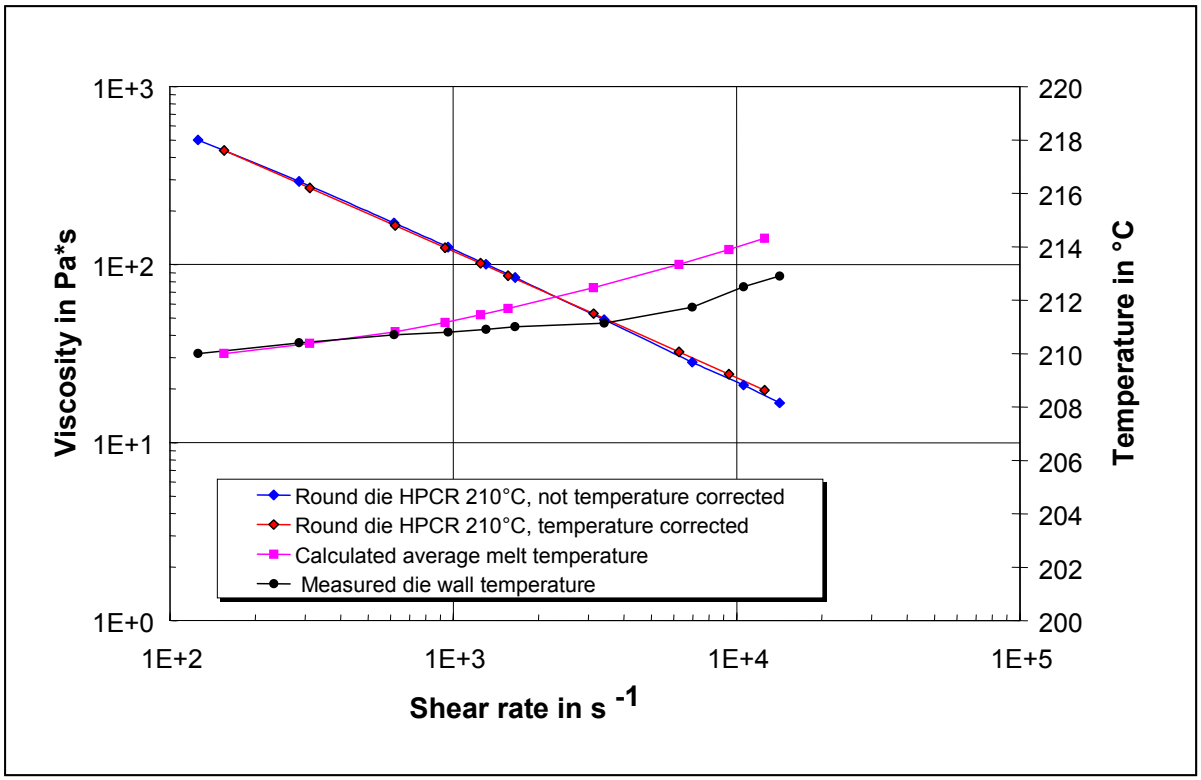

Figure 69: True viscosity curves measured on high pressure capillary rheometer (HPCR) at 210°C with and without temperature correction and with the calculated melt temperature.

The viscosity measurement at high volume rates were performed using an Engel injection moulding machine with a clamping force of 1300 kN, equipped with a 50 mm diameter screw. The experimental investigations were done with the material PS 495F from BASF at melt temperatures of 210°C, 230°C and 250°C. The viscosity values measured on the injection moulding machine rheometer (IMMR) at three melt temperatures with temperature corrections are shown in figure 70.

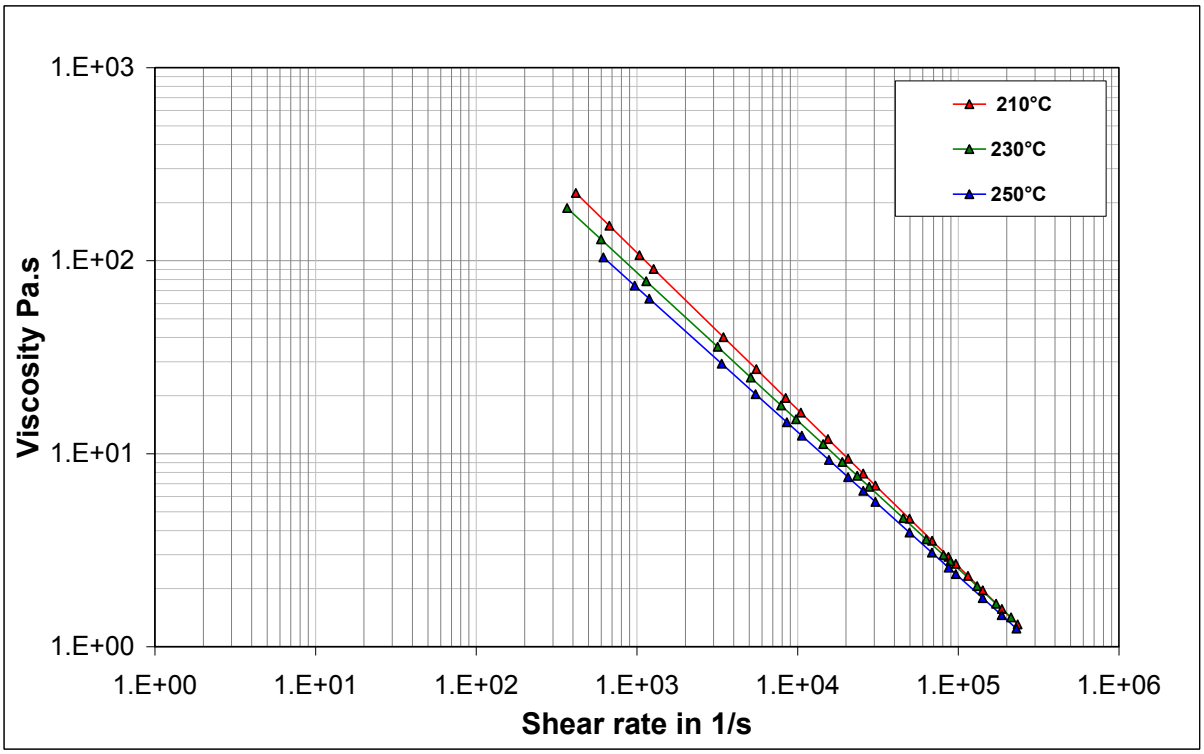

Figure 70: Viscosity curves measured with IMMR with temperature correction for PS 495F at three different temperatures.

In order to investigate the pressure dependency of viscosity of PS 495F, the viscosity measurements were carried out in the high pressure capillary rheometer with the back pressure chamber. The viscosity curves were measured at three different melt temperatures of 210°C, 230°C and 250°C and at the back pressures of 100, 300 and 500 bar. Figure 71 shows the true viscosity curves measured at 230°C with and without back pressures. In figure 71, the viscosity value measured at 1000 s^{-1} with 500 bar back pressure is 145.74 Pa.s, which is approximately 62.52 % higher than the viscosity value (89.67 Pa.s) measured at ambient pressure. It clearly shows, the PS 495F material has higher pressure dependency of viscosity in compare to the PP HG313MO. The thermoplastic materials with bulky side group show the increased pressure dependency.

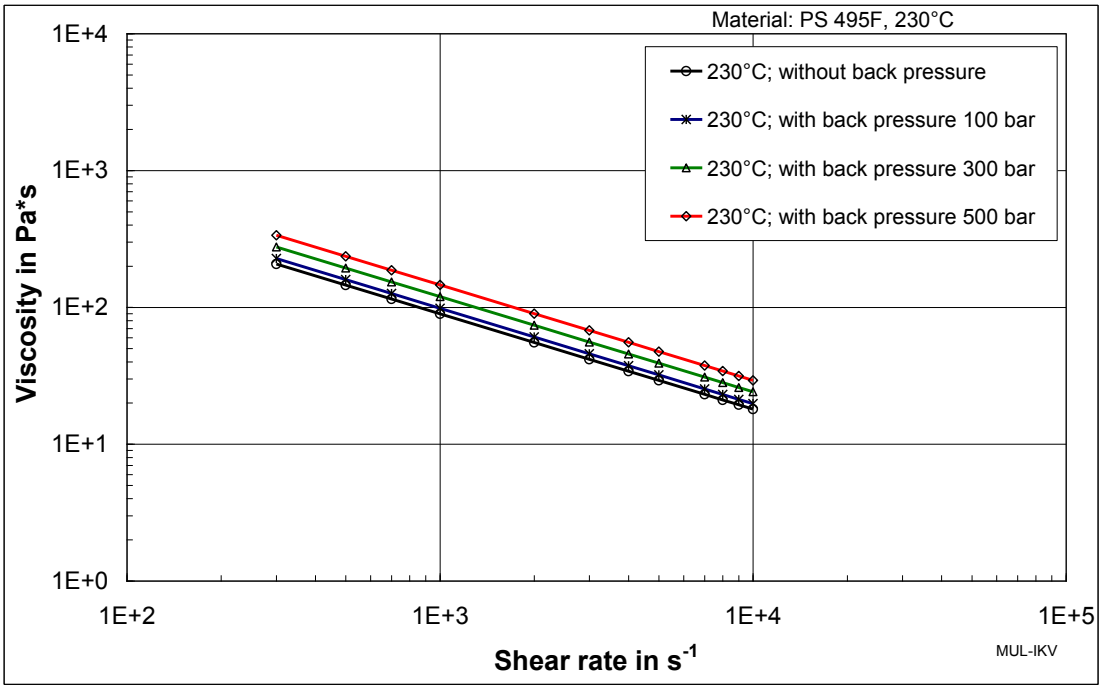

Figure 71: True viscosity curve of PS 495F at 230°C measured with and without back pressure in the high pressure capillary rheometer.

The viscosity of PS 495F up to wall shear rate of 42000 s^{-1} was measured in the injection moulding machine rheometer (IMMR) with back pressure of up to 400 bar with a slit die (slit height H of 1 mm). Figure 72 shows the true viscosity curves measured at different back pressures for PS 495F at test temperature of 210°C.

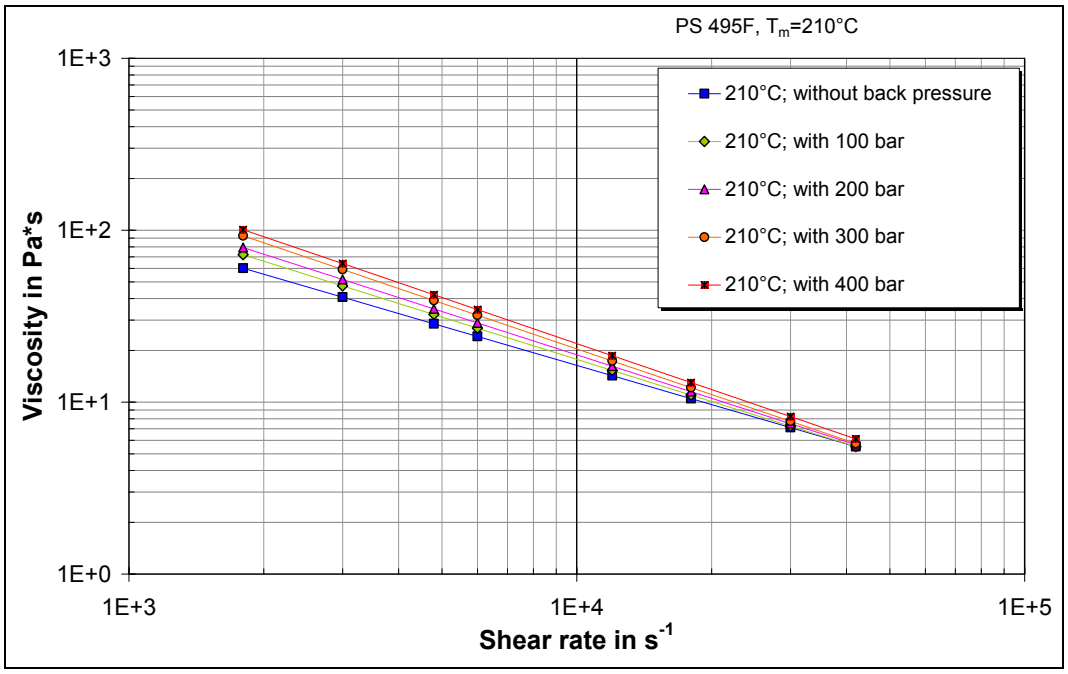

Figure 72: True viscosity curve of PS 495F at 210°C measured with and without back pressure in IMMR.

Figure 73 shows the pressure and temperature invariant master curve of PS 495F at a reference temperature of 230°C. For the temperature- and pressure shifting, the viscosity curve measured with the rotational rheometer and the viscosity curves measured with and without back pressure in IMMR were taken into account for the shifting. The calculated pressure coefficient of viscosity for the chosen PS 495F is 31.28×10^{-9} Pa^{-1}. The approximation coefficients of the Carreau-WLF viscosity model are listed in table 11.

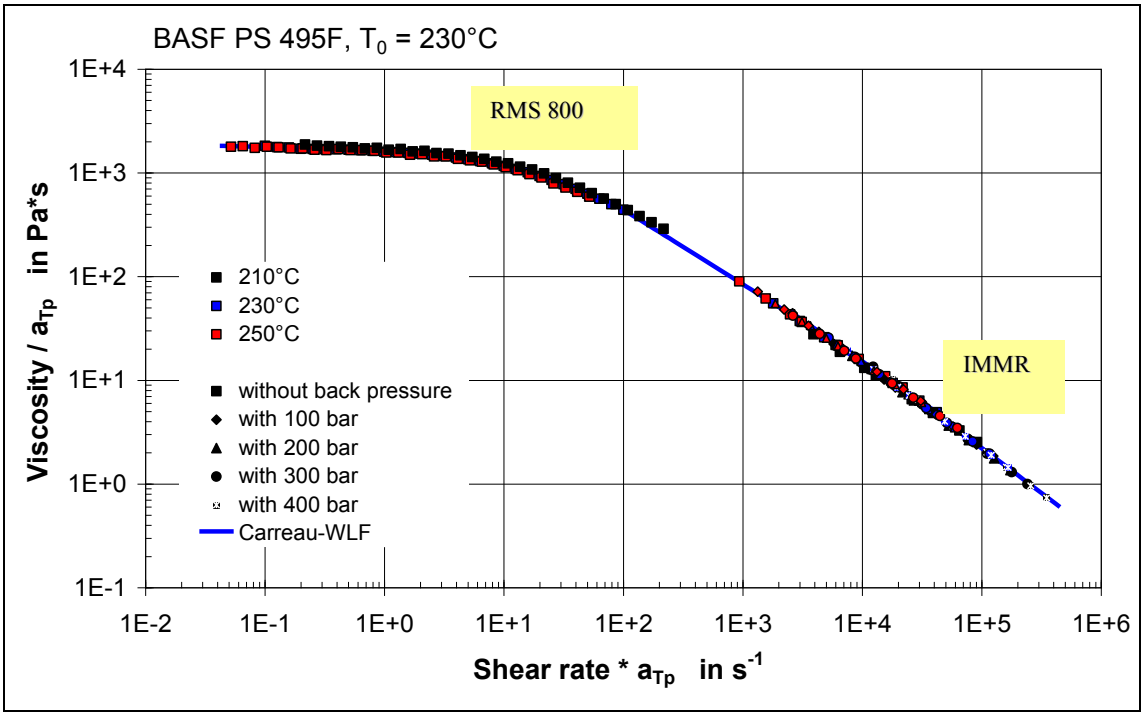

Figure 73: Temperature and pressure invariant master curve of PS 495F at a reference temperature 230°C.

Table 11: Material constants for PS 495F using Carreau- and WLF- model

A	1722.8	Pas
B	0.04497	s
C	0.784	/
T_0	230	°C
T_s	90	°C
β_τ	31.28×10^{-9}	Pa^{-1}

7.5.8.3 Bayblend T65

The viscosity measurements of ABS/PC Bayblend T65 were measured at test temperature of 240°C, 260°C and 280°C. Granulates were pre-dried in the vacuum oven at the corresponding drying condition. At lower shear rates from 0.001 s^{-1} to 100 s^{-1} were carried out on the rotational rheometer RMS 800 from Rheometrics Inc., Piscataway, N.J., USA. The shear rates higher than 100 s^{-1} were measured in the high pressure capillary rheometer with the round capillary die [32]. Figure 74 shows the true viscosity curves after the temperature correction at three melt temperatures measured in the high pressure capillary rheometer. The viscosity values of the Bayblend T65 is relatively higher than the viscosity values of PP HG313MO and PS 495F.

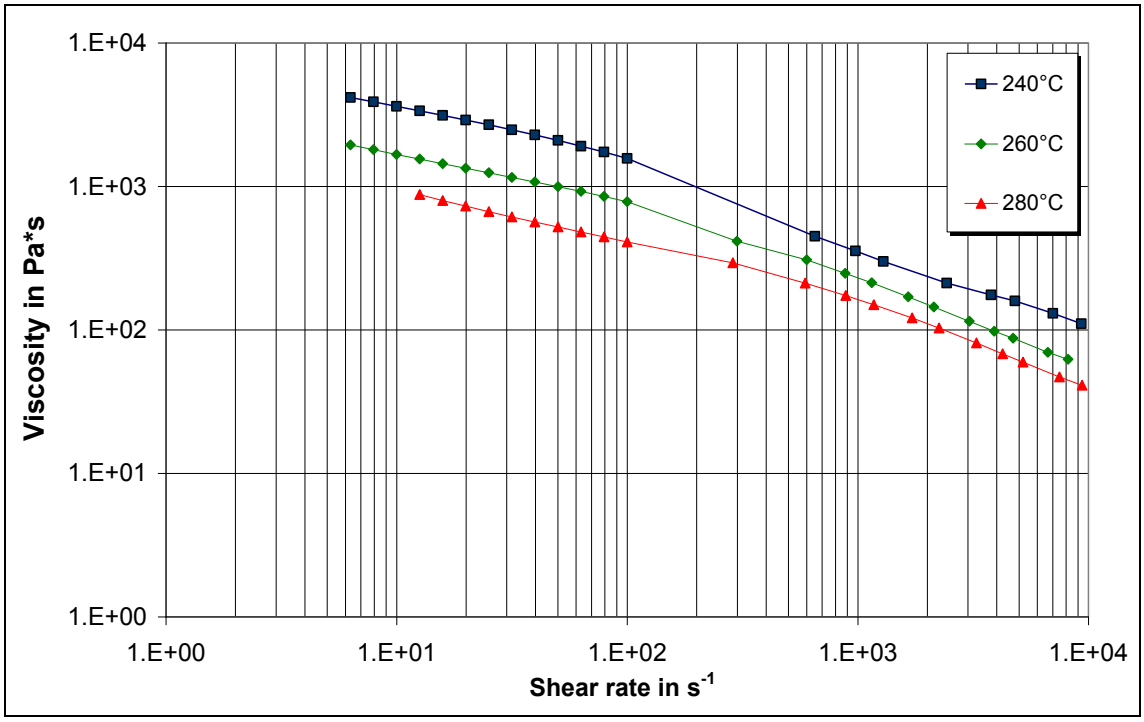

Figure 74: True viscosity curves of Bayblend T65 at three melt temperature measured in the high pressure capillary rheometer and RMS 800.

The pressure dependency of Bayblend T65 was investigated by carried out the viscosity measurements in the high pressure capillary rheometer with the back pressure chamber. The viscosity measurements were carried out at 260°C with back pressures of 200 bar and 400 bar. Figure 75 shows the measured viscosity curves of Bayblend T65 at 260°C measured with and without back pressure. The viscosity measurements on the IMMR provide unreliable viscosity results. Due to extreme frictional heating, the slit-die wall temperature goes above the material degradation temperature-limit in IMMR. This problem is discussed in detail in the work of Narnhofer.M [42].

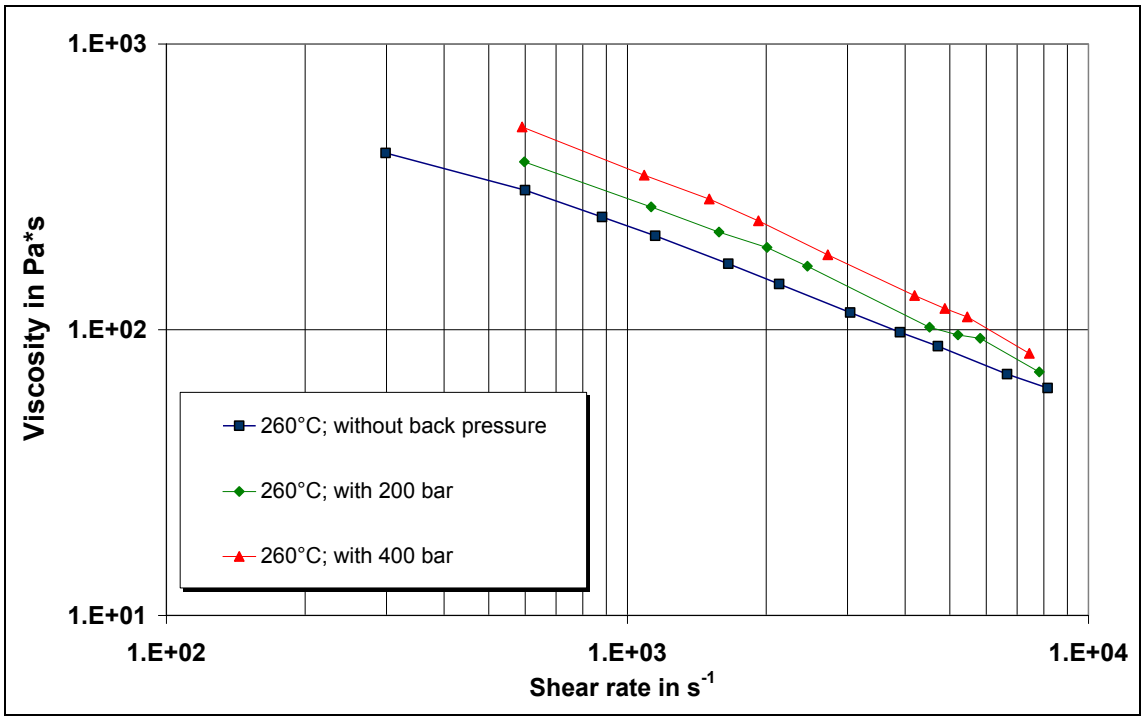

Figure 75: True viscosity curve of Bayblend T65 at 260°C measured with and without back pressure in the high pressure capillary rheometer.

Figure 76 shows the pressure and temperature invariant master curve of Bayblend T65 at a reference temperature of 260°C. For the temperature- and pressure shifting, the viscosity curve measured with the rotational rheometer and the viscosity curves measured with and without back pressure in the high pressure capillary rheometer were taken into account for the shifting. The calculated pressure coefficient of viscosity for the chosen Bayblend T65 is 23.93×10^{-9} Pa^{-1}. The approximation coefficients of the Carreau-WLF viscosity model are listed in table 12.

Table 12: Material constants for ABS/PC Bayblend T65 using Carreau- and WLF- model

A	1961	Pas
B	0.0366	s
C	0.591	/
T_0	260	°C
T_s	158.63	°C
β_τ	23.93×10^{-9}	Pa^{-1}

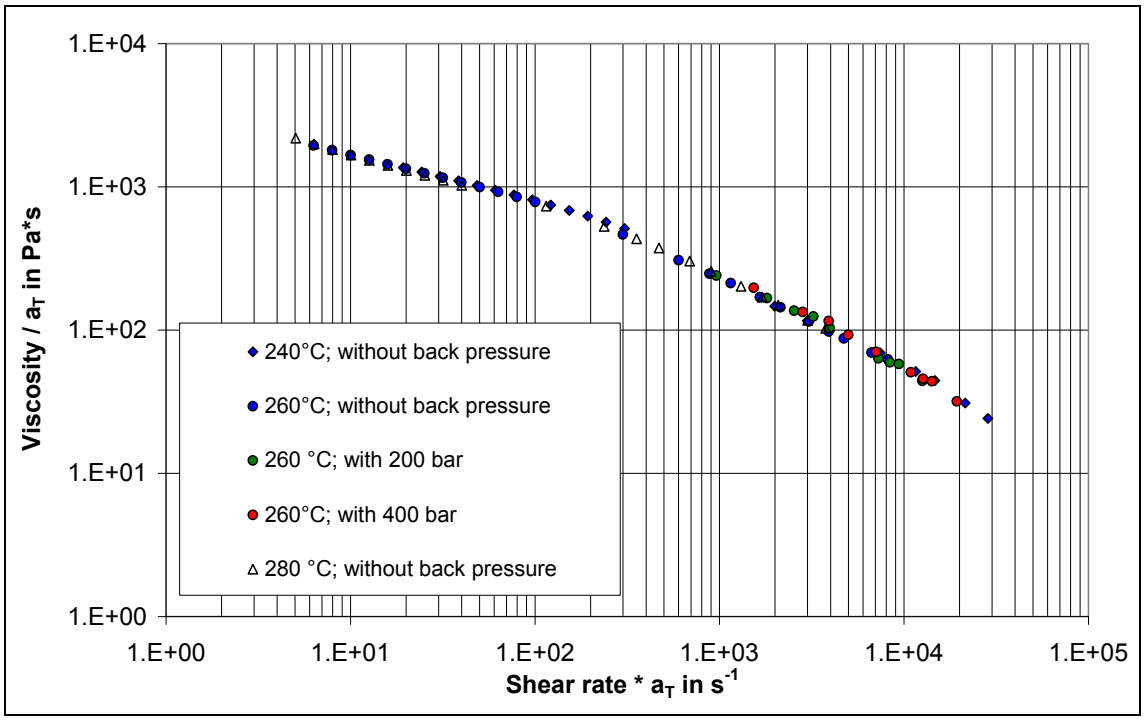

Figure 76: Temperature and pressure invariant master curve of Bayblend T65 at a reference temperature 260°C.

7.6 Thermal conductivity

7.6.1 Theoretical background

Thermal conductivity is one of the most important properties that influence injection moulding pressure predications. Accurate measurement of thermal conductivity had been reported to be important for the simulation of flow and cooling process. Thermal conductivity is one the significant parameter among the other important parameters such as specific heat, viscosity, and pvT-data. Thermal conductivity is an essential property for heat flow calculation.

When analysing the thermal process, the thermal conductivity (λ) is the most significantly used property that helps to quantify the transport of heat through the material. By definition energy is transported proportionally to the speed of sound. Accordingly, the thermal conductivity follows the relation as in equation 144 [37].

$$\lambda \approx c_p \cdot \rho \cdot u \cdot l \qquad (144)$$

where:

c_p specific heat capacity at constant pressure (J/kg K)

ρ density (kg/m^3)

u speed of the sound (m/s)

l molecular separation (m)

Amorphous polymers show an increase in thermal conductivity with increasing temperature, up to the glass transition temperature (T_g). Above T_g the thermal conductivity decreases with increasing temperature. Thermal conductivity for semi-crystalline polymers, however, shows an abrupt increase when temperature drops below the crystallization temperature. This is because of the appearance of the crystalline phase, which creates regions of higher thermal conductivity. Furthermore, the thermal conductivity of melts increase with hydrostatic pressure. Figure 77 shows a schematic thermal conductivity diagram for various thermoplastics.

Anisotropy in thermoplastic polymers plays a significant role in the thermal conductivity. Highly drawn semi-crystalline polymer samples have a much higher thermal conductivity because of the orientation of the polymer chains in the direction of the draw. The higher thermal conductivity of inorganic fillers increases the thermal conductivity of the filled polymers.

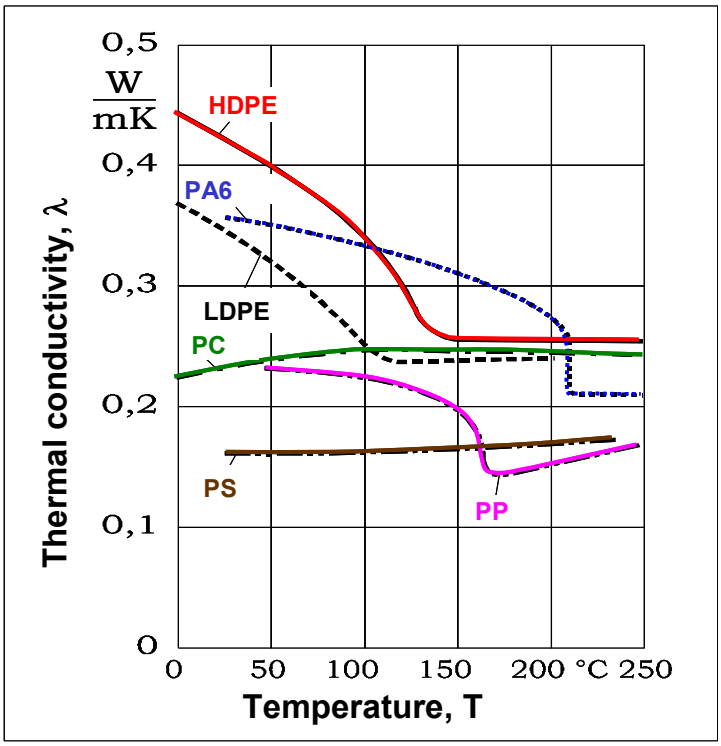

Figure 77: Thermal conductivity of various thermoplastics [37].

There is a rapidly growing need for thermal conductivity of polymers at the processing conditions of these materials, which are generally at high temperatures and pressures. The transient line source method has established itself as an accepted technique for thermal conductivity measurements. The technique is particularly efficient with polymer melts. The line-source technique is capable of high speed measurements lasting typically 15-30 s permitting tests to be completed well before thermal degradation effects become important [80].

7.6.2 Measurement techniques

The thermal conductivity as a function of temperature is measured at the Institute of Plastics Processing by the apparatus namely K-System II, manufactured by Advanced CAE Technology Inc. USA. The apparatus is based on the method called transient Line-Source method [81]. Figure 78 shows the K-System II measurement system. The sample cell is a long cylindrical reservoir, open at one end, through which the probe is inserted. The other end of the cell can be opened to discharge the sample when the measurement is completed. The cell is heated externally to provide an uniform temperature environment for the sample. The line source consists of a heater wire that runs along the whole length of the probe, with a temperature sensor located half-way down its length. The probe needs to be calibrated with a material of known thermal conductivity.

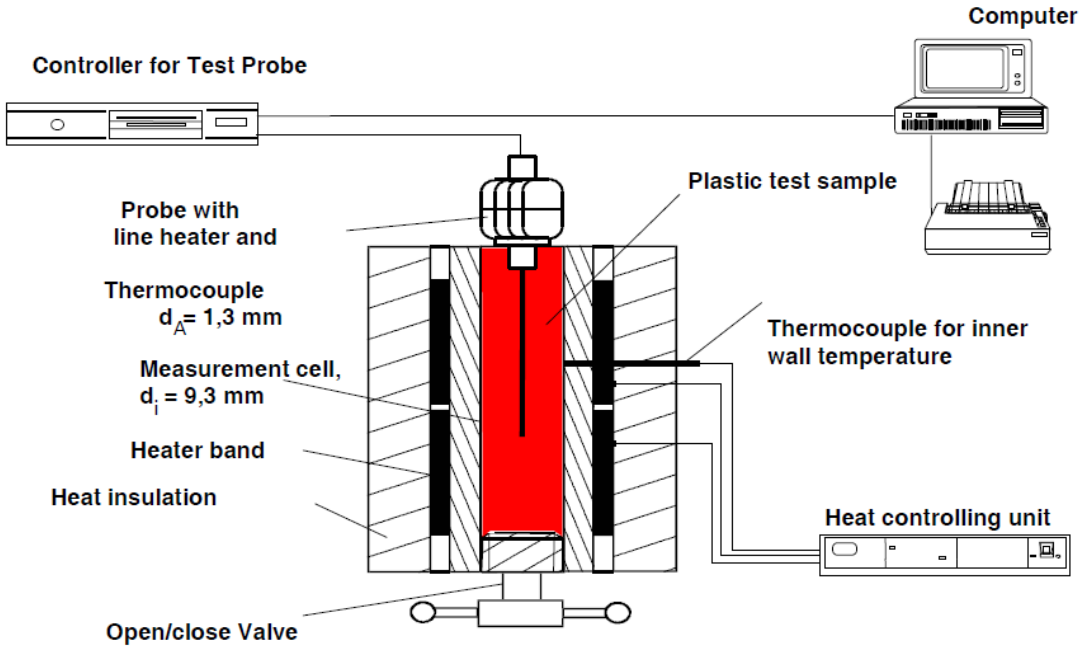

Figure 78: Measuring apparatus K-System II for thermal conductivity measurement [39].

The pre-dried pellets of the polymer are loaded into the measurement cell, which is maintained above the melting temperature of the material. The pellets melt and are compacted carefully to obtain a uniform sample without any gas entrapment. The probe is inserted into the sample and the system is allowed to equilibrate. Measurements are made by supplying a known, constant voltage to the probe heater. The temperature transient is recorded for 30 sec. A plot of temperature against log time plotted as shown in figure 79.

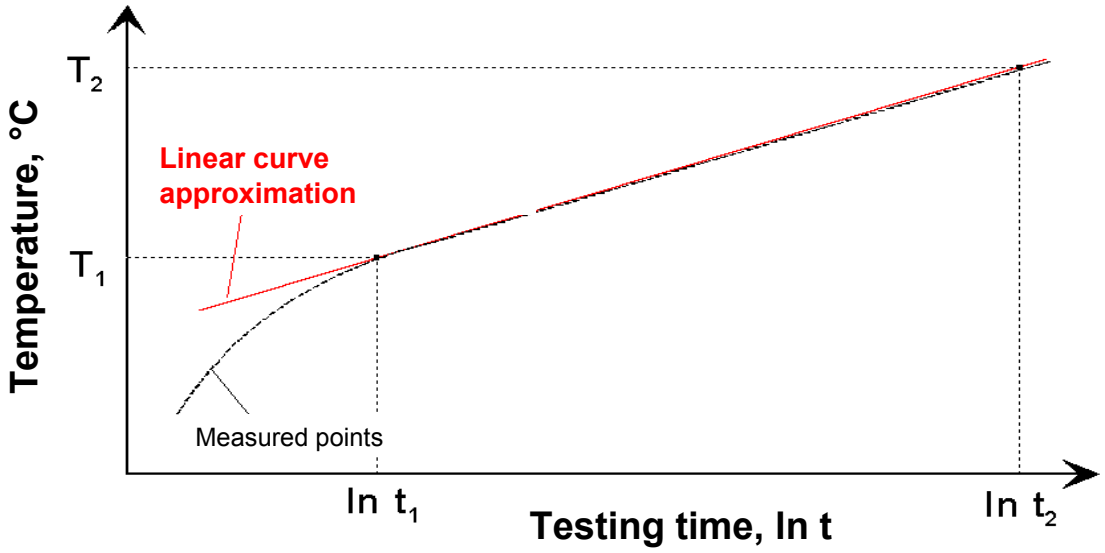

Figure 79: Measured temperature over the time in K-System II.

Usually the plot of the measured temperature over the log time is a straight line. Thermal conductivity can be calculated from the slop of this line. Since the amount of heat added during the measurement is small, the system returns to equilibrium quickly and multiple measurements can be made to ensure the reproducibility. The thermal conductivity λ, is calculated from the equation 145.

$$\lambda = \frac{\Phi' \cdot k}{4 \cdot \pi} \cdot \frac{\ln\left(\frac{t_2}{t_1}\right)}{T_2 - T_1} \qquad (145)$$

Where:

λ thermal conductivity (W/m K)

Φ' heat flow per unit length (W/m)

k probe constant (/)

T_1 temperature (°C) at time t_1

T_2 temperature (°C) at time t_2

For measurement of thermal conductivity as a function of temperature, the sample is prepared at the highest processing temperature. For thermally stable materials, it is possible to carry out the entire temperature range with a single sample. Reading are taken as soon as the system stabilizes at the set temperature and the system is cooled to the next temperature.

The thermal conductivity measurement as a function of both temperature and pressure was carried out in the high pressure capillary rheometer (HPCR) with the help of the specially designed conductivity probe by Göttfert Werkstoff-Prüfmaschinen GmbH, Buchen, Germany. The thermal conductivity measurement device integrated into a HPCR is shown in figure 80.

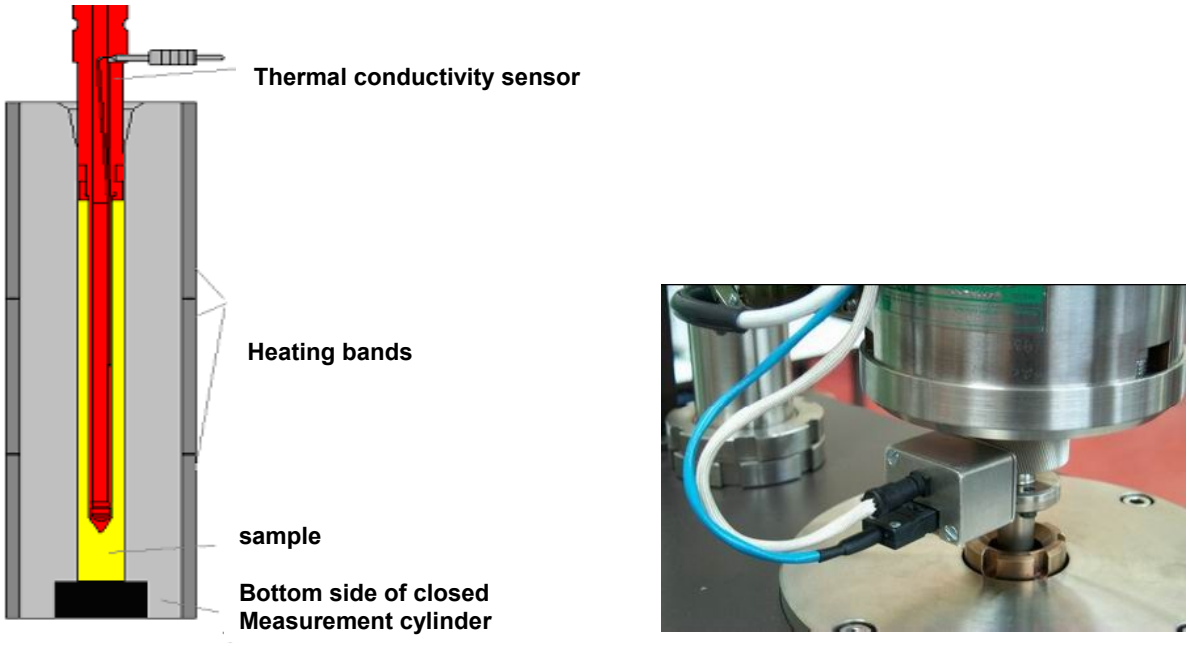

Figure 80: Thermal conductivity probe integrated into a HPCR [80].

The barrel is closed at the bottom instead of inserting a capillary. A defined volume of polymer granulates into the barrel. The thermal conductivity probe is moved into the barrel and the sample flows into the annular gap between probe and barrel. The probe consists of a thin walled piston with a heating bar and a thermocouple in the centre. With a high accuracy power supply a defined heat flow is generated through the sample. The increase of temperature in the probe is measured. Thermal conductivity is then calculated from the temperature increase and the heat flow. At the upper end of the probe, a sealing ring is placed to generate different pressures on the sample. A maximum pressure near 2000 bar can be built up [82]. The pressure can be measured in molten status of the sample by the pressure transducer normally placed before the capillary, which is now closed. Below the melting point, a force sensor in the socket for the thermal conductivity probe can measure the pressure.

7.6.3 Experimental results

The thermal conductivity as a function of temperature was measured with K-System II. The used measurement standard is ASTM D5930-97. The measured thermal conductivity curves as a function of temperature for PS 495F and PP HG313MO are shown in figure 81. The thermal conductivity as a function of temperature and pressure

was measured on the high pressure capillary rheometer with the help of the thermal conductivity measurement sensor from Göttfert Werkstoff-Prüfmaschinen GmbH, Buchen, Germany. The thermal conductivity of PS 495F melt as a function of temperature and pressure is shown in figure 82.

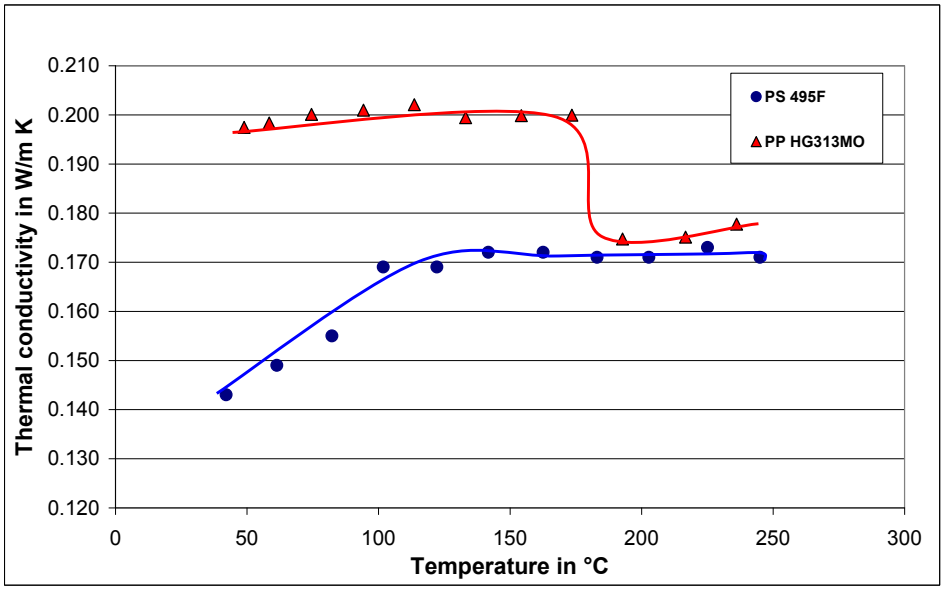

Figure 81: The thermal conductivity (λ) as a function of temperature.

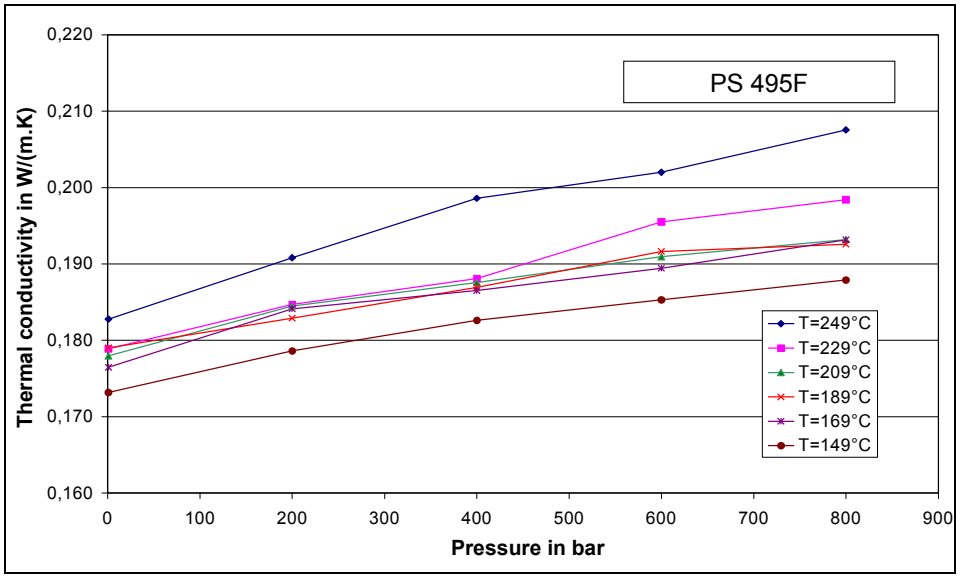

Figure 82: The thermal conductivity (λ) as a function of temperature and pressure in the melt state for PS 495F.

The measured thermal conductivity value increases linearly with increasing pressure. For the investigated PS 495F, 1 to 2 % increase of thermal conductivity value was measured for 100 bar pressure increase. The thermal conductivity values measured as a function of temperature and pressure for ABS/PC Bayblend T65 is shown in figure 83. The thermal conductivity values were measured as a function of temperature at the

hydrostatic pressures of 200, 500 and 800 bar [42]. In the melt range, the thermal conductivity values increase about 10 - 15% for the pressure difference of 800 bar.

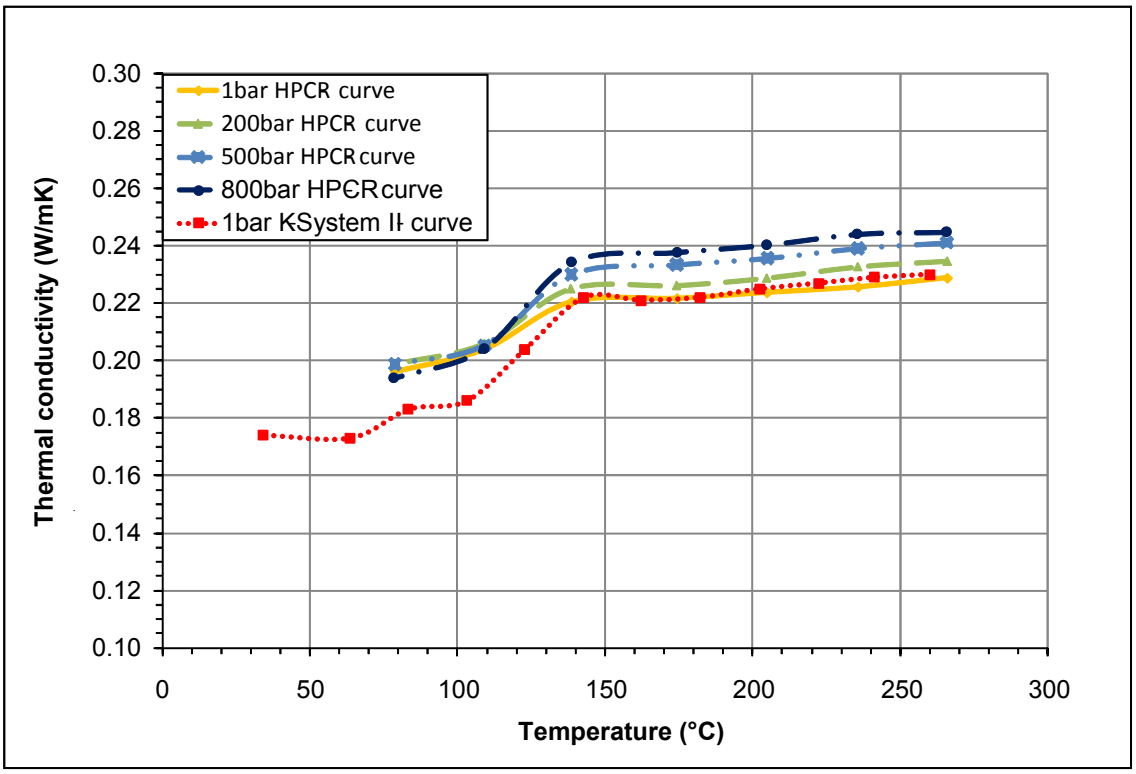

Figure 83: The thermal conductivity (λ) of Bayblend T65 as a function of temperature and pressure.

7.7 Specific heat capacity

7.7.1 Theoretical background

The specific heat represents the energy required to change a unit mass of material by one degree in temperature. It can be measured either constant pressure (c_p) or constant volume (c_v). Since specific heat at constant pressure includes the effect of volumetric change, it is lager than the specific heat at constant volume. However, the volume changes of a polymer with changing temperatures have a negligible effect on the specific heat. Hence, one can usually assume that specific heat at constant volume or constant pressure are same [37]. The specific heat changes only modestly in the range of practical processing temperature.

The semi-crystalline thermoplastics display a discontinuity in specific heat at the melting point of the crystallites. This discontinuity in specific heat includes heat that is required to melt the crystallites which is usually called as heat of fusion. Hence, the specific heat is dependent on the degree of crystallinity.

7.7.2 Measurement method

The specific heat capacity measurements for chosen thermoplastics were carried out using DSC 200, manufactured by Netsch Gerätebau GmbH, Germany. The used method followed the DIN 51005 standard, for the determination of specific heat capacity (C_p) by using Differential Scanning Calorimeter (DSC). The DSC 200 equipment used is shown in figure 84.

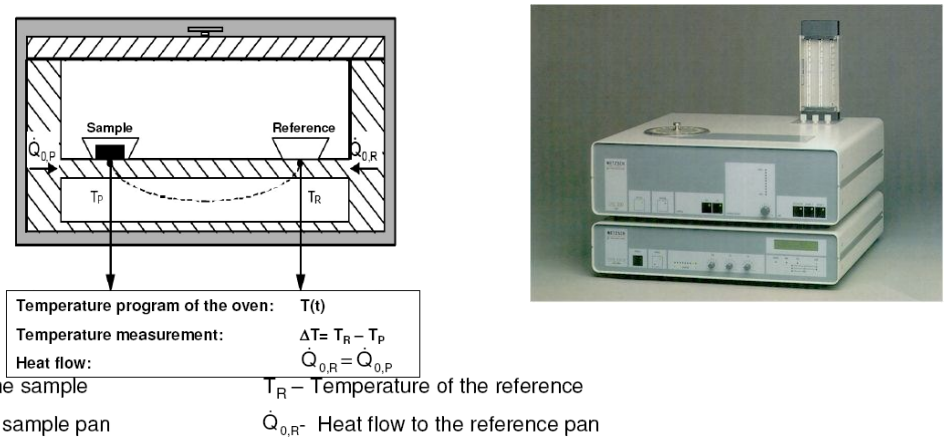

Figure 84: DSC measurement technique (left) and the photo of DSC 200 (right)

First, a temperature scan was performed using empty pans in both chambers to establish a baseline. A specimen of mass m is then loaded into one of the pans, and the

scan is repeated. If the heat capacities on the sample and the reference sides differ, the subsequent different heat flow causes temperature gradients at the sensor. Sensors record these gradients and measure thereby every difference in heat flows. The specific heat (C_p) is calculated from the difference in heat flow, ΔQ between the baseline and the specimen needed to change the temperature by an amount ΔT.

$$C_p = \frac{\Delta Q}{m \Delta T} \tag{146}$$

7.7.3 Experimental results

Figure 85 shows the measured specific heat (c_p) curve for PP HG313MO. The curve shows a typical cp-curve of the semi-crystalline polymer. The calculated crystallization melt peek enthalpy (ΔH) is 95.86 J/g [32].

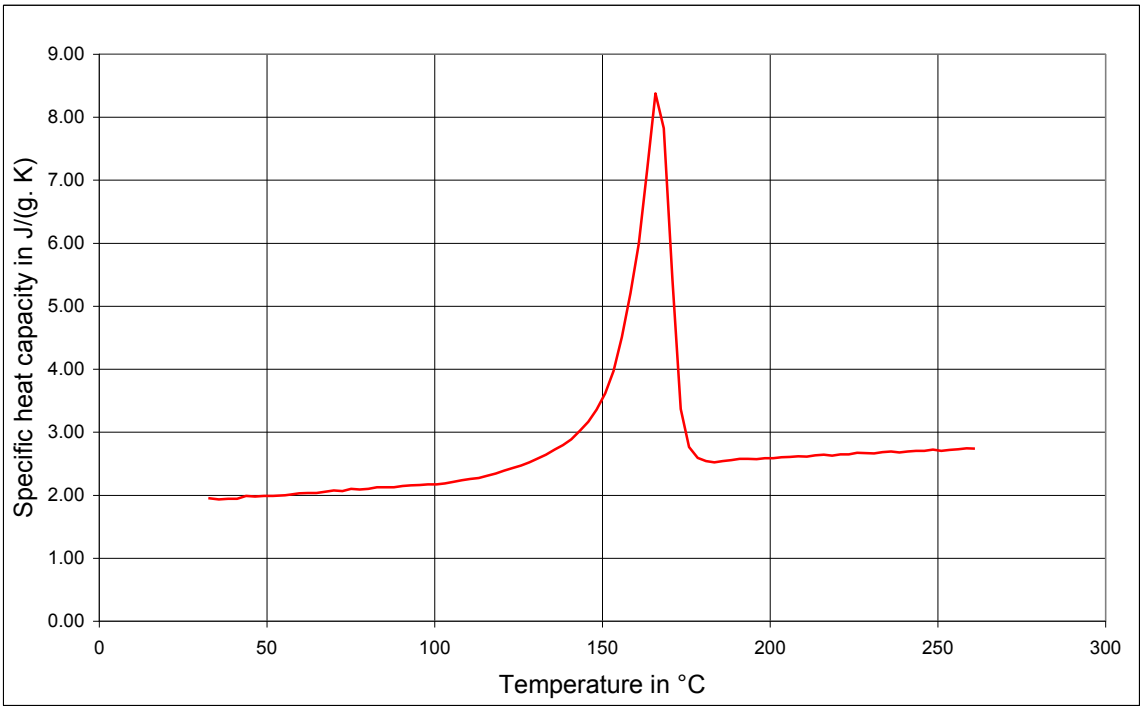

Figure 85: Specific heat capacity of PP HG313MO.

Figure 86 and 87 shows the measured c_p-curve for PS 495F and Bayblend T65. The cures represent the typical amorphous polymers with a stepwise increase in c_p value at the glass transition range. The c_p-curve of Bayblend T65 shows two stepwise increments, which correspond to the T_g of SAN and T_g of PC materials.

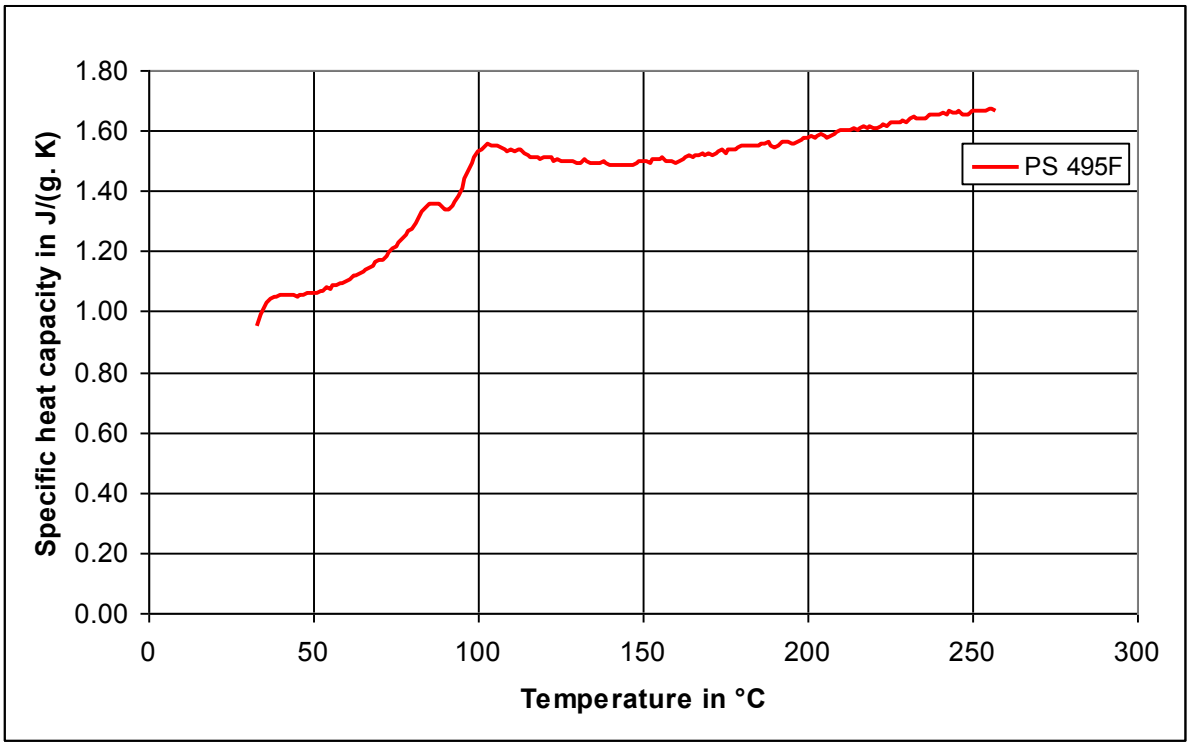

Figure 86: Specific heat capacity of PS 495F.

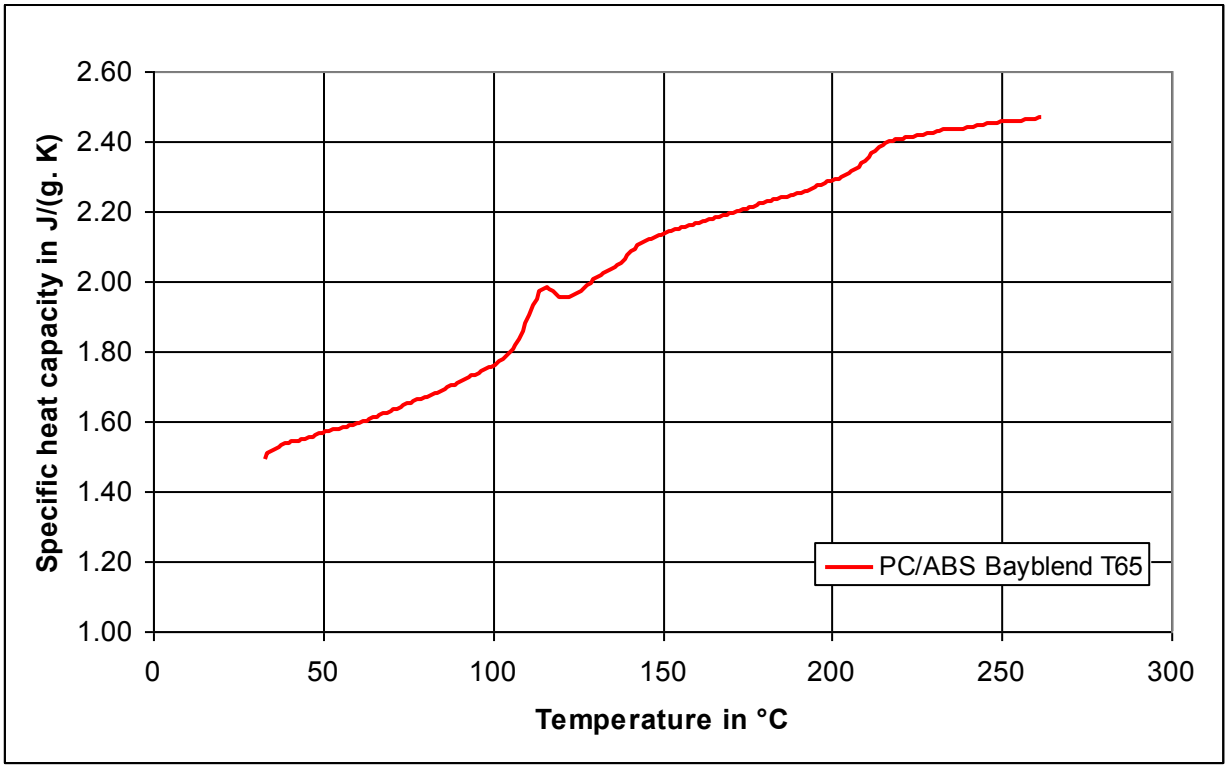

Figure 87: Specific heat capacity of Bayblend T65.

8 Simulation for a model thin-wall part

The developed calculation procedure and the simulation software are explained in the previous chapters (see chapters 5 and 6). The improved material data which is discussed in the previous chapter such as viscosity data, pvT-data, thermal conductivity data and specific heat values for all chosen thermoplastics were integrated into the material database of the simulation software *Xmeltsoft V.1.0*. A model thin-wall part was chosen for the expansion injection moulding process. In order to verify the applicability of the developed calculation model for the practical application of the expansion injection moulding simulation, the simulation was done for the chosen model thin-wall part using the simulation software. The chosen thin-walled part is the check-card, which has a rectangular form with the part wall thickness of 0.5mm (figure 88). The dimension of the check card part is 84 x 54 x 0.5 mm and the part volume is 2.29 cm^3. ENGEL Austria GmbH, Schwertberg, Austria, provided the check-card mould.

Figure 88: Engel check card part with a wall thickness of 0.5 mm.

The necessary material data for the simulation are the isobaric pvT-diagram, the compressibility of the melt, the shear viscosity as a function of temperature and pressure, the thermal conductivity as a function of temperature, the No-flow temperature and the specific heat capacity as a function of temperature. The important process parameters for the simulation are the chosen melt temperature, the mould wall temperature, and the total volume of the melt in the screw antechamber as well as in the hot runner nozzle. The simulations were carried out for three thermoplastic materials such PP HG313MO and PS 495F. The chosen parameters and the simulation results for above mentioned thermoplastic materials are explained below.

8.1 Simulation of the check-card part for PP HG313MO

For PP HG313MO material, the expansion injection moulding simulation was carried out for calculating the needed compression pressure (p_c) for the chosen mass of the melt cushion (m_0). The simulation was performed for the check-card part with the part

volume of 2.29 cm^3. The check-card part has maximum flow length of 73 mm from its injection point. The total flow length is divided into 7 segments for the minimum filling pressure calculation Figure 89 shows the part dimension which is taken into account for the calculation of the minimum filling pressure (p_E). Table 13 shows the each segment details and its corresponding segmental volume.

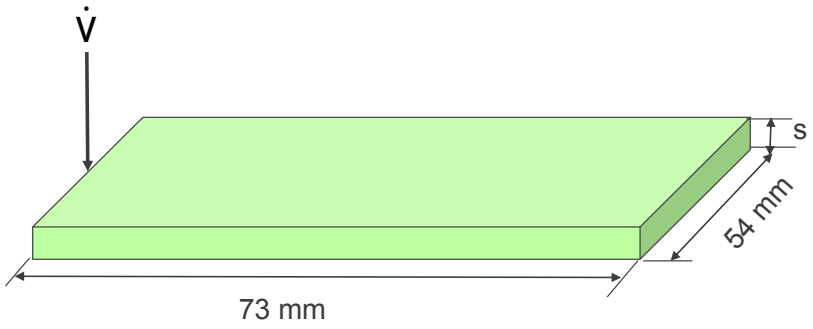

Figure 89: Part dimension taken into consideration for the segmentation.

Table 13 shows the each segment details and its corresponding segmental volume. The total specific part volume is 1.91 cm^3. As discussed earlier, the part is segmented into seven small segments with a serial connection. The total required filling pressure is the sum of the pressure drops at all segments. For the calculation of pressure drop at each segment, the effect of frozen skin layer thickness and change in melt viscosity due to temperature changes are taken into account.

Table 13: Segmental details for the calculation of pressure drop

7 Segments H = 0.5 mm; B = 54 mm	I	L_1 =10 mm	V_1 = 0.27 cm^3
	II	L_2 =10 mm	V_2 = 0.27 cm^3
	III	L_3 =10 mm	V_3 = 0.27 cm^3
	IV	L_4 =10 mm	V_4 = 0.27 cm^3
	V	L_5 =10 mm	V_5 = 0.27 cm^3
	VI	L_6 =10 mm	V_6 = 0.27 cm^3
	VII	L_7 =13 mm	V_7 = 0.351 cm^3
			V_{total} = 1.97 cm^3

The chosen process parameters for the simulation check-card part with PP HG313MO are shown in table 14.

Table 14: Chosen process parameters for PP HG313MO

Chosen process parameters for PP HG313MO	
Melt temperature	230 °C
Mould wall temperature	30 °C
No-Flow Temperature	120 °C
Part volume	2.29 cm^3
Part mass	2.05 g
Chosen volume of the melt	120.56 cm^3
Mass of the melt cushion (m_0)	97.26 g
Total number of cavities	Single cavity
Needed shot weight (m)	2.05 g

The simulation was performed with the help of *Xmeltsoft*. Figure 90 shows the calculated frozen skin layer thickness distribution along the flow length. The calculated maximum frozen skin layer thickness is 0.045 mm. Figure 91 shows the comparison of the calculated pressure drops along the flow length with and without taking into account the frozen skin layer distribution. Taking the frozen skin layer into account the calculated filling pressure is significantly higher than the calculated pressure value when neglecting the frozen skin layer. The calculated filling pressure was taken as an end pressure. Then the calculation of the needed compression pressure was carried out for the chosen mass of the melt cushion. The results of the simulation are shown in table 15.

The calculated minimum required filling pressure is 595 bar, which is taken as the end pressure for the calculation of maximum compression pressure. The calculated compression pressure is 828 bar. The calculated approximated filling time after the iterative calculation is 0.041 s.

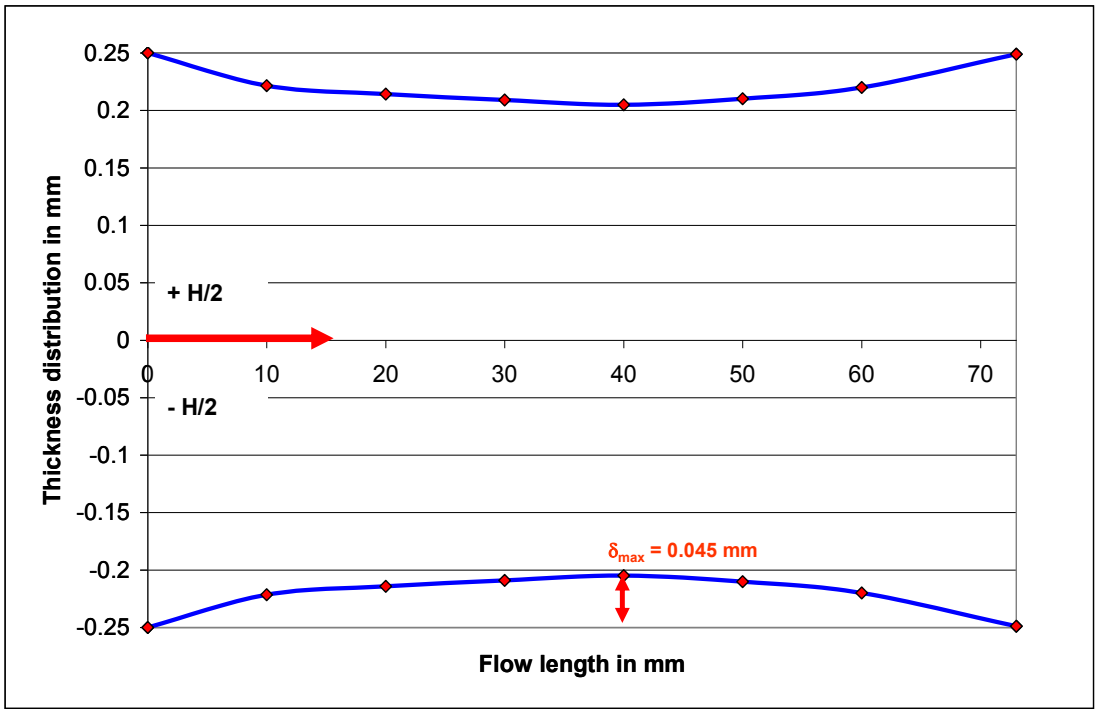

Figure 90: Calculated frozen skin layer thickness distribution for PP HG313MO.

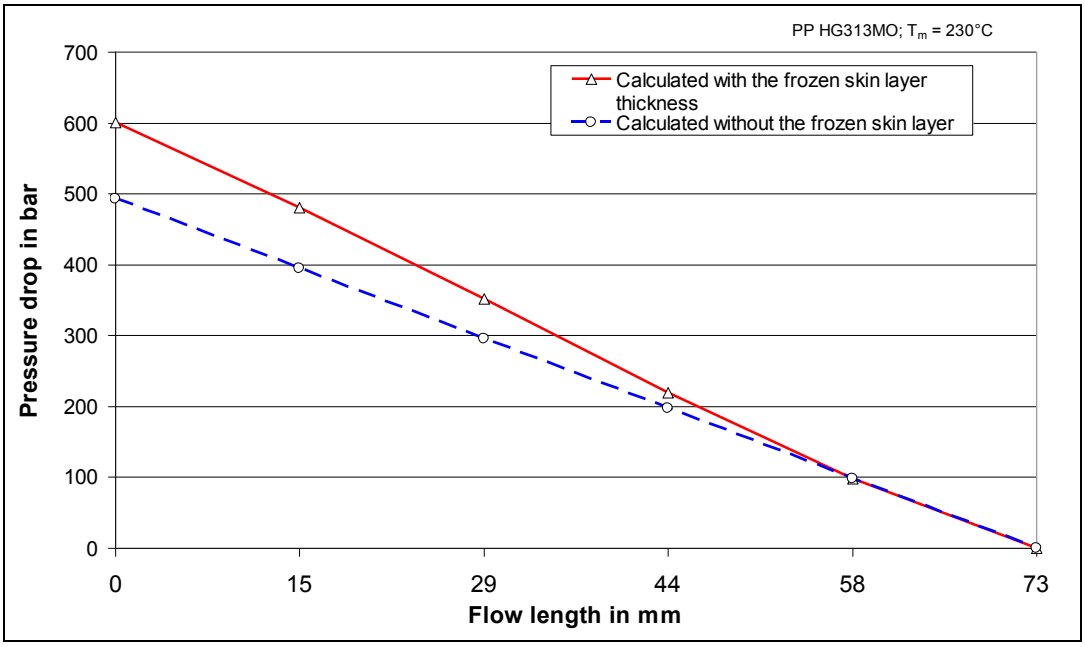

Figure 91: Calculated pressure drop values along the flow length of the check card part.

Table 15: Simulation results for PP HG313MO

Approximated filling time	0.041	s
Calculated end pressure (p_E)	600	bar
Calculated compression pressure (p_c)	828	bar

The pressure drop in the injection unit as a function of time after opening the shut-off nozzle was simulated according to the equation 95. During the expansion process, the melt pressure in the screw antechamber drops from the compression pressure value of 828 bar to the end pressure value of 600 bar. The time constant (k') represents how fast this curve comes to the end pressure value. With the filling time of 0.042 s, the calculated time constant value is 37.72 s^{-1}.

The volumetric flow with the shut-off nozzle closed is zero and grows constantly during the time until the needle valve open completely. Steinbichler et al. [5] informed that the complete opening of the needled valve takes about 5 to 10 ms. For the optimum mass flow rate calculation, we have to account the needle valve opening time in the pressure drop prediction. For the current simulation, we account the needle valve opening time of about 8 ms. Figure 92 shows the simulated pressure drop profile in front of the screw for PP HG 313MO.

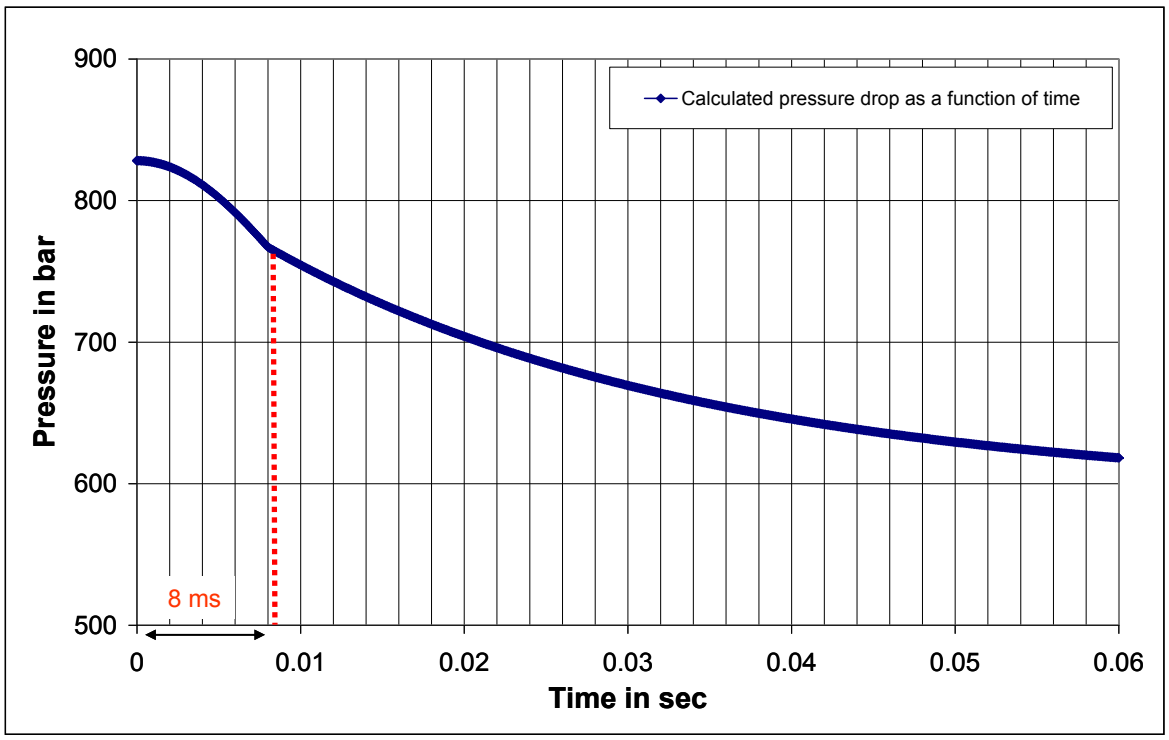

Figure 92: The pressure profile during the expansion calculated for PP HG313MO.

As shown in figure 92, the slop of pressure drop curve has two different regions. Up to 8 ms the pressure drop is very moderate. After that, the pressure drop is very fast and finally it reaches the end pressure value. During the calculation of the pressure drop as a function time, the time constant value is increasing from 0 to 37.72 s^{-1} till the time limit reaches the value of 8 ms. Then the time constant is kept at constant value till time limit reaches the filling time. Figure 93 shows calculated mass flow rate as a function of time.

The generated mass flow rate increases from zero to the maximum value until the complete opening of the needle value. After the complete opening, the mass flow rate

drops from its maximum value to an end value until the pressure equalisation takes place when the cavity is full or the shut-off nozzle is closed.

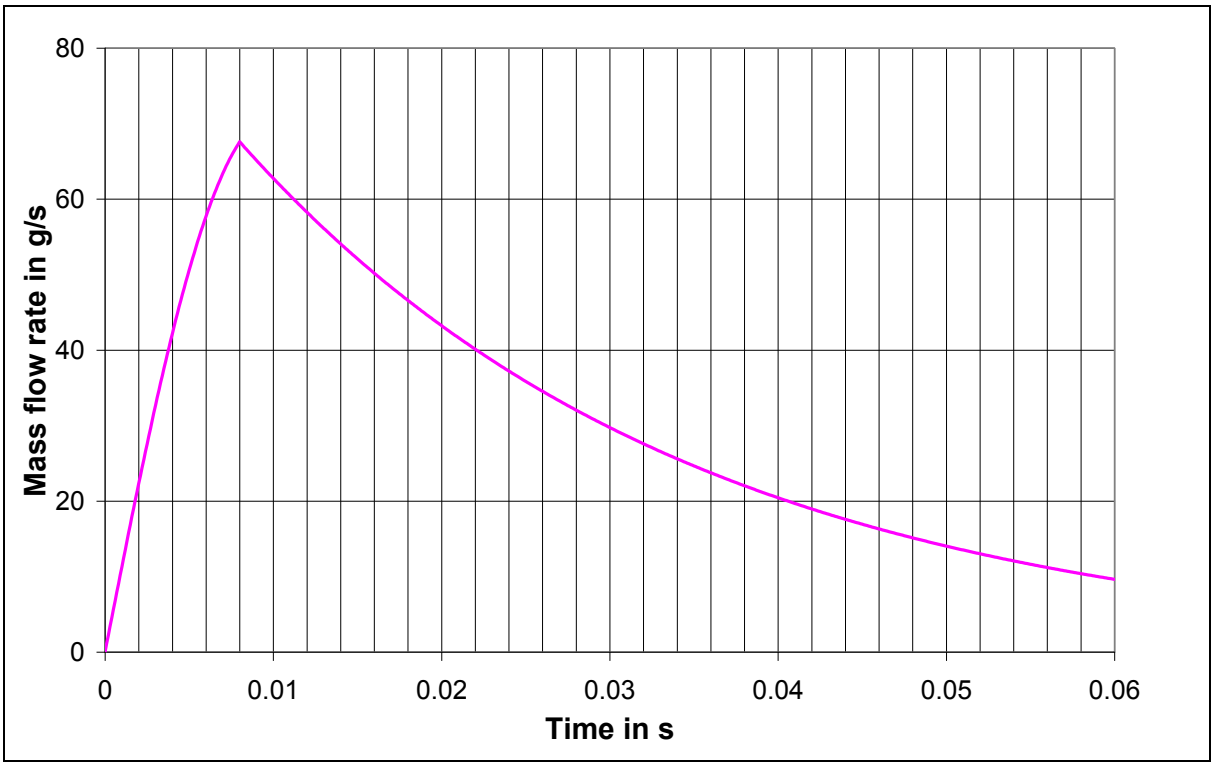

Figure 93: Calculated mass flow rate as a function of time for PP HG313MO.

The simulation result of PP HG313MO is verified experimentally by producing the check-card parts with pre-calculated compression pressure and the chosen process parameters on the injection moulding machine. The comparison of simulation result with the experimental result will be discussed in the next chapter.

8.2 Simulation of the check-card part for PS 495F

For PS 495F material, the simulation was performed in the same manner as of PP HG313MO material. The check-card part was segmented into seven segments as mentioned in table 13. Table 16 shows the chosen process parameters for PS 495F.

Table 16: Chosen process parameters for PS 495F

Chosen process parameters for PS 495F	
Melt temperature	230 °C
Mould wall temperature	40 °C
No-Flow Temperature	140 °C
Part volume	2.29 cm^3
Part mass	2.38 g
Chosen volume of the melt	120.56 cm^3
Mass of the melt cushion (m_0)	121.52 g
Total number of cavities	Single cavity
Needed shot weight (m)	2.38 g

Figure 94 shows the calculated frozen skin layer thickness distribution along the flow length. The calculated maximum frozen skin layer thickness is 0.057 mm. The Investigated PS 495F shows a thicker frozen skin layer distribution in comparison with PP HG313MO. For the semi-crystalline material, the formation of frozen skin layer is hindered by the heat fusion due to the crystallization effects. Figure 95 shows the comparison of the calculated pressure drops along the flow length with and without taking into account the frozen skin layer distribution. The results of the simulation are shown in table 17.

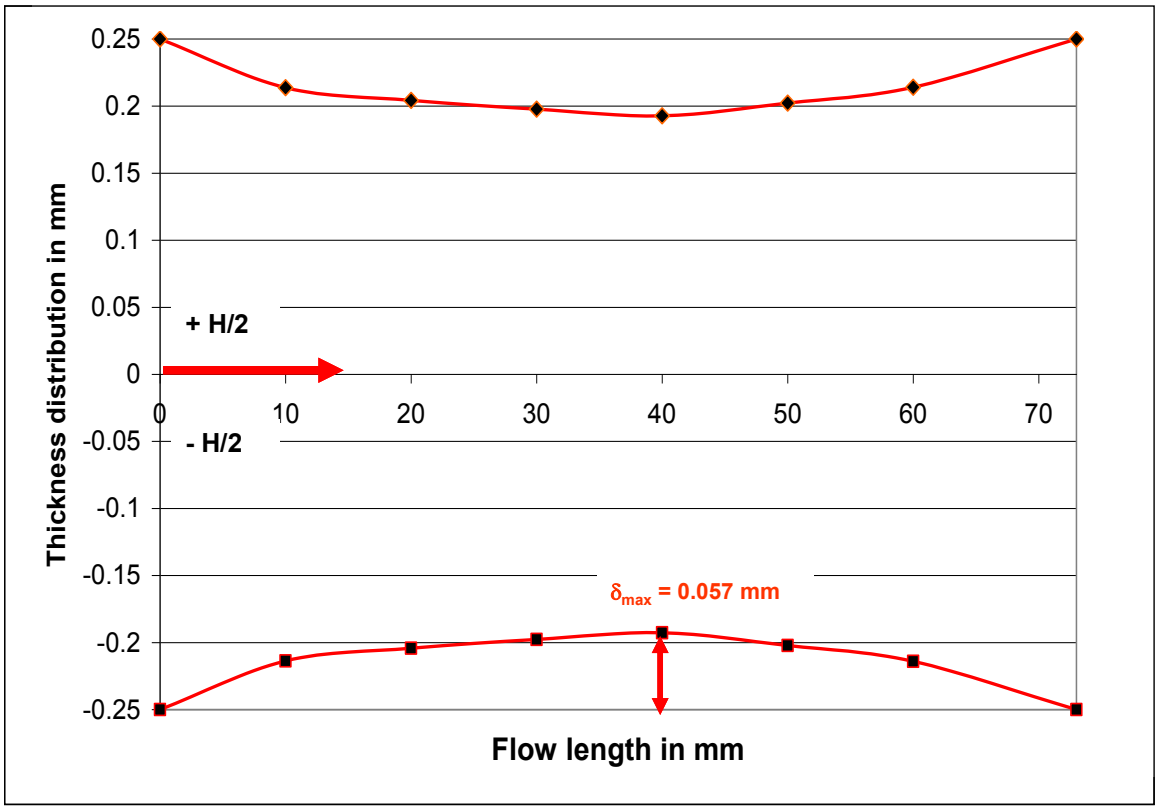

Figure 94: Calculated frozen skin layer thickness distribution for PS 495F.

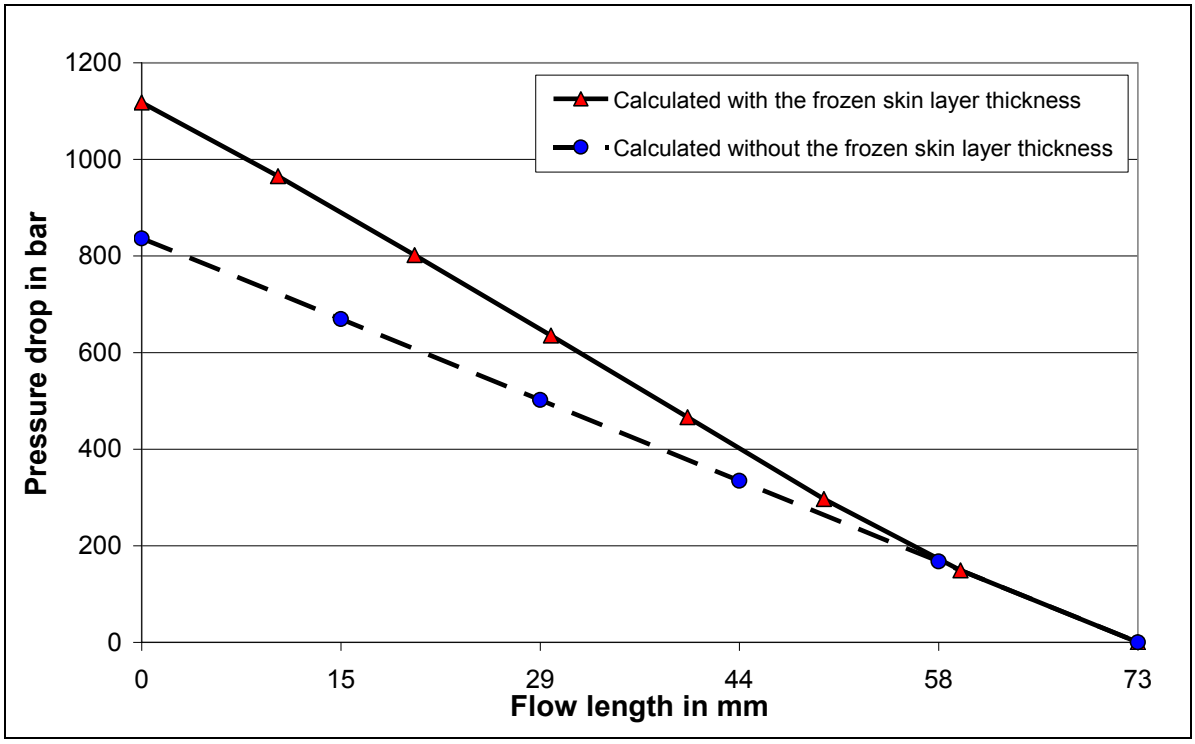

Figure 95: Calculated pressure drop values along the flow length of the check card part calculated for PS 495F.

Table 17: Simulation results for PS 495F

Approximated filling time	0.045	s
Calculated end pressure (p_E)	1118	bar
Calculated compression pressure (p_c)	1590	bar

During the expansion process, the melt pressure in the screw antechamber drops from the compression pressure value of 1590 bar to the end pressure value of 1118 bar (Figure 96). With the filling time of 0.045 s, the calculated time constant value is 65.27 s^{-1}. Figure 97 shows calculated mass flow rate as a function of time.

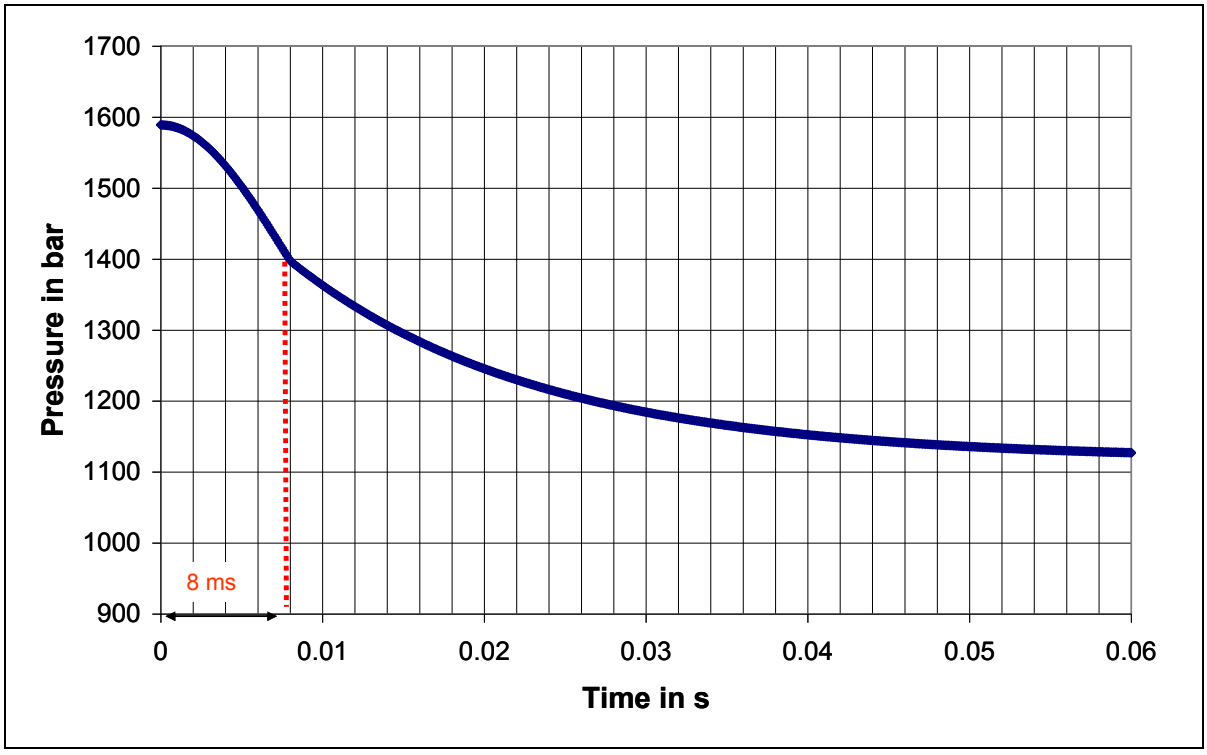

Figure 96: The pressure profile during the expansion calculated for PS 495F.

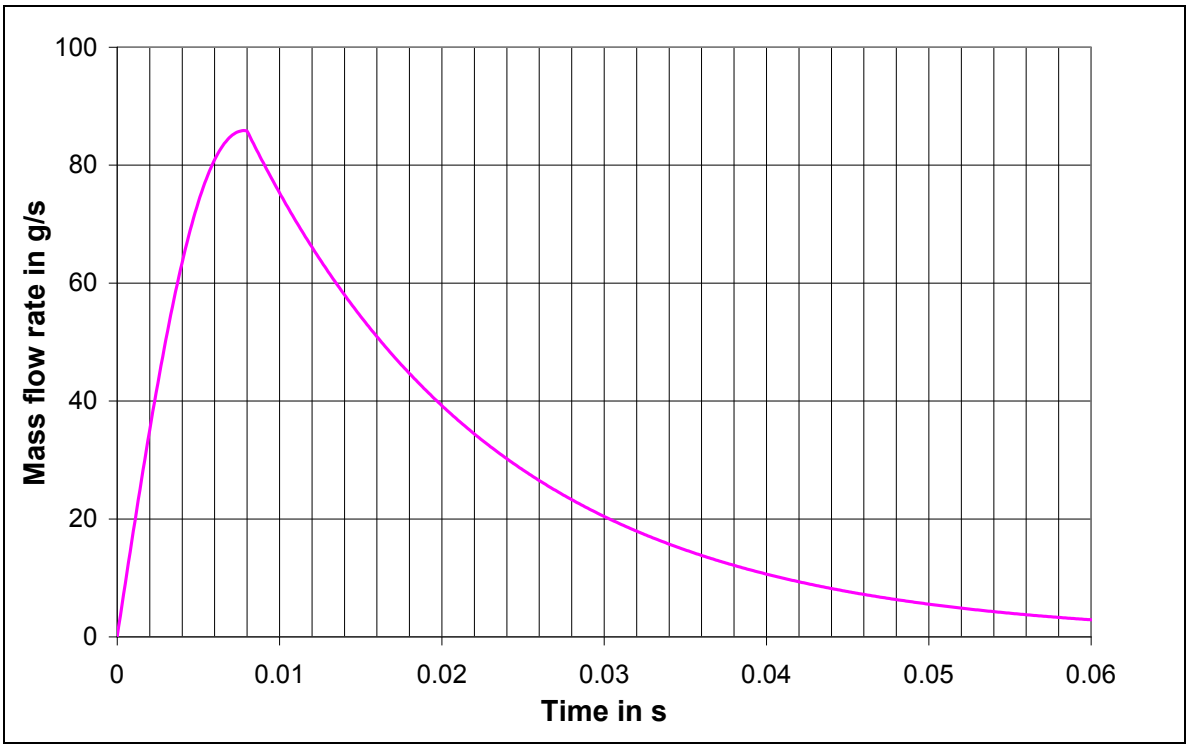

Figure 97: Calculated mass flow rate as a function of time calculated for PS 495F.

8.3 Simulation of the check-card part for Bayblend T65

For Bayblend T65 material, the simulation was performed in the same manner as of PP HG313MO and PS 495F material. The check-card part was segmented into seven segments as mentioned in table 13. Table 18 shows the chosen process parameters for Bayblend T65.

Table 18: Chosen process parameter for Bayblend T65

Chosen process parameters for ABS/PC Bayblend T65	
Melt temperature	260 °C
Mould wall temperature	80 °C
No-Flow Temperature	165 °C
Part volume	2.29 cm^3
Part mass	2.58 g
Chosen volume of the melt	120.56 cm^3
Mass of the melt cushion (m_0)	133.07 g
Total number of cavities	Single cavity
Needed shot weight (m)	2.58 g

Figure 98 shows the calculated frozen skin layer thickness distribution along the flow length. The calculated maximum frozen skin layer thickness is 0.050 mm. Figure 99 shows the comparison of the calculated pressure drops along the flow length with and without taking into account the frozen skin layer distribution. The calculated required minimum filling pressure with the account of the frozen layer is 1558 bar, which is higher than the calculated pressure without the influence of the frozen skin layer. The viscosity of the ABS/PC is relatively higher than the PS 495F and the PP HG313MO, so the formation frozen skin layer increases the flow resistance and thus it requires higher filling pressure. The results of the simulation are shown in table 19.

Table 19: Simulation results for Bayblend T65

Approximated filling time	0.087 s
Calculated end pressure (p_E)	1558 bar
Calculated compression pressure (p_c)	2815 bar

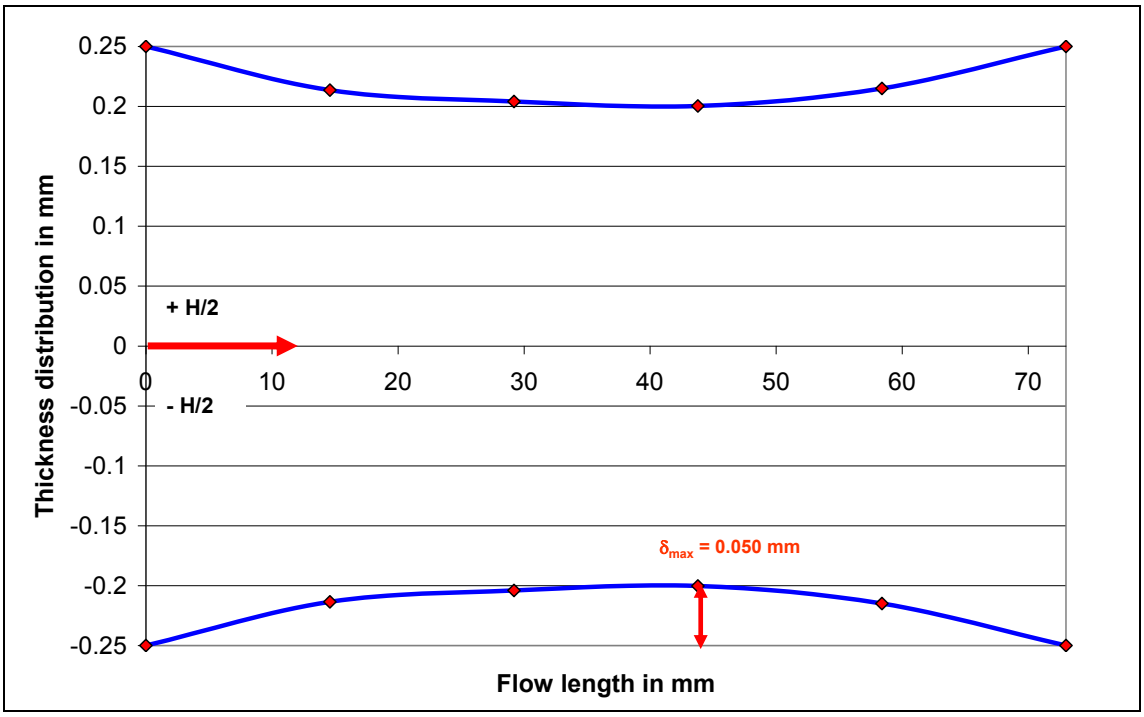

Figure 98: Calculated frozen skin layer thickness distribution for Bayblend T65.

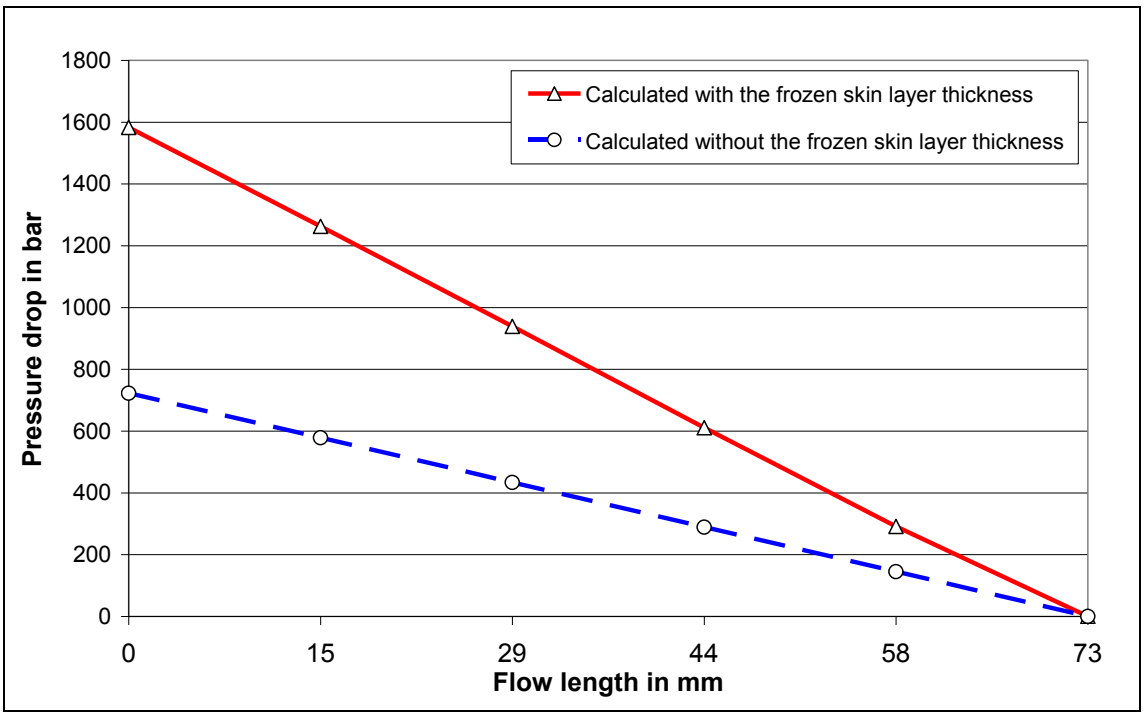

Figure 99: Calculated pressure drop values along the flow length of the check card part calculated for Bayblend T65.

During the expansion process, the melt pressure in the screw antechamber drops from the compression pressure value of 2815 bar to the end pressure value of 1558 bar (Figure 100). With the filling time of 0.087 s, the calculated time constant value is 30 s^{-1}. Figure 101 shows calculated mass flow rate as a function of time.

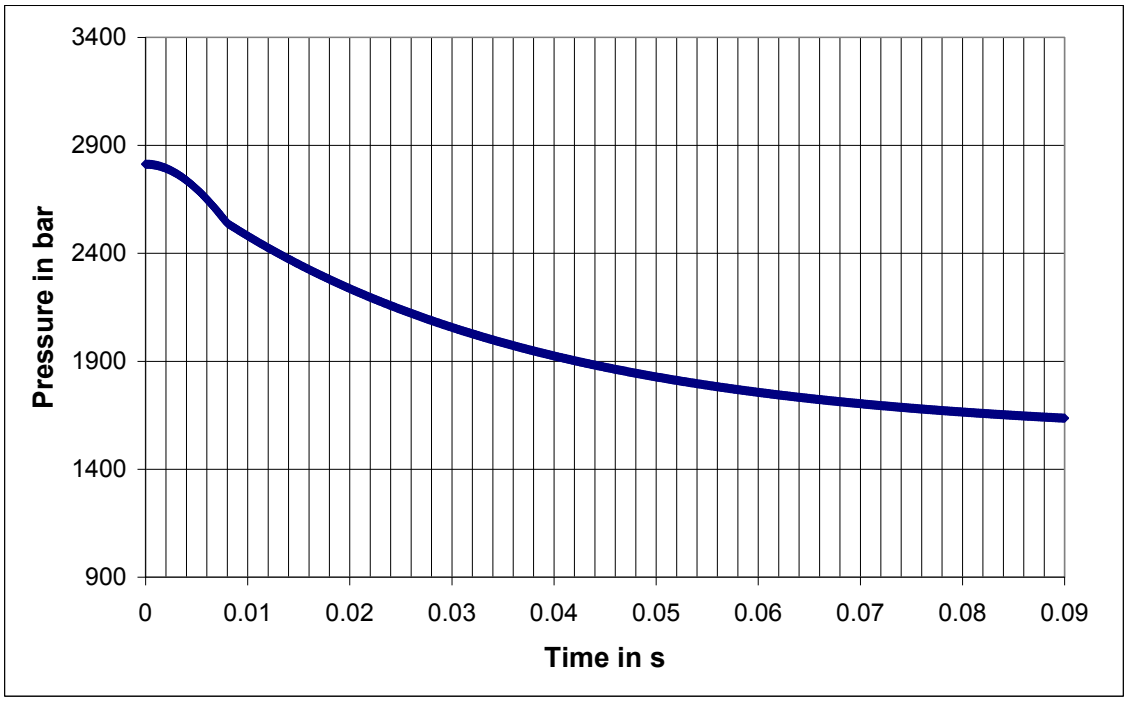

Figure 100: The pressure profile during the expansion calculated for Bayblend T65.

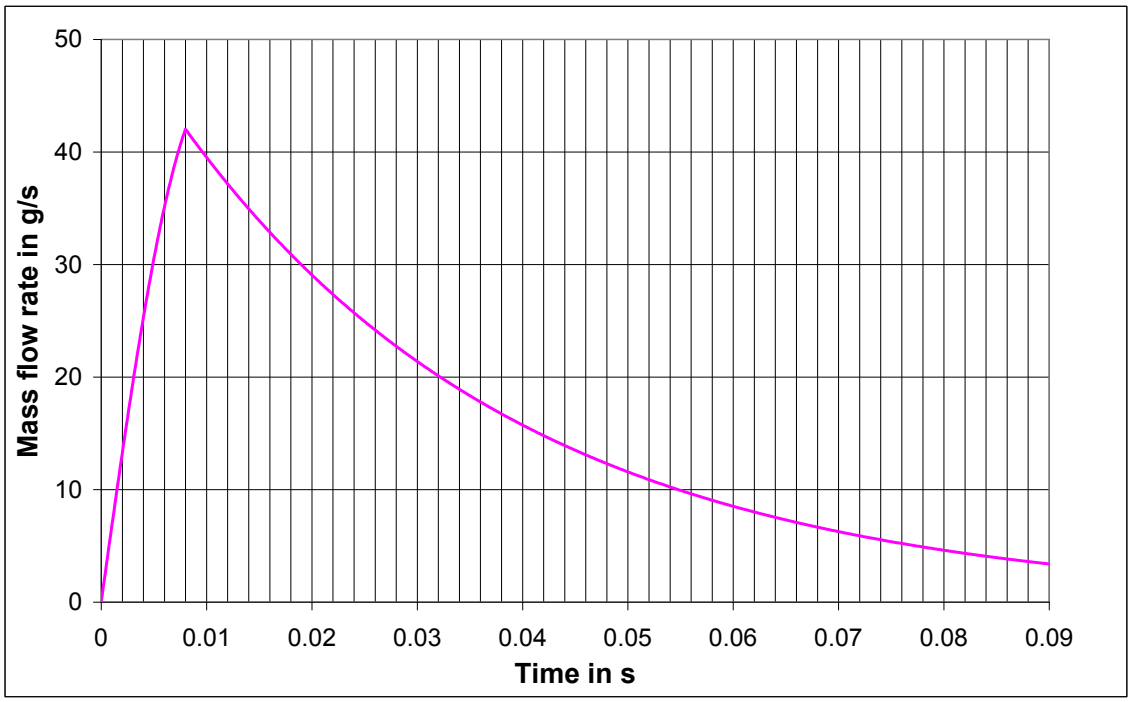

Figure 101: Calculated mass flow rate as a function of time calculated for Bayblend T65.

9 Systematic expansion injection moulding experiments

In order to verify the simulation results, the experiments were carried out on the injection moulding machine with the help of the check-card mould. The main objects of the experimental works were to verify the simulation results and analyse the influence of the process parameters such as compression pressure, melt temperature, volume of the compressed melt and melt residence time on the final quality of the expansion injection moulded parts. For that purpose, ENGEL Austria GmbH had provided a hybrid injection moulding machine and the check-card mould. The expansion injection moulding experiments were carried out for the chosen three thermoplastic materials such as PP HG313MO, PS 495F and ABS/PC Bayblend T65.

9.1 Experimental setup

9.1.1 Injection moulding machine

The injection moulding machine used was a hybrid injection moulding machine (figure 102) type Engel VC 940/130 with a clamping force of 1300 kN. The injection moulding machine has the electrical injection unit and hydraulic clamping system. With the electrical injection unit, the screw can be placed in any desired axial position and be kept at precisely this position even with high pressures. The injection screw diameter of 50 mm was used. The maximum achievable specific injection pressure is 2400 bar [83]. The maximum possible swept volume is 432 cm^3. The melt pressure and temperature in front of the screw are measured with the pressure transducer and infrared temperature sensor mounted at the measuring flange just before injection nozzle. The pressure transducer used at the measuring flange has the pressure measurement limit of 1800 bar. The special X-melt program is integrated in the machine control unit of the ENGEL CC200, which is the machine control program.

Figure 102: Injection moulding machine ENGEL VC 940/130

9.1.2 Check card mould

The check card mould is a two plate single cavity mould with a hot runner shut-off nozzle. The volume of the hot runner nozzle is 13.5 cm^3. The needle of the hot runner shut-off nozzle is operated by pneumatic control. The gate type is a pin-point type gate. The mould has two cavity pressure transducers (type Kistler 6157B) with the pressure measurement range of 2000 bar. The two cavity pressure transducers are placed 52 mm apart from each other. The ejection of the moulded part is achieved by compressed air. Figure 103 shows the photographic view of the experimental setup and the mould halves.

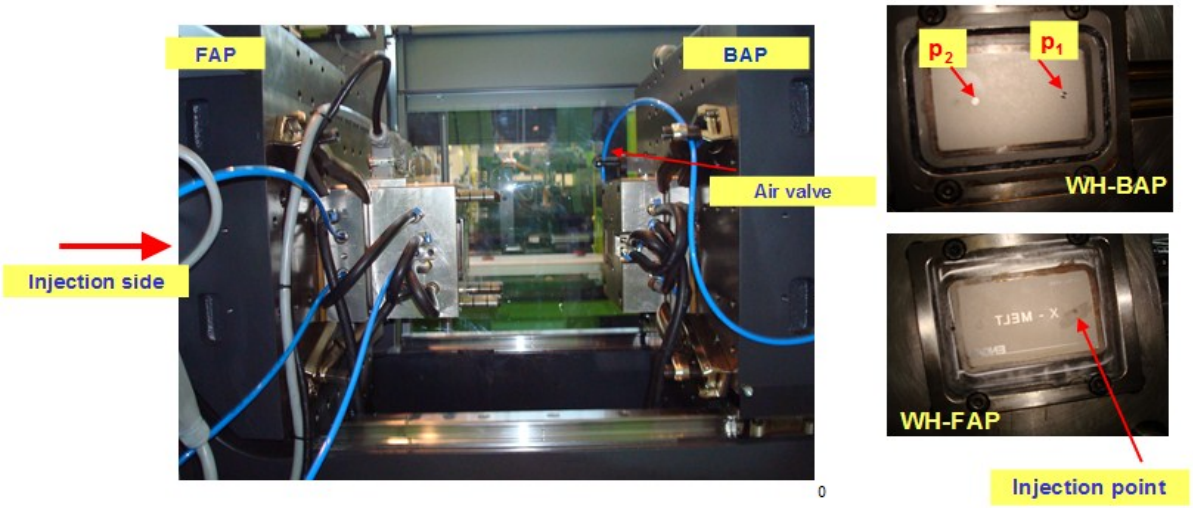

Figure 103: Experimental setup of the check card mould mounted on ENGEL VC 940/130 (Left) and mould halves of check card mould (right); FAP fixed mould half, BAP movable mould half.

9.1.3 Experimental procedure

The expansion injection moulding process cycle is shown in figure 104. At first, the mould halves are closed and the pre-set clamping force is built up. After the injection nozzle attains its pre-set contact pressure, the compression phase starts. In the compression phase, the screw moves in axial direction until the melt pressure reaches the pre-set compression pressure. Once the maximum pre-compression pressure is reached, the machine tries to regulate the pressure until the end of the compression time. At the end of the compression time, the hot runner shut-off nozzle opens for the expansion of the compressed melt. During the expansion phase, the melt pressure in the screw antechamber drops from maximum compression pressure to the end pressure, which acts as the holding pressure. The compressed melt is allowed to expand until the needle valve is open. The duration of the needle valve opening can be set in the machine control unit. Afterwards the metering stroke starts with the backward movement of the screw. At the end of the cooling phase, the mould halves open and the moulded part is ejected from the mould by compressed air.

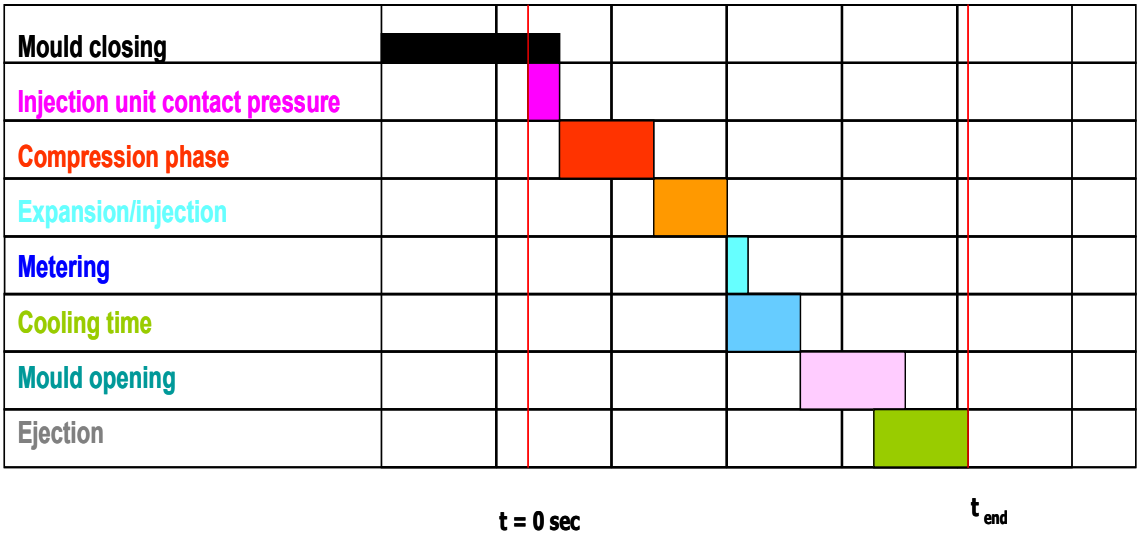

Figure 104: The expansion injection moulding process cycle

Figure 105 shows the typical pressure profile in the screw antechamber during the complete process cycle.

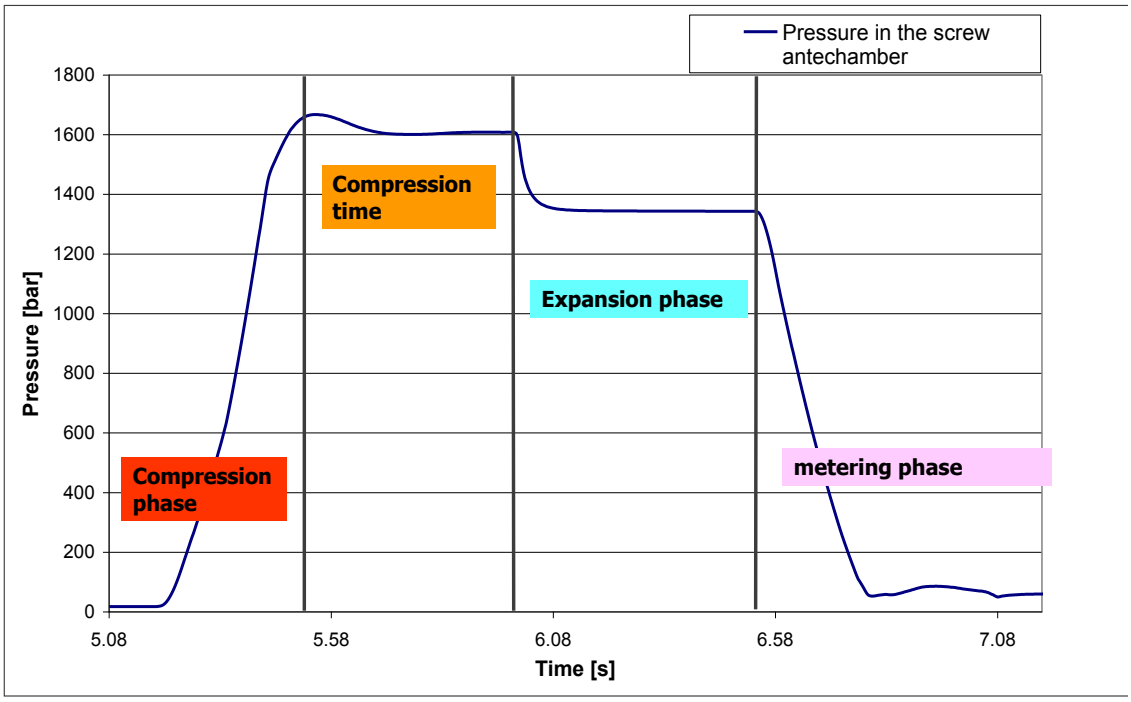

Figure 105: The pressure profile in the screw antechamber during complete process cycle.

9.2 Experimental results for PP HG313MO

9.2.1 Mould filling analysis

A mould filling analysis was carried out for check-card part with different compression pressure to find the required compression pressure for the optimum filling of part. The chosen compression pressures were 650 bar, 750 bar, 850 bar, 950 bar and 1150 bar [40]. The melt temperature chosen was 230°C and the mould wall temperature was kept at 30°C. The swept volume of about 80 cm^3 was metered in front of the screw. The total volume of the compressed melt is 120 cm^3. The chosen compression time was 0.5 s. The compression time was set in the machine control program in order to regulate the pre-set compression pressure before end of the compression phase. After the end of the compression phase, the needle valve of the hot runner nozzle was kept open for about 0.5 s. Subsequently the filled part is allowed to cool in the mould for about 3 sec before the part ejection. Figure 106 shows the produced check-card parts with different compression pressures for the investigated PP HG313MO. The unfilled parts were produced with the pre-compression pressure range up to 750 bar. The optimum part filling was found with the pre- compression pressure of 850 bar.

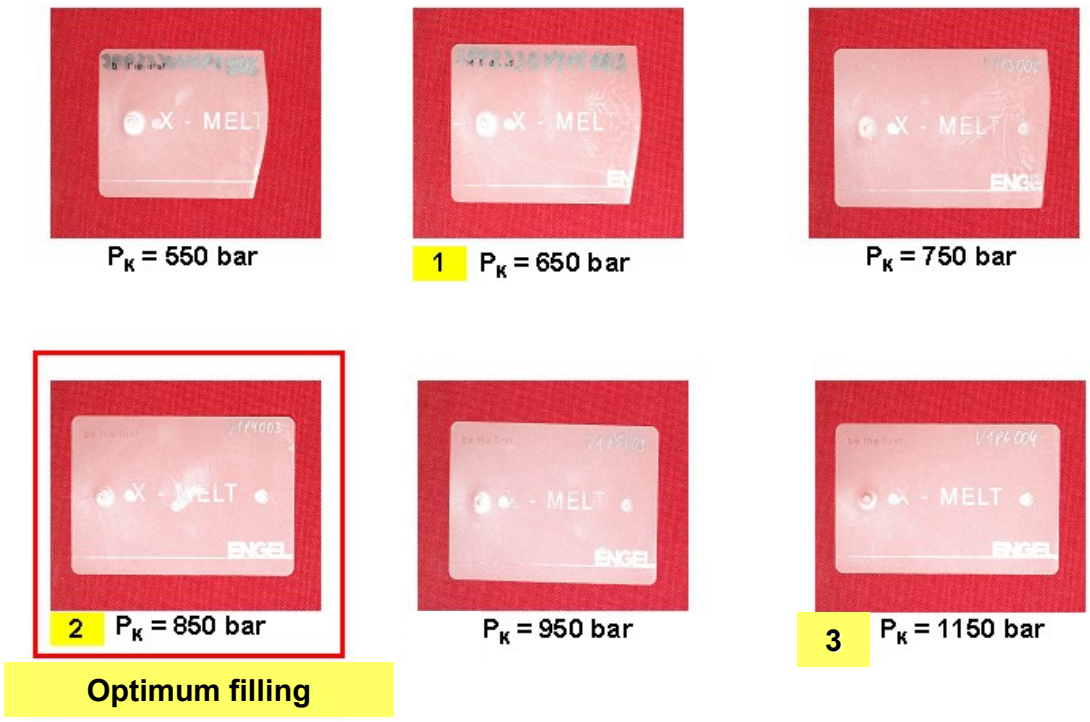

Figure 106: Photos of the produced check-card parts at different compression pressures.

The detail experimental results of the filling analyses with pre-compression pressures of 650 bar, 850 bar and 1150 bar are discussed below. The check-card parts produced at these three conditions are marked as 1, 2 and 3 in figure 106. Figure 107 shows the measured pressure profile at the screw antechamber, the screw position, and measured cavity pressures near and far from the injection point for the filling analysis done with pre-compression pressure of 650 bar.

As shown in figure 107, at the end of the compression phase the melt pressure in front of the screw reaches the pressure value of 635 bar. By opening the needle valve of the hot runner nozzle, the compressed melt is allowed to expand. The needle valve of the hot runner nozzle was kept open for about 0.5 s. During the expansion phase, the melt pressure in front of screw drops rapidly to the end pressure value of 530 bar. The end pressure remains constant until the shut-off nozzle of hot runner is closed. During the expansion phase, the screw position remains constant. The cavity pressure near the injection point increases to the maximum pressure value of about 350 bar before the needle valve is closed. The cavity pressure sensor located far from the injection point shows no cavity pressure reading. It clearly indicates us that the melt front is not reached the location of second pressure sensor. Figure 108 shows the measured melt temperature with the infrared (IR) temperature sensor at the screw antechamber during

the complete cycle. The melt temperature increases about 10.11°C during the compression.

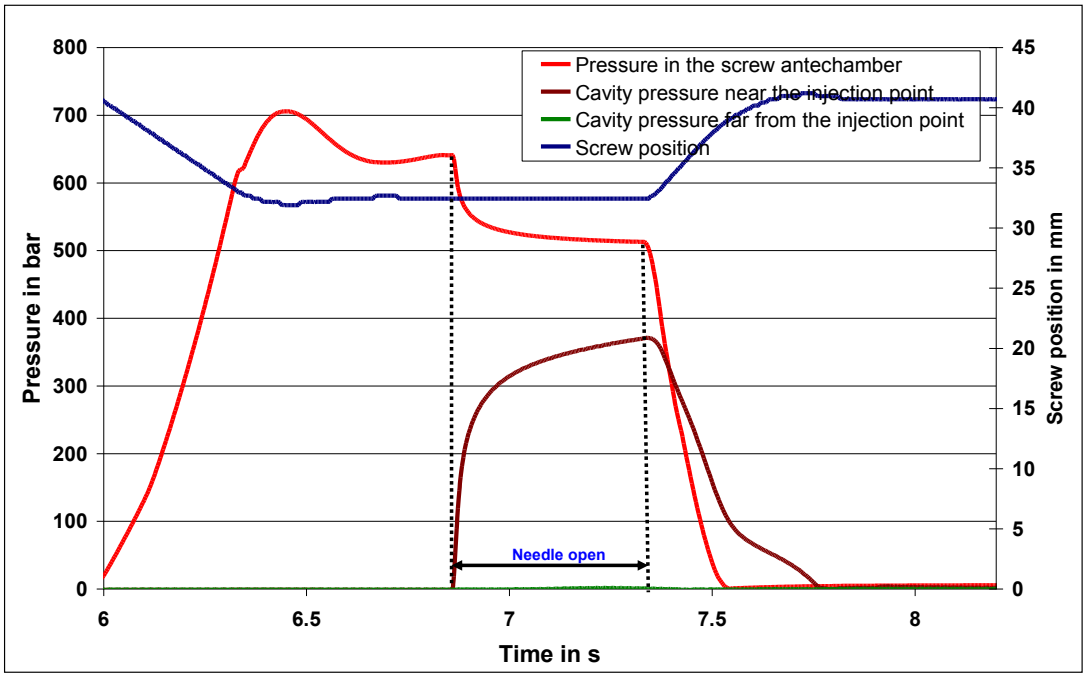

Figure 107: Measured pressures at the screw antechamber, in the cavity (near the injection point and far from the injection point) and the screw position during the complete cycle for PP HG313MO at 230°C with pre-compression pressure of 650 bar.

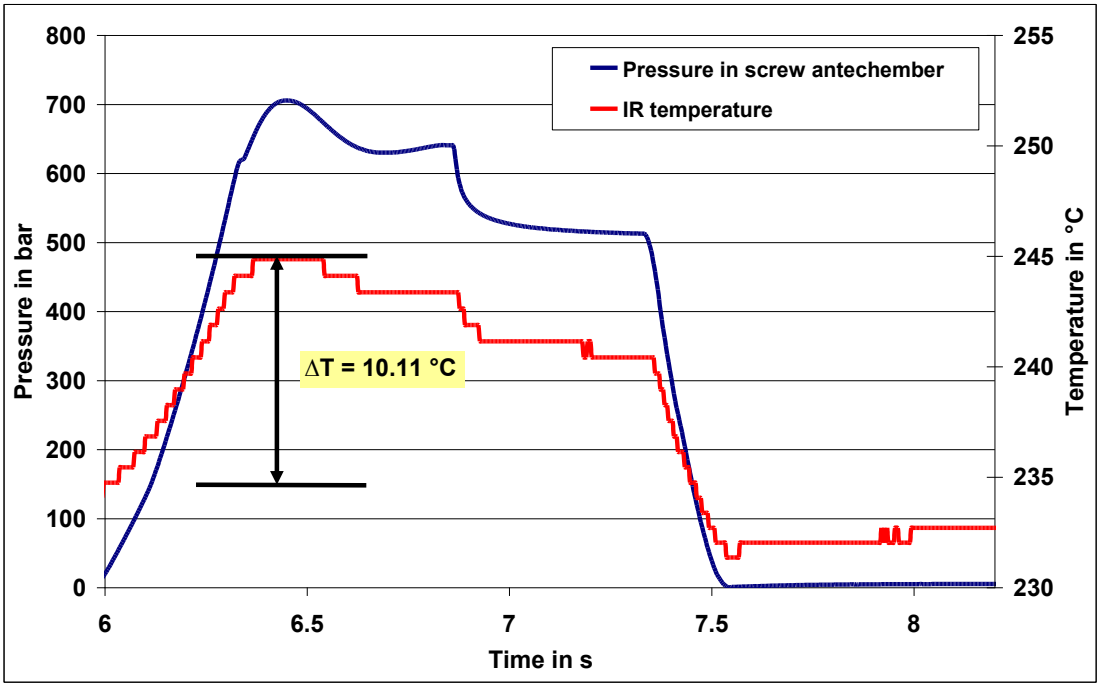

Figure 108: Measured melt pressure and IR temperature at the screw antechamber with 650 bar pre-compression pressure for PP HG313MO at 230°C

Figure 109 shows the measured pressure profile at the screw antechamber, the screw position, and measured cavity pressures near and far from the injection point for the filling analysis done with pre-compression pressure of 850 bar. By increasing the compression pressure from 650 bar to 850 bar produces a completely filled part. As shown in figure 109, the pressure at the screw antechamber remains at the pressure value of 837 bar at the end of the compression phase. After the needle valve opening, the pressure at the screw antechamber drops from the pressure value of 837 bar to the end pressure value of 650 bar. The cavity pressure near the injection point reaches the maximum value of 520 bar and the cavity pressure far from the injection point reaches the maximum value of 225 bar.

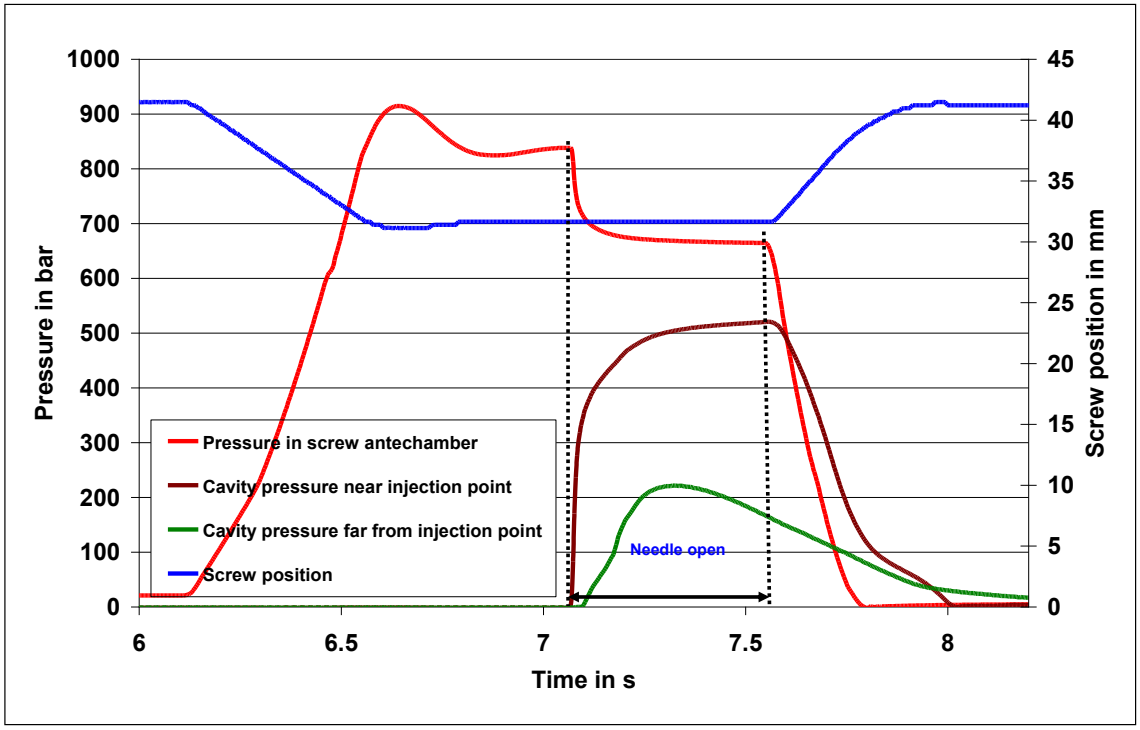

Figure 109: Measured pressures at the screw antechamber, in the cavity (near the injection point and far from the injection point) and the screw position during the complete cycle for PP HG313MO at 230°C with pre-compression pressure of 850 bar.

With the *"Xmeltsoft V.1.0"* simulation program, the calculated compression pressure for PP HG313MO was 828 bar (see chapter 8.1). The simulation result agrees well with the experimental results. The completely filled part is produced with the melt pre-compression of 850 bar. Figure 110 shows the measured melt temperature with the infrared (IR) temperature sensor at the screw antechamber during the complete process cycle. The melt temperature increases about 13.15°C during the melt compression. With the simulation program, the calculated compression heat under the adiabatic condition is 10.52°C.

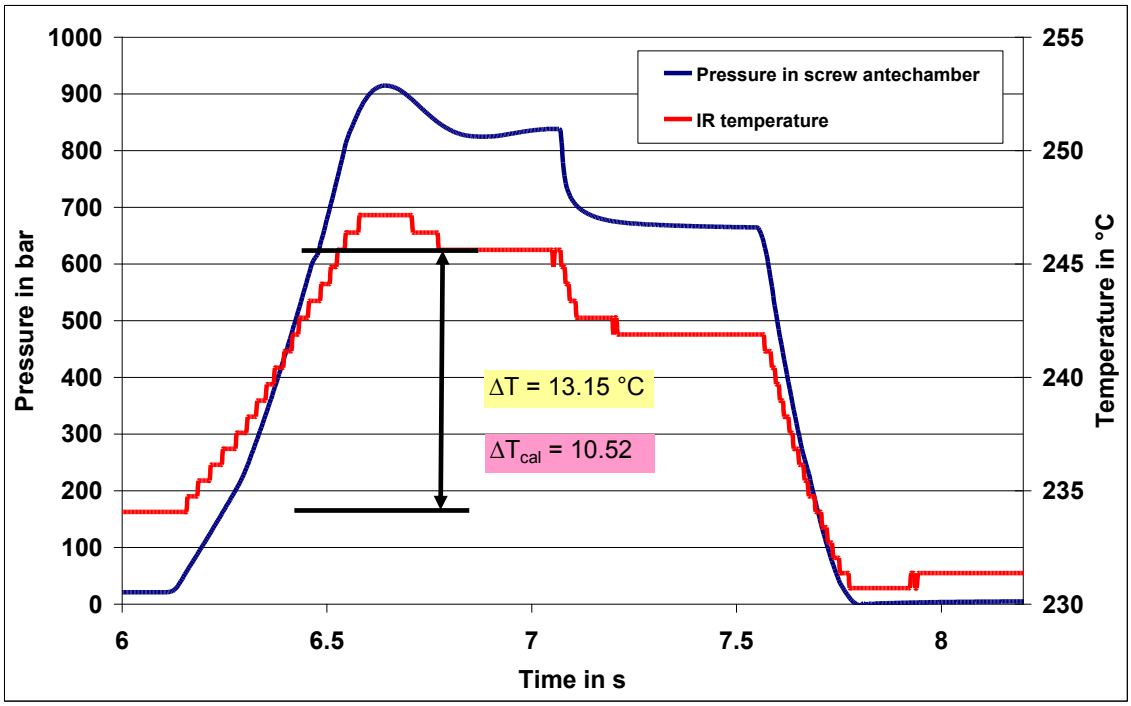

Figure 110: Measured melt pressure and IR temperature at the screw antechamber with 850 bar pre-compression pressure for PP HG313MO at 230°C

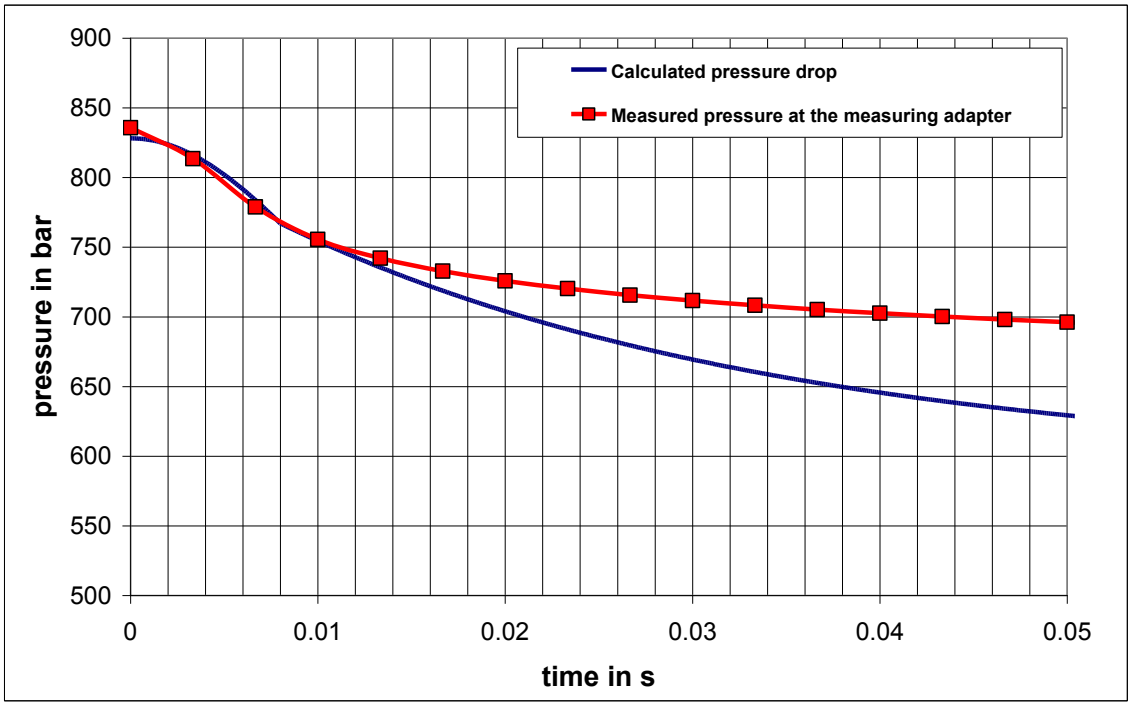

Figure 111: Comparison of the measured pressure drop in the screw antechamber with the calculated pressure drop for PP HG313MO with the compression pressure of 828 bar.

Figure 111 shows the comparison of the measured pressure profile at the screw antechamber during the expansion phase with the simulated pressure profile. In the

simulation, the pressure drop is calculated as a function of time by using the equation 147.

$$p(t) = (p_c - p_E) \cdot \exp(-k' \cdot t) + p_E \qquad (147)$$

In figure 111, at starting the calculated pressure drop is fitting well with the measured pressure drop, with time progress the both pressure profile curves deviate from one another. The simulated pressure as a function of time falls relatively faster than the measured pressure profile. Further, in figure 111 the measured pressure profile reaches the end pressure value of 690 bar, which is comparatively higher than the end pressure value reached in the simulated pressure profile. With the simulation, the calculated end pressure is 600 bar. In the simulation, the required end pressure (p_E) is calculated at the injection point of the cavity (marked with blue arrow mark in figure 112). During the measurement, the pressure drop is measured at the measuring adapter mounted before nozzle of the injection unit as shown in figure 112. Therefore, the end pressure reached at end of the expansion phase is measured at the location of the measuring adapter in the injection unit (marked with red arrow mark in figure 112). To calculate the exact pressure at the injection point, one has to account the pressure losses happened at the injection nozzle die and at the hot runner nozzle. The used check-card mould hot runner nozzle not has the pressure sensor to measure the pressure profile at the hot runner nozzle.

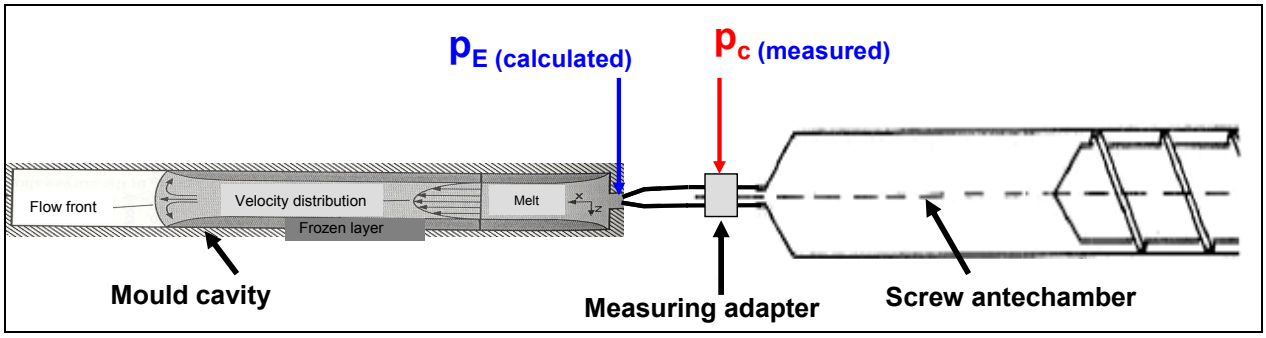

Figure 112: Schematic representation of the experimental system

Another important observation while comparing the measured and simulation pressure profiles is that the simulated pressure profile falls faster than the measured pressure profile with the forward time steps. One possible reason for this difference is that in the simulation, the time constant (k') is kept at a constant value during the entire expansion phase. In equation 147, the time constant (k') characterizes how fast the calculated pressure p(t) falls to the end pressure value. The equation 147 calculates the pressure drop occurs at injection unit when the melt is allowed to expand into a free volume i.e, the flow resistance is not taken into account. Nevertheless, in reality the melt flow resistance is increasing with the time progress. In order to account this effect in the

calculation, one has to change the time constant value as a function of time during the mould filling phase.

By calculating the die conductance (k_{die}), one can define the flow resistance depends on the flow geometry. The die conductance (k_{die}) for a rectangular geometry is calculated by equation 148.

$$k_{die} = \frac{B \cdot S^{m+2}}{2^{m+2} \cdot (m+2) \cdot L^{m}} \tag{148}$$

where:

S wall thickness (m)

B width (m)

L length (m)

m flow exponent of the power law viscosity model as in equation 149

$$\tau^{m} = \left(\frac{1}{\phi}\right) \cdot \dot{\gamma}$$

$$\phi = \left(\frac{1}{K}\right)^{\frac{1}{n}} \text{ and } m = \frac{1}{n} \tag{149}$$

The total die conductance (k_{die}) for the serial connection is calculated by equation 149.

$$\frac{1}{k_{die}} = \left[\sum_{i} \frac{1}{k_i^{\frac{1}{m}}}\right]^{m} \tag{150}$$

For the given segment, if the calculated die conductance value is small then the flow resistance is very high at that segment. The unit of the die conductance is cm^3. The calculated die conductance at each segment along the flow length of the check-card part is shown in figure 113. For the calculation of die conductance at each segment, the reduced wall thickness due to the formation of frozen skin layer is accounted.

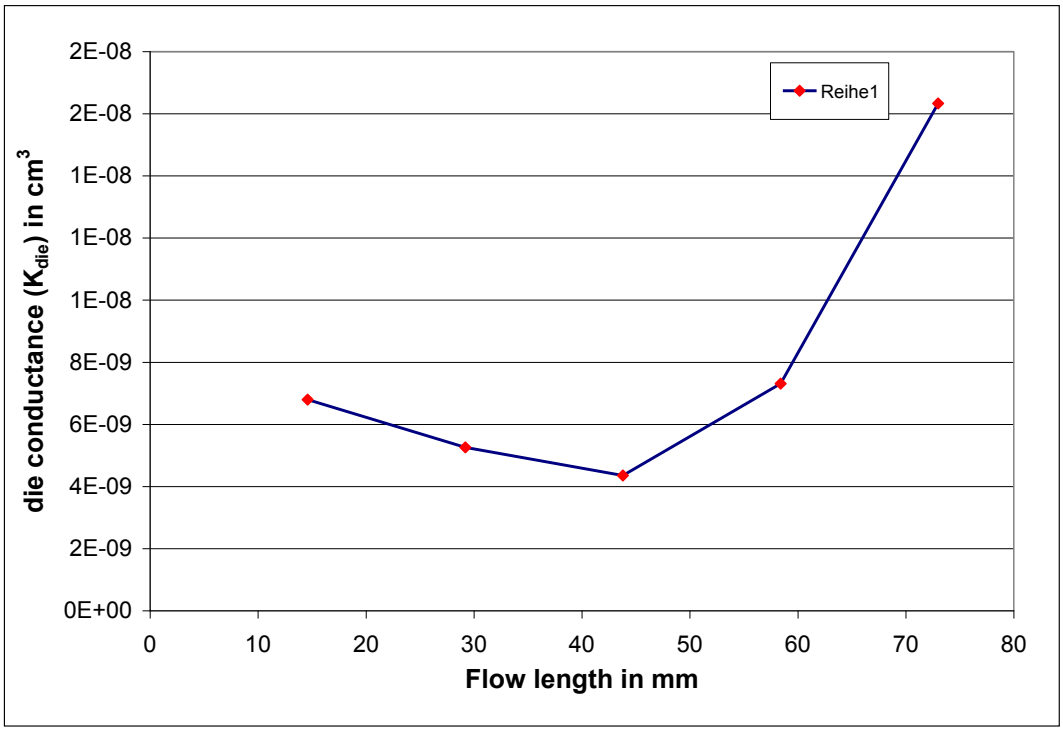

Figure 113: Calculated die conductance value at each segment along the flow length.

As shown in figure 113, the die conductance value changes at each segments. In the same manner, the time constant (k') in equation 147 has to be changed to account the melt flow resistance in the cavity. However, the complexity of such modelling is that the technique to associate the time constant (unit: s^{-1}) with the die conductance (unit: cm^3). Nevertheless, this is not the scope of this present work. To account the flow resistance in the pressure drop profile, the present model to calculate the exponential pressure drop using equation 147 has to be modified or further variation has to be done.

Figure 114 shows the measured pressure profile at the screw antechamber, the screw position, and measured cavity pressures near and far from the injection point for the filling analysis done with pre-compression pressure of 1150 bar. The cavity pressures near and far from the injection point reach the maximum value of 738 bar and 352 bar. Figure 115 shows the measured melt temperature with the infrared (IR) temperature sensor at the screw antechamber during the complete cycle. The melt temperature increases about 16.02°C during the compression, which clearly signifies the important of compression heat while compressing the melt with high pressure. The check-card parts produced with high compression pressures are used for the investigation of process induced material degradation analyses on the moulded parts.

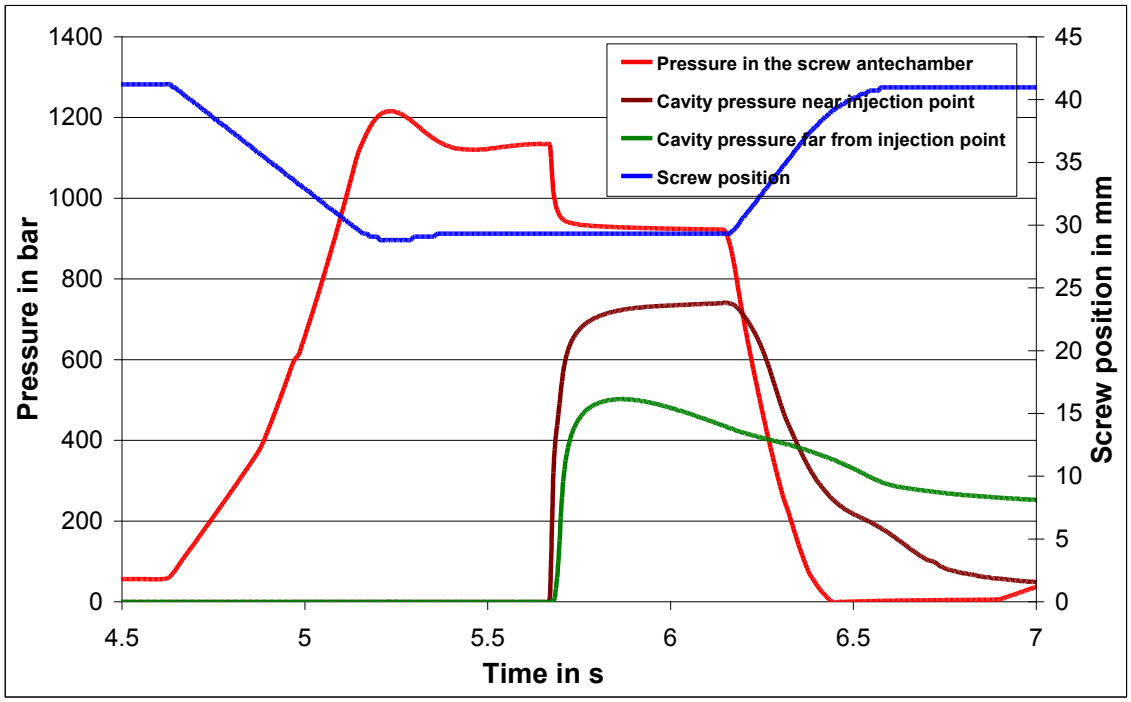

Figure 114: Measured pressures at the screw antechamber, in the cavity (near the injection point and far from the injection point) and the screw position during the complete cycle for PP HG313MO at 230°C with pre-compression pressure of 1150 bar.

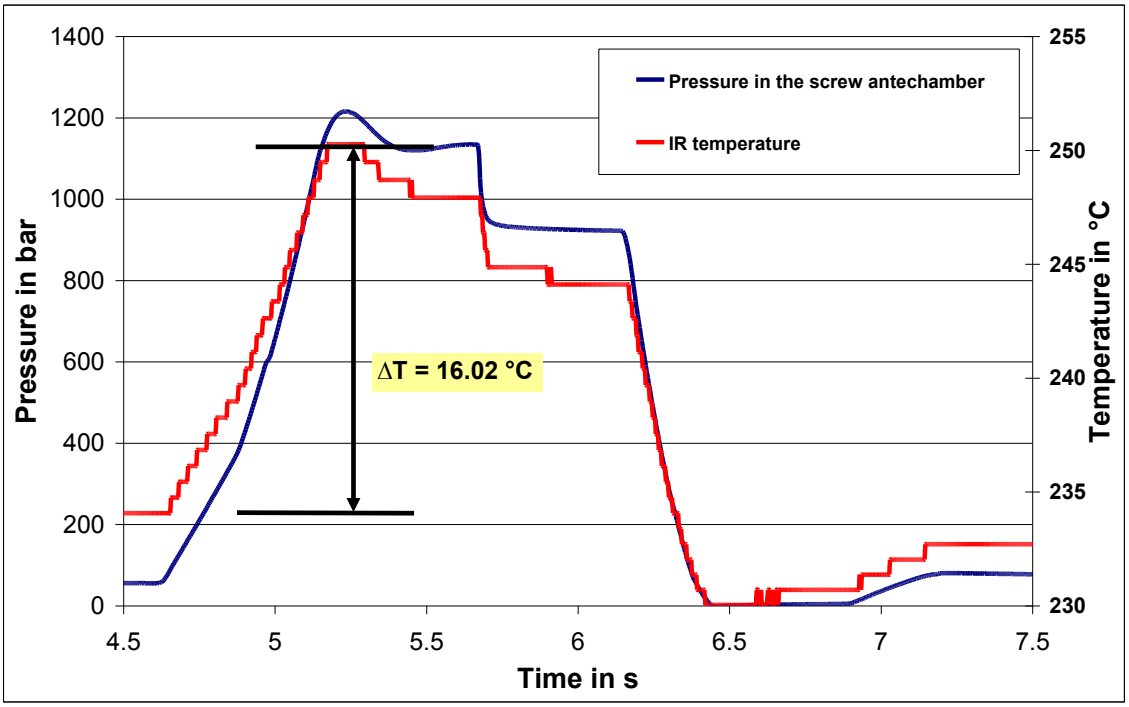

Figure 115: Measured melt pressure and IR temperature at the screw antechamber with 1150 bar pre-compression pressure for PP HG313MO at 230°C

The check-card part has the total flow length of 73 from its injection point. The flow lengths achieved with different compression pressures are listed in table 20. The part weights of the check-card parts produced with different compression pressures are also listed in table 20. As specified in table 20, the realized flow length of moulded part is increase with the increasing compression pressure from 550 bar to 850 bar. The part weight increases linearly with the increasing pre-compression pressure. The theoretical part weight is 2.05 g. Figure 116 shows the weights of check-card parts produced at different compression pressures.

Table 20: Effect of compression pressure on the part weight and the flow length

Pre-compression pressure (bar)	Part weight (g)	Flow length (mm)
550	1.39	51.62
650	1.61	60.08
750	1.84	68.61
850	1.97	73.00
950	2.02	73.00
1150	2.12	73.00

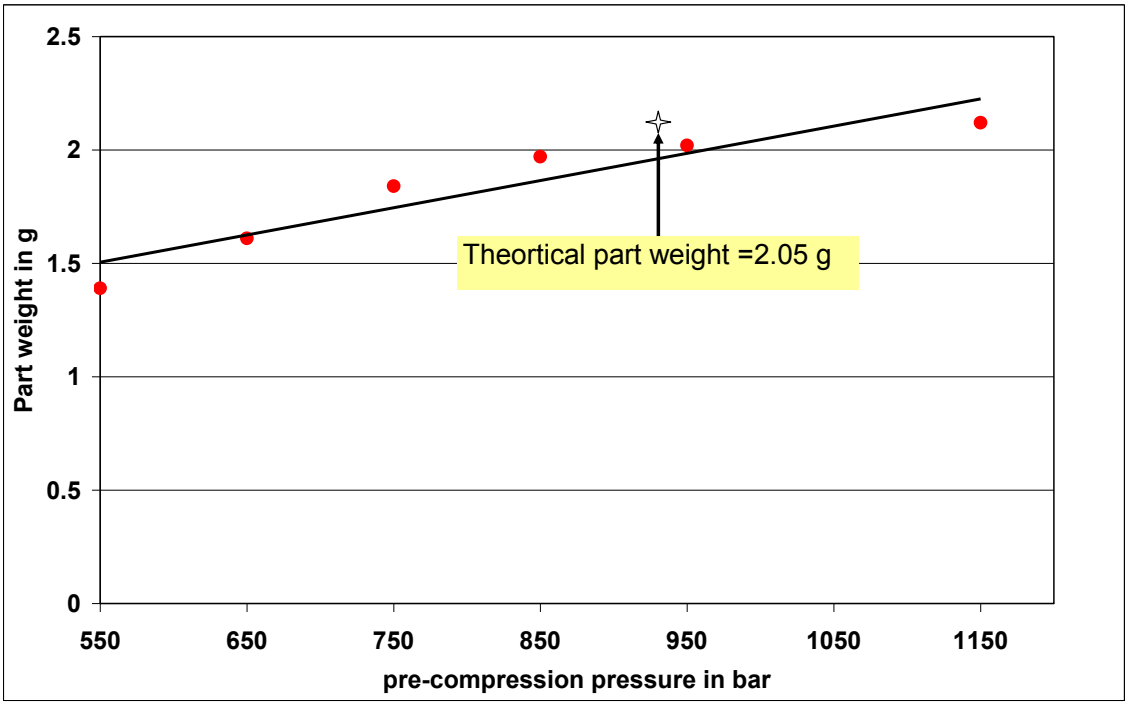

Figure 116: Weights of check-card parts produced at different compression pressures for PP HG313MO.

9.2.2 Influence of the needle-valve opening duration on the part quality

In the standard injection moulding, after the volumetric mould filling, the melt is compressed to ensure that the mould contours are shaped. The compression phase is followed by the holding pressure phase. This holding pressure phase is necessary as the plastic have a high thermal contraction due to reduction in volume as a result of cooling. The point at which the transfer of filling- to packing phase happens is called the switch-over point. Unlike the standard injection moulding, in the expansion injection moulding during the melt expansion the injection screw is kept at constant position. During the expansion phase, the melt pressure drops from the pre-set compression pressure to the end pressure. Up on the volumetric filling of the cavity, this end pressure acts as a holding pressure. The end pressure remains constant until closing of the hot runner shut-off nozzle. Therefore, the duration of needle-valve opening has a significant influence on the part quality. In order to analysis the influence of needle-valve opening duration on the part weight, series of experiments were carried out with different needle-valve opening duration. The compression pressure chosen for these analyses was 950 bar. The chosen duration of the needle-valve opening are 0.02 s, 0.04 s, 0.15 s and 0.5 s. Figure 117 shows the measured pressure profile at the screw antechamber with different durations of needle-valve opening.

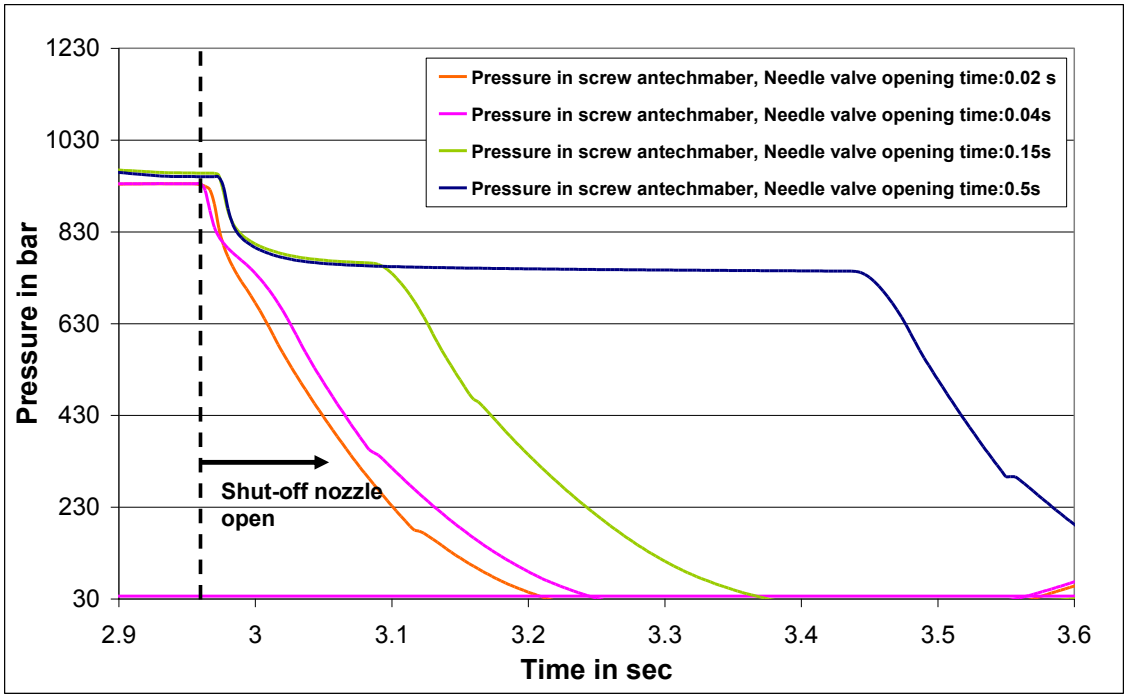

Figure 117: Pressure profiles at the screw antechamber after the shut-off nozzle opened with different opening durations for PP HG313MO.

Table 21 shows the measured maximum cavity pressure at near and far from the injection point with the different needle-valve opening time. With the increasing opening

duration, the measured cavity pressures also increasing. The flow length and part weight are taken as the quality parameters to analyse the influence of the needle-valve opening duration. With the lowest needle-valve opening duration of 0.02 s, the part is not completely filled and the realized flow length is 70.10 mm. The complete part filling was realized with the needle valve opening time of 0.04 s. Table 22 shows the flow lengths and part weights achieved with different needle-valve opening durations. Figure 118 shows the plot of mould part weight versus the needle valve opening duration.

Table 21: Effect of the needle-valve opening duration on the measured cavity pressure near and far from the injection point

Duration of the opening (s)	Max. cavity pressure near the injection point (bar)	Max. cavity pressure far from the injection point (bar)
0.02	351.15	49,6
0.04	410	210
0.05	420	220
0.15	548	353.92
0.5	600.24	378

Table 22: Effect of the needle-valve opening duration on the part weight and the flow length

Duration of the opening (s)	Part weight (g)	Flow length (mm)
0.02	1.73	70.10
0.04	1.81	73.00
0.05	1.82	73.00
0.15	1.87	73.00
0.5	1.96	73.00

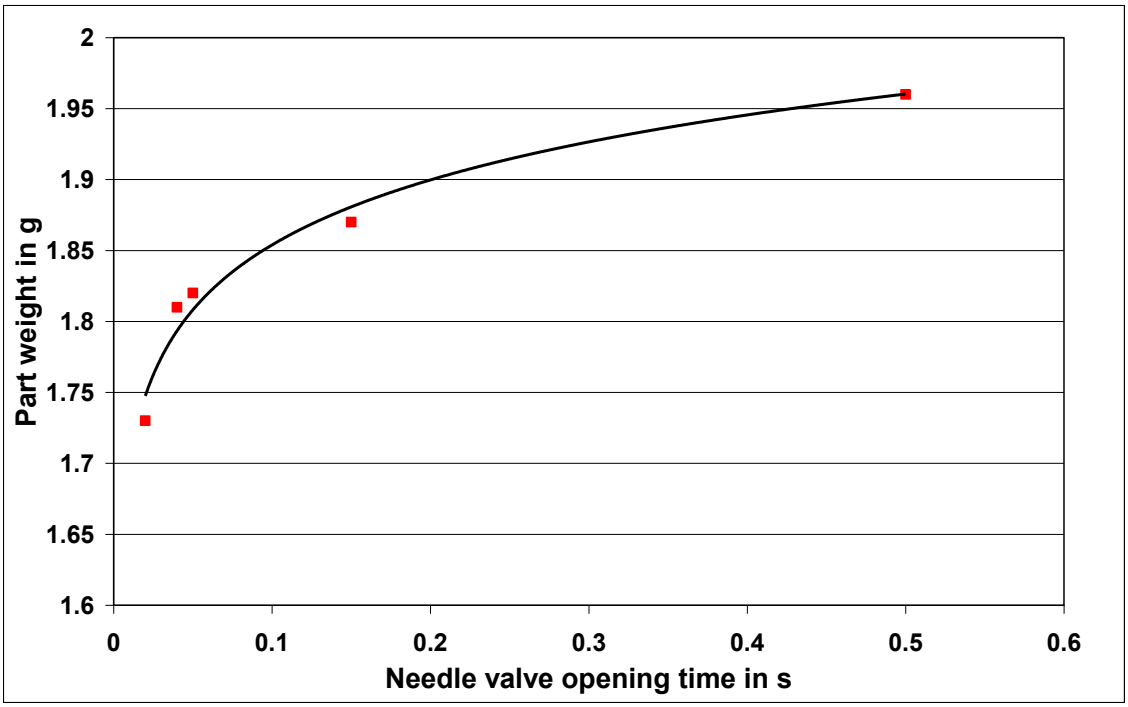

Figure 118: Weights of check-card parts produced with different needle valve opening durations for PP HG313MO.

9.3 Experimental results for PS 495F

9.3.1 Mould filling analysis

For the chosen PS 495F material, the experiments were carried out at the different compression pressures of 1300 bar, 1450 bar and 1600 bar at the melt temperature of 230°C and the mould wall temperature of 40°C [84]. The chosen compression time was 0.5 s, and after the compression phase, the shut-off nozzle was kept open for 0.5 s. The photos of the produced check card parts are shown in figure 119. The optimum filling of the cavity was found at a pre-set compression pressure of 1600 bar.

Figure 119: Photos of the produced check-card parts at different compression pressures.

Figure 120 shows the screw position, the measured pressure profile at the screw antechamber and the measured cavity pressures at points both near and far from the injection point. At the end of the compression phase, the pressure in the screw antechamber remains value of 1556 bar. After opening the shut-off nozzle, the cavity pressure near the injection point reaches the maximum value of 896 bar and the cavity pressure far from the injection point reaches a maximum value of 316 bar. At the end of the expansion phase, the pressure in the screw antechamber drops to the pressure value of 1276 bar.

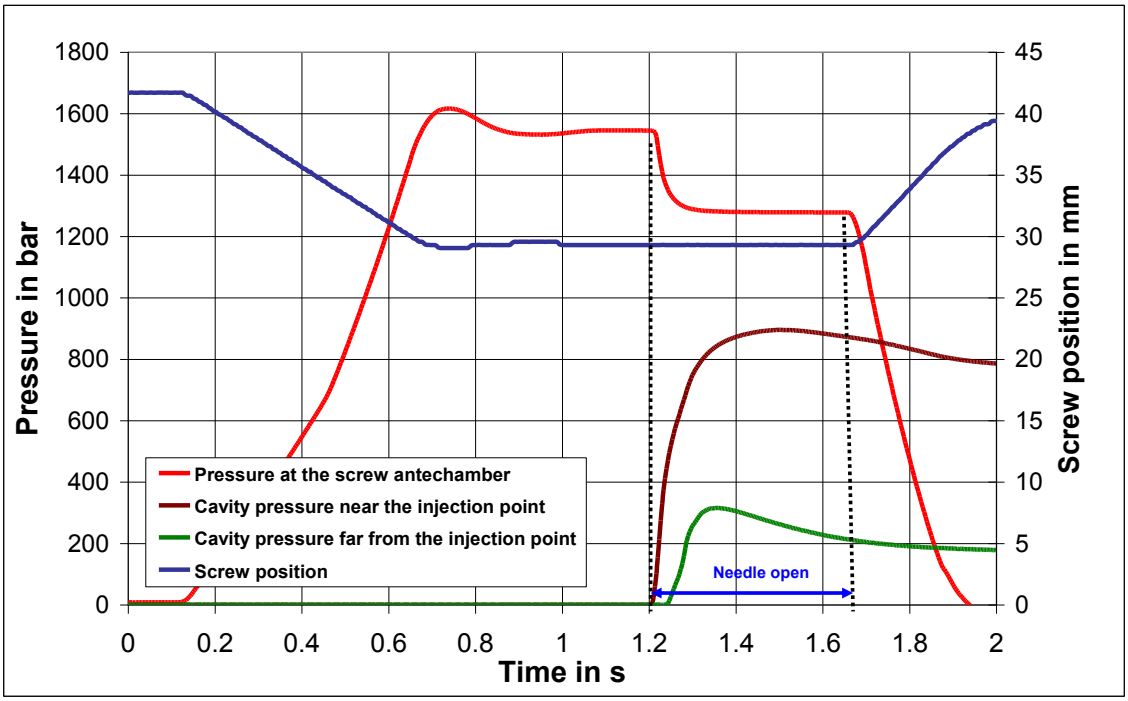

Figure 120: Measured pressures at the screw antechamber, in the cavity (near the injection point and far from the injection point) and the screw position during the complete cycle for PS 495F at 230°C with pre-compression pressure of 1600 bar.

With the *"Xmeltsoft V.1.0"* simulation program, the calculated compression pressure for PS 495F was 1590 bar (see chapter 8.2). The simulation result agrees well with the experimental results. The completely filled part is produced with the melt pre-compression of 1600 bar. Figure 121 shows the measured melt temperature with the infrared (IR) temperature sensor at the screw antechamber during the complete cycle. The melt temperature increases about 13°C during the compression. The calculated compression heat in the simulation is 10.82°C.

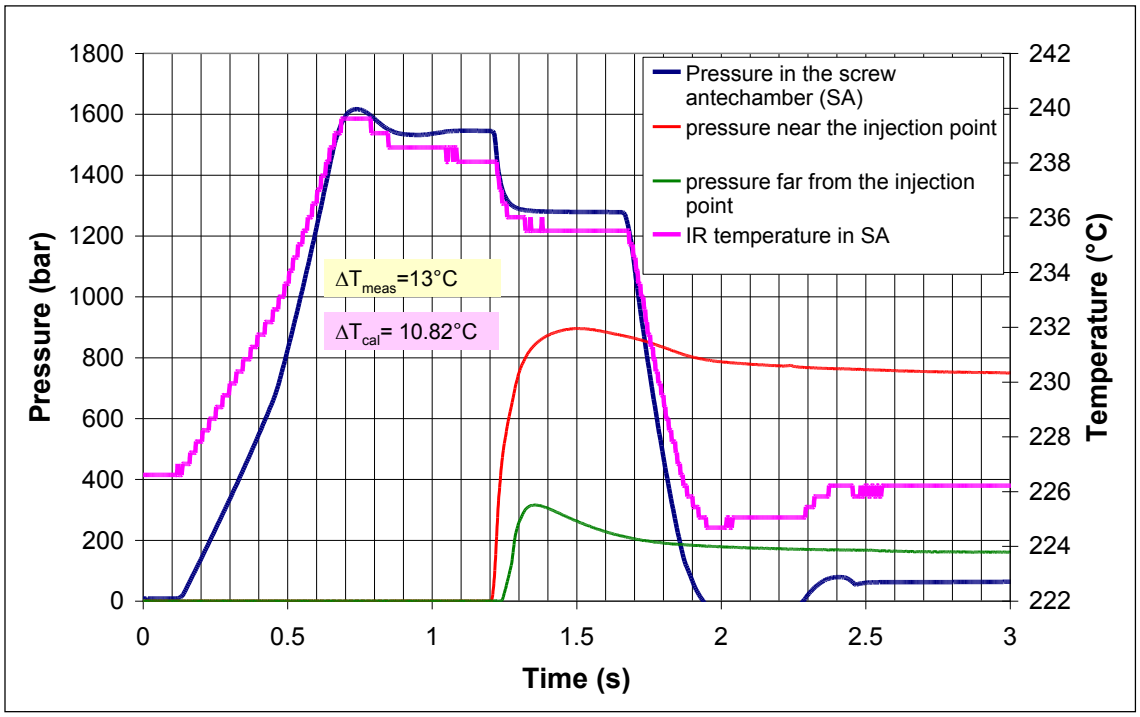

Figure 121: Measured melt pressure and IR temperature at the screw antechamber with 1600 bar pre-compression pressure for PS495F at 230°C

The flow lengths achieved with different compression pressures are listed in table 23. The part weights of the check-card parts produced with different compression pressures are also listed in table 23. The theoretical part weight calculated for PS 495F is 2.38 g.

Table 23: Effect of compression pressure on the part weight and the flow length for PS 495F

Pre-compression pressure (bar)	Part weight (g)	Flow length (mm)
1300	2.140	66.40
1450	2.339	72.00
1600	2.485	73.00

The influence of the needle-valve opening duration was also investigated for PS 495F material in the work [82]. For the investigated PS 495F, the influence of the needle-valve opening duration has similar kind of influence like the PP HG313MO.

9.4 Experimental results for ABS/PC Bayblend T65

9.4.1 Mould filling analysis

The filling study for ABS/PC Bayblend T65 was performed at four different compression pressures (1200 bar, 1500 bar, 1700 bar and 1800 bar) [84]. The chosen melt temperature was 260°C and the mould wall temperature was 80°C. To realize such high mould wall temperature, the moulded is heated with the hot oil. The photos of the produced check card parts are shown in figure 122.

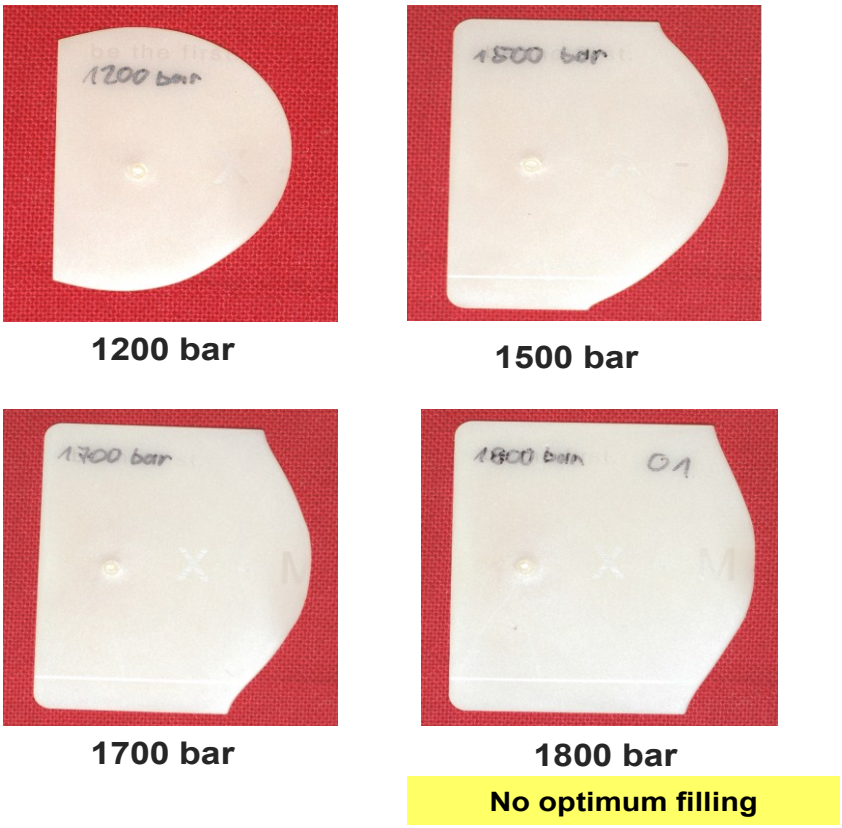

Figure 122: Photos of the produced check-card parts at different compression pressures.

No optimum filling was found with the investigated compression pressure range. With the *"Xmeltsoft V.1.0"* simulation program, the calculated compression pressure for ABS/PC Bayblend was 2815 bar (see chapter 8.3). With the pre-compression pressure of 1800 bar, the realized flow length is 38.60 mm. Due to the pressure limitation (max. 1800 bar) of the pressure transducer mounted on the measurement flange; it was not possible to perform the filling study with higher compression pressure range.

Additionally, the filling study was performed with the higher melt temperature and the wall temperature. With the pre-compression pressure of 1800 bar, the melt temperature was raised from 260°C to 270°C and the mould wall temperature was increased from 80°C to 100°C [84]. Figure 123 shows the effect of increased melt temperature as well as the wall temperature on the flow length and weight of the produced part. By increasing the melt temperature and the wall temperature, the higher flow length was realized. However, the parts were not completely filled. The DSC analysis of Bayblend T65 material shows that the thermal degradation starts at the temperature range, which higher than 270°C [42].

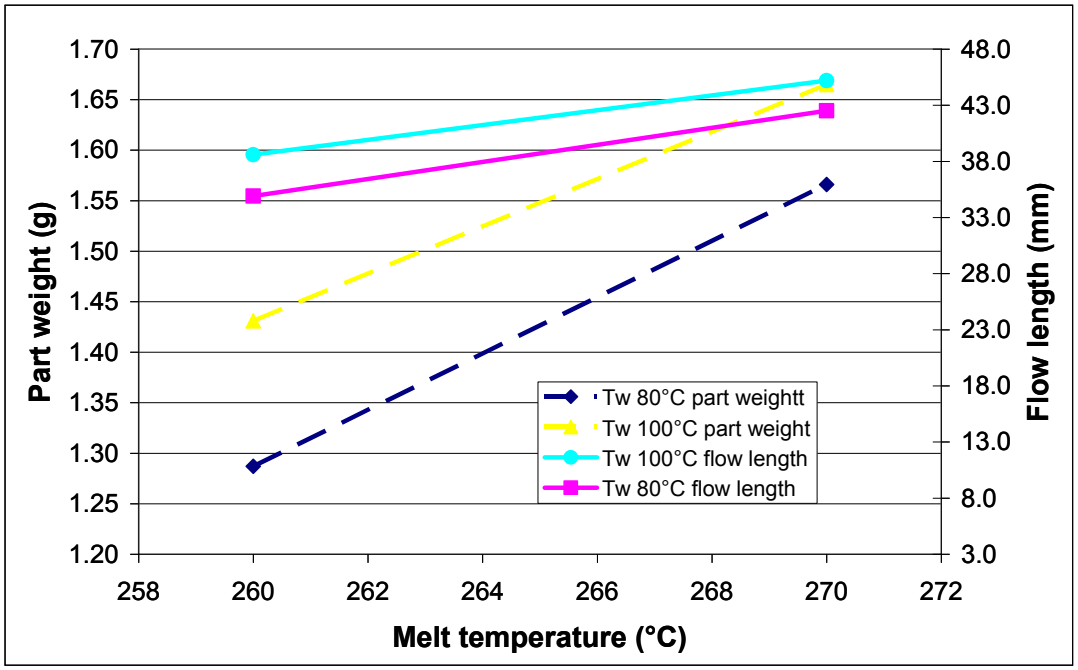

Figure 123: Effect of the chosen melt temperature and the mould wall temperature on the produced part with pre-compression pressure of 1800 bar for Bayblend T65.

With in the master thesis [84], a factorial design of experiments were carried out to find the influence of the process parameters such as the melt temperature, the mould wall temperature, the compression pressure and the duration of the needle-valve opening on the part weight. The result of the investigation clearly showed that for the investigated PP HG313MO, the compression pressure has a major influence on the produced part weight. The chosen melt temperature and the duration of the needle-valve opening are the second major influencing process parameters next to the compression pressure [84].

10 Molar mass degradation analyses of the moulded part

In expansion injection moulding, one possible problem is that the melt undergoes high thermo-mechanical loads in terms of residence times and very high shear rates during the filling phase of the thin wall parts. For thermally sensitive materials, repeated thermo-mechanical loads during the compression- and expansion- phases and the high shear rate during the filling phase can lead to material degradation. Within this present study, the effect of shear rate, compression pressure and melt residence time on material degradation was investigated. The molar mass analyses were carried out with the help of Size Exclusion Chromatography (SEC). The SEC analyses were carried out at the Institute of Chemistry of Polymeric Materials. To investigate the influence of the shear rate on the thin wall moulded part, the samples were collected from different sections of the moulded part with the help of the microtome cutting machine. Figure 124 shows the approach used for performing the molar mass degradation analyses of the expansion injection moulded check-card part.

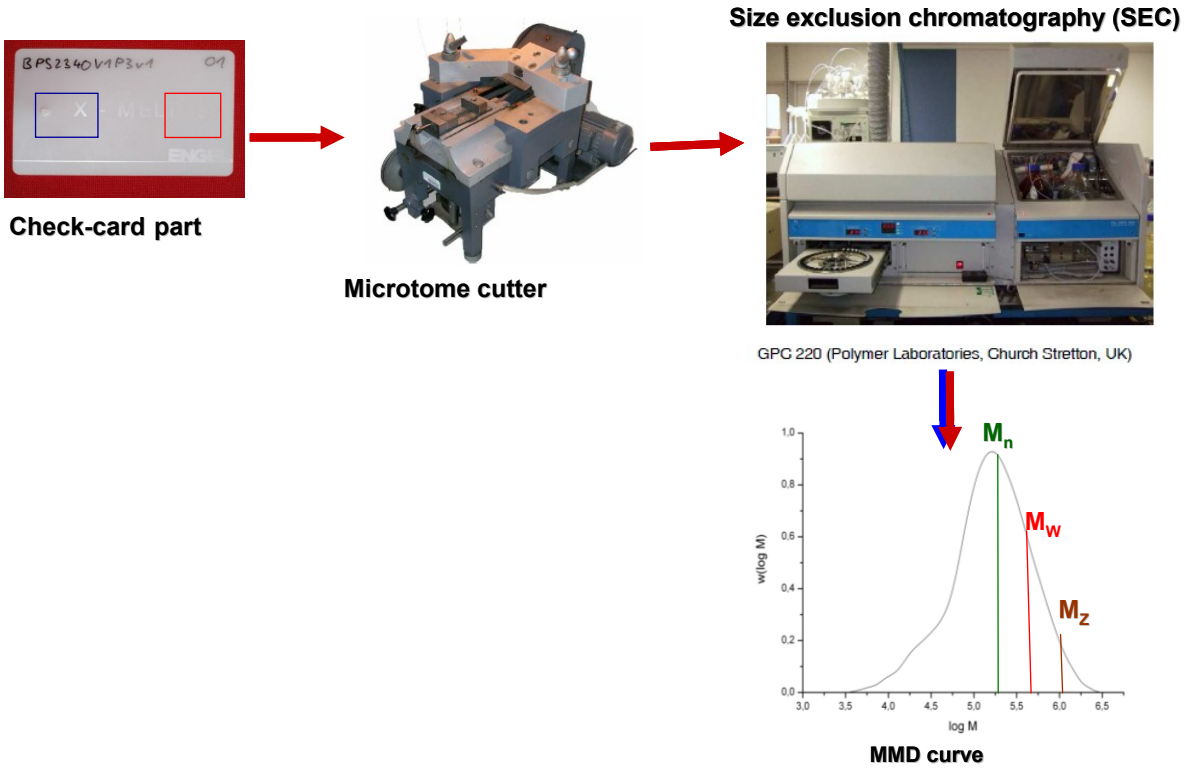

Figure 124: Approach used for performing the molar mass degradation analyses of the moulded parts.

10.1 Theoretical background about molar mass of polymers

A polymeric material may consist of polymer chains of various lengths or repeat units. Hence, the molecular mass is determined by the average or mean molar mass. The properties of polymeric material are strongly linked to the molar mass of the polymer. The stiffness properties reach a maximum value with the increasing molar mass, whereas the flow temperature increases with the increasing molar mass. The degradation temperature steadily decreases with increasing molar mass [37].

Monomers, the building blocks of polymers, have a single molar mass. After the polymerisation, not every polymer molecule contains the exact same number of monomer units. This results in a distribution of chain lengths or molar mass. Depending on the type and conditions of polymerization, this molar mass distribution can be very narrow or quite broad. Figure 125 shows the molar mass distribution (MMD) curve of a typical thermoplastic.

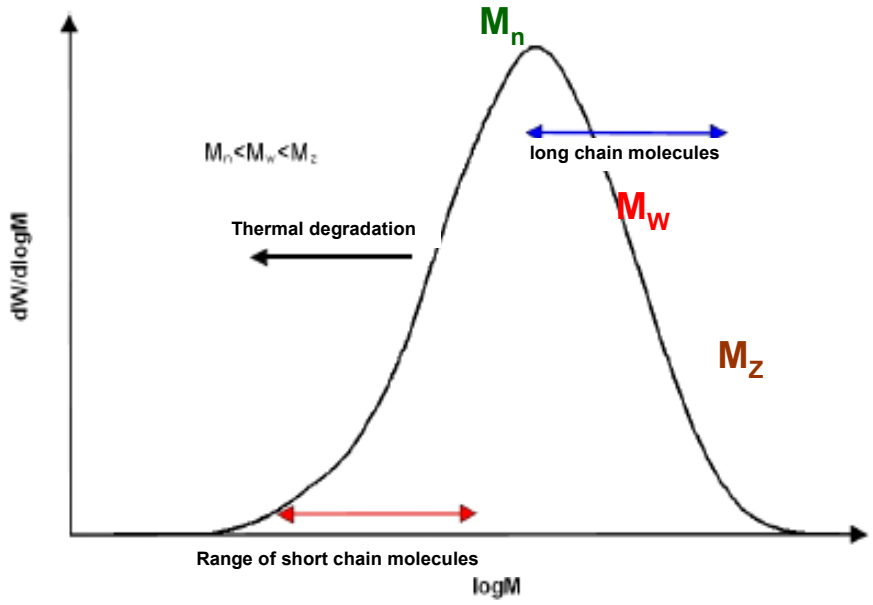

Figure 125: Typical molar mass distribution (MMD) curve of a typical thermoplastic.

Polymer molecules, even one of the same types, come in different sizes (chain lengths), so the average molecular weight will depend on the method of averaging. The number average molecular weight is the ordinary arithmetic mean or average of the molecular weights of the individual macromolecules. In a typical distribution curve the average values are related to each other as follows $M_n < M_w < M_z$. Polydispersity index (PDI) of a sample is defined as M_w divided by M_n and gives an indication just how narrow a distribution is. Both the molecular mass distribution and the average molecular mass

are among the most important determinants of the polymer performance. The gel permeation chromatography is widely used to measure accurately determine polymer molar mass distributions. The gel permeation chromatography is also termed as size exclusion chromatography (SEC). Lederer. K [85] had investigated the thermal degradation of polypropylene during injection moulding. He observed the change in the molar mass distribution curve caused by molecular degradation of PP in injection moulding with the help of SEC.

10.2 Over view of the size exclusion chromatography

The experimental setup and the basic steps in obtaining an MMD for a polymer sample are shown schematically in figure 126. An appropriate mobile phase is delivered to a chromatographic column filled with a suitable stationary phase by a pump at a constant and reproducible flow rate. Into this solvent stream, a small amount (typically 0.01 to 1.0mg) of the polymer sample is injected. When a sample is injected into the column, the polymer molecules are separated according to their hydrodynamic volumes. Hence polymer molecules larger than the pores of the packing material cannot enter the pores and are eluted first. Small molecules, however, have access to the pores and will therefore elute at last. The separated fractions are detected by the detector, the signal of which must represent the concentration of the polymer with good accuracy. From the concentration curve, MMD is calculated.

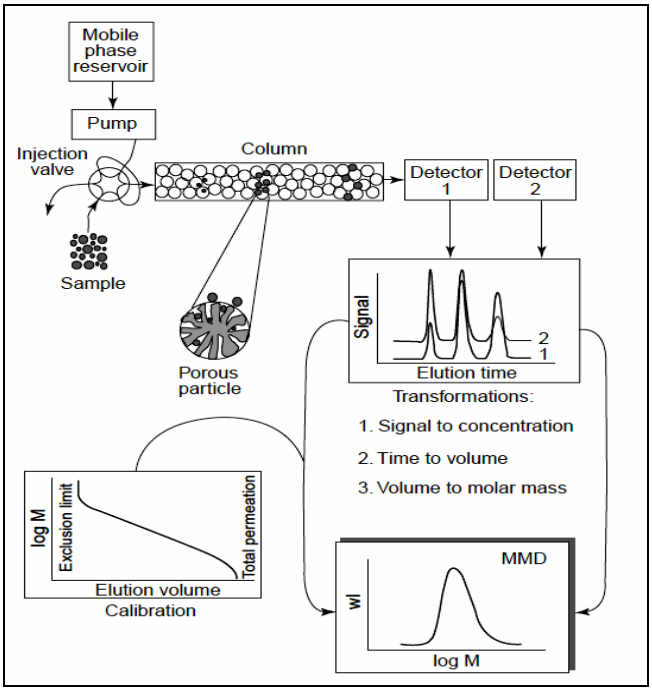

Figure 126: Schematic representation of SEC [86].

10.3 Experimental setup and evaluation technique for MMD

In order to investigate the process-induced material degradation on the expansion injection moulded parts, the MMD curves of the samples collected from the moulded parts were measured with the help of size exclusion chromatography (SEC). The SEC used for the investigation was type SEC 200 (figure 127) and SEC 50 from Polymer Laboratories, Church Stretton, UK.

Figure 127: SEC 200 (Polymer Laboratories, Church Stretton, UK).

The analyses were carried out at the Institute of polymeric materials, Montanuniversitaet Leoben. The molar mass distribution of the samples was determined at 135±0.02°C with a GPC 220 chromatograph equipped with a differential refractive index (DRI) detector (Polymer Laboratories) and a differential viscometer 210 R (Viscotek, Houston. TX. USA). A set of two columns was used, which were packed with cross-linked styrene-divinylbenzene (PLgel® Mixed-A LS, particle size: 20 µm, length: 300 mm, i. d.: 7.5 mm; Polymer Laboratories).

1,2,4-Trichlorobenzene (Acros Organics, Geel, Belgium) containing 0.0125% (w/v, mixed at 23°C) 2,6-di-tert-butyl-(4-methylphenol) (BHT) was used as solvent and as eluent after filtration through a 0.45-µm PTFE-filter. Prior to entering the pump, it was degassed with an online degasser PL-DG2 (Erc Inc., Kawaguchi City, Japan). The flow rate was 0.5 ml/min.

The polymer solutions were prepared with amounts between 8 and 20 mg of the polymer (dependents up on the availability) in 10 ml of solvent with the concentration of 0.8 to 2 mg/ml and the solution were flushed with nitrogen for 15 min at room temperature to avoid oxidative degradation during dissolution. The nitrogen was purified

with Oxisorb® gas-cleaning system (Linde AG, Höllriegelskreuth, Germany) and contained less than 0.0001% (v/v) oxygen. The samples were then gently shaken at 150°C for 2 hours and filtrated through a 0.2 µm filter prior to injection.

The calculation of the weight average molecular weight (M_w), the centrifugal average molecular weights (M_z), the number average molecular weight (M_n) and the Polydispersity index were calculated according to the method of universal calibration [87].

10.4 Sample preparation technique for SEC analyses

Figure 128 shows the typical shear rate distribution across the cavity. When the molten thermoplastic melt is injected into the cavity, the molten melt freezes immediately at cool cavity, which causes the formation of frozen layers on the both side of the cavity walls. The molten melt moves forward in between these frozen layers. The melt flow velocity is maximum at the centre of the cavity, thus the maximum shear rate happens at the region between the frozen skin layer and the flowing molten melt.

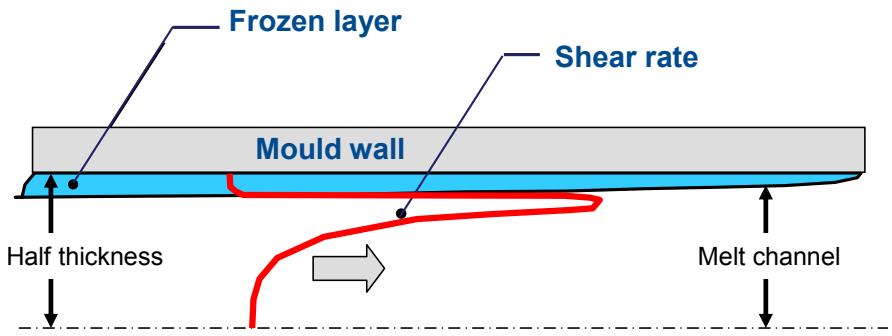

Figure 128: Shear rate distribution across the cavity.

To investigate the influence of the shear rate on the thin wall moulded part, the samples were collected from different sections of the moulded check-card part with the help of the microtome cutting machine. As shown in figure 129, the samples were collected by cutting three layers with a thickness of 10 µm each. The first sample was taken from the outer layer, which corresponds to the frozen skin layer. The second sample was taken from the zone below, which corresponds to the high shear region. The third sample was taken from the zone in the middle of the part (middle layer). The cutting thickness of the outer layer, which corresponds to the frozen skin layer, was chosen by taking the average of the calculated thickness distribution values along the flow length. In addition, the samples were collected as mentioned in the above manner from points both near and far from the injection point. The detail method of sample preparation technique is explained in the works of [40] and [84].

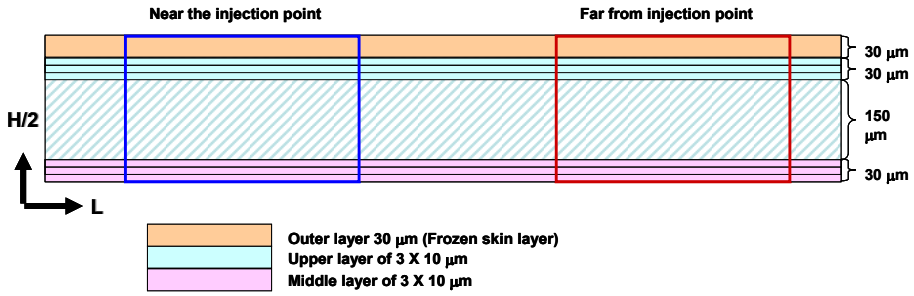

Figure 129: Microtome cutting layers on the check card part.

The results acquired out of SEC analyses are the molar mass distribution curve (MMD), the number average molar mass (M_n), the weight average molar mass (M_w), the z-average molar mass (M_z) and the polydispersity index ($PDI=M_w/M_n$). The values of M_w and M_z represent the higher molar mass fractions of the polymer molecules. If the polymer is degraded by high temperatures, the distribution curve shifts to lower molecular weight [83]. In the case of a statistical breakdown of polymer molecules, the values of M_w and M_z decrease while the value of M_n increases. The polydispersity value decreases with a thermal decomposition. Due to very difficult sample preparation and a limited amount of material, the measurement uncertainty is approximately five percent.

10.5 Results of the molar mass analyses for check-card parts

10.5.1 For check-card produced with PP HG313MO

For the investigation of process induced degradation analyses, the PP check card parts produced with compression pressures of 950 bar and 1150 bar were used for the investigation [40]. The samples were prepared from the moulded parts as mentioned above manner with the help of the microtome-cutting machine. Figure 130 shows the measured MMD curve of the PP raw material.

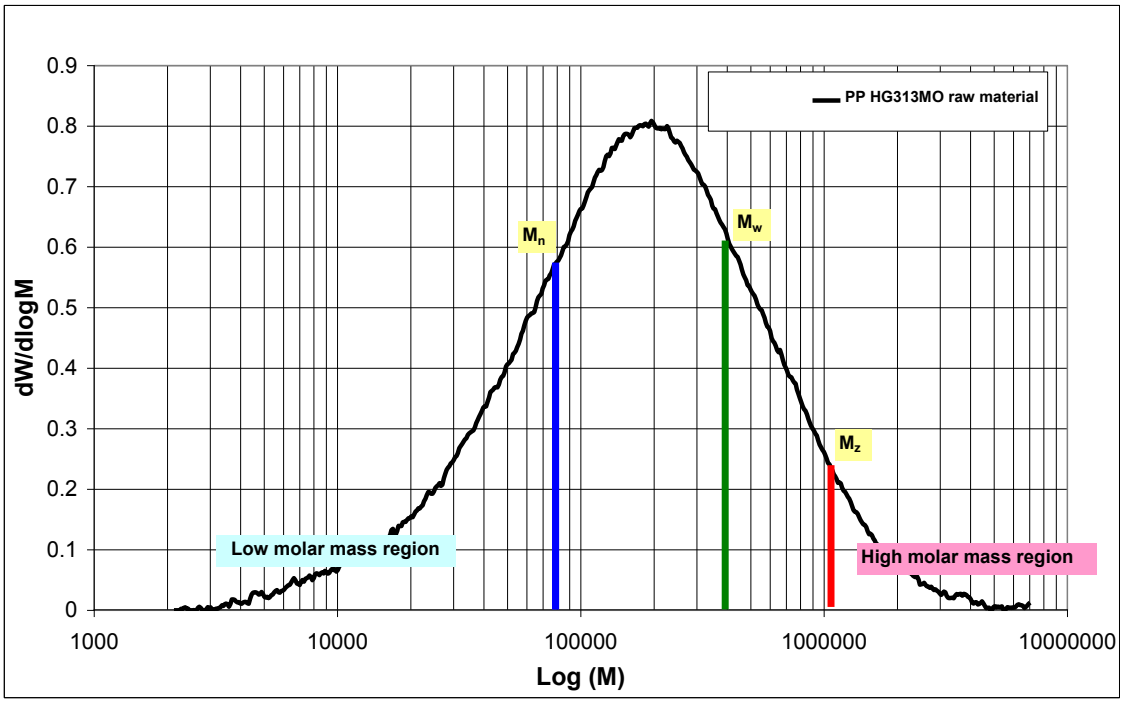

Figure 130: MMD curves of PP HG313MO raw material, the measured values of M_n, M_w and M_z are indicated in bars.

Figure 131 shows the MMD curves of the samples collected near to the injection point at outer, upper, and middle layer of the part produced with 1150 bar compression pressure in comparison with the MMD curve of the raw material.

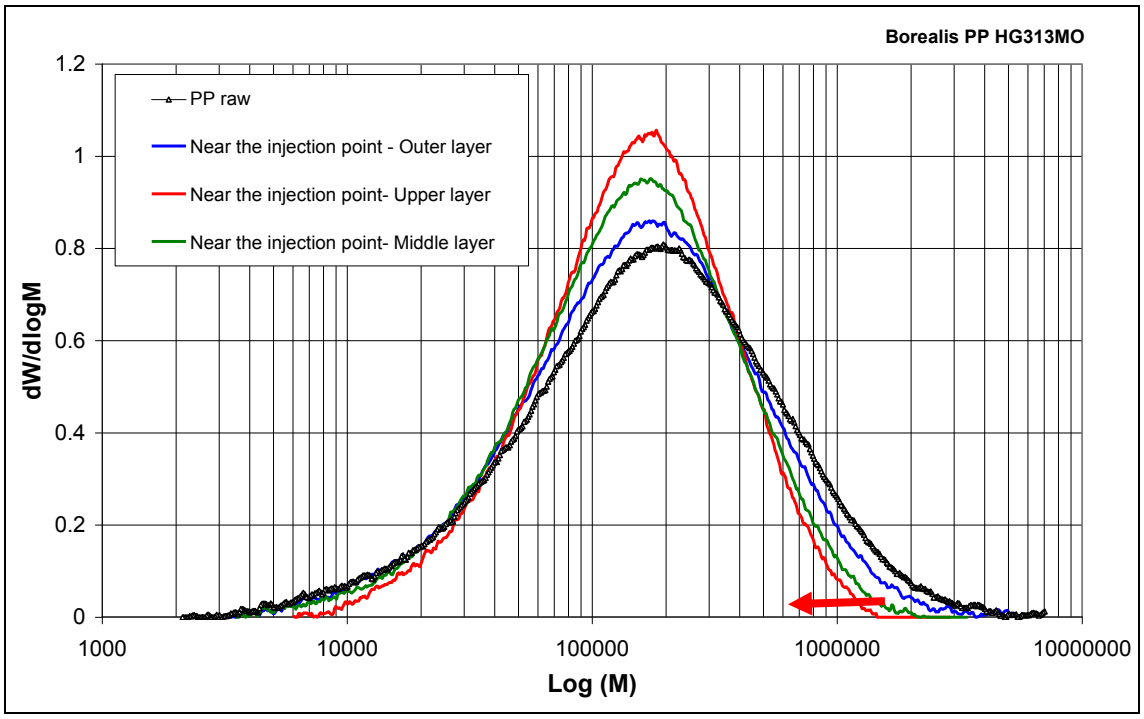

Figure 131: MMD curves of the raw material and samples collected from near the injection point at outer, upper and middle layers of the part produced with 1150 bar compression pressure (shifting of high molar mass region to low molar mass region is indicated by the red arrow mark).

The measured values of M_n, M_w, M_z and PDI for the samples collected near to the injection point are listed in table 24.

Table 24: Results of the SEC analyses for the samples collected near to the injection point

	Raw material	Outer layer	Upper layer	Middle layer
M_n (g/mol)	76600	77300	92600	78600
M_w (g/mol)	336500	270900	208600	220600
M_z (g/mol)	1026600	760500	375900	450900
PDI (/)	4.39	3.51	2.25	2.81

Figure 132 shows the MMD curves of the samples collected far from the to the injection point at outer, upper, and middle layer of the part produced with 1150 bar compression pressure in comparison with the MMD curve of the raw material. The measured values of M_n, M_w, M_z and PDI for the samples collected far from the injection point are listed in table 25.

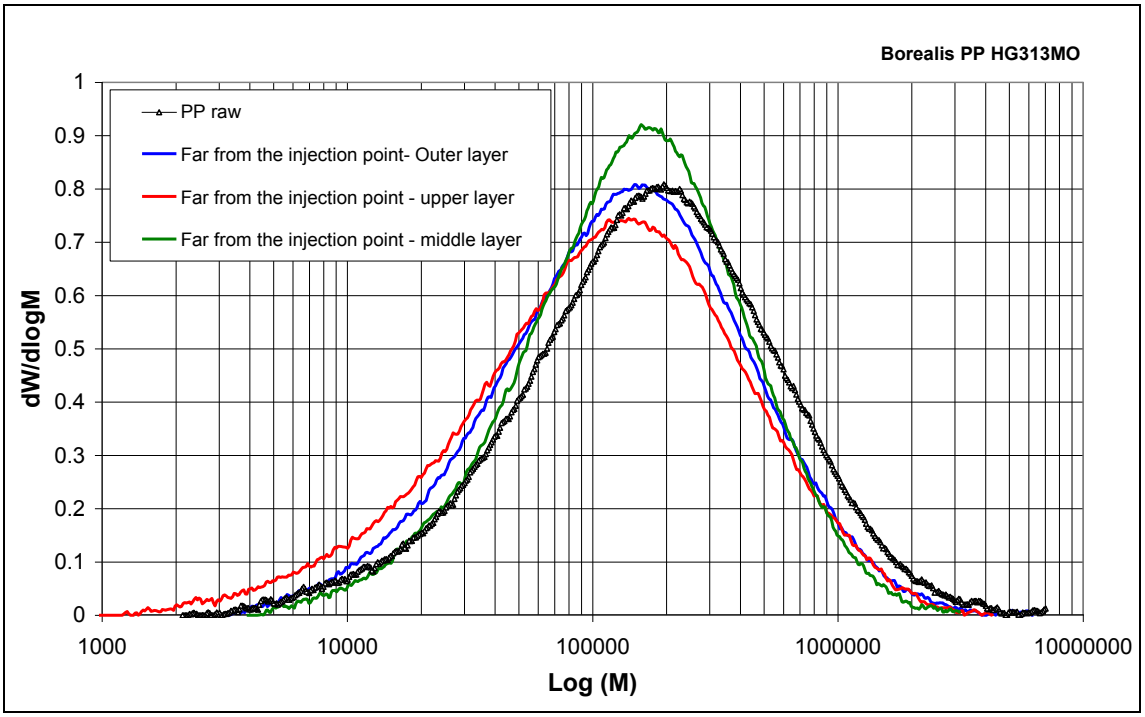

Figure 132: MMD curves of the raw material and samples collected from far the injection point at outer, upper and middle layers of the part produced with 1150 bar compression pressure.

Table 25: Results of the SEC analyses for the samples collected far from the injection point

	Raw material	Outer layer	Upper layer	Middle layer
M_n (g/mol)	76600	65448	67500	56000
M_w (g/mol)	336500	250368	227300	238300
M_z (g/mol)	1026600	758303	652800	488500
PDI (/)	4.39	3.83	3.37	4.26

The above results of the molar mass analyses clearly show that the MMD curves of the samples collected from the moulded part are shifted to the low molar mass region in comparison to the MMD curve of the raw material. Table 26 shows the percentage difference of the measured values of M_w, M_z and M_n for the samples collected at the three zones from the moulded part (near the injection point) in comparison with the those values measured for PP raw material.

Table 26: Percentage differences of M_z, M_w and M_z

	Difference in M_z	Difference in M_w	Difference in M_n
Outer layer	-25 %	-19.5 %	+ 0.92 %
Upper layer	-63 %	-38 %	+ 21 %
Middle layer	-56 %	-34 %	+ 2.7 %

The MMD curve of the upper layer (high shear region) shows a significant material degradation as compared to the MMD curves of the outer and middle layers. The sample collected at the upper layer is just beneath the frozen skin layer, where theoretically, a high shear rate prevails during the part filling. Due to the high shear rate, the entangled long chain polymeric molecules start to orient along the shear direction at first. When the oriented molecules are further stressed, then a breakage of long chain molecules can occur which leads to an increase in M_n value and a decrease in M_w and M_z values. As seen in table 26, the M_z and M_w values of the samples collected from the moulded part at the upper region (high shear region) are relatively lower than the values measured for the PP raw material and the M_n value is relatively higher than the value measured for the PP raw material.

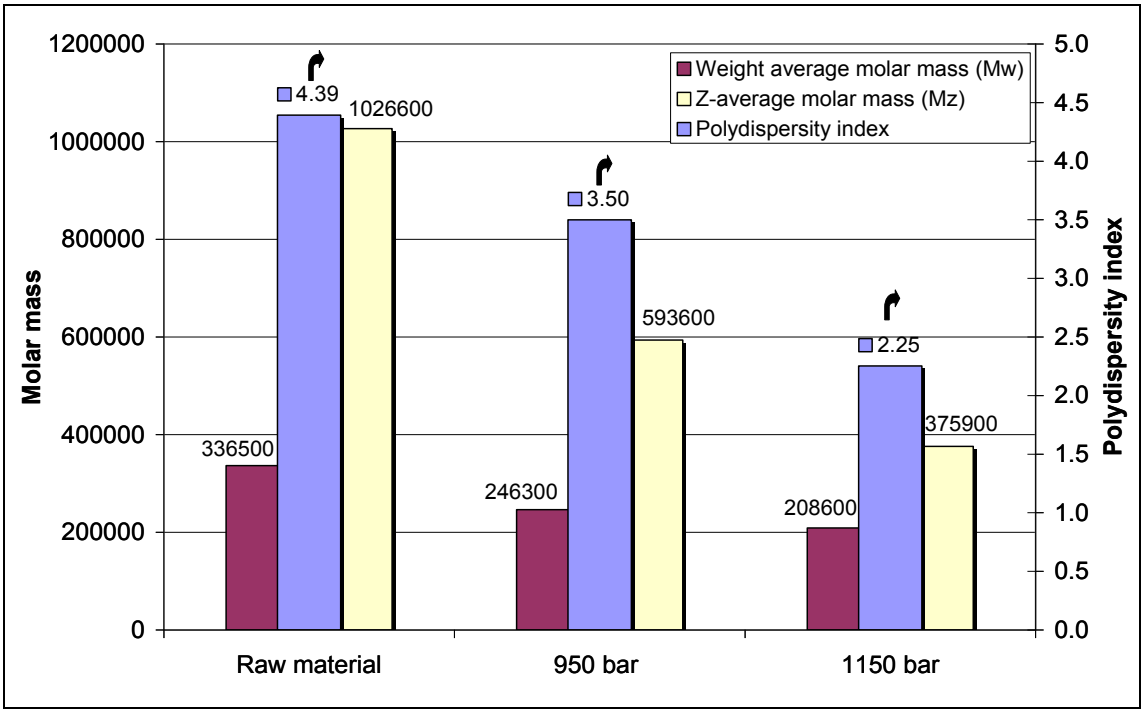

Figure 133: Influence of the compression pressure on the molar mass values for the samples collected at the upper layer.

The influence of the compression pressure on the molar mass degradation of the moulded part is shown in figure 133. With 950 bar pre-compression pressure, the M_w

value reduces about 26% in compare to the M_w value of the raw material. With 1150 bar pre-compression pressure, the M_w value drops of about 38% in compare to the M_w value of the raw material. The compression pressure has a very considerable influence on the molar mass degradation for the investigated PP. The results of the material degradation analyses carried out for PP check-card parts significantly showed for the investigated samples that the influence of the shear rate and compression pressure on material degradation is inevitable. In order to estimate the influence of the molar mass degradation on the mechanical properties of the moulded part, the mechanical testing such as tensile and impact testing has to be carried out.

10.5.2 For check-card produced with PS 495 F

For the investigation of process induced degradation analyses, the PS check card parts produced with compression pressures 1450 bar and 1600 bar were used for the investigation [84]. Figure 134 shows the MMD curve of the PS 495F raw material. The weight of average molar mass of the PS 495 is relatively lower than the M_w value of the PP HG313MO. Table 27 shows the values of M_n, M_w, M_z and PDI measured for PS 495F raw material.

Table 27: Measured values of M_z, M_w, M_z and PDI for PS 495F raw material

Raw material	
M_n (g/mol)	81196
M_w (g/mol)	221860
M_z (g/mol)	478648
PDI (/)	2.73

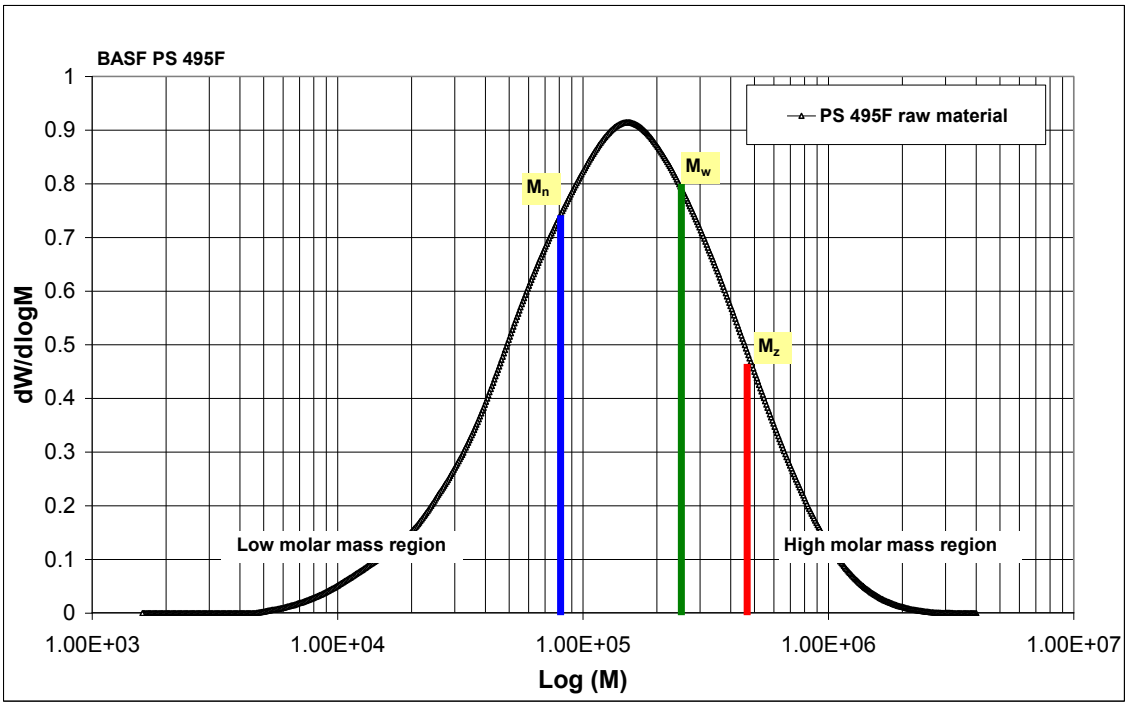

Figure 134: MMD curves of PS 495F raw material, the measured values of M_n, M_w and M_z are indicated in bars.

Figure 135 shows the MMD curves of the samples collected near to the injection point at outer, upper, and middle layer of the part produced with 1600 bar compression pressure in comparison with the MMD curve of the raw material. The measured values of M_n, M_w, M_z and PDI for the samples collected near to the injection point are listed in table 28.

Table 28: Results of the SEC analyses for the samples collected near to the injection point

	Raw material	Outer layer	Upper layer	Middle layer
M_n (g/mol)	81196	85226	80408	81880
M_w (g/mol)	221860	221059	206103	204434
M_z (g/mol)	478648	415759	391126	387333
PDI (/)	2.73	2.59	2.56	2.50

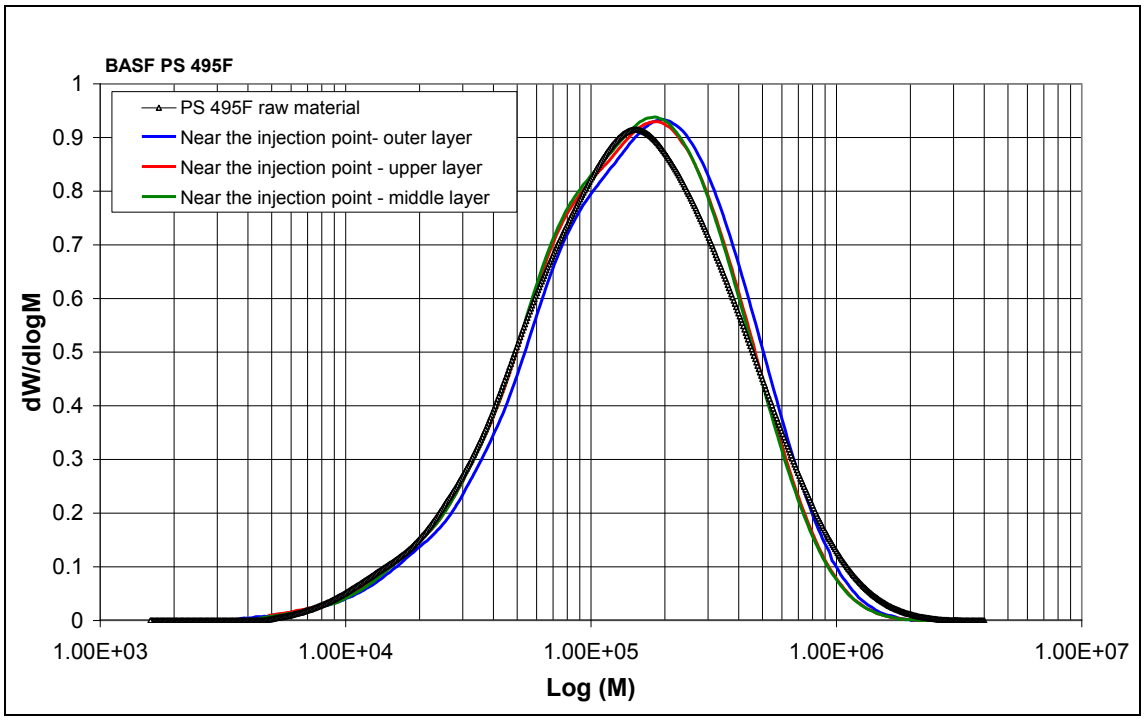

Figure 135: MMD curves of the raw material and samples collected from near the injection point at outer, upper and middle layers of the part produced with 1600 bar compression pressure.

Figure 136 shows the MMD curves of the samples collected far from the to the injection point at outer, upper, and middle layer of the part produced with 1600 bar compression pressure in comparison with the MMD curve of the raw material. The measured values of M_n, M_w, M_z and PDI for the samples collected far from the injection point are listed in table 29.

Table 29: Results of the SEC analyses for the samples collected far from the injection point

	Raw material	Outer layer	Upper layer	Middle layer
M_n (g/mol)	81196	86796	73375	75600
M_w (g/mol)	221860	232491	191204	189446
M_z (g/mol)	478648	449041	370259	356410
PDI (/)	2.73	2.68	2.61	2.51

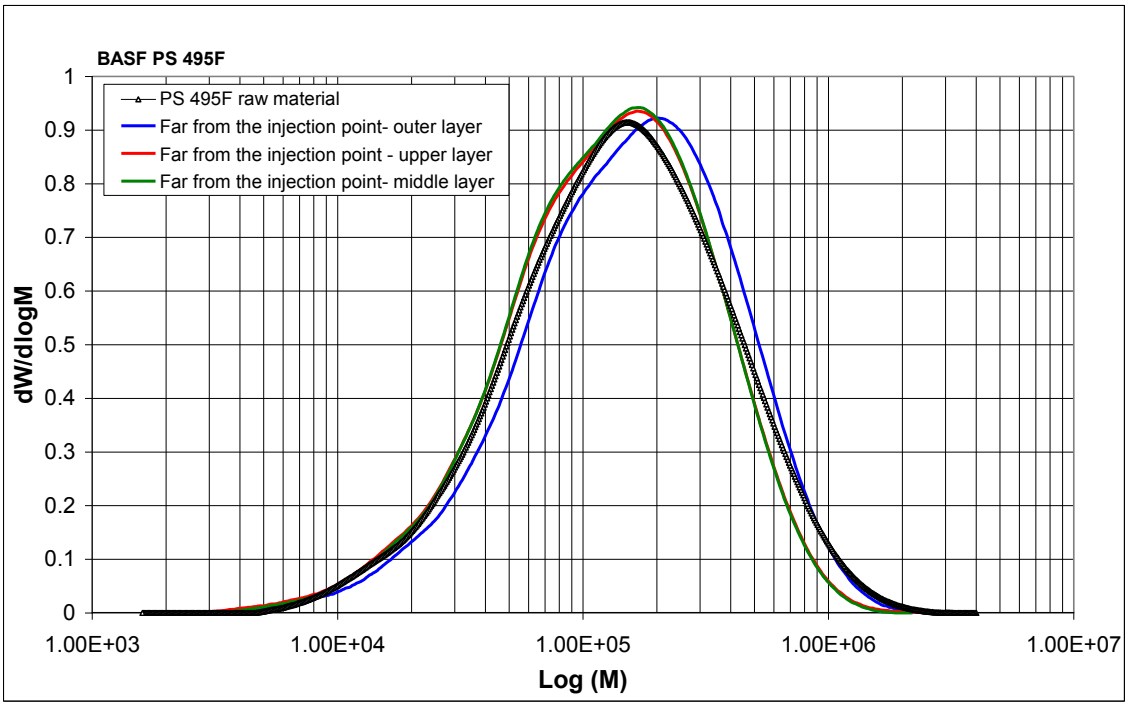

Figure 136: MMD curves of the raw material and samples collected from far from the injection point at outer, upper and middle layers of the part produced with 1600 bar compression pressure.

Table 30 shows the percentage difference of the measured values of M_w, M_z and M_n for the samples collected at three zones from the moulded part (near the injection point) in comparison with the those values measured for PS raw material.

Table 30: Percentage differences of M_z, M_w and M_z for PS 495F

	Difference in M_z	Difference in M_w	Difference in M_n
Outer layer	-13 %	-0.31 %	+ 4.6 %
Upper layer	-18.5 %	-7.2 %	+ 0 %
Middle layer	-18.8 %	-7.8 %	+ 0.8 %

The PS 495F samples from the three different zones, which are, collected both at near and far from the injection point of the moulded parts, shows a slight degradation in compare to the PS raw material. The molar mass values of the samples collected at the upper layer (higher shear region) and the middle layer show a minimum difference in the measured values. The M_w values of the samples collected from the moulded parts show 7.2 % reduction in value in compare to the M_w value of the raw material. In order to access the effect of 7.2% reduction of M_w on the mould part quality, one has study the mechanical properties of the moulded parts. Since that is not the scope of this

present work, no mechanical testing was carried out within this present work. The results of the molar mass analyses show that the process-induced degradation effect on PS 495F is comparatively lesser than the investigated PP HG313MO material.

10.6 Molar mass degradation analyses for a practical thin-wall part

In addition to the molar mass degradation analyses on the check-card part, the molar mass degradation analyses were carried out on a practical thin-wall part. The practical part used for the investigation was Engel's battery cover part with a wall thickness of 0.17 mm. (Figure 137). The dimension of the battery cover part is 52 x 38 x 0:17 mm. The battery cover mould has four cavities and the parts are gated via four submarine gates with sub-runners and a hot runner system with a needle-valve.

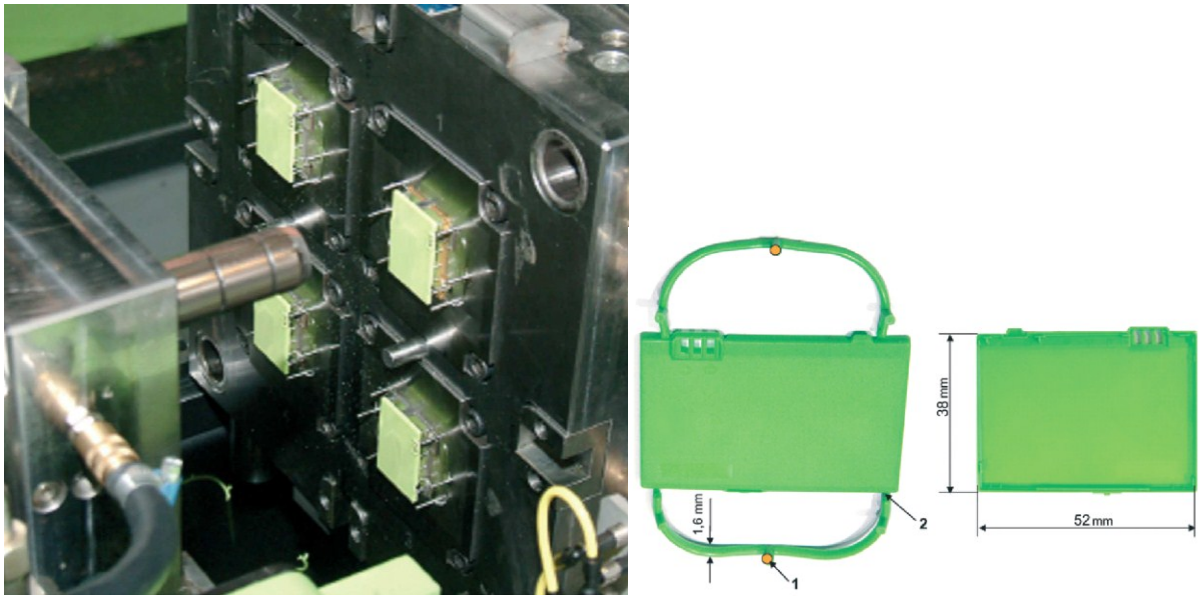

Figure 137: Photo of Engel four cavities battery cover mould (left) and the battery cover part with the runner system (right) [5].

For analyzing the influence of the process-induced material degradation during the expansion injection moulding on the battery cover parts, the battery cover parts are produced with the materials of PP HG313MO and PS 495F [84]. The battery cover parts were produced on Engel injection moulding machine type VC 940/130. The molar mass degradation analyses were carried out with the help of SEC at the Institute of Polymeric Materials, Montanuniversitaet Leoben. The samples for the molar mass degradation analyses were collect as a bulk sample from the moulded parts, since the cutting of such thin-wall part thickness into small thicknesses in very complicated.

10.6.1 Results of the molar mass analyses for battery cover parts

For the used PP HG313MO material, the parts were produced with compression pressure of 1100 bar and at a melt temperature of 230°C [84]. To analyze the influence of the melt residence time in the injection unit on the material degradation, the molar mass analyses were carried out for the parts produced at 1, 5, 10, 15 and 20 injection shots. Due the very thin wall thickness of the moulded parts, the bulk samples for the SEC analyses were collected out of moulded parts. Figure 138 shows the MMD curves of the samples collected from the part produced at the 10th and the 20th injection shot along with the MMD curve of the raw material.

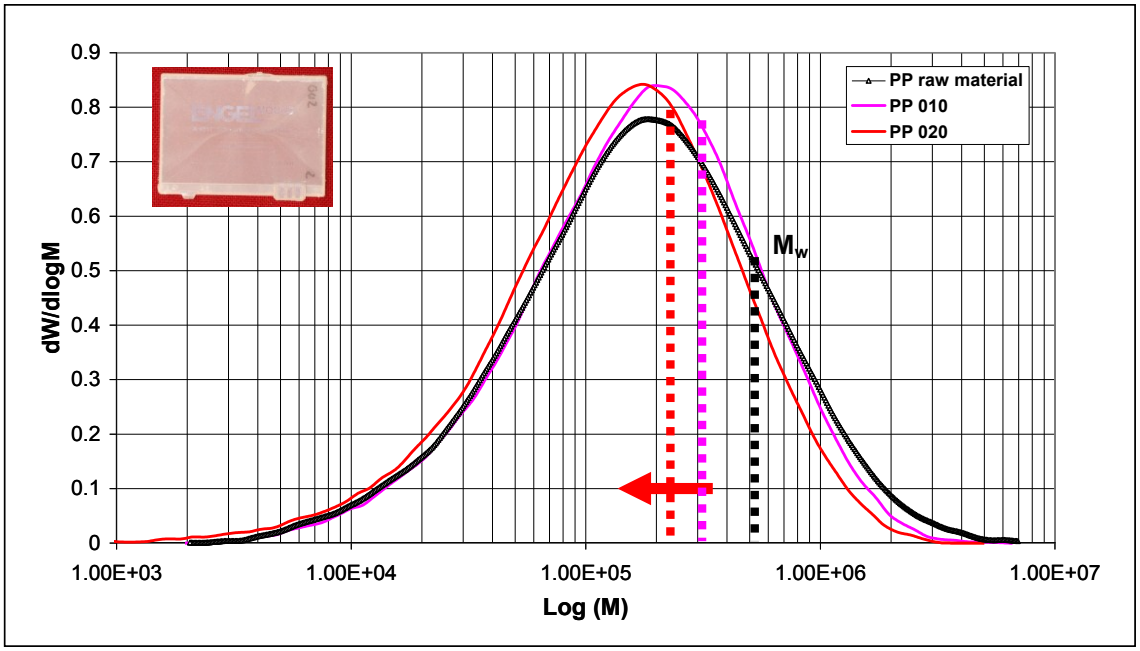

Figure 138: MMD curves of the raw material and samples collected from the moulded parts at the 10th and the 20th injection cycles, the measured values of M_w are indicated with bars in different colours.

Figure 138 clearly shows that for the investigated PP material, the increasing number of injection cycle shows a clear shifting of the measured MMD curve to the low molar mass region. The molar mass values of the samples collected from the battery cover parts at 1, 5, 10, 15 and 20 injection shots are listed in table 31. Especially in the values of M_z and M_w it can be seen that an increasing number of injections results in molecular degradation of the polymer samples. This effect can also be observed in the molar mass distribution (MMD) curves. The M_w and M_z values of the sample collected from the 20th injection cycle are relatively lower than the corresponding values measured for the raw material. The centrifugal average molar mass (M_z), which represents the long-chain

polymer molecules in the high molar mass region reduced about 43.56 % in compare to the M_z value of the raw material.

Table 31: Results of the SEC analyses for the battery cover part

	Granulate	Part 1	Part 5	Part 10	Part 15	Part 20
M_n (g/mol)	76600	77100	86000	80300	73000	58100
M_w (g/mol)	356500	328000	323400	295000	245800	241500
M_z (g/mol)	1026600	874100	802100	722800	588700	579400
PDI	4.4	4.3	3.8	3.7	3.4	4.2

Figure 139 shows the variation of the weight average molar mass with the increasing injection cycle number. Table 32 shows the percentage difference of the measured values of M_w for the samples collected from the moulded parts of the 1st,10th and 20th injection cycles in comparison with the those values measured for PP raw material.

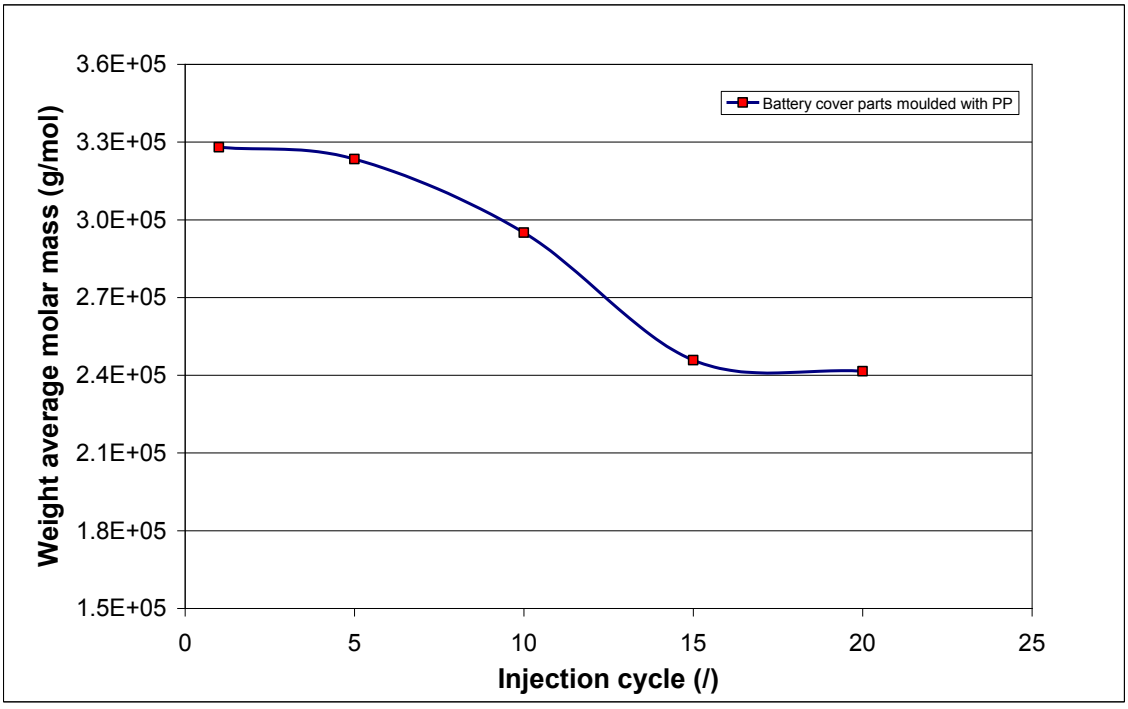

Figure 139: the variation of the weight average molar mass with the increasing injection cycle number.

Table 32: Percentage differences of M_w for battery cover mould parts with PP HG313MO

	Difference in M_w
1st injection shot	-7.9 %
10th injection shot	-17.25 %
20th injection shot	-32.25 %

The weight average molar mass value of the 20th part is about 32% less than the weight average molar mass value of the granulate. The results of the above analyses clearly signify that for the investigated PP HG313MO material the melt resistance in the barrel has much influence on the molar mass degradation of the material in the moulded part.

For the used PS 495F material, the parts were produced with compression pressure of 1800 bar and at a melt temperature of 230°C [84]. To analyze the influence of the melt residence time in the injection unit on the material degradation, the molar mass analyses were carried out for the parts produced at 1, 5, 10, 15 and 20 injection shots. Due the very thin wall thickness of the moulded parts, the bulk samples for the SEC analyses were collected out of moulded parts. Figure 140 shows the MMD curves of the samples collected from the part produced at the 10th and the 20th injection shot along with the MMD curve of the raw material. The molar mass values of the samples collected from the battery cover parts for PS 495F at 1, 5, 10, 15 and 20 injection shots are listed in table 33

Table 33: Results of the SEC analyses for the battery cover part moulded with PS 495F

	Granulate	Part 1	Part 5	Part 10	Part 15	Part 20
M_n (g/mol)	81200	77100	80500	79800	71200	63300
M_w (g/mol)	221900	223700	226500	223300	212600	200700
M_z (g/mol)	478600	426700	422800	414900	411200	399900
PDI	2,7	4,3	3,8	2,8	3,0	3,2

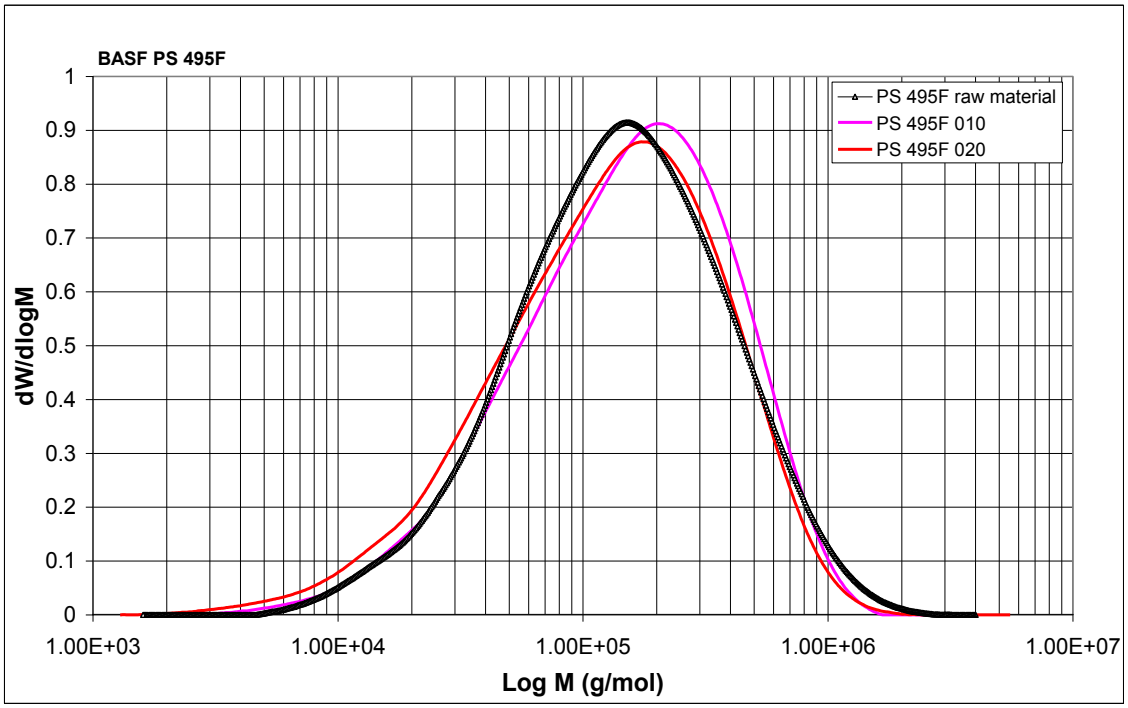

Figure 140: MMD curves of the raw material and samples collected from the moulded parts at the 10th and the 20th injection cycles.

The Polystyrene samples show only a slight molecular degradation with an increasing number of injection cycles. The z-average value represents the high molar mass fractions and therefore shows the degree of degradation most clearly, which reduced about 16 % while comparing the values measured for the sample collected from 20th injection cycle with the PS 495F raw material. Table 34 shows the percentage difference of the measured values of M_w for the samples collected from the moulded parts of the 1st,10th and 20th injection cycles in comparison with the those values measured for PS raw material.

Table 34: Percentage differences of M_w for battery cover mould parts with PS 495 F

	Difference in M_w
1st injection shot	0.8 %
10th injection shot	0.6 %
20th injection shot	-9.5 %

The weight average molar mass (M_w) lowered of about 9.5% in compare to the PS raw material, which indicates a minimum amount of the degradation for the investigated PS 495F. For the battery cover parts moulded with PS material, the material degradation that is relatively less than the PP material degradation. The results of the material degradation analyses carried out with this work significantly show that for the

investigated materials that the influence of the shear rate, compression pressure, and the melt residence time on material degradation is inevitable. However, the material degradation analyses still have to be carried out for various thermoplastic materials to access their sensitivity towards the process-induced material degradation. Further In order to estimate the influence of the molar mass degradation on the mechanical properties of the moulded part, the mechanical testing such as tensile, and impact testing has to be carried out.

11 Future perceptive

Within this research work, a simple theoretical model was developed for the expansion injection moulding. The developed model enables us to calculate the amount of shot weight comes out during the expansion phase for the chosen melt cushion, the compression pressure and the end pressure. The mass flow rate as a function of time is calculated based on the constantly changing pressure in the screw antechamber and the changing specific volume of the melt with the changing pressure in the screw antechamber. Nevertheless, in actuality the amount of expansion volume and the generated mass flow rate are also depend on the elastic deformation of the components in expansion injection moulding.

11.1 Influence of elastic deformation in expansion injection moulding

In expansion injection moulding, the elastic deformations of the machine units such as the deformation of the plasticizing unit, the injection screw, and the hot runner nozzle are unavoidable due to the very high compression pressures involved in the process. Steinbichler et al. [5] showed that for the investigated thin walled battery cover part, the total elastic deformations of the machine units account by 21 % volume of the moulded part.

During the compression phase, the screw is moved in axial direction by drive system and compresses the melt in the screw antechamber to the required pre-compression pressure with the hot runner nozzle closed. On opening the nozzle, melt flows into the mould cavity and the pressure in the screw antechamber falls. This change in the melt pressure in the screw antechamber can be calculated by taking into account the expansion of the plastic melt and the elastic deformation of the relevant parts of the injection unit.

In expansion injection moulding the relevant parts of the injection units such as screw, injection cylinder and hot runner system are subjected to high stress during the compression of the melt. Due to high stress, the steel parts undergo an elastic deformation due to compression stress of the melt. Up on the expansion, the stress is released which leads to an elastic recovery of the steel parts. These changes in volume due to elastic deformation of parts have to be account in the total expansion volume. However, this effect is not taken into account in the present developed calculation model for the reason of simplification.

For establishing the influence of the elastic deformation of the components in expansion injection moulding, a simple calculation was done. At first, the elastic deformation of the

screw was approximately estimated for a know screw dimension. The screw specifications are listed in table 35.

Table 35: The screw specifications

Diameter of the screw	50 (mm)
Length of the screw	1092 (mm)
Cross sectional area of the screw	16.61 (cm^2)
Elastic modulus of the steel	210 GPa

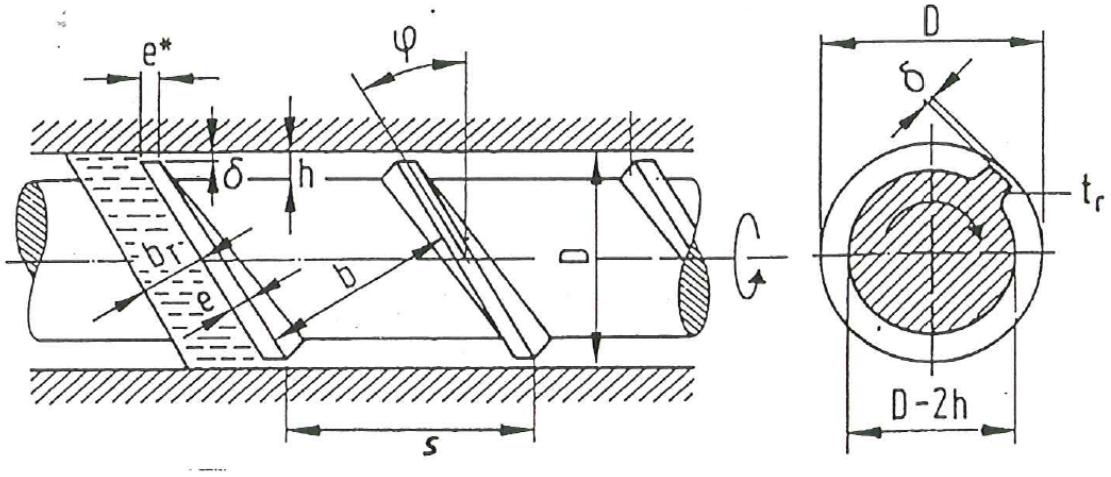

Figure 141: The cross-sectional view of the typical injection screw.

The cross-sectional area (figure 141) of the screw is calculated by using equation 151.

$$A_s = \frac{(D-2h)^2 \cdot \pi}{4} + \frac{e \cdot h}{\sin\varphi_m} \qquad (151)$$

where:

A_s the cross-sectional area of the screw (m^2)

D diameter of the screw (m)

e, h and φ_m are the screw parameters

The calculation was done for the case of expansion injection moulded check-card part with PS 495F material, in which the melt is compressed to the pre-compression pressure of 1600 bar. After the expansion, the pressure in the screw antechamber

drops to the pressure value of 1270 bar. The total pressure drop (p_c-p_E) is 330 bar. The change in length due to pressure difference of 330 bar is calculated by equation 152.

$$\Delta L_s = \frac{(p_c - p_E) \cdot L_s}{E} \tag{152}$$

where:

ΔL_s the change in length due to deformation (m)

L_s length of the screw (m)

E the elastic modulus of the steel (GPa)

The corresponding volume change due to expansion of about 330 bar pressure difference is calculated by equation 153:

$$\Delta v_s = \frac{D^2 \cdot \pi}{4} \cdot \Delta L_s \tag{153}$$

where:

ΔV_s the change in volume due to expansion (m^3)

ΔL_s the change in length due to deformation (m)

The calculated volume change at 330 bar pressure difference is 0.28 cm^3, this volume change accounts 12.43 % of the total volume of the check-card part (2.29 cm^3). This simple calculation signifies the important of elastic deformation on the calculation of the expansion volume. Together with the elastic deformation of the injection cylinder and the elastic deformation of the hot runner nozzle, the total elastic deformation of the machine parts account significant influence on the expansion volume. Therefore, in future as a further development, the present process model for the calculation of the expansion volume, has to be modified to account the influence of the elastic deformation.

11.2 Further development potentials for EIM process simulation

As a future perspective, the current calculation program *Xmeltsoft V.1.0* has to be modified to adopt a parallel segmentation technique. For that, a survey of the different complex injection moulded part geometries has to be done. As a further improvement in the calculation of the frozen skin layer thickness distribution, a numerical calculation method such as finite difference method (FDM) has to be implemented for the 3D calculation of the frozen skin layer distribution.

The developed physical model has to be integrated into the FEM simulation software such as CADMOULD 3D-F from simcon kunststofftechnische Software GmbH, Germany, to improve the commercial applicability of the expansion injection moulding in thin walled injection moulding market.

12 Summary and conclusion

Expansion injection moulding (EIM) is an innovative injection moulding technique used to produce thin-wall parts with small shot weights in a very short cycle time. Expansion injection moulding is only suitable for small shot weight, since the compressed volume in front of the screw should be ten times the shot weight. To reduce development times in the field of expansion injection moulding it is intended to use simulation programs. Due to the different processing technique of the expansion injection moulding from the standard injection moulding, the applicability of currently available simulation programs for the simulation of EIM is not possible. For this reason, it is necessary to develop suitable calculation software based on a physical model for this technique. As a main objective of this work, a physical model was developed to calculate the shot weight coming out of the injection unit during the expansion phase for a given maximum compression pressure, end pressure and melt cushion. The minimum required filling pressure is chosen as an end pressure. The methodical approach for the calculation of the minimum required filling pressure is segmentation of the longest flow path into several serially connected small segments. In a serial connection, the volume flow rate at every segment is the same but the pressure drop of each segment is different. The total required filling pressure is the sum of the pressure drops at all segments. To improve the calculation accuracy, the effect of the frozen skin layer thickness is also taken into account. For that, the model proposed by Dietz and White is used to calculate the thickness of the frozen skin layer. From the calculated frozen skin layer distribution at each segment the reduced wall thickness is obtained. These values are used for the calculation of the pressure drops at every segment. Further, the change in melt temperature at each segment due to the effect of dissipative heating and cooling is also taken into account for the calculation of melt viscosity. The calculated minimum pressure required to fill the cavity is chosen as an end pressure (p_E). From the input values of the end pressure, part mass, mass of the compressed melt, melt temperature, melt compressibility and specific volume from p-v-T data, we can calculate the maximum compression pressure in order to fill the cavity during the expansion phase.

Based on the calculation approach, calculation software called *Xmeltsoft V.1.0* was developed with the help of the computer programming language VBA for the simulation of the expansion injection moulding for simple part geometries. The developed software is supplied as an Excel Add-in. The user can install the calculation program within the Excel environment. The developed software is supplied with the integrated material database with the complete material data for four materials.

For the simulation of the expansion injection moulding process, practically reliable material data such as viscosity data measured at higher shear rates as a function of

temperature and pressure, high accurate pvT data measured up to 2500 bar and thermal conductivity as a function of temperature and pressure are most important requirements to improve simulation accuracy. To fulfil this needs, a complete material data is measured for three chosen thermoplastic materials such PP HG313MO, PS 495F and Bayblend T65 in the practically relevant processing conditions. In addition to the strand rheological measurements, the viscosity measurements were carried out on the injection moulding machine with the rheological injection mould. For more accurate viscosity data, the measured viscosity values were temperature corrected taking into account the shear heating. The effect of pressure on viscosity was also investigated by performing the viscosity measurement with different back pressures. The experimental investigation on pressure dependency clearly signifies the importance of pressure dependent viscosity data. A temperature- and pressure- independent viscosity curve is obtained by shifting the measured viscosity curves by 45° into a reference curve based on the time-, temperature-, and pressure superposition principle. The pressure coefficient of viscosity at constant shear stress is calculated for all three thermoplastic materials. The values of pressure coefficient of viscosity calculated for PP, PS and ABS/PC blend are 24.6×10^{-9} Pa^{-1}, 31.28×10^{-9} Pa^{-1}, and 23.93×10^{-9} Pa^{-1} respectively, these value fit close with the literature value mentioned for the same type materials.

The measured material data for three materials are integrated into material database for the requirement for the simulation. The check-card part with a wall thickness of 0.5 mm was chosen as a model part, which was simulated with the developed calculation program for the chosen three thermoplastics materials of PP, PS and ABS/PC. With the intent of verification, the simulation results were compared with the experimental results. The check cards were produced on a hybrid injection mouldings machine (Type VC 940/130) supplied by ENGEL Austria GmbH. The model part (check card) was completely filled using PP and PS, but not completely filled with PC/ABS due to the limited specific injection pressure of the used injection moulding machine. For the investigated PP and PS material, the simulation results are agreeable with the experimental results.

Further, the process induced material degradation was studied on the expansion injection moulded parts. To analyze the influence of the shear rate on the moulded part, the samples were collected at the different regions of the moulded part with the help of a microtome cutting machine. The process-induced material degradation analyses were done for the check-card part mould with PP and PS materials. For the investigated PP material, the results of the molar mass analyses show that the different thickness layers of the moulded part have different molar mass values. In particular, the material collected in the high shear region below the frozen skin layer has a significantly lower molar mass than does the middle layer. A value of about 38% reduction in the weight

average molar mass is observed for the sample collected at the high shear region. In addition to that, the compression pressure also has a considerable influence on material degradation. The investigated PS material shows relatively small amount of the degradation in compare to PP material. In order to find the influence of melt resistance time on the material degradation, the samples from the practical thin-wall part with wall thickness of 0.17 mm produced at different injection cycle were investigated. For the investigated PP material, the increasing number of injection cycle shows a clear shifting of the measured MMD curve to the low molar mass region. The weight average molar mass value of 20^{th} part is about 32% less than the weight average molar mass value of the granulate. For the battery cover parts moulded with PS material, the analyses of the material degradation showed a reduction of weight average molar mass of about 9.5%, which is relatively less than the PP material degradation. Apart from already investigated thermo plastic materials, detailed process analyses have to be done to investigate the applicability of the expansion injection moulding technique with additional thermoplastic materials. The analysis of the material degradation on the expansion injection moulded part with different thermoplastic materials has to be carried out. To estimate the influence of the molar mass degradation on the mechanical properties of the moulded part, the mechanical testing such as tensile and impact testing is recommended.

13 List of Literatures

[1] N.N: Nexus Market Analysis for MEMS and micro-systems III 2005-2009

[2] Neuy, C.; Zucker, J.: Expertise at the micro-Level. Kunststoffe international, 97(6), 2007.

[3] Pokorny, P.: Brachliegende Potenziale genutzt: Expansionsspritzgießen- eine neue Idee in der Dünnwandtechnik, KU Kunststoffe, 91 (7) 2001.

[4] Steinbichler, G.: Präzisionsspritzgießen- Maschinen und prozesstechnische Besonderheiten, 17. Leobener Kunststoff-Kolloguium, 2003.

[5] Steinbichler, G.; Lampl, A.; Pöttler, A.: Amazingly thin, Kunststoffe Plast Europe, 12, 2004.

[6] N.N.: Company brochure, Firmenschrift über Hydrospeicher, Hydac International GmbH, Sulzbach, 2004.

[7] Lampl, A.: Expansionsspritzgießen, eine Variante der Spritzgießtechnik, Österr. Kunststoff-Zeitschrift, 37, 2006.

[8] Rogelj, S.; Krajnc, M.: Pressure and Temperature Behaviour of Thermoplastic Polymer Melts During High-Pressure Expansion Injection Moulding. Polymer Engineering And Science, 48 (9), p. 1815-1823, 2008.

[9] Langecker, G. R.: Druckentspannungsspritzgießen- Prozessbeschreibung. Internal report, Institute of Polymer Processing, Montanuniversitaet Leoben. 2006.

[10] Rajganesh, J.; Friesenbichler, W.; Langecker, G.; Steinbichler, G.: Physical Model for the Expansion Injection Molding Process and Degradation Effects on the Injection Molded Parts due to Extreme Processing Conditions. 25th Polymer Processing Society meeting (PPS-25) Program & Abstracts. 2009.

[11] Rajganesh, J.; Friesenbichler, W.; Steinbichler, G.: Virtuelle Prozessauslegung beim Expansionsspritzgießen. Kunststoffe, 10, p. 204 - 208, 2010.

[12] Rajganesh, J.; Friesenbichler, W.; Steinbichler, G.: Virtual Process Design in Expansion Injection Molding. Kunststoffe international, 10, p. 148 -152, 2010.

[13] Friesenbichler, W.; Rajganesh, J.; Steinbichler, G.; Aust, N.: Physical model for the expansion injection molding process and degradation effects on the injection molded parts. 4th International PMI Conference - Conference Proceedings, p. 220 - 226, 2010.

[14] Steinbichler, G.: Methoden und Verfahren zur Optimierung der Bauteilentwicklung für die Spritzgießfertigung. Dissertation, Universitaet Erlangen-Nuernberg, 2008.

[15] Vetter, K.; Jungmeier, A.; Kühnert, I.; Ehrenstein, G.W.: Expansion-injection-molding (EIM) by cavity near melt compression. The Global conference on micro manufacture 4M/ICOMM, p. 115-118, 2009.

[16] Hellwege, K.H.; Knappe, W.; Lehmann, P.: Die Wärmeausdehnung einiger teilkristalliner Hochpolymerer im Temperaturbereich von -60 bis +300 °C. Kollloid-Zeitschrift & Zeitschrift für Polymere, 183 (1), p. 29-36,1962.

[17] Menges, G.; Thienel, P.; Kremper, W.: Physical Behavior of Thermoplastics When Plotting p-v-T Diagrams Under Various Measuring Conditions. Plastverarbeiter, 28, p.632-637, 1977.

[18] Menges, G.; Thienel, P.: Measuring Device for Recording pvT Curves at Practical Cooling Rates. Kunststoffe, 65, p.696-699,1975.

[19] Rudolph, N.; Kühnert, I.; Schmachtenberg, E.; Ehrenstein, G.W.: Pressure solidification of Amorphous Thermoplastics. Polymer Engineering and science, p. 154-161, 2009.

[20] Kennedy, P.: Flow Analysis of Injection Molds. Carl Hanser Verlag, Munich, Vienna, New York, 1995.

[21] Schümmer, P.; Worthoff, R.H.: An elementary method for the evaluation of a flow curve. Chemical Engineering Science, 38, p.759-763,1978.

[22] N, N.: Cadmould Handbuch, Bedienungsanleitung der Simcon kunststofftechnische Software GmbH, Herzogenrath, 2005.

[23] Viana, J.C.: Development of the skin layer in injection moulding: Phenomenological model. Polymer, 45, p. 993-1005, 2004.

[24] Dietz, W.; White, J.L.: Ein einfaches Modell zur Berechnung des Druckverlustes während des Werkzeugfüllvorganges und der eingefrorenen Orientierung beim Spritzgießen amorpher Kunststoffe. Rheologica Acta, 17(6), p. 676-692, 1978.

[25] Dietz, W.: Die Wärme- und Temperaturleitfähigkeit von Kunststoffen. Colloid and Polymer Science, 255, p.755-772,1977.

[26] Lampl, A.:Näherungsweise Berechnung der optimalen Füllzeit. Unpublished internal report, Engel Austria GmbH, Schwertberg, 2008.

[27] Casey D. Doyle.: MS Office 97 Visual Basic Programmer's Guide (Microsoft Professional Editions Series), Microsoft Press, 1997.

[28] Microsoft® Excel-Visual Basic® programmer's guide (Microsoft professional editions). Microsoft Press, 1995.

[29] Jacobson, R.: Microsoft Excel/Visual Basic step by step. McGraw-Hill Osborne Media, 2004.

[30] Liengme, B.: A guide to Microsoft Excel for scientists and engineers. Butterworth-Heinemann, 1997.

[31] Korol, J.: Excel 2003 VBA programming with XML and ASP. Dreamtech Press, 2006.

[32] Kipperer, M.: Stoffdatenmessung an drei für das Expansionsspritzgießen geeigneten Materialien, Bachelorarbeit am Institut für Kunststoffverarbeitung, Montanuniversität Leoben, 2008.

[33] PP HG 313 MO, Material data sheet: URL: http://www.borealisgroup.com/datasheets/ 10015499, heruntergeladen 2007.

[34] PS 495F, Datenblatt: URL: http://www.basf.com/plastics, heruntergeladen 2008.

[35] Bayblend T65, Datenblatt: URL:http://plastics.bayer.com/ plastics/emeal/n/ product/bablend/product_datasheets/Bayblend_T65_ISO/gradeId-9087/data sheethtml.jsp, heruntergeladen 2010.

[36] Patrick, A. R.: Pressure-volume-temperature relationships for polymeric liquids: A review of equations of state and their characteristic parameters for 56 polymers. Journal of applied polymer science, 48, p.1061 -1080, 1993.

[37] Osswald, T.A.; Menges, G.: Materials science of polymers for engineers, Hanser Verlag, 2003.

[38] Ehrenstein, G.; Riedel, G.; Trawiel, P.: Praxis der Thermischen Analyse von Kunststoffen, 2. Auflage, Carl Hanser Verlag, München, 2003.

[39] Langecker, G.R.: Vorlesungsunterlagen aus Kunststoffverarbeitung I. Montanuniversität, Leoben. 2006.

[40] Juster, H.: pvT-Daten für Polypropylen und Expansionspritzgießversuche mit vergleichender Prozess-Simulation und Molmassenbestimmung, Bachelorarbeit am Institut für Kunststoffverarbeitung, Montanuniversität Leoben, 2010.

[41] Mach. M.: Messung der Druckabhängigkeit der Viskosität an zwei für das Expansionsspritzgießen geeigneten Polymeren, Bachelorarbeit am Institut für Kunststoffverarbeitung, Montanuniversität Leoben, 2010.

[42] Narnhofer, M.: Untersuchungen zur Druck- und Temperaturabhängigkeit der Viskosität und der Wärmeleitfähigkeit von polymeren Werkstoffen, Masterarbeit am Institut für Kunststoffverarbeitung, Montanuniversität Leoben, 2010.

[43] Vlachopoulos J., Strutt D.: The Role of Rheology in Polymer Extrusion, http://www.polydynamics.com/Role_of_Rheology_in_Extrusion.PDF [accessed July 21, 2008].

[44] Takahashi, H.; Matsuoka, T.; Kurauchi, T.: Rheology of Polymer Melts at High Shear Rate. J. Applied Polymer Science, 30, p.4669-4684, 1985.

[45] Takahashi, H.; Matsuoka, T.: Rheological Behaviour of SAN/PC Blends Under Extremly high Shear rates. J. Applied Polymer Science, 37, p.1837-1853, 1989.

[46] Haddout, A.; Villoutreix, G.: Polymer Melt Rheology at High Shear Rates. International Polymer Processing XV, 3, p. 291-296, 2003.

[47] Maxwell, B.; Jung, A.: Hydrostatic pressure effect on polymer melt viscosity. Mod. Plastics, 35, p. 174-182, 1957.

[48] Lobo, H.; Bonilla, J.V.: Handbook of plastic analysis, Marcel Dekker, Inc., New York, 2003.

[49] Cardinales, R.: Evaluation and comparision of routes to obtain pressure Coefficients from high-pressure capillary rheometry data. Rheological Acta, 46, p. 495-505, (2007).

[50] Couch, M.A.; Binding, D.M.: High pressure capillary rheometry of polymeric fluids. Polymer, 41, p. 6323-6334, 2000.

[51] Sedlacek, T.; Zatloukl, M.; Filip, P.; Boldizar, A.; Saha, P.: On the effect of pressure on the shear and elongational viscosities of polymer melts. Polym Eng Sci, 44, p.1328–1337, 2004.

[52] Laun, H.M.: Pressure dependent viscosity and dissipative heating in capillary rheometry of polymer melts. Rheol Acta, 42, p. 295–308, 2003.

[53] Goubert, A.; Vermant, J.; Moldenaers, P.; Göttfert, A.; Ernst, B.: Comparison of measurement techniques for evaluating the pressure dependence of viscosity. Appl Rheol, 11, p. 26–37, 2001.

[54] Hay, G.; Mackay, M.E.; Awati, K.M.; Park, Y.: Pressure and temperature effects in slit rheometry. J Rheol, 43, p. 1099–1116, 1999.

[55] Koran, F.; Dealy, J.M.: A high pressure sliding plate rheometer for polymer melts. J Rheol, 43, p.1279–1290, 1999.

[56] Kadjick, S.E.; van den Brule, B.H.A.A.: On the pressure dependency of the viscosity of molten polymers. Polym Eng Sci, 34, p.1535–1546, 1994.

[57] Laun, H.M.: Polymer melt rheology with a slit die. Rheol Acta, 22, p.171–185, 1983.

[58] Penwell, R.C.; Porter, R.S.; Middleman, S.: Determination of the pressure coefficient and pressure effects in capillary flow. J Polym Sci, 9(2), p. 731–745, 1971.

[59] Choi, S.Y.: Determination of melt viscosity as a function of hydrostatic pressure in an extrusion rheometer. J Polym Sci, 2 (6), p. 2043–2049, 1968.

[60] Semjonow, V.: Über ein Rotationsviskometer zur messung der druckabhängigkeit der Viskositat Hochpolmers schmelzen. Rheol Acta, 2, p.138–143, 1962.

[61] Dudvani, I.J.; Klein, I.: Analysis of polymer melt flow in capillaries including pressure effects. SPE Journal, p. 41-45, 1967.

[62] Utracki, L.A.: Pressure dependency of Newtonian Viscosity. Polym. Eng. Sci., 23, p. 446-451, 1983.

[63] Utracki, L.A.: A Method of Computation of the Pressure Effect on Melt Viscosity. Polym. Eng. Sci., 25, p. 655-668, 1985.

[64] Park, H.E.: Measurement of pressure coefficient of melt viscosity: drag flow versus capillary flow. Rheo. Acta, 47, p. 1023-1038, 2008.

[65] Laun, H.M.: Capillary rheometry for polymer melts revisited. Rheol Acta, 43, p. 509–528, 2004.

[66] Agassant, J.F.: Polymer Processing: Principles & Modelling, Carl Hanser Verlag, Munich, Vienna, New York, 1991.

[67] Friesenbichler, W.: Polymer Melt Rheology at High Shear Rates using a new Micro-Rheology Technique. 21st Annual Meeting of the Polymer Processing Society, Leipzig, 2005.

[68] Duretek, I.; Friesenbichler, W.; Schuschnigg, S.; Jegadeesan, R.; Langecker G.R.: Study on Rheological Behaviour of Polymer Melts at High Shear Rates Using a New Micro-Rheology Technique, Conference of the Society of Plastic and Rubber Engineers, "The Past and the Future of Polymer Engineering, Technology and Science", Zagreb, p. 117-130, 2006.

[69] Schuschnigg, S.: Rheologiche Untersuchungen bei hohen Scher-gechwindigkeiten mit Hilfe eines Mikrorheologie-Schlizdüsen Messsystem, Diplomarbeit am Institut für Kunststoffverarbeitung, Montanuniversität Leoben, 2004.

[70] Selvasankar, R.: Rheological characterisation of polymer melts on an injection moulding machine using a new slit die measurement system, Master thesis at Institute of Plastics Processing, University of Leoben, 2008.

[71] N.N.: Produktbeschreibung - Gegendruckkammer für das Hochdruckkapillarrheometer, Göttfert Werkstoff-Prüfmaschinen GmbH, Buchen, Deutschland, 2002.

[72] Knappe, W.: Slip flow of non-plasticized PVC compounds. Rheological Acta, 25, p. 296-307,1986.

[73] Bader, C.: Rheologische Messungen auf der Spritzgießmachine – Aspekte zur Entwicklung eines Prozeßüberwachungssystems. Kunststoffe, 3, 1991.

[74] Amano, O.: Pressure dependent viscosity of polymer melts. ANTEC, p. 504-51, 2000.

[75] Kelly, A. L.: High shear strain rate rheometry of polymer melts. Journal of Applied Polymer science, 114, p. 864-873, 2009.

[76] Takahashi, H.: Rheology of polymer melts in high shear rate. Journal of Applied Polymer science, 30, 1985.

[77] Friesenbichler, W.; Rajganesh, J.; Lucyshyn, T.; Filz, P.; Webelhaus, K.: Measurement of pressure dependent viscosity and its influence on injection molding simulation. 4th International PMI Conference, Ghent, 2010.

[78] Friesenbichler, W.: New Rheological Injection Mould to Measure Pressure Dependent Viscosity in High Shear Rate Range. 25th Annual Meeting of the Polymer Processing Society, Goa, 2009.

[79] Friesenbichler, W.; Duretek, I.; Rajganesh Jegadeesan.: Praxisnahe Viskositäten für die Simulation. Kunststoffe, 3, p. 37 - 40, 2010.

[80] Lobo, H.:Thermal conductivity of polymers at high temperatures and pressures, ANTEC, p. 862-865,1990.

[81] Lobo, H.; Cohen, C.: Measurement of Thermal Conductivity of Polymer Melts by the Line source Method. ANTEC, p. 609-611, 1988.

[82] N, N.: Die thermische Leitfähigkeitsmessung, Produktbeschreibung der Göttfert Werkstoff-Prüfmaschinen GmbH, Buchen.

[83] URL: http://www.engelglobal.com/engel_web/global/de/media/de_prod_dl_e-motion_low.pdf (2009).

[84] Battisti, M.: Analyse des Prozessablaufs und des verarbeitungsbedingten Materialabbaus beim Expansionsspritzgießen, Masterarbeit am Institut für Kunststoffverarbeitung, Montanuniversität Leoben, 2010.

[85] Lederer, K.: Thermal degradation of polymeric materials. Polimeri, 14(6), p.253-257, 1993.

[86] Meyers, R.A.: Encyclopedia of Analytical chemistry - Size-exclusion chromatography of polymers, John Wiley & Sons Ltd, Chichester 2000

[87] Benoît, H.; Rempp, P.; Grubisic, Z.: A universal calibration for gel permeation chromatography. Journal of Polymer Science B, Polym. Lett, 5(9), p. 753-759, 1967.

14 List of symbols and units

Symbol	Description	Units
A_k	Compression work	J
a	Constant	-
a_{eff}	Effective thermal conductivity	m^2/s
a_T	Temperature shifting factor	-
a_{Tp}	Temperature and pressure shifting factor	-
A	Material constant of Carreau viscosity model	Pa.s
B	Material constant of Carreau viscosity model	s
C	Material constant of Carreau viscosity model	-
Br	Brinkmann number	-
Ca	Cameron number	-
B	Width	m
D	Diameter	m
C_v	Specific heat capacity at constant volume	
$c_{,p}$	Specific heat capacity at constant pressure	$J/kg \cdot K$
C_1	Material constant of WLF equation	
C_2	Material constant of WLF equation	
E_0	Activation energy	J/mol
F	Rest moisture	%
f	Frequency	Hz
H	Enthalpy	J
k_{die}	Die conductance	m^3
k'	Time constant	s
K_{1m}	Coefficient of pvT approximation for melt state	m^3 bar /g
K_{2m}	Coefficient of pvT approximation for melt state	m^3 bar /g °C

K_{3m}	Coefficient of pvT approximation for melt state	bar
K_{4m}	Coefficient of pvT approximation for melt state	bar
K_{1s}	Coefficient of pvT approximation for solid state	m^3 bar /g
K_{2s}	Coefficient of pvT approximation for solid state	m^3 bar /g °C
K_{3s}	Coefficient of pvT approximation for solid state	bar
K_{4s}	Coefficient of pvT approximation for solid state	bar
K_{5s}	Coefficient of pvT approximation for solid state	cm^3/g
K_{6s}	Coefficient of pvT approximation for solid state	1/°C
K_{7s}	Coefficient of pvT approximation for solid state	1/bar
K_8	Coefficient of pvT approximation for transition	°C
K_9	Coefficient of pvT approximation for transition	1/ bar
L	Length	m
L_i	Length of the segment i	m
M	Molar mass	g/mol
M_n	Number average molar mass	g/mol
M_w	Weight average molar mass	g/mol
M_z	Centrifugal average molar mass	g/mol
m_{sam}	Mass of the sample	g
m	mass of the shot weight	g
m_0	mass of the melt cushion	g
$\dot{m}$	mass flow rate	kg/s
n	power law exponent	-
p_E	End pressure	bar
p_c	compressions pressure	bar
p_{St}	back pressure	bar
$\dot{Q}$	Heat flow	J

R	Universal gas constant	$J/mol \cdot K$
r	Radius	m
R_i	Inner radius	m
R_a	Outer radius	m
s	Wall thickness	m
s_i	Wall thickness of the segment i	m
t_f	Filling time	s
t_c	Contact time	s
$t_{f\,app}$	Approximated filling time	s
T	Temperature	°C
T_g	Glass transition temperature	°C
T_K	Crystallization temperature	°C
T_M	Melt temperature	°C
T_{NO}	No-Flow Temperature	°C
T_W	Mould wall temperature	°C
$\overline{T}$	Average bulk melt temperature	°C
$\dot{V}$	Volume flow rate	m³/s
v	specific volume	m³/kg
$v\ (p_E, T)$	melt specific volume at end pressure	m³/kg
$v\ (p_c, T)$	melt specific volume at compression pressure	m³/kg
v_f	melt flow front velocity	m/s
V_{tot}	Part total volume	m³
V_i	Segmental volume of the segment i	m³
Z	Shot number for multi-shot EIM process	-
α_i	Coefficient of volume expansion	1/K
$\dot{\gamma}$	Shear rate	1/s

$\dot{\gamma}_{rep}$	Representative shear rate	1/s
δ	Thickness of the frozen skin layer	m
τ	Shear stress	Pa
η	Viscosity	Pa.s
η_0	Zero shear viscosity	Pa.s
η_{rep}	Representative shear viscosity	Pa.s
κ_i	Isothermal compressibiliy	1/Pa
β^*	Pressure coefficient of viscosity at constant shear stress	1/Pa
β_τ	Pressure coefficient of viscosity at constant shear stress	1/Pa
λ	Thermal conductivity	W/m K
ρ	Density	kg/m³
ϕ	consistency	$Pa^{-1/n}.s^{-1}$
Δs	Reduction in wall thickness	m
ΔL_s	Change in length of the screw	m
ΔV_s	Change in volume to due to elastic deformation	m